UPPER BOUND ANALYSIS FOR DRAG ANCHORS IN SOFT CLAY

A Dissertation

by

BYOUNG MIN KIM

Submitted to the Office of Graduate Studies of
Texas A&M University
in partial fulfillment of the requirements for the degree of

DOCTOR OF PHILOSOPHY

December 2005

Major Subject: Civil Engineering

UPPER BOUND ANALYSIS FOR DRAG ANCHORS IN SOFT CLAY

A Dissertation

by

BYOUNG MIN KIM

Submitted to the Office of Graduate Studies of
Texas A&M University
in partial fulfillment of the requirements for the degree of

DOCTOR OF PHILOSOPHY

Approved by:

Co-Chairs of Committee,	Charles Aubeny
	Don Murff
Committee Members,	Giovanna Biscontin
	Jerome J. Schubert
Head of Department,	David V. Rosowsky

December 2005

Major Subject: Civil Engineering

ABSTRACT

Upper Bound Analysis for Drag Anchors in Soft Clay. (December 2005)

Byoung Min Kim, B.S., Korea University;

M.S., Korea University

Co-Chairs of Advisory Committee: Dr. Charles Aubeny
Dr. Don Murff

This study presents an upper bound plastic limit analysis for predicting drag anchor trajectory and load capacity. The shank and fluke of the anchor are idealized as simple plates. The failure mechanism involves the motion of the anchor about a center of rotation, the coordinates of which are systematically optimized to determine the minimum load at the shackle. For a given anchor orientation, the direction of the shackle force is varied to establish a relationship between the magnitude and direction of the shackle load. Coupling this relationship to the Neubecker-Randolph anchor line solution produces a unique solution for the magnitude and orientation of the shackle force. The anchor is then advanced a small increment about the optimum center of rotation and the process is repeated. The upper bound method (UBM) provides a practical means to determine the trajectory of the anchor and the anchor load capacity at any point in the trajectory. To better understand of the anchor behavior, extensive parameter studies were carried out varying the properties of the anchor, anchor line, and soil. The UBM show good agreement with six full-scale tests covering several different anchor types and centrifuge model tests.

ACKNOWLEDGMENTS

I would like to acknowledge the support of Department of the Interior Minerals Management Service (Cooperative Agreement No. 1435-01-99-CA-31003), the Offshore Technology Research Center and his colleagues at Texas A&M University.

I would like to express my sincere thanks and gratitude to my advisor, Dr. Charles Aubeny for invaluable guidance and encouragement over the past three and half years.

I would also like to thank Dr. Don Murff for providing insight, guidance and suggestions. I am deeply impressed with his knowledge, idea, care and philosophy of life. In many senses, he has been a mentor and a father to me; he always shared his enthusiasm and knowledge in a most generous way and gave motivation.

I also appreciate Dr. Giovanna Biscontin and Dr. Jerome J. Schubert for serving on the advisory committee.

I deeply appreciate my Deborah. She has been always with me when I was depressed. Her encouragement and dedication enable me to finish my work.

Finally, I would like to thank my parents for having always believed in me. Without their support, I would never have achieved this work.

TABLE OF CONTENTS

CHAPTER Page

CHAPTER Page

CHAPTER Page

LIST OF FIGURES

FIGURE Page

FIGURE Page

FIGURE Page

FIGURE Page

FIGURE Page

FIGURE Page

FIGURE Page

FIGURE Page

FIGURE Page

FIGURE Page

FIGURE Page

LIST OF TABLES

TABLE Page

TABLE Page

CHAPTER I

INTRODUCTION

1.1 Offshore structures

Offshore production platforms include steel jackets and gravity structures. A jacket structure is supported by steel pipe piles, and gravity structures have massive mat foundations. In water depths deeper than 500m, conventional structures become impractical to install and maintain. Floating systems such as large floating structures moored to the seabed by anchors are being used for deeper water. These systems enable floating structures to remain on station, so that drilling and production operations can be carried out at a stable platform. Two different mooring systems are currently used in deep water-the catenary mooring system and the taut mooring system. An example of a spread mooring is shown in Fig. 1.1.

Anchorages for mooring systems can be provided by gravity anchors, anchor piles, drag anchors or suction caissons. Gravity anchors tend to be very inefficient for such systems. Installing piles in deep water is technically difficult and expensive. Although drag anchors are economically attractive, the uncertainties in installation and capacity dissuade operators from using them for permanent facilities.

This dissertation follows the style and format of the *Journal of Geotechnical and Geoenvironmental Engineering*.

The drag anchors are very attractive for anchoring moorings in deep water, because the cost for installation is relatively low. For this reason they have been widely used for temporary moorings. Drag anchors have high holding capacity relative to low anchor weight even in soft clay conditions. Moreover, they can be easily retrieved after completion of a project and reused on other projects.

For drag anchors, a priori prediction of depth of penetration and anchor holding capacity tends to be more uncertain than for other anchorage systems such as piles and suction caissons. Soil conditions, geometry and weight of the drag anchor, and size of anchor line influence depth of penetration and anchor capacity. Because of this complex behavior, operators have basically depended on empirical methods to predict depth of anchor penetration and anchor capacity (e.g., Naval Civil Engineering Laboratory, 1987).

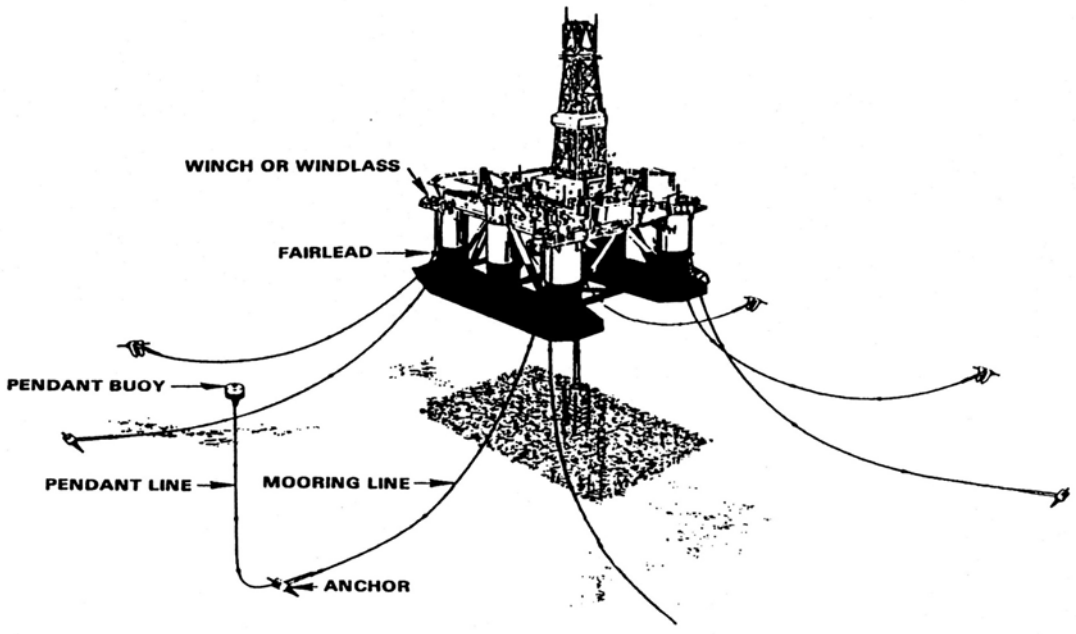

Fig. 1.1 Spread mooring system anchored to drag anchors (API 1995)

1.2 General description of drag anchor

Some of the first anchors consisted of large stones, baskets full of stones and sacks filled with sand. Steel was later used for anchors, with enhancements made by adding flukes to fix them to the bottom. However these anchors were often structurally weak and sometimes failed under load. Another improvement was made in the 19th century by removal of the stock, the crosspiece at the top of an anchor. This enables a fluke to fully penetrate into the soil. A stockless anchor was invented in 1821 and soon was in widespread use, because it is easy for handling and stacking. Stockless anchors are still used today.

The first commercial drag anchor was apparently developed by Hawkins in 1821 (Stewart, 1992). Since then large number of anchor types has been developed and commercialized. Some of them were improved while others disappeared. A drag anchor penetrates into the seabed, as it is dragged horizontally with wire or chain to generate a required capacity. A drag anchor can develop typical holding capacity of 5 to 55 times its self-weight. The holding capacity of a drag anchor is mobilized primarily by bearing resistance and side resistance on the anchor fluke and friction along the embedded portion of the mooring line.

Drag anchor designs have been primarily developed by trial and error based on many tests and field applications. A number of anchor types have been proposed as shown in Fig. 1.2.

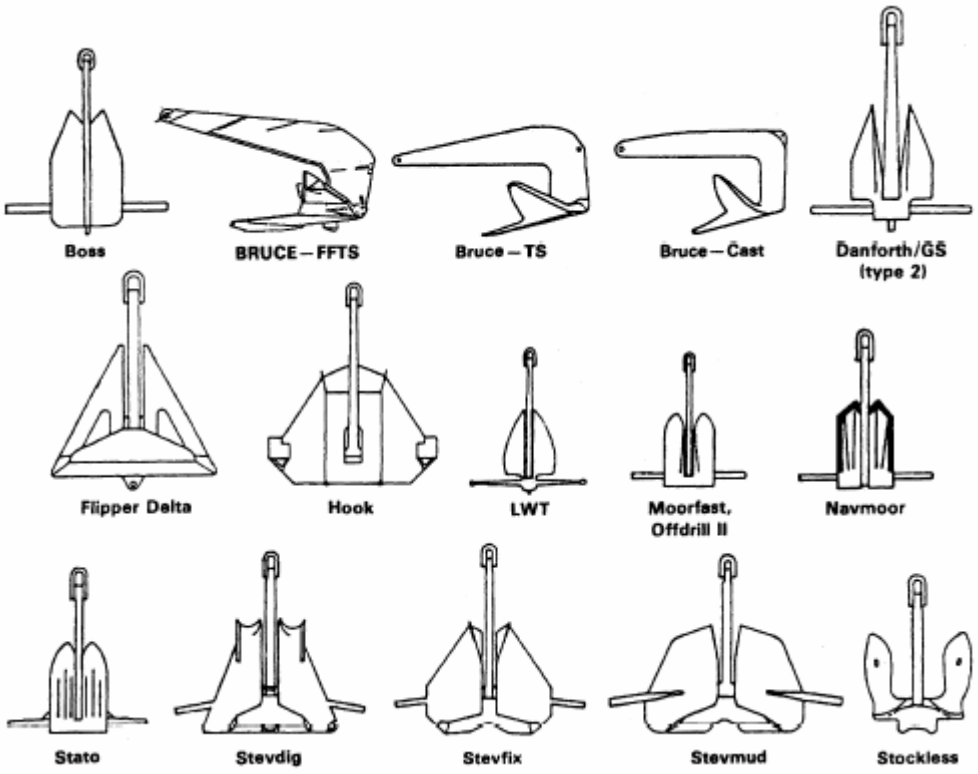

Fig. 1.2 Drag embedment anchors (NCEL, 1987)

Generally drag anchors consist of a fluke, a shank and an attachment point or a shackle as shown in Fig. 1.3.

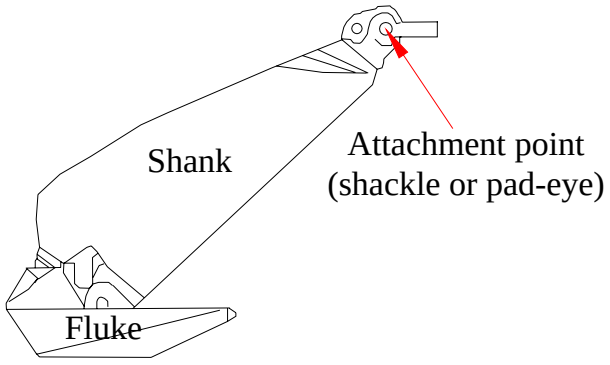

Fig. 1.3 Components of drag anchor system

1.3 Type of drag anchors

1.3.1 Drag embedment anchor (DEA)

Drag embedment anchors have been designed to penetrate into soil as deeply as possible to develop the maximum capacities of the fluke and shank as well as the anchor line. During an anchor embedment on seabed, penetration into the soil is typically achieved by dragging with an anchor-handling vessel (AHV). As the anchor penetrates, the anchor capacity increases with depth due to the increase in soil strength and the increased soil-anchor line contact.

Today drag embedded anchors are usually employed for temporary mooring systems with catenary mooring in deep water. Fig. 1.4 shows two of the most widely used drag embedded anchors for deep water. These anchors have twin shank to reduce resistance of soil and have high holding capacities.

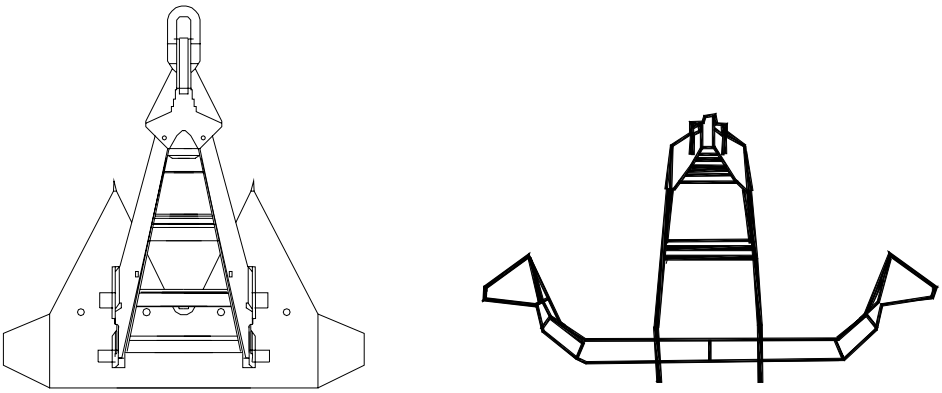

(a) Stevpris of Vryhof anchor (b) FFTS MK4 of Bruce anchor

Fig. 1.4 Drag embedment anchors

1.3.2 Vertically loaded anchor (VLA)

Vertically loaded anchors have been developed for taut mooring systems (TMS). The design allows the anchor to develop high vertical capacity and is appropriate for high angle loading. The anchor lines in a TMS have significant angles to the horizontal at the seabed to reduce the required anchor system footprint and to stiffen the mooring. It is a relatively complex operation to deploy the anchor line and it requires a high capability anchor handling vessels. Theses anchors are designed to resist both the vertical and horizontal loads. In this case, the fluke is connected to the anchor line by various methods such as through a connecting rigid bar (shank) or through a bridle arrangement as shown in Fig. 1.5. The anchor capacity is developed mainly by the fluke, which can be considered as a large bearing plate.

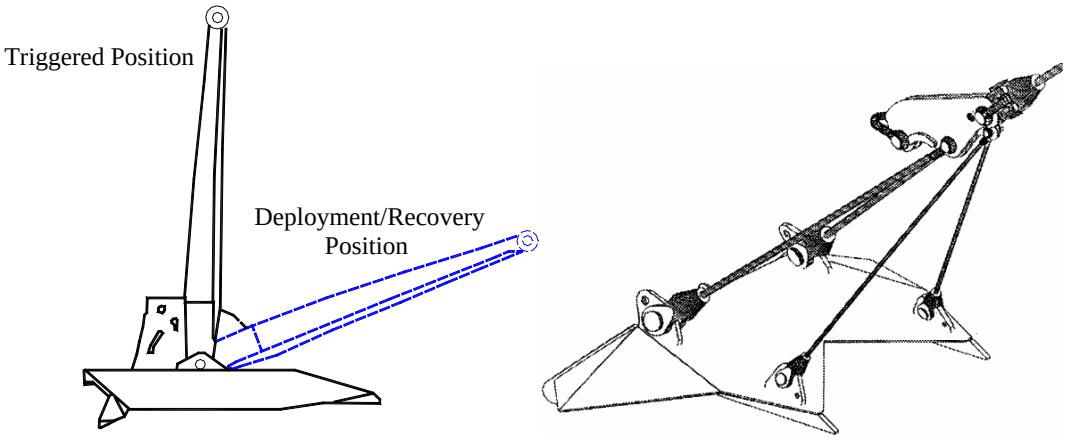

(a) Dennla MK3 (rigid bar) (b) Vryhof Stevmanta (bridle)

Fig. 1.5 Examples of vertically loaded anchor

The installation process of a VLA is similar to a DEA, but it is intended to penetrate deeper than a DEA. The anchor initially penetrates parallel to the fluke and rotates later in the process until the ultimate penetration is achieved. There are several methods used to “set the anchor” so that the fluke becomes approximately normal to the anchor line. This is achieved by a mechanical mechanism which modifies the anchor structure configuration. For example, the anchor can be set by a shear pin mechanism in both Bruce Dennla and Vryhof Stevmanta anchors. After the anchor reaches at a certain depth then shear pin is broken, and the anchor mode changes from installation to vertical loading. Fig. 1.6 shows the process of changing mode for the Vryhof Stevmanta anchor. In normal loading mode the anchor acts as an embedded plate with a high pull-out resistance (Murff and Anderson, 2001).

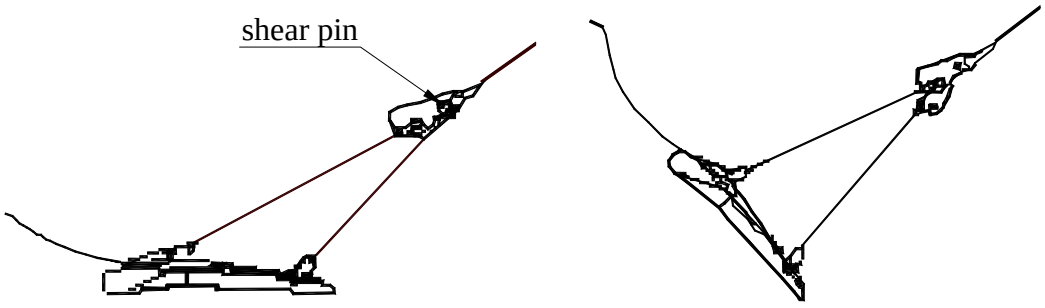

(a) installation mode (b) normal mode

Fig. 1.6 Type mode of the Stevmanta anchor (Vryhof 1999)

1.4 Installation of drag embedded anchors in clay

According to Vryhof Anchors (1999), the installation procedure of DEA generally consists of the following main steps.

1) Preparing the drag anchor and anchor line on the anchor handling vessel (AHV).
2) Adjusting the fluke-shank angle for the soil type.
3) Connecting the anchor line to the shackle.
5) Positioning the AHV for lowering the anchor. AHV moves to a distant location, generally less than the water depth from the rig.
6) The anchor is embedded on the seabed and it penetrates into the soil as the anchor is dragged by AHV.
7) Finishing installation when the anchor line load reaches to the design installation capacity.

As the drag anchor penetrates into the soil, the anchor line assumes a reverse curvature below the seabed as shown in Fig. 1.7 and its capacity increases with depth. Simultaneously, the anchor is dragged a certain horizontal distance until the requisite capacity is reached or until no further capacity gain is possible. After completing embedment, the anchor is able to develop anchor capacity larger than or equal to the installation load without further dragging of anchor.

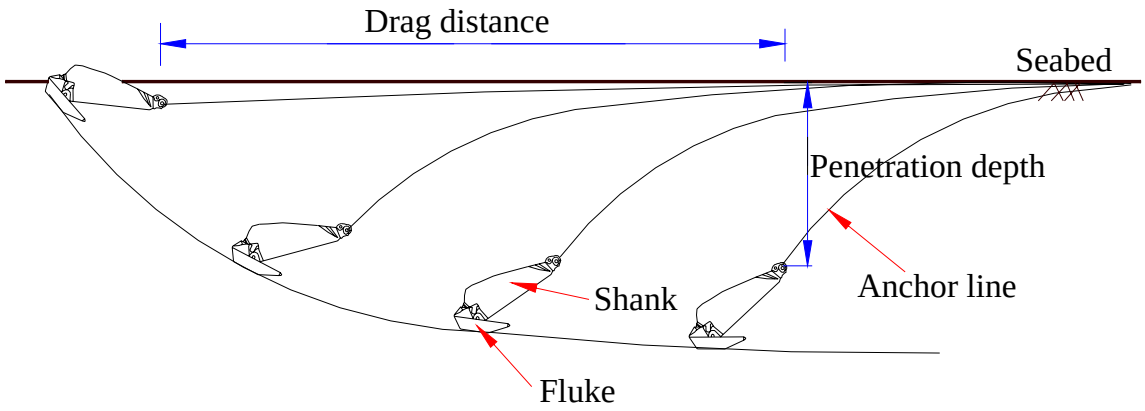

Fig. 1.7 Profile of penetration into seabed

1.5 Typical soil condition

Soil conditions of seabed are a most important factor for design of offshore structures. For clay soils the undrained soil strength profile is a key parameter for estimating of anchor behavior. In many offshore areas, the undrained shear strength increases with depth. However, in some areas, shear strength can be nearly uniform with depth or even layered in areas where the site history is more complex.

Soil conditions in deepwater such as in the Gulf of Mexico tend to be normally consolidated with small undrained shear strengths at the seabed, increasing linearly with depth. Undrained soil strength can be estimated by the equation;

$$S_u = A + B \times z \qquad (1.1)$$

where A = undrained shear strength at the seabed

B = shear strength gradient

z= depth below the mudline

The typical soil type in Gulf of Mexico (GOM) is highly plastic clay with liquid limits in range LL=65 to 100 and plastic limits on order of 25. In the case of deep water, the soil tends to be normally consolidated with high water contents of more than 100% at the seabed, decreasing as depth increases (Aubeny et al. 2001). Typical Gulf of Mexico strength profiles show that undrained soil strengths are typically 2-5 kPa at the seabed. Soil strength linearly increases with depth with a typical strength gradient ranging from 1.0 to 2.0 kPa/m. As shown in Fig. 1.8, the typical undrained soil strength profile in the GOM is within the shadow area.

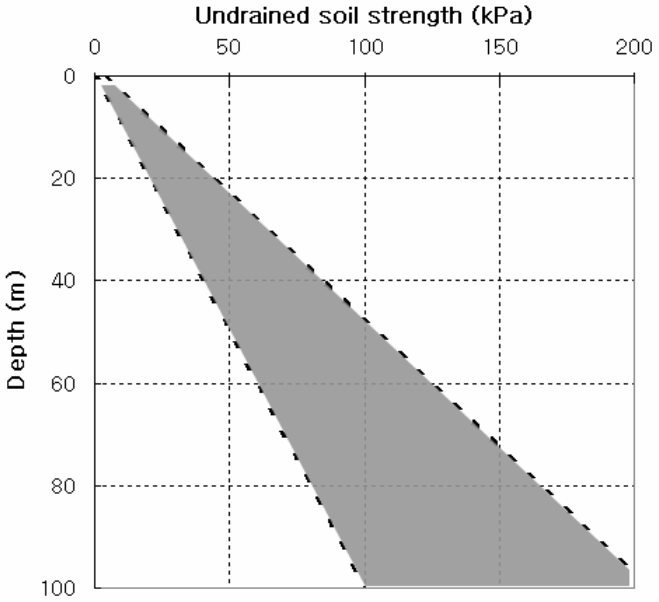

Fig. 1.8 Undrained shear strength profile in Gulf of Mexico

1.6 Objective of research

The objective of the research proposed herein is to develop a simplified model for predicting the capacity of plate anchors embedded in cohesive soils under general conditions of loading. The analytical studies are based on upper bound plastic limit analysis methods. The upper bound method will be applied to determine the anchor trajectory and the anchor capacity at any point in the trajectory consistent with the compatible anchor line behavior. The embedded drag anchor components are idealized as simple symmetric plates and bars connected to each other at fixed angles. The failure mechanism involves a rotation of the rigid anchor about a center of rotation to be determined in the analysis.

The anchor line force for a given embedment depth and anchor orientation is determined using an upper bound limit analysis approach. The analysis considers the anchor to experience a virtual rotation about some center of rotation. The anchor line force is determined by equating the rate of work performed by the anchor line and known anchor weight to the internal rate of energy dissipation associated with the anchor moving through the soil. The total energy dissipation rate is determined by integrating the unit dissipation over the various anchor surfaces. The upper bound analysis procedure produces a curve relating anchor line force to anchor line inclination angle at the pad-eye. The intersection of this curve with the anchor line equation yields a unique solution for anchor line force. The location of center of rotation is optimized by systematically varying it to find the minimum anchor line load. The anchor is then advanced a small increment by rotating about the optimum center of rotation. If the

center of rotation is an infinite distance from the anchor, then the anchor undergoes pure translation. If the center of rotation is near the anchor, then the anchor motion is primarily rotation.

This optimization process effectively identifies the specific failure mechanism that is as close to equilibrium as possible for the general mechanism in question. Because the failure mechanism selected includes all possible failure mechanisms, the optimized solution is the exact solution for the particular yield surface functions assumed. The proposed new method provides a practical means of estimating drag anchor load capacity and trajectory. In this study, results from the new proposed method will be compared with empirical methods, other equilibrium methods and field load tests.

CHAPTER II

BACKGROUND

2.1 Mooring system

Mooring systems are a basic component of floating offshore structures including floating drilling units, floating production systems and storage units used temporarily or permanently. Several different mooring system concepts have been developed for these applications.

The mooring line can be mainly classified as two types-catenary mooring system and taut leg mooring system. Both types of mooring system lines are generally consist of three parts - forerunner, middle line and top line. Depending on the mooring system requirements, the type of line for each part may be different. Table 2.1 shows the general mooring system used in current practice.

Table 2.1 Main components of mooring systems

	Mooring system	
	Catenary mooring system	Taut leg mooring system
Anchor type	Drag embedment anchor	Vertically loaded anchor
Forerunner	Chain	Wire
Middle part	Steel cable	Polyester cable
Top part	Chain	Chain

A forerunner is the part of an anchor line which is connected to the shackle point of the anchor and it is partially embedded into soil. The different types of forerunner can significantly affect penetration depth of the anchor during installation. For example, an anchor with a wire forerunner usually penetrates deeper than the same anchor with the chain forerunner as shown in Fig. 2.1, since shear and bearing resistance along the chain is larger that that of wire.

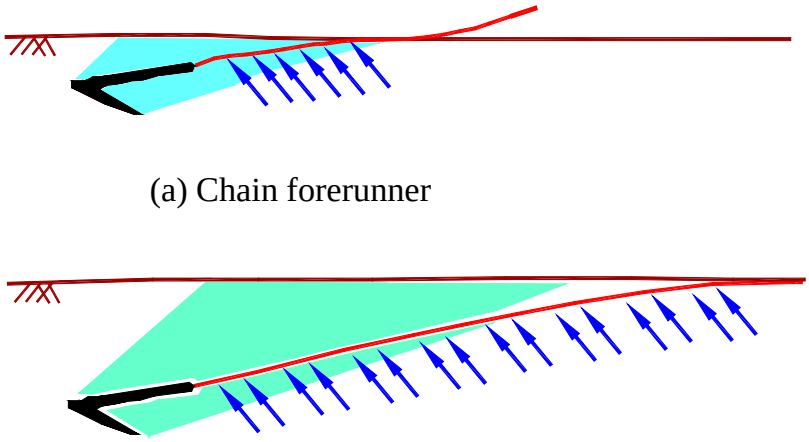

(a) Chain forerunner

(b) Wire forerunner

Fig. 2.1 The penetration of drag anchor in different forerunner (Vryhof 1999)

2.1.1 Catenary mooring system

Catenary mooring systems (CMS) are widely used in the offshore industry. A CMS is a conventional mooring system and requires a large footprint. It can be used to stabilize flexible structures in water depth of up to 1000m. The catenary mooring arrives at seabed horizontally as shown Fig. 2.2. Therefore, a CMS uses the horizontal force of the mooring lines to supply the restoring forces which maintain the moored unit on station. As water depth increases, the self-weight of mooring line and footprint become larger. Such a large footprint may interfere with neighboring mooring line or pipeline facilities.

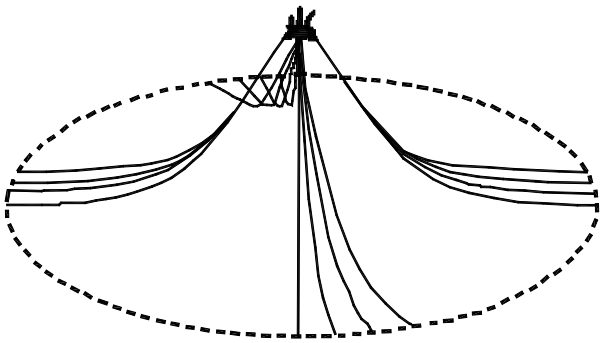

Fig. 2.2 Catenary mooring system (Ruinen 2000)

2.1.2 Taut leg spread mooring system

For exploration and production in deep water beyond 1000m, the weight of the mooring line discourages operators from using the catenary mooring system in the design of floating structures. For this reason taut leg mooring systems (TMS) have been developed. Taut Leg mooring systems are generally used for permanent or semi-permanent mooring systems such as floating production storage and offloading vessels (FPSO) and they require an anchor that can exert high vertical capacity. As suggested in Fig. 2.3, the taut leg mooring reaches the seabed at angles of 30 to 45. Thus, it can resist both horizontal and vertical forces, while catenary mooring system resists only horizontal forces at the seabed. Currently, synthetic fiber ropes are used with suction caissons, vertical loaded anchors, and a suction embedded plate anchors for taut leg mooring systems. For these reasons, a TMS has lighter, shorter, and much smaller footprint than that of a CMS.

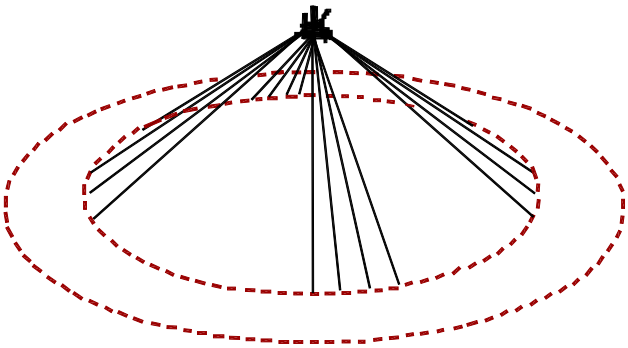

Fig. 2.3 Taut leg mooring system (Ruinen 2000)

2.2 Anchor line equation

As an anchor penetrates the forerunner cuts through the soil with the anchor and forms an inverse curvature as shown in Fig. 2.4.

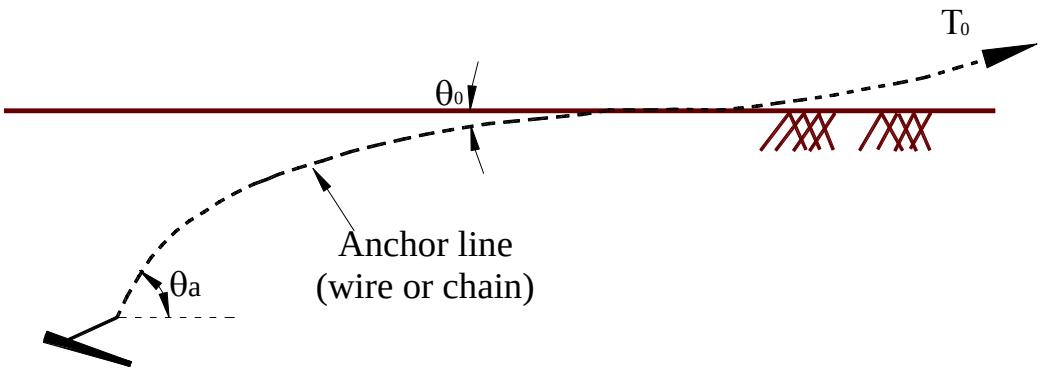

Fig. 2.4 General arrangement of drag embedded anchor and forerunner

Gault and Cox (1974) developed a solution for predicting the anchor line behavior. The governing differential equations including the self-weight of the anchor line as well as the soil bearing and frictional resistance was derived by Vivatrat et al. (1982).

$$\frac{dT}{ds} = F + w\sin\theta \qquad (2.1)$$

$$T\frac{d\theta}{ds} = -Q + w\cos\theta \qquad (2.2)$$

Where T = line tension load

θ = line angle of the tension force to the horizontal

ds =element length

w = buoyant weight of the line per unit length.

F = shearing resistance per unit length on line segment

Q = bearing resistance per unit length on line segment

They suggested a solution to these non-linear equations using an iterative finite difference method.

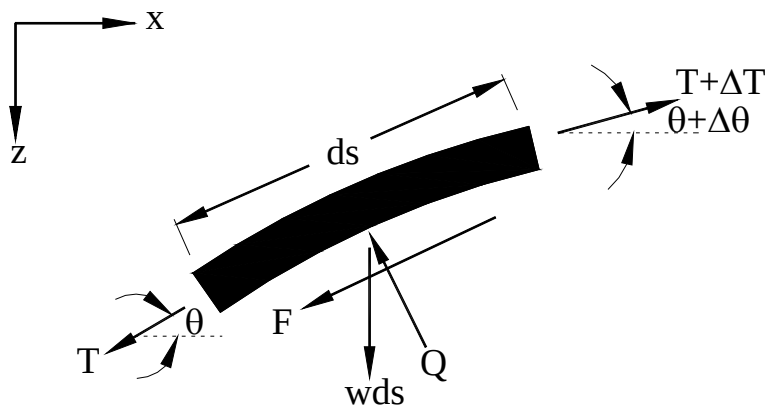

Fig. 2.5 Schematic of anchor line forces (Vivatrat et al., 1982)

Fig. 2.5 shows the shearing and bearing forces acting on a line element. The shearing component, *F*, is caused by the soil adhesion to the line and the bearing component, Q, is developed by soil normal resistance. Both *Q* and *F* represent the forces a unit length of anchor line and can be calculated by the following formulas using average stresses multiplied by effective diameter.

$$Q = (E_n d)q \tag{2.3}$$

$$F = (E_t d)f \tag{2.4}$$

The average stresses, q and f, can be expressed in terms of a resistance factor N_c and α, multiplied by the local soil shear strength, as

$$q = N_c s_u \tag{2.5}$$

$$f = \alpha s_u \tag{2.6}$$

where

d = effective anchor line diameter of the chain or wire

E_n, E_t = multipliers to account for the effective chain widths in the normal and tangential directions respectively. For wire, $E_n = E_t = 1$

N_c = bearing resistance factor for anchor line

α = adhesion factor = 1 for full adhesion; =0 for no adhesion

s_u = undrained shear strength

Table 2.2 Adhesion factor for wire and chain (DNV RP-E302, 1999b)

Wire	Lower bound	Default value	Upper bound
α_{soil}	0.2	0.3	0.4
Chain	Lower bound	Default value	Upper bound
α_{soil}	0.4	0.5	0.6

In many cases, α can be taken as $1/s_t$ where s_t is the sensitivity of clay. As indicated in Table 2.2, α typically varies from 0.2 to 0.6 and can be dependent on set-up time. Degenkamp and Dutta (1989), DNV RP-E302 and Vivatrat et al., (1982) discussed the values of E_n and E_t in relation to the geometry of standard anchor chains

based on model test results. They recommended the values as shown in Table 2.3. For chain the value of d is the diameter of the stock from which the chain is made.

Table 2.3 Recommended parameters for analysis of anchor line

Parameters	Recommended Value	
Multiplier for effective widths in the bearing direction (E_n)	Degenkamp and Dutta, 1989	2.5d
	DNV RP-E302, 1999b	2.6d
	Vivatrat et al., 1982	2.6d
Multiplier for effective widths in the shearing direction (E_t)	Degenkamp and Dutta, 1989	8.0d
	DNV RP-E302, 1999b	10d
	Vivatrat et al., 1982	10d
Bearing capacity factor (N_c)	Degenkamp and Dutta, 1989	5.1 ~ 7.6
	DNV RP-E302, 1999b	9 ~14
	Vivatrat et al., 1982	9 ~ 11
The relative magnitude of F and Q $\mu = \frac{F}{Q}$	Degenkamp and Dutta, 1989	0.4 to 0.6

Degenkamp and Dutta (1989) carried out laboratory modeling of anchor chains in clay. According to their results, N_c is 5.14 at the seabed and 7.6 at a depth of $2.4E_nd$. Neubecker and Randolph (1995) used this value in modeling performance of embedded anchor chains. But this value is lower than that of other researchers suggested such as DNV(1999b) or Vivatrat et al., (1982). Using this information, Eqs. 2.1 and 2.2 can be solved for the relationship between line tension at the anchor line attachment point, T_a and line tension at a certain depth, T_o.

Neubecker and Randolph (1995) suggested a closed form solution to these equations by linearizing the equations i.e. they neglect anchor line weight and used small angle assumptions for θ. Their solution is given in the following equations.

$$T_o = T_a \exp^{\mu(\theta_a - \theta_o)} \tag{2.7}$$

$$\frac{T_a}{2}(\theta_a^{\,2} - \theta_o^{\,2}) \approx \int_z^{z_a} Q dz = (z_a - z)\overline{Q} \tag{2.8}$$

where θ_a = anchor line angle with horizontal at the anchor shackle

θ_o = anchor line angle with the horizontal at depth z

T_a = line tension at shackle

T_o = line tension at depth z

$\overline{Q}$ = average bearing resistance over the depth range z to z_a

z_a = depth to shackle from seabed

z = a generic depth between seabed and z_a at which line tension is desired

μ = relative magnitude of bearing and shearing forces

For a linearly increasing soil strength profile $\overline{Q}$ is expressed by the following

$$\overline{Q} = E_n d N_c \left[A + \frac{B(z_a + z)}{2} \right] \tag{2.9}$$

where A = undrained shear strength at the seabed

B = shear strength gradient with depth

For the general case where the line angle is nearly to zero at the seabed, Equation (2.8) can be simplified to

$$\frac{T_a \theta_a^{\,2}}{2} = z_a \overline{Q} \qquad (2.10)$$

This equation indicates the relationship between anchor line angle, θ_a and anchor line load at the shackle, T_a, directly in terms of the anchor depth and the average anchor line bearing resistance over depth.

It should be noted that self-weight of anchor line is not considered in Eqs. 2.8 and 2.10. The anchor line weight does not play a key role in the case of hard soils, but can be important in soft soils near the mudline. Here the anchor line can penetrate due to its self-weight. It should be noted that Neubecker and Randolph (1995) suggested that this self weight can be considered in their solution by assuming the anchor line is weightless and thereafter reducing the profile of bearing resistance per unit length by an amount corresponding to the anchor line weight per unit length.

2.3 Anchor capacity

Anchor capacity is primarily influenced by fluke area and penetration depth. Thus it is increased with increasing fluke area and penetration depth. When the anchor reaches ultimate holding capacity, it can not resist any additional load, i.e. it will fail.

2.3.1 Failure mechanism of anchor failure

Anchor failure mechanisms can be divided into two types as shown in Fig. 2.6. In the case of a shallow anchor, the failure mechanism will be a slip surface extending from the anchor to the soil surface as shown in Fig. 2.6a and 2.6b. In the case of a deep anchor, the failure is contained within the soil as shown in Fig. 2.6c. Fig. 2.7 shows displacement vectors in a deep failure mechanism. In this figure, displacement vectors flow from the upper surface of the anchor plate to the lower surface. These failure mechanisms are supported by numerical analysis by Merifield (1999) and O'Neill et al.(2003).

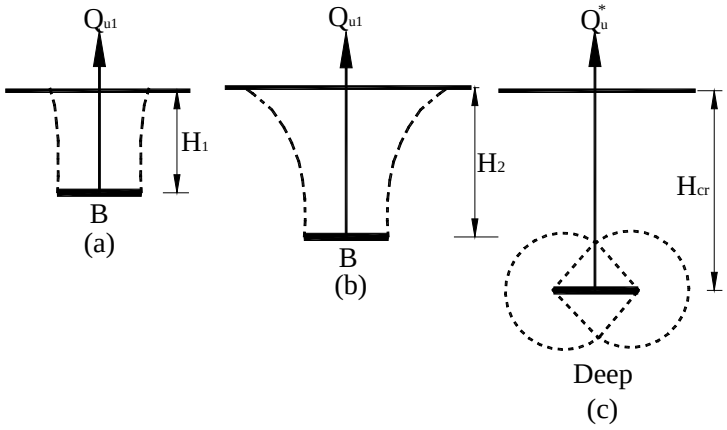

Fig. 2.6 Shallow and deep anchor behavior (Merifield 2003)

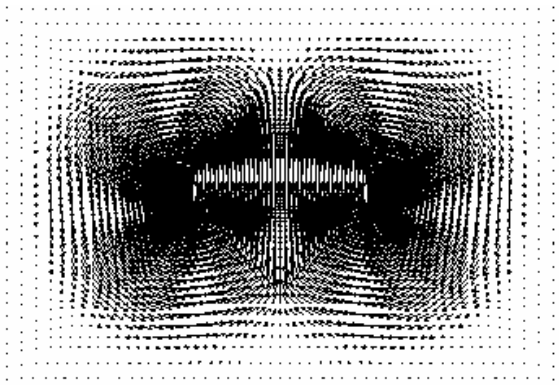

Fig. 2.7 FE calculated soil displacements in deep anchor (O'Neill et al. 2003)

2.3.2 The bearing capacity factor, N_c

The bearing capacity factors, N_c, can be determined using various techniques such as the limit analysis or finite element methods to solve the governing equations. Typical values of bearing factors from 9 to 15 for deeply embedded plate anchors (Foxton, 1997).

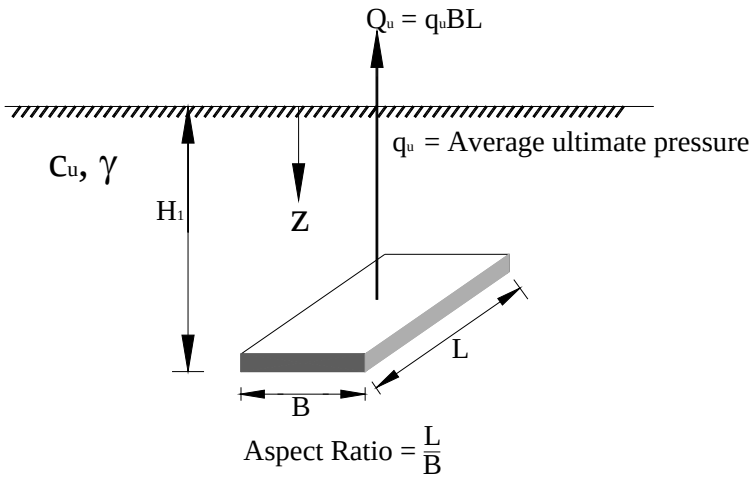

Fig. 2.8 Rectangular anchor in clay (Merifield 2003)

$$q_u = \frac{Q_u}{A} = c_u N_c \tag{2.11}$$

where A= anchor area

c_u = undrained soil strength

N_c =bearing capacity factor

N_c is a function of the embedment ratio (H/B) and shape of fluke, and is expression in terms of the normalized quantity, $\gamma H / c_u$. Ultimate anchor capacity increases with depth to a limiting value as shown in Fig. 2.9. This limiting value indicates that the anchor develops a deep failure mechanism.

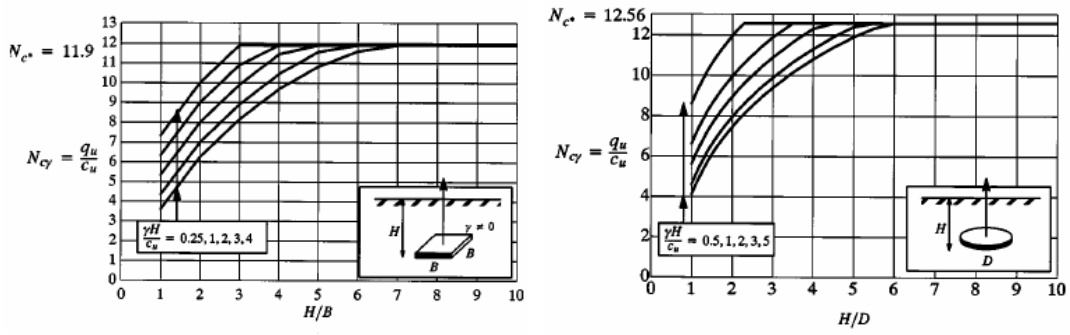

(a) square anchor (b) circular anchor

Fig. 2.9 Effect of overburden pressure in clay (Merifield 2003)

Assuming the anchor develops a fully plastic failure mechanism, Graaf et al. (1997) suggested an N_c of 12.6 for deeply embedded anchor plates. Neubecker and Randolph (1996b) employed an N_c of 9 for analytical solutions of drag embedment anchor performance. Merifield et al. suggested a limiting N_c of 11.16 for infinite strip

anchor (2001), and 11.9 for square plate anchor (2003). O'Neill et al.(2003) suggested an N_c of 11.87 for a rectangular anchor in deep depth.

2.4 Factors influencing the behavior of anchors

Anchor capacity can vary depending on whether an anchor is being installed or is in use currently. During installation, the anchor penetrates until the required resistance is achieved. After completing penetration, the anchor has a "holding capacity" which is greater than or equal to the installation load without any additional penetration. If the applied load exceeds the capacity at a given depth of penetration, the anchor can penetrate until the soil is able to resist the applied load or until it reaches its ultimate capacity (Ruinen and Degenkamp 1999). However, in some cases the anchor exerts a resistance larger than the installation load without further penetration. This implies that some factors have influenced the capacity of the anchor since installation. A number of researchers have conducted tests to determine what factors affect the anchor capacity. Based on the results of these tests, several important factors have been identified and are described below.

2.4.1 Effect of consolidation

During penetration the anchor disturbs the soil and the soil strength is weakened temporarily. After the anchor installation is complete, the soil reconsolidates and its strength regains as time elapses. The time required to reconsolidate depends on the soil type. In an analytical model this can be described by the adhesion factor, which depends on the soil sensitivity, S_t. The ratio between the undisturbed, undrained shear strength, S_u, and remolded strength, S_r is as follows;

$$S_t = S_u / S_r \tag{2.12}$$

Because not all of the soil adjacent to the anchor is disturbed, the set-up effect factor is less than the sensitivity index indicates. The minimum α is usually defined by a reciprocal of the sensitivity, i.e.

$$\alpha_{\min} = 1/S_t \tag{2.13}$$

The degree of consolidation that can be applied to the side resistance of fluke and shank can be evaluated by investigating the drainage characteristics adjacent to the drag anchor. The amount of disturbance is affected by the anchor geometry and soil characteristics such as sensitivity (DNV 1999a, RP- E301).

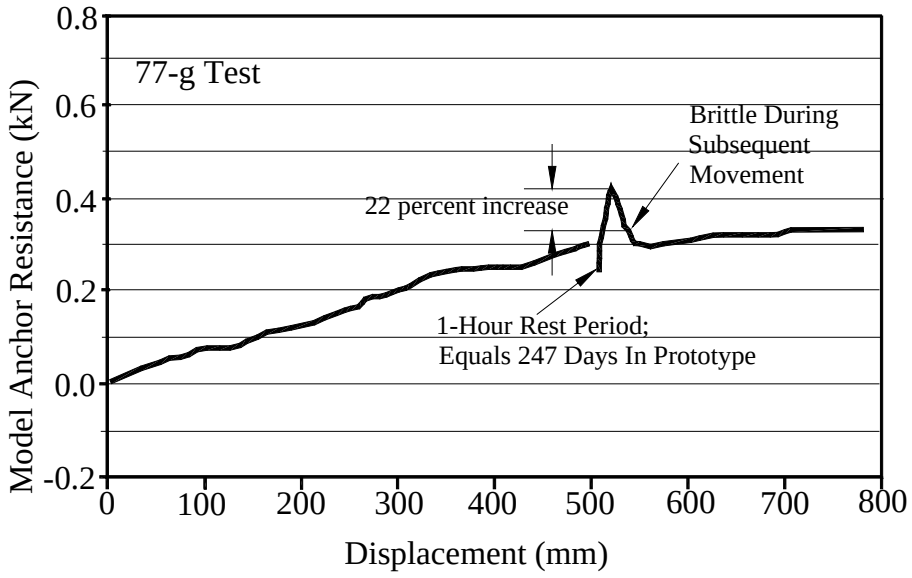

Fig. 2.10 Effects of anchor consolidation for 15 kips prototypes (Dunnavant and Kwan, 1993)

Dunnavant and Kwan (1993) tested centrifuge models of Vryhof Stevpris anchors with prototype weights of 1.1kips and 15kips. Fig. 2.10 shows the measured relationship between the anchor resistance and the drag distance for the model anchor in one test. As shown in Fig. 2.10, the anchor penetrated and stopped at a 500mm (38.5m prototype) of drag distance, after one hour (247 days prototype) of centrifuge time the anchor resistance increased 22 percent. However the increased capacity was lost by a little displacement of anchor. This implies that consolidation makes the anchor capacity higher but this increased strength has a brittle behavior as shown in Fig. 2.10. This effect should be considered in cases when the anchor installation process is disrupted and the anchor has to be penetrated further.

2.4.2 Effect of cyclic loading

Cyclic loading due to hurricanes, storms or waves can also influence undrained shear strength of the soil in the adjacent to the anchor. Dunnavant and Kwan (1993) tested anchors after cyclically loading them. This study indicates how cyclic loading affects the resistance of drag anchors in soft clay.

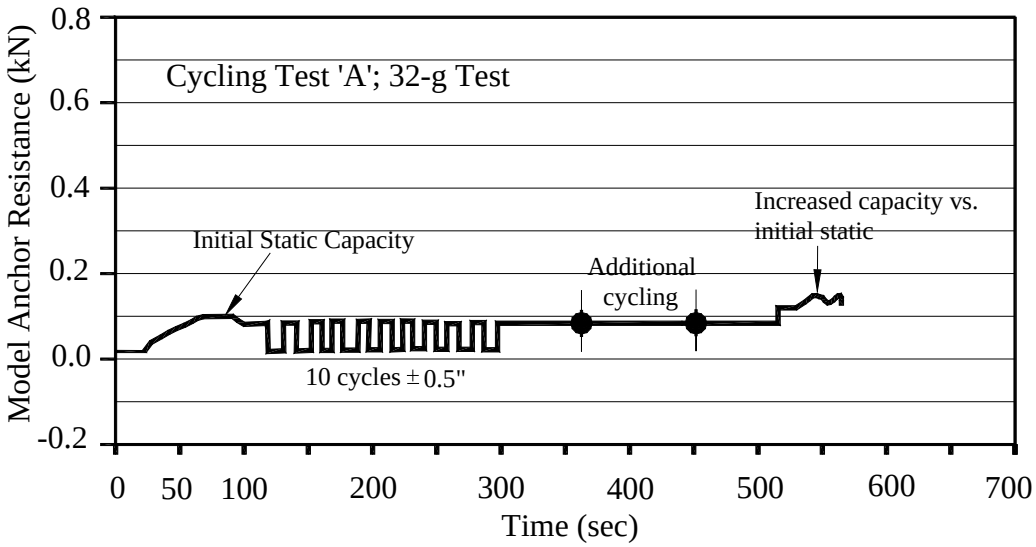

Fig. 2.11 Effects of cyclic loading (Dunnavant and Kwan, 1993)

Fig. 2.11 shows that anchor capacity is increased by 20 to 50% of initial static capacity after experiencing cycling load, partly because of the further penetration of the anchor.

2.4.3 Effect of loading rate

Increasing the loading rate also increases the soil resistance, so that the anchor holding capacity increases with respect to total dynamic loads (Vryhof 1999). The tests of Stevamanta and Denla anchors carried out in Onsϕy, Norway in 1998 showed that a reduction in the loading speed resulted in an immediate drop in line tension amounting to about 15 to 20 % per 1-2m/min of magnitude change in speed (Dahlberg and Strøm, 1999).

The loading rate affects pore-pressure dissipation and viscous inter-granular forces. The higher loading rate reduces the rate of pore water dissipation which tends to decrease capacity but increases viscous inter-granular forces which leads to an increase in the anchor capacity. This behavior is consistent matched with research on the effect of loading rate of axial pile capacity under undrained conditions (Bea and Audibert, 1979). From this study they suggested the following relationship.

$$Q_1 / Q_2 = U_r \tag{2.14}$$

$$U_r = (v_1 / v_2)^n \tag{2.15}$$

where Q_1 and Q_2 represent the pile capacity at loading rates v_1 and v_2

U_r = Loading rate factor

n = Dimensionless exponent

If this relationship is directly applied to the anchor problem, it suggests that the capacity of the anchor under design loading can be increased beyond that for installation

conditions. As shown in Fig. 2.12, Vryhof Anchors (1999) suggested 1.1 to 1.3 as loading rate factors for anchors embedded in clay soils. In this figure, the two curves represent undrained shear strength of 10kPa and 50kPa, respectively. The loading rate factor can be used to estimate the maximum anchor capacity under design loading conditions after installation of anchor.

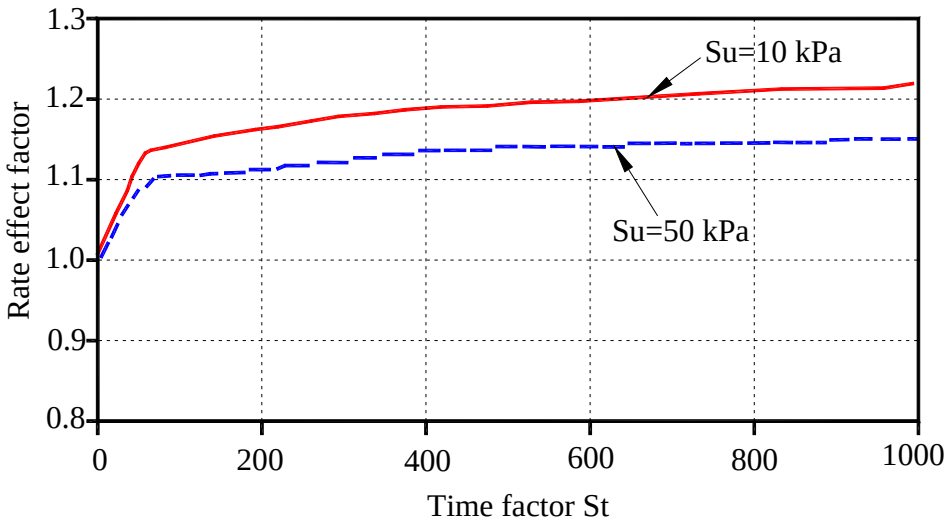

Fig. 2.12 Effects of loading rate (Vryhof 1999)

CHAPTER III

OVERVIEW OF EXISTING METHOD

There are three general appearances that have been used to estimate drag anchor capacity, empirical methods, limit equilibrium methods, and plastic limit analysis methods. These are discussed in detail in the following sections.

3.1. Empirical method (design chart)

3.1.1 NCEL method

The Naval Civil Engineering Laboratory (NCEL, 1987) developed a convenient empirical prediction method to predict anchor capacity. While developing this method, NCEL carried out many prototype scale anchor tests under various soil conditions. The tests were conducted to evaluate the anchor performance and application of diverse Navy and commercial drag anchors. According to test results, the anchor capacity increases with anchor weight. This correlation has been formulated the simple equation.

$$F = a \times (\frac{W_a}{C})^b \qquad (3.1)$$

where F =anchor capacity in kip

a = parameter for capacity in kips

W_a =anchor weight in kips

b= exponent constant

C= 10 kips

The parameters *a* and *b* have been suggested by NCEL for diverse anchors. As an example, the suggested values of *a* and *b* are *a* = 250 kips, *b* = 0.92 and *a* = 189 kips, *b* = 0.92 for Bruce FFTS and Vryhof Stevpris anchors, respectively. Fig. 3.1 shows the relation between anchor capacity and anchor weight on a log-log plot. Fig. 3.2 shows anchor capacity versus drag distance. This plot was developed based on the field tests mentioned previously. From these charts, the capacity at a certain drag distance can be estimated. As discussed in Section 2.2, anchor performance is affected by anchor geometry and weight as well as by the characteristics of the anchor line. It should be noted that the NCEL charts have been developed using chain anchor lines. Therefore, there is uncertainty in predicting performance of anchor with wire anchor lines. Some anchor manufacturing companies, for instance Bruce and Vryhof Anchors, have developed their own charts for anchor capacity and penetration depth in various soil conditions for each of their commercial anchor types. These charts will be discussed in Section 3.1.2 and 3.1.3 for Vryhof and Bruce anchors, respectively.

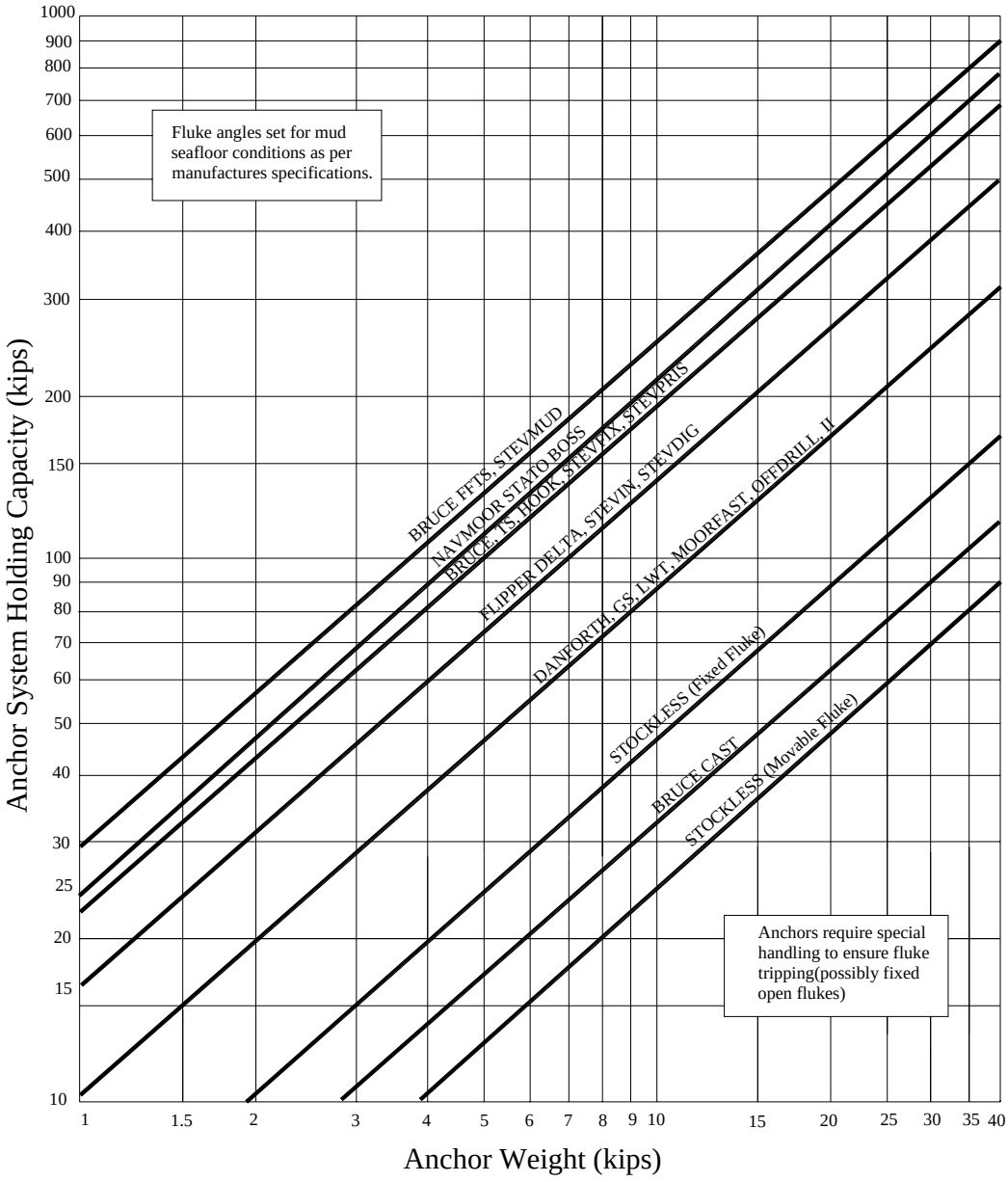

Fig. 3.1 Design chart for anchor capacity in Clay (NCEL, 1987)

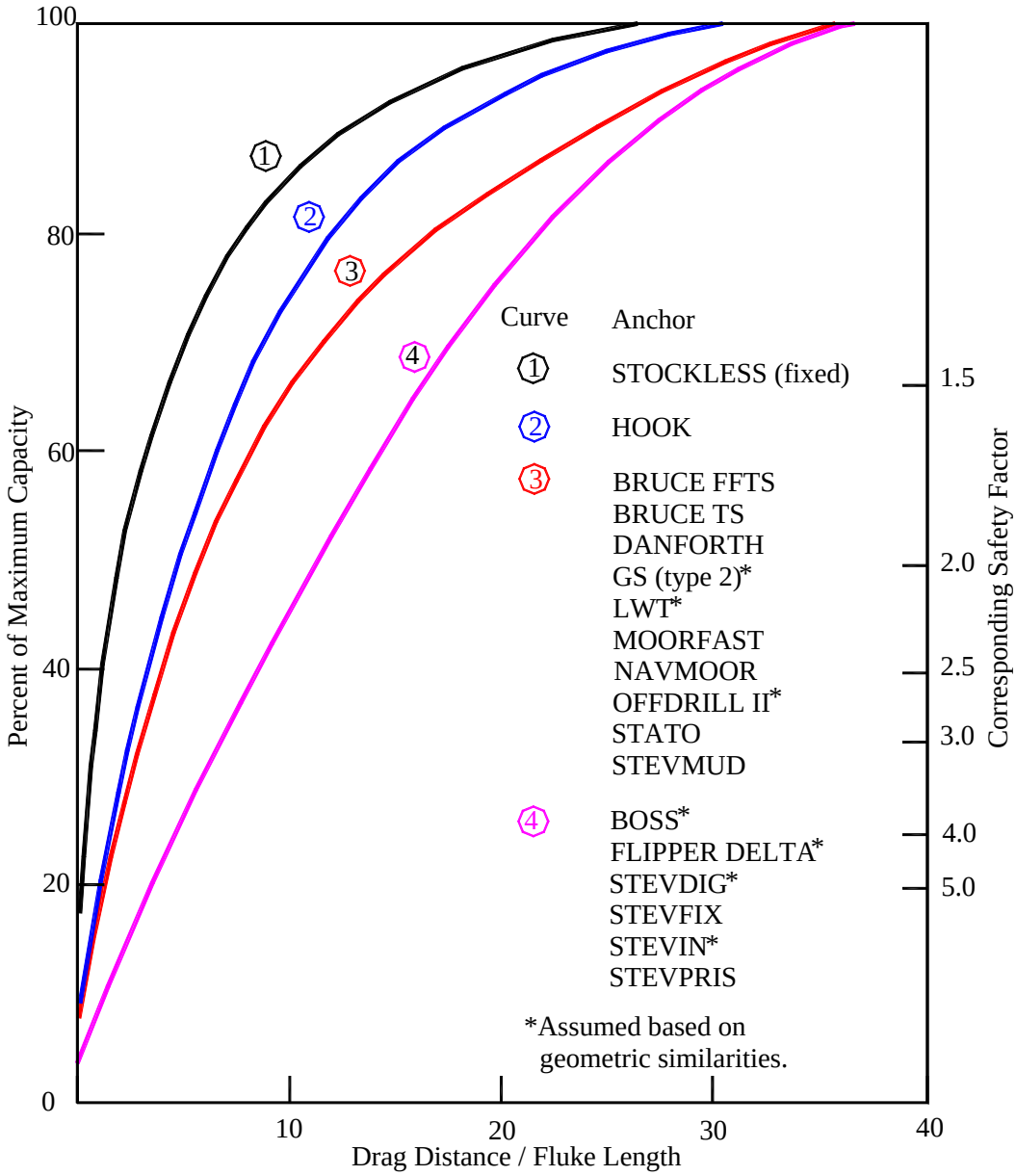

Fig. 3.2 Development of anchor capacity with penetration depth (NCEL, 1987)

3.1.2 Vryhof anchors

Vryhof anchors (1999) proposed specific values of parameters, *a* and *b*, which are used in Eq. 3.1 for predicting ultimate holding capacity (UHC). These values depend on the soil type, anchor and anchor line condition such as wire or chain. Table 3.1 shows these values.

Table 3.1 Parameters *a* and *b* for Vryhof Stevpris

Soil condition	Anchor line	*a*	*b*
Very soft clay	Chain	48	0.92
Very soft clay	Wire	66.3	0.92
Medium clay	Both	67	0.92
Hard clay and sand	Both	86	0.92

The design charts shown in Fig. 3.3 and 3.4 indicate the design curves for anchor weight versus anchor capacity and anchor weight versus penetration depth (and drag distance), respectively. In Fig. 3.3, the Stevpris MK5 design line for very soft clay represents soils with undrained shear strength of 4kPa at the mudline and undrained strength gradient of 1.5kPa/m. A 50^{o} fluke-shank angle is typical use in very soft clay while the optimal fluke-shank angle for sand and hard clay is 32°. The medium clay design line can be applicable in silt and firm to stiff clays and the fluke-shank angle should also be set at 32° for optimal performance (Vryhof 1999).

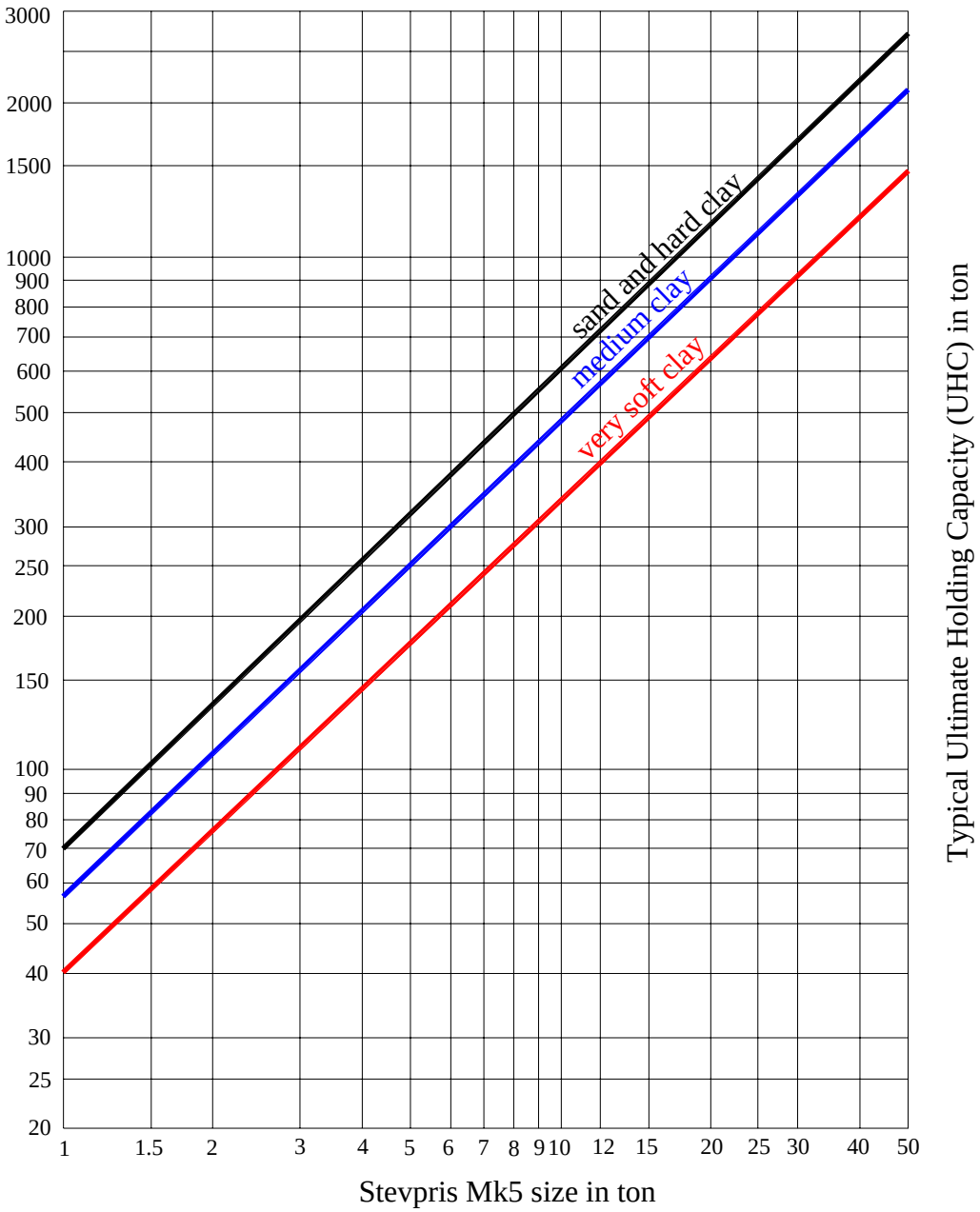

Fig. 3.3 Design curves for capacity of Vryhof Stevpris MK5 (Vryhof 1999)

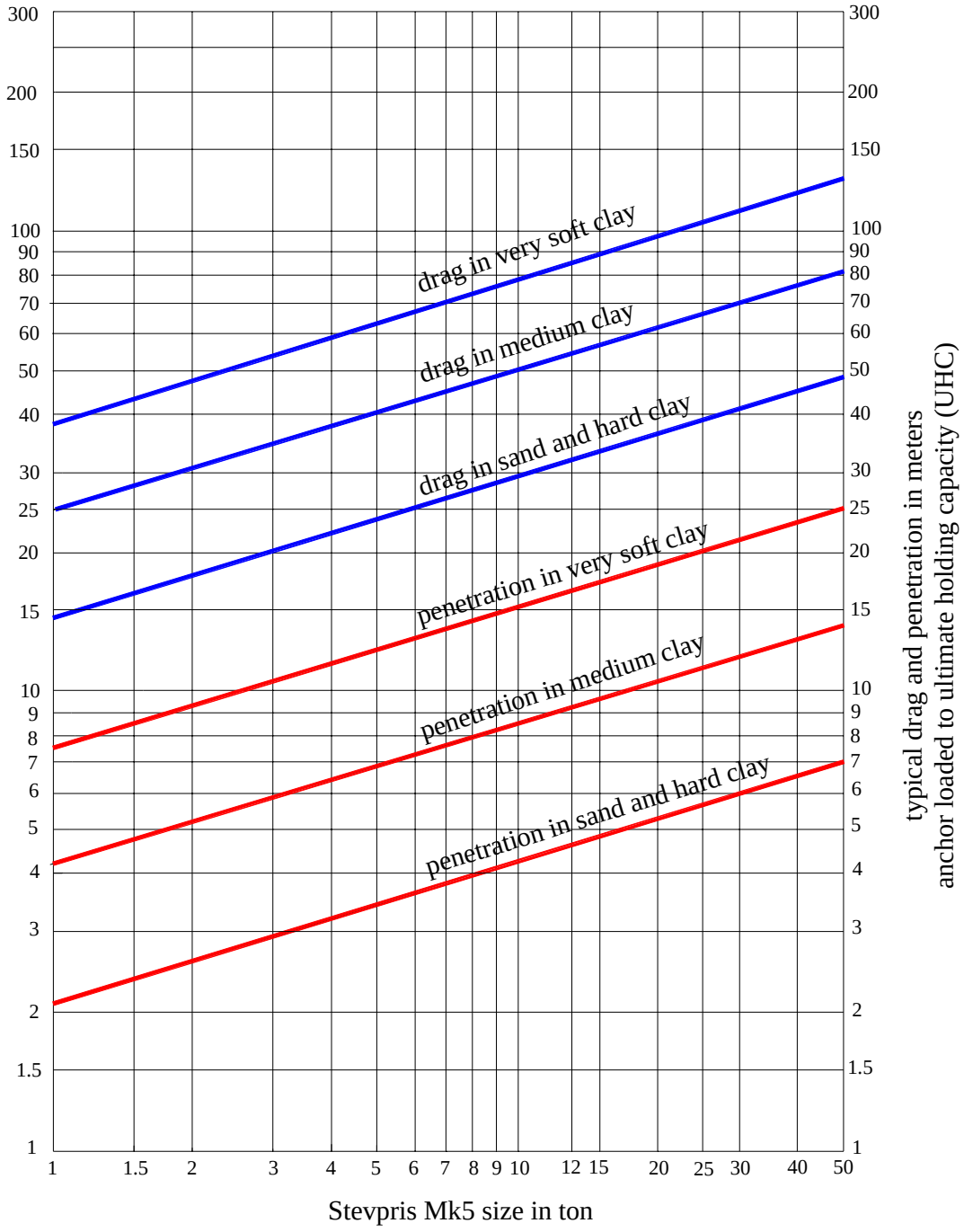

Fig. 3.4 Chart of penetration depth and drag distance versus anchor weight for Vryhof Stevpris MK5 in various soil type (Vryhof 1999)

3.1.3 Bruce anchors

Bruce anchors has also provided similar design curves and corresponding equations for the Bruce FFTS anchor based on NCEL tests as shown in Fig. 3.5. Table 3.2 shows the specific values of parameters, a and b for predicting ultimate holding capacity. Bruce FFTS MK4 design line for mud and soft clay is based on undrained soil strength of zero at the seabed and an undrained soil strength gradient of 1.57kpa/m i.e. a strength described by the equation $S_u = 1.57z$ with S_u in kPa and z in meters below the mudline.

Table 3. 2 Parameters a and b for Bruce MK4

Soil condition	Anchor line	*a*	*b*
In Sand	Chain	46.86	0.94
In soft clay or mud	Wire	49.66	0.92
In soft clay or mud	Chain	39.95	0.92

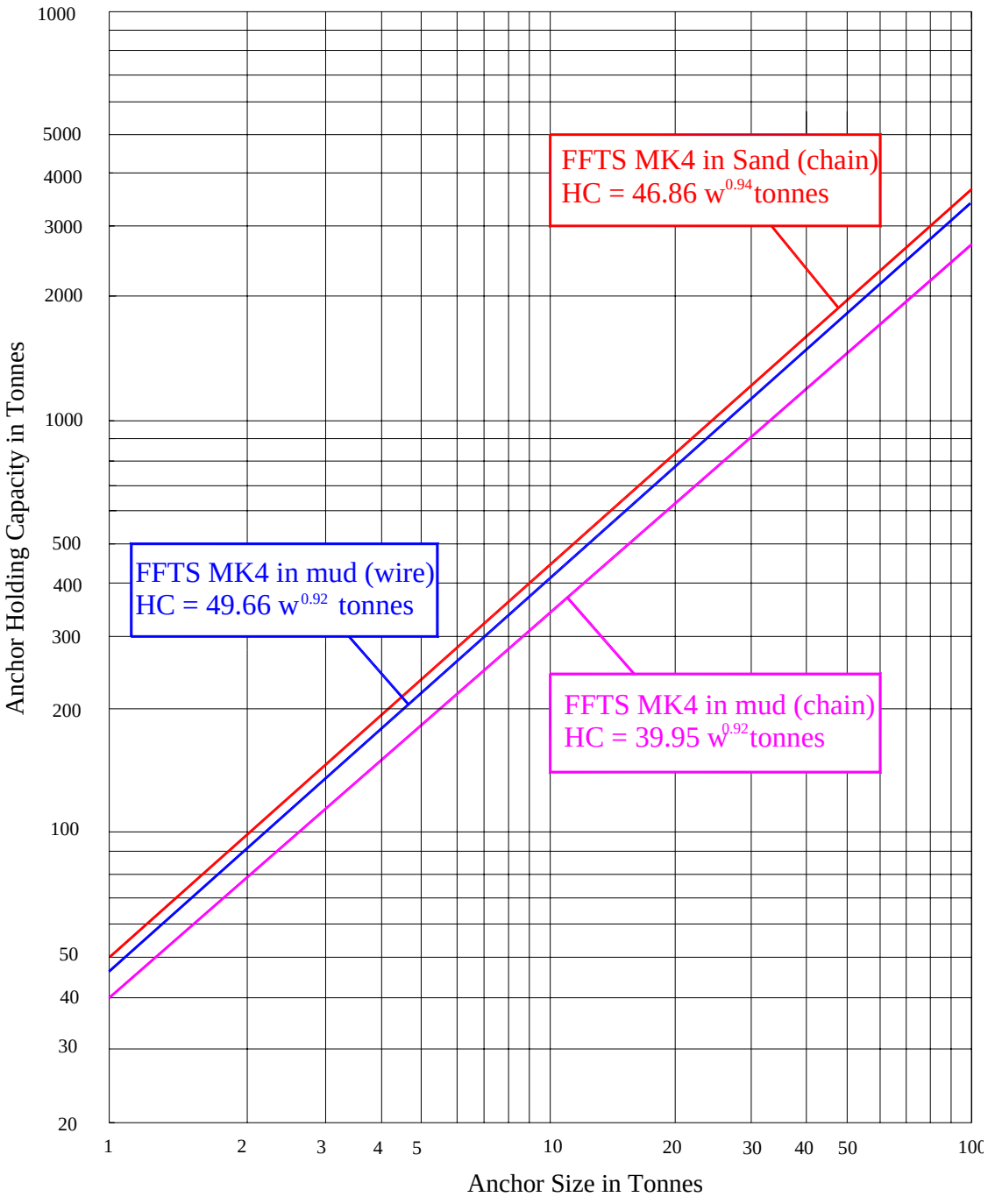

Fig. 3.5 Design curve of Bruce FFTS MK4 (Bruce Anchors)

3.2. Limit equilibrium method

Stewart (1995), Neubecker and Randolph (1996b), Dahlberg (1998) and Thorne (1998) proposed prediction methods based on limit equilibrium for predicting anchor capacity and trajectory. In these methods, the soil resistance act on all elements of an anchor such as shank and fluke. Each method has a unique approach for estimating the direction and magnitude of the soil resistance. As shown in Fig. 3.6, it is assumed that the forces acting on the components of the drag anchor are in equilibrium at any snapshot in time. In Fig. 3.6, F_{tf} and F_{ts} indicate shearing resistance on fluke and shank, respectively and F_{pf} and F_{ps} indicate bearing resistance on fluke and shank, respectively

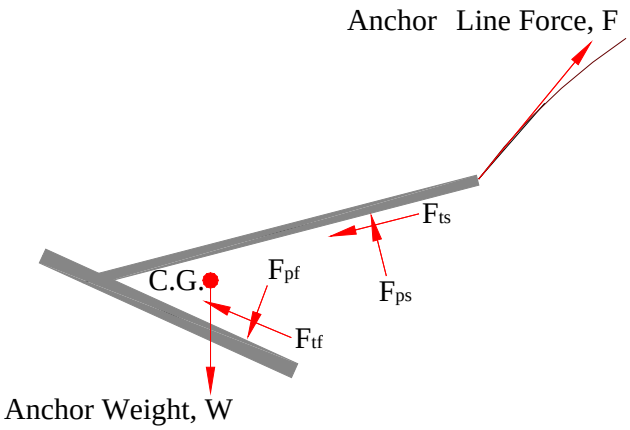

Fig. 3.6 Body forces on anchor

The entire trajectory of a drag anchor can be predicted by step by step calculation. As the anchor penetrates, its orientation should be changed in small increments to satisfy force and moment equilibrium for a given depth. The anchor translates until the fluke is parallel to the seabed by repeating the incremental translation and rotation. Eventually an anchor reaches the ultimate penetration depth where it exerts

ultimate anchor capacity. For the purposes of illustration we include below additional details of two of the methods mentioned above, especially methods of Newbecker and Randolph (1996b) and Thorn (1998)

3.2.1 Neubecker and Randolph

Neubecker and Randolph (1996b) developed a simplified method for predicting the trajectory of a drag anchor in soft clay. In this method, the anchor translates parallel to the fluke of the anchor with the fluke orientation adjusted to satisfy equilibrium condition at each step. The anchor penetrates until fluke is parallel to the sea bed.

As shown in Fig. 3.7, the geotechnical resisting force T_p, acting at the padeye of the anchor parallel to the fluke is expressed as:

$$T_p = fA_p N_c s_u \qquad (3.2)$$

where T_p =soil resistance parallel to the fluke

f = form factor for the anchor

A_p = projected anchor area (in the direction of travel)

N_c =bearing capacity factor taken as 9

s_u =local undrained shear strength

It is evident from moment equilibrium that for a weightless anchor there will also be geotechnical forces acting normal to the fluke T_n. The resultant force T_w at the shackle will make an angle θ_w as shown in Fig. 3.7. T_w can be expressed as follows;

$$T_w = \frac{T_p}{\cos\theta_w} \qquad (3.3)$$

They proposed the form factor *f*, and the angle θ_w, which can be determined by field tests or centrifuge model tests or by analysis. These properties are assumed to be unique for any anchor and they can describe the behavior of the anchor in soft clays. It should be noted that the resultant force, T_w, is independent of the anchor weight, but anchor weight must be considered when the actual padeye force, T_a, is calculated. The relationships between the angles can be expressed as:

$$\theta_a = \theta_w + \psi - \beta \tag{3.4}$$

In case of the field condition, the anchor weight is not a significant factor in the behavior of the anchor, thus, ψ can be ignored.

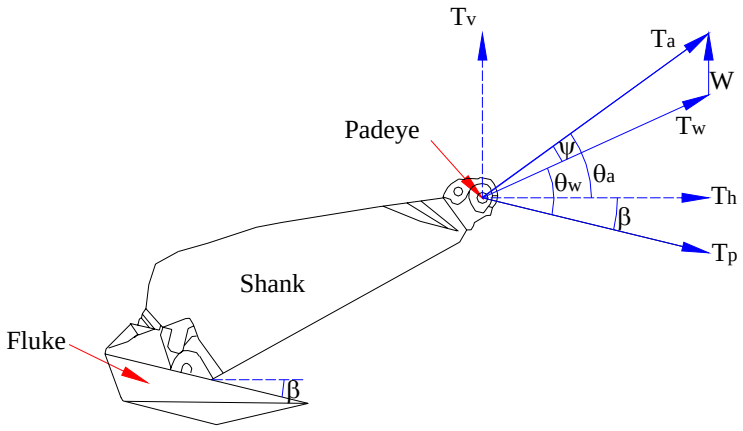

Fig. 3.7 Force equilibrium of anchor for Neubecker and Randolph (1996b)

3.2.2 Thorne (1998)

Thorne suggested a method for the estimating the trajectory of drag anchors in normally consolidated soils based on geotechnical principles. The forces acting on the anchor represent the equilibrium forces for a given depth and anchor orientation. Fig. 3.8 shows the concept of drag force which is expressed as follows.

$$drag\ \ force = DA_i \cdot DF_i \cdot S_u \qquad (3.5)$$

where DA_i and DF_i indicates the area and drag factor for the i_{th} component, respectively.

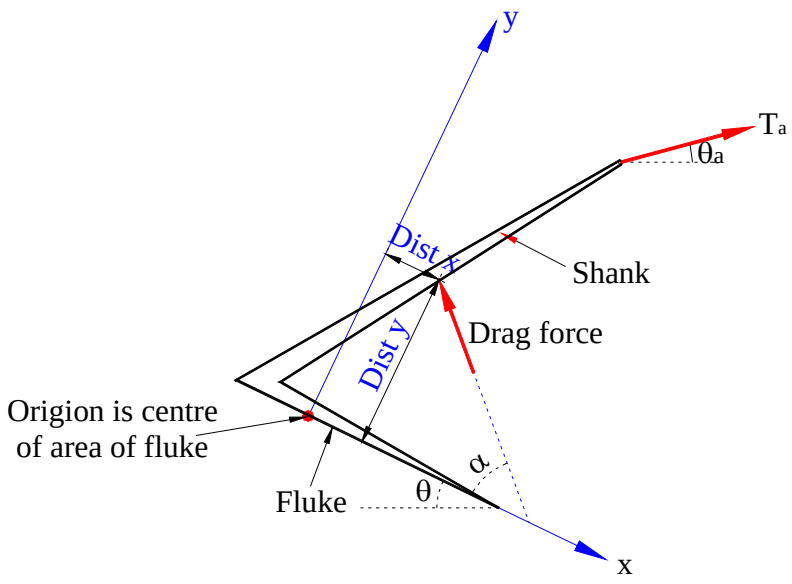

Fig. 3.8 Elements for conventional anchor (Thorne 1998)

Fig. 3.9 shows the drag forces acting on the anchor and the anchor line tension. Drag forces can be classified as follows: total drag force normal to fluke (TDFN), total drag force parallel to fluke (TDFP), total moment of drag forces about center of area of fluke (TDFM).

$$TDFN = \sum_{i=1}^{i=n} -DA_i \cdot DF_i \cdot S_u \cdot \sin\alpha_i \tag{3.6a}$$

$$TDFP = DA_f \cdot DF_f \cdot S_u + \sum_{i=1}^{i=n} DA_i \cdot DF_i \cdot Su \cdot \cos\alpha_i \tag{3.6b}$$

$$TDFM = \sum_{i=1}^{i=n} DA_i \cdot DF_i \cdot S_u \cdot (Distx_i \cdot \sin\alpha_i + Disty_i \cdot \cos\alpha_i) \tag{3.6c}$$

where α_i = angle of drag force *i* to plane of fluke;

$Distx_i$ = *x* coordinates of center of area of drag element *i*;

$Disty_i$ = *y* coordinates of center of area of drag element *i*;

The equilibrium equation can be written by summing forces normal and parallel to the fluke and moment about the center of area of the fluke. Then, equations of the equilibrium in the parallel and normal direction and moment about the fluke center can be described as follows.

$$T_a \cos(\theta + \theta_a) = TDFP - W\sin\theta \tag{3.7a}$$

$$F_n = T_a \sin(\theta + \theta_a) - W\cos\theta - TDFN \tag{3.7b}$$

$$\begin{aligned} M = {} & T_a\{S_x \sin(\theta + \theta_a) - S_y \cos(\theta + \theta_a)\} \\ & + TDFM - W(Y_w \sin\theta + X_w \cos\theta) \end{aligned} \tag{3.7c}$$

In the above equations, F_n indicates the normal force exerted on the fluke by the soil and it acts at the center of area of the fluke. M indicates moment about the center of the area of the fluke applied to the fluke by the soil.

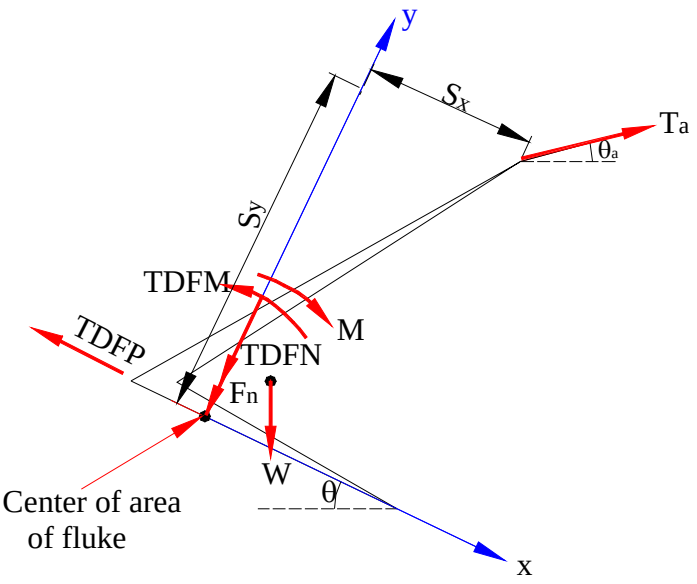

Fig. 3.9 Equilibrium of anchor during penetration (Thorne 1998)

3.3 Plastic limit analysis method

O'Neill et al. (2003) proposed the yield loci method in which they have used plasticity concepts to estimate the capacity of drag anchor under combined loading conditions of vertical load (V), horizontal load (H) and moment (M) as shown in Fig. 3.10. As a drag anchor is installed in soft undrained clay, local plastic flow of the soil occurs around the drag anchor.

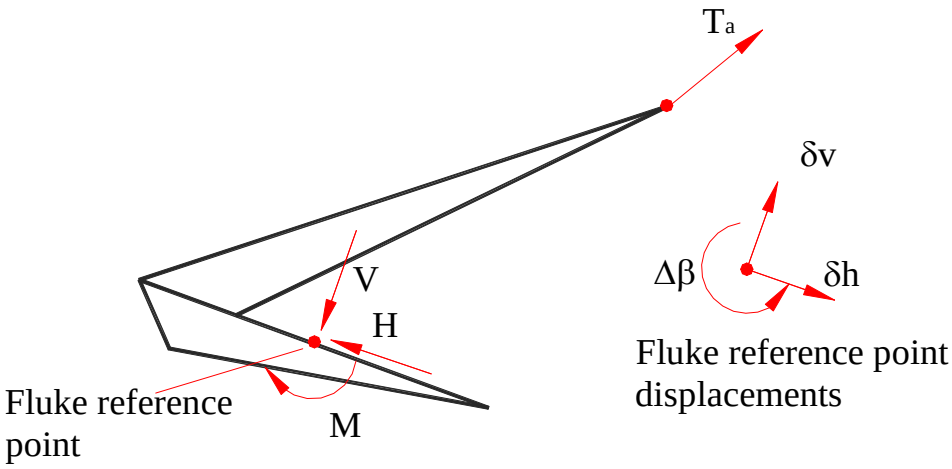

Fig. 3.10 Loads and displacements at failure for a simplified drag anchor (O'Neill, et al. 2003)

The yield locus of the anchor under general loading can be expressed as a mathematical equation, $f(V,H,M) = 0$ as shown in Fig. 3.11. The equation can be used to obtain the anchor capacity under various loading combinations and can also serve as a yield surface to predict the anchor displacement i.e. act as a plastic potential function which describes the plastic vertical and horizontal displacements and rotation of the fluke when it fails the soil around it.

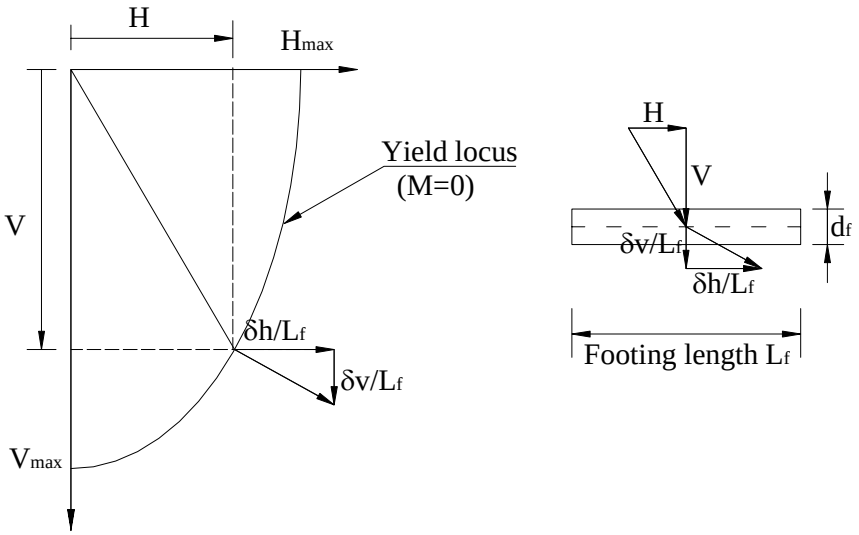

Fig. 3.11 The yield locus and plastic potential function (O'Neill, et al. 2003)

Finite element analysis and limit analysis have been used to develop the yield surface by examining the interactions between the fluke and the undrained soft clays around the fluke. Once the yield surface has been developed it can be used to estimate the incipient anchor displacement and rotation under a prescribed load. As in the limit equilibrium methods, a small increment of displacement and rotation is imposed and the new displacement directions are thus determined. This process is repeated until the anchor depth remains constant.

CHAPTER IV

PLASTIC LIMIT ANALYSIS

4.1 Introduction

Limit analysis provides powerful tools for estimating the load-carrying capacity of a structure. Limit analysis is more efficient and consistent in solving the collapse problem of plastic structures compared to the equilibrium method. The limit equilibrium method considers equilibrium of a soil mass but requires an assumption regarding the distribution of soil resistance. Plastic limit analysis provides a well defined methodology for estimating lower bound capacities using statically admissible stress distribution or upper bound capacities using kinematically admissible mechanism.

In this chapter, the assumptions and the basic concepts of lower and upper bound theorems are described. This includes the concept of rigid–perfect plasticity, yield criterion, associated flow rule, and normality of yield surface.

4.2 Basic concepts of limit analysis

4.2.1 Rigid perfect plasticity

Fig. 4.1 shows a stress-strain relationship of both a real soil and an elastic plastic idealization. As can be seen in this figure, this curve is consisted of an initial almost linear portion with a peak stress followed by softening to a residual stress. This curve can be obtained by laboratory tests such as simple triaxial compression tests or simple

shear tests. For the application of stability problems in limit analysis, small amounts of strain softening can be neglected. Thus we can simplify this curve as two straight lines which are shown dashed in this Figure.

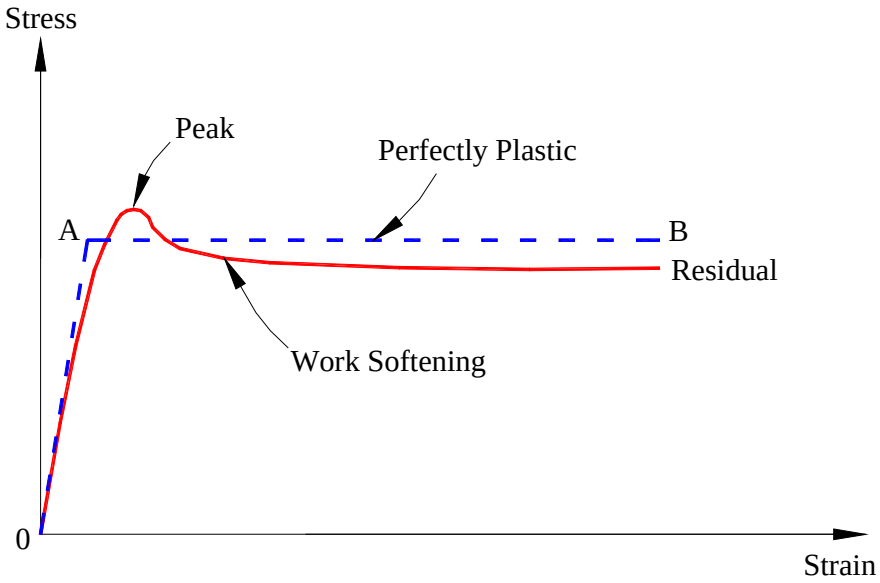

Fig. 4.1 Stress-strain relationship for ideal and real soils (Chen, 1990)

Fig. 4.2, shows a rigid-plastic idealization in which elastic deformations from *0* to *A* are not considered. This model is used in limit analysis method such as lower and upper bound applications since we are only concerned with capacities, not deformations. This figure shows the stress-strain curve and an analogy model for a rigid-perfectly plastic material. From Fig. 4.2, we can see that there is no deformation up to a value of σ_0, called the yield stress. When σ_0 is reached the strain increases without limit.

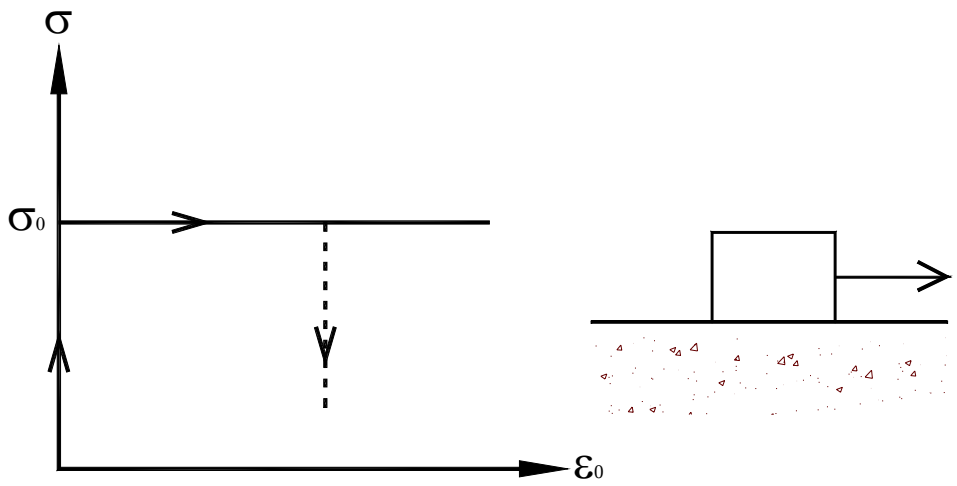

Fig. 4.2 Stress-strain curve for rigid perfectly plastic soil

For small strains, the stress-strain curve often shows perfectly plastic behavior to a reasonable approximation. This is applicable to ductile materials such as soft clay. In addition, the elastic deformation of clay is small enough to be ignored when compared to its plastic deformation. Therefore, the rigid-perfect plasticity model is considered to be a reasonable assumption for clays undergoing small deformations.

4.2.2 Yield criterion

An essential element of plastic limit analysis is the yield surface which is the locus of the points representing yielding defined in stress space. The yield surface is a function that explains the interactions among stresses in a continuum that cause the material to yield. For a perfectly plastic material, a yield surface is the boundary between possible and impossible states of stress. The possible states of stress are within strength

limit of the material and are therefore bounded by the yield surface. As can be seen in Fig. 4.3, a state of stress outside the yield surface is not possible.

A yield function can be defined mathematically as following:

$$F(\sigma_{ij}) = 0 \qquad (4.1)$$

where F=yield function

σ_{ij} =stress tensor defining the stress state (i,j =1,2,3 in a three dimensional continuum).

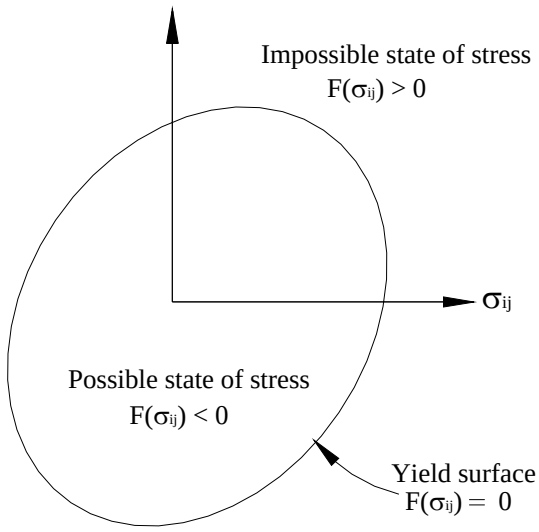

Fig. 4.3 Yield surface and stress state in the stress space

Any point inside of the yield surface, corresponds to the condition, $F(\sigma_{ij}) < 0$; any point on the yield surface, corresponds to the condition, $F(\sigma_{ij}) = 0$; and any point outside the yield surface, corresponds to the condition, $F(\sigma_{ij}) > 0$.

In geotechnical engineering problems, Tresca yield criterion or the von Mises criterion are typically used for undrained analysis. In the Tresca the soil yields when the maximum shear stress reaches its shear strength. The maximum shear stress is related to the difference in the major and minor principal stresses, i.e.

$$\frac{\sigma_1 - \sigma_3}{2} = S_u \quad \text{or} \quad f(\sigma_{ij}) = \sigma_1 - \sigma_3 - 2S_u = 0 \qquad (4.2)$$

where, σ_1 and σ_3 are major and minor principal stresses

S_u = undrained soil strength

Fig. 4.4 shows the Tresca criterion for plane stress conditions. In this case the out of plane stress affects the surface.

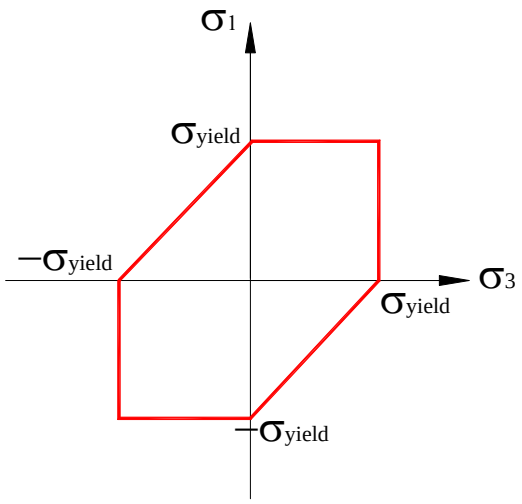

Fig. 4.4 Tresca criterion for plane failure

The von Mises criterion is also known as the maximum distortional energy criterion, and is met when the following criterion is satisfied.

$$\frac{1}{2}\left[(\sigma_1-\sigma_2)^2+(\sigma_2-\sigma_3)^2+(\sigma_3-\sigma_1)^2\right]=\sigma_y{}^2 \qquad (4.3)$$

where $\sigma_y=\sigma_{yield}$ = the yield stress measured under uniaxial stress conditions

In the case of plane stress, i.e., σ_2 = 0, the von Mises criterion reduces to,

$$\sigma_1{}^2-\sigma_1\sigma_3+\sigma_3{}^2=\sigma_y{}^2 \qquad (4.4)$$

This equation represents an ellipse as shown in Fig. 4.5. Fig. 4.5 shows that Tresca criterion is inside of von Mises criterion. This indicates that Tresca criterion is more conservative than the von Mises criterion when the yield stress is measured in uniaxial stress conditions.

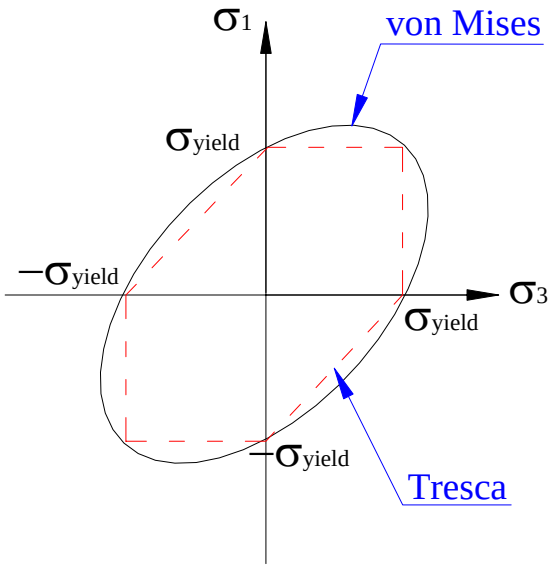

Fig. 4. 5 Comparison of Tresca and von Mises failure criteria

4.2.3 Associated flow rule and normality condition

For perfectly plastic material a plastic potential function $G(\sigma_{ij})$ is defined which determines the relative strain magnitudes that is, $\dot{\varepsilon}_{ij}^{p} = \lambda \frac{\partial G}{\partial \sigma_{ij}}$. If the material is a stable (no softening), perfectly plastic material then the plastic potential function *G* is identical to the yield function, *F*, that is,

$$\dot{\varepsilon}_{ij}^{p} = \lambda \frac{\partial F}{\partial \sigma_{ij}} \qquad (4.5)$$

where λ = positive scalar multiplier factor

If the yield surface and the plastic potential surface for a material are identical (*F*=*G*), then the material is said to obey the normality rule. In other words, the plastic strain increment vector is in the direction of the outward normal to the yield surface. This is called an associated flow rule, and is shown schematically in Fig. 4.6 where p' and *q* are stress measures defining yield.

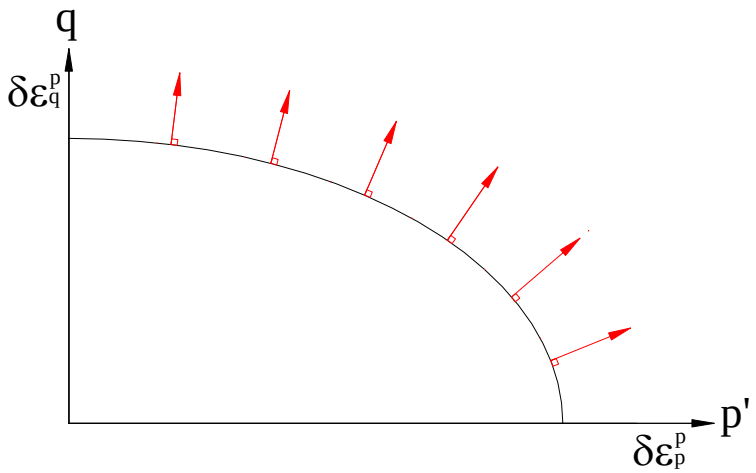

Fig. 4.6 Normality or associated flow

4.3 Principal of virtual work

Both lower and upper bound theorems are based on the principle of virtual work. In limit analysis, it is assumed that deformations in geometry of the body at incipient plastic collapse are small, so that changes of geometry can be ignored. For this reason, the original geometry of the body is used for virtual work derivations. In the virtual work equation, two independent conditions are considered, namely, the equilibrium stress set and the compatibility strain set. In Eq.4.6, the superscripts *A* and *B* indicate the equilibrium and compatibility sets, respectively, such that the virtual work equation is

$$\int_S T_i^A v_i^B ds + \int_V X_i^A v_i^B dV = \int_V \sigma_{ij}^A \dot{\varepsilon}_{ij}^B dV \qquad (4.6)$$

where σ_{ij}^A =the stresses, real or virtual, in equilibrium with the external forces T_i^A on the boundary and the body forces X_i^A in the body; $\dot{\varepsilon}_{ij}^B$ =the strain or deformations compatible with real or virtual velocity field v_i^B; S,V refer to the boundary surface and the volume of the body, respectively.

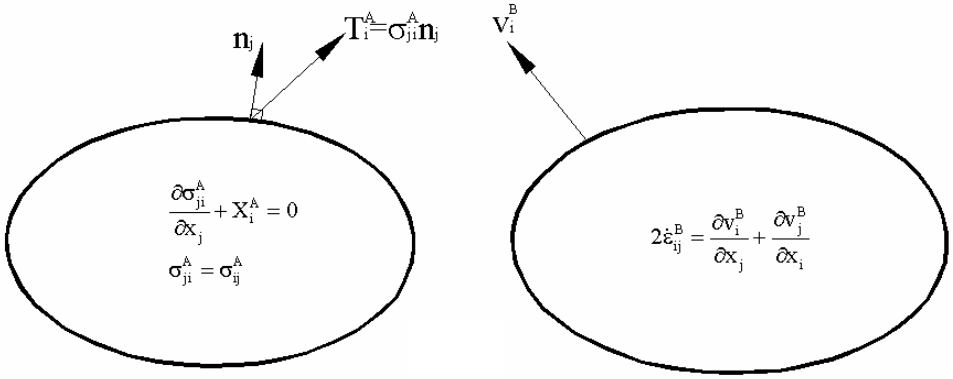

(a) Equilibrium (b) Compatible

Fig. 4.7 Two independent sets in the virtual work equation

4.4 Lower bound theorem

If a stress field does not violate the yield criterion at any point is in equilibrium with the surface tractions and body forces, then such a stress field is said to be statically admissible. It can be shown that collapse does not occur in a today with a statically admissible stress field, i.e., the true collapse load is clearly larger than or equal to the external load implied by such a condition. This can be expressed in virtual work equations as

$$\int_s T_i^L v_i ds + \int_v X_i^L v_i dV = \int_v \sigma_{ij}^L \dot{\varepsilon}_{ij} dV \le \int_v \sigma_{ij} \dot{\varepsilon}_{ij} dV \qquad (4.7)$$

where σ_{ij}^L = statically admissible stress field in equilibrium with the tractions T_i^L and the body forces X_i^L

σ_{ij} = actual stress field

$\dot{\varepsilon}_{ij}$ = actual strain rate field

v_i = actual velocity field

It should be noted that only the equilibrium and the stress boundary conditions are satisfied in lower bound theorem. The implied kinematics (i.e, compatibility, flow rule) are not considered in this theorem. Lower bound solution to the true collapse load can be estimated by trial and error assuming various statically admissible stress fields. Solutions that give higher collapse loads are close to the exact solution.

4.5 Upper bound theorem

In a kinematically admissible velocity field, if the plastic collapse load is calculated by equating internal energy dissipation rate to the external work rate by the boundary forces then the calculated load is either greater than or equal to the true collapse load. This can be expressed in the virtual work equation as:

$$\int_S T_i^U v_i^U \, dS + \int_v X_i^U v_i^U \, dV = \int_v \sigma_{ij}^U \dot{\varepsilon}_{ij}^U \, dV \geq \int_v \sigma_{ij} \dot{\varepsilon}_{ij}^U \, dV \qquad (4.8)$$

where, v_i^U =kinematically admissible velocity field compatible

with the strain rate field $\dot{\varepsilon}_{ij}^U$

σ_{ij}^U =stress field in equilibrium with the upper bound loading T_i^U and X_i^U

σ_{ij} =actual stress field

It should be noted that σ_{ij}^U is not in general the actual stress field invoked in the body due to the applied traction vectors T_i and body forces X_i, unless v_i(x) happens to be the true mechanism of collapse in the body. However, σ_{ij} is the stress field that would cause the virtual plastic strain increment $\dot{\varepsilon}_{ij}^p$.

4.5.1 Energy dissipation in continuous deformation regions

To estimate the energy dissipation in continuous deformation regions, the yield criteria such as Tresca or von Mises is required. In the case of plane strain, the Tresca and von Mises yield criteria have the identical form of the yield function (Murff 2002).

$$f = \left[\frac{(\sigma_x - \sigma_y)^2}{4} + \frac{1}{2}\tau^2{}_{xy} + \frac{1}{2}\tau^2{}_{yx} \right]^{1/2} - S_u = 0 \qquad (4.9)$$

From the flow rule, the strain rates are expressed as

$$\dot{\varepsilon}_x = \lambda \frac{\partial f}{\partial \sigma_x} = \lambda \frac{1}{2}\left[\frac{(\sigma_x - \sigma_y)^2}{4} + \frac{1}{2}\tau_{xy}^2 + \frac{1}{2}\tau_{yx}^2 \right]^{-1/2} \frac{2(\sigma_x - \sigma_y)}{4}$$

$$\dot{\varepsilon}_y = \lambda \frac{\partial f}{\partial \sigma_y} = \lambda \frac{1}{2}\left[\frac{(\sigma_x - \sigma_y)^2}{4} + \frac{1}{2}\tau_{xy}^2 + \frac{1}{2}\tau_{yx}^2 \right]^{-1/2} \frac{-2(\sigma_x - \sigma_y)}{4}$$

$$\dot{\varepsilon}_{xy} = \lambda \frac{\partial f}{\partial \tau_{xy}} = \lambda \frac{1}{2}\left[\frac{(\sigma_x - \sigma_y)^2}{4} + \frac{1}{2}\tau_{xy}^2 + \frac{1}{2}\tau_{yx}^2 \right]^{-1/2} \tau_{xy}$$

Above equations are simplified as follows;

$$\dot{\varepsilon}_x = \lambda \frac{(\sigma_x - \sigma_y)}{4S_u} \qquad (4.10a)$$

$$\dot{\varepsilon}_y = -\lambda \frac{(\sigma_x - \sigma_y)}{4S_u} \qquad (4.10b)$$

$$\dot{\varepsilon}_{xy} = \lambda \frac{\tau_{xy}}{2S_u} \qquad (4.10c)$$

The volumetric strain rate is

$$\dot{\varepsilon}_v = \dot{\varepsilon}_x + \dot{\varepsilon}_y = 0 \tag{4.11}$$

This is true for all purely cohesive materials when solids are not compressible (i.e, undrained conditions). The internal energy dissipation rate based on a kinematically admissible velocity field is as

$$\dot{D} = \sigma_{ij}\dot{\varepsilon}_{ij}^{p} \tag{4.12}$$

The strain rates are

$$\dot{\varepsilon}_{ij}^{p} = \lambda \frac{\partial f}{\partial \sigma_{ij}} \tag{4.13}$$

Substituting Eq. 4.13 into Eq. 4.12,

$$\dot{D} = \lambda \sigma_{ij} \frac{\partial f}{\partial \sigma_{ij}} \tag{4.14}$$

Carrying out this operation it can be shown that

$$\dot{D} = \lambda S_u \tag{4.15}$$

Substituting Eqs. 4.10a, 4.10b and 4.10c into the yield function Eq. 4.9, then λ can be expressed as follows:

$$\lambda = (2\dot{\varepsilon}_x^2 + 2\dot{\varepsilon}_y^2 + 2\dot{\varepsilon}_{xy}^2 + 2\dot{\varepsilon}_{yx}^2)^{1/2} \tag{4.16}$$

Then, by substituting Eq. 4.16 into Eq. 4.15, the dissipation is

$$\dot{D} = S_u(2\dot{\varepsilon}_x^2 + 2\dot{\varepsilon}_y^2 + 2\dot{\varepsilon}_{xy}^2 + 2\dot{\varepsilon}_{yx}^2)^{1/2} \tag{4.17}$$

Now since

$$\dot{\varepsilon}_x = -\dot{\varepsilon}_y \quad \text{and} \quad \dot{\varepsilon}_{xy} = \dot{\varepsilon}_{yx}$$

We can simplify Eq. 4.17 to

$$\dot{D} = 2S_u(\dot{\varepsilon}_x^2 + \dot{\varepsilon}_{xy}^2)^{1/2}$$

This is a function of energy dissipation for a continuously deforming region in plane strain. In case of the three-dimensional condition, the following functions are derived

von Mises: $\dot{D} = S_u(2\dot{\varepsilon}_{ij}\dot{\varepsilon}_{ij})^{1/2}$ (4.18)

Tresca: $\dot{D} = 2S_u\left|\dot{\varepsilon}\right|_{shear\,\max} = \left|\dot{\gamma}\right|_{\max} S_u$ (4.19)

4.5.2 Energy dissipation in slip surfaces

Slip surfaces are idealized as discontinuous surfaces with a thin transition layer. Consider two rigid blocks with a simple shear deforming transition region between two blocks. As shown in Fig. 4.8, the bottom rigid block is stationary but the upper rigid block translates with a velocity, v_o.

In the deforming region, the velocity field is

$$v_x = \frac{v_0}{t}y \quad and \quad v_y = v_z = 0 \tag{4.20}$$

Therefore, the only non-zero strains are then $\dot{\varepsilon}_{xy}$ and $\dot{\varepsilon}_{yx}$. Thus,

$$\dot{\varepsilon}_{xy} = \dot{\varepsilon}_{yx} = \frac{1}{2}\left(\frac{\partial v_x}{\partial y} + \frac{\partial v_y}{\partial x}\right) = \frac{1}{2}\frac{v_0}{t} \tag{4.21}$$

Substituting this value into Eq. 4.19, the dissipation per unit volume is

$$\dot{D} = 2S_u\left(\left(\frac{v_0}{2t}\right)^2\right)^{1/2} = \frac{S_u v_0}{t} \tag{4.22}$$

The total dissipation in the deforming region can be estimated by integration over the total volume, then

$$\dot{D}_{Tot} = \int_V \dot{D} dV = \dot{D} \times Volume = \frac{S_u v_0}{t} \times 1 \times t = S_u v_0 \qquad (4.23a)$$

Thus, we can see that dissipation does not depend on the thickness of the deforming region. As the thickness of deforming region approaches to the zero, then the dissipation for a slip surface is

$$\dot{D} = S_u v_0 \qquad (4.23b)$$

where v_o = the relative velocity of slip along the slip surface.

It should be noted that both Tresca and von Mises yield criteria induce the same results even if the meaning of S_u is somewhat different in each criterion.

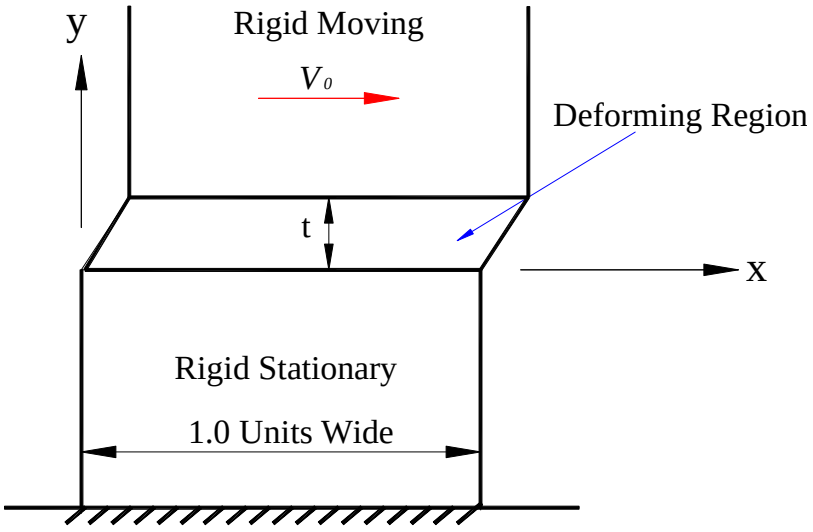

Fig. 4.8 Deformation in the slip surface (Murff 2002)

4.5.3 Example of application of the upper bound method

In order to illustrate how the upper bound method for undrained analysis apply to geotechnical engineering problem, consider the passive pressure problem shown in Fig. 4.9. The object of this problem is to find the load *F*, which will cause passive failure of a wall of height, *H*.

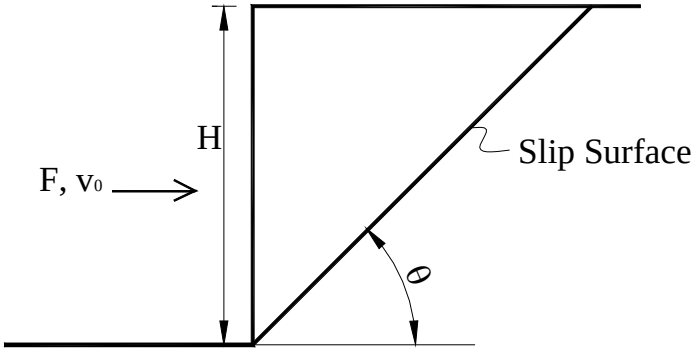

Fig. 4.9 Example of upper bound methods (Murff 2002).

It is assumed that the wall pushes a rigid wedge of soil along the slip surface. The wall moves with virtual velocity v_o, and the wedge must slip tangentially along the surface. The resultant velocity, v_R, of the wedge is indicated in Fig. 4.10.

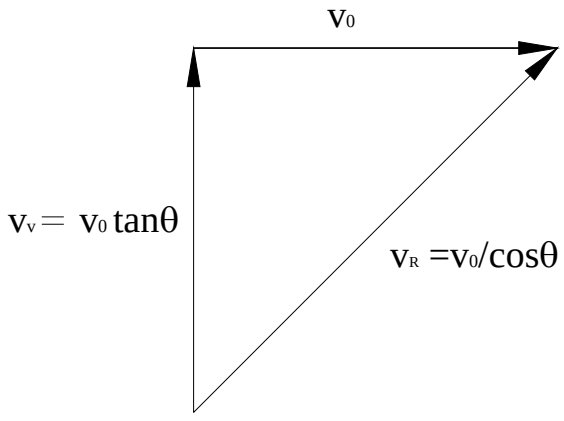

Fig. 4.10 Velocity field of example slope

The dissipation rate is

$$\dot{D}_{Tot} = v_R \cdot s_u \cdot \frac{H}{\sin\theta} = \frac{v_o s_u H}{\sin\theta\cos\theta} \tag{4.24}$$

The work rate of the external loads must include the work rate done by the soil weight. Thus the total work rate is

$$\dot{W} = Fv_o - \frac{1}{2}\gamma H^2 \cot\theta \times v_o \tan\theta \tag{4.25}$$

Equating external work rate to internal dissipation rate and canceling virtual velocities, we get

$$F = \frac{1}{2}\gamma H^2 + \frac{S_u H}{\sin\theta\cos\theta} \tag{4.26}$$

To find the best upper bound for *F*, the θ value that minimizes *F* can be found by differentiating, and solving for θ as follows

$$\frac{\partial F}{\partial\theta} = 0 = \frac{S_u H}{\sin^2\theta} - \frac{S_u H}{\cos^2\theta} \tag{4.27}$$

$$\theta = 45^\circ$$

Then, substituting $\theta = 45^\circ$ into the Eq. 4.26 for *F* , it leads to following Eq. 4.28.

$$F = \frac{1}{2}\gamma H^2 + 2S_u H \tag{4.28}$$

4.5.4 Systematic approach to upper bound plastic limit analysis

In order to apply assumptions and conditions illustrated in this chapter to the upper bound plastic limit analysis of a drag embedded anchor, the following procedures are required (Murff 2002).

(1) Establish a yield function, $f(\sigma_{ij}) = 0$

(2) Assume associated flow, $\dot{\varepsilon}_{ij} = \lambda \frac{\partial f}{\partial \sigma_{ij}}$

(3) Determine the dissipation rate as a function of strain rate, $\dot{D} = D(\dot{\varepsilon}_{ij})$

(4) Determine a kinematically admissible mechanism, $v_i = f(x, y)$

(5) For the mechanism equate virtual work rate to internal dissipation rate,

$$\sum W_i u^*_i = \int_v \dot{D} dv$$

(6) Solve for the unknown force

(7) Optimize the solution with respect to geometric parameter defining the mechanism.

4.5.5 Generalization of the upper bound method

The foregoing sections have detailed the development of the upper bound method applied to a continuum. This approach can be further generalized to apply to a system of forces and moments characterizing the yield of a perfectly plastic “structure” (or in our case soil-anchor system).

Prager(1959) showed that a system of forces that characterize a stress state of a perfectly plastic structure can be treated as generalized stresses and the corresponding displacements as generalized strains. “For a given set of generalized stresses $Q_1 \cdots Q_n$, the generalized strain rates $\dot{d}_1 \cdots \dot{d}_n$ are work rate conjugates of the stresses, that is

$$\dot{W} = Q_1\dot{q}_1 + \cdots + Q_n\dot{q}_n \qquad (4.29)$$

where $\dot{W}$ is the work rate of the generalized stresses on the plastic strain rates.” (Murff 1999).

Interaction failure diagrams for forces, Q_i can then be treated as generalized yield surfaces and the plastic limit analysis methods can then be applied using these generalized definition of stress and strain.

CHAPTER V

UPPER BOUND ANALYSIS OF DRAG ANCHOR

A methodology for predicting drag anchor installation performance is described in detail in this chapter. This approach employs the upper bound method of plasticity which relies on assumed mechanism of deformation. An external anchor line force F acts on the anchor inclined at an angle θ_f from horizontal causing it to rotate about a center of rotation (x_0, y_0) at an angular velocity $\dot{\beta}$. The upper bound analysis equates the rate of external work $\dot{W}_{ext}$ performed by F and the anchor weight W to the rate of internal energy dissipation in the soil $\dot{D}$, to compute the magnitude of F. The coordinates of the center of rotation are optimized to seek a minimum anchor line force F_{min} for a given θ_f. This process is repeated for various inclination angle, θ_f to establish the locus of points relating F_{min} to θ_f. As will be discussed subsequently, the intersection between this locus and the inverse catenary line equation relating anchor line tension to inclination angle at the shackle point establishes unique values of anchor force and inclination angle for a given step in the drag embedment process. The definitions related to the mechanism geometry are as shown in Fig. 5.1.

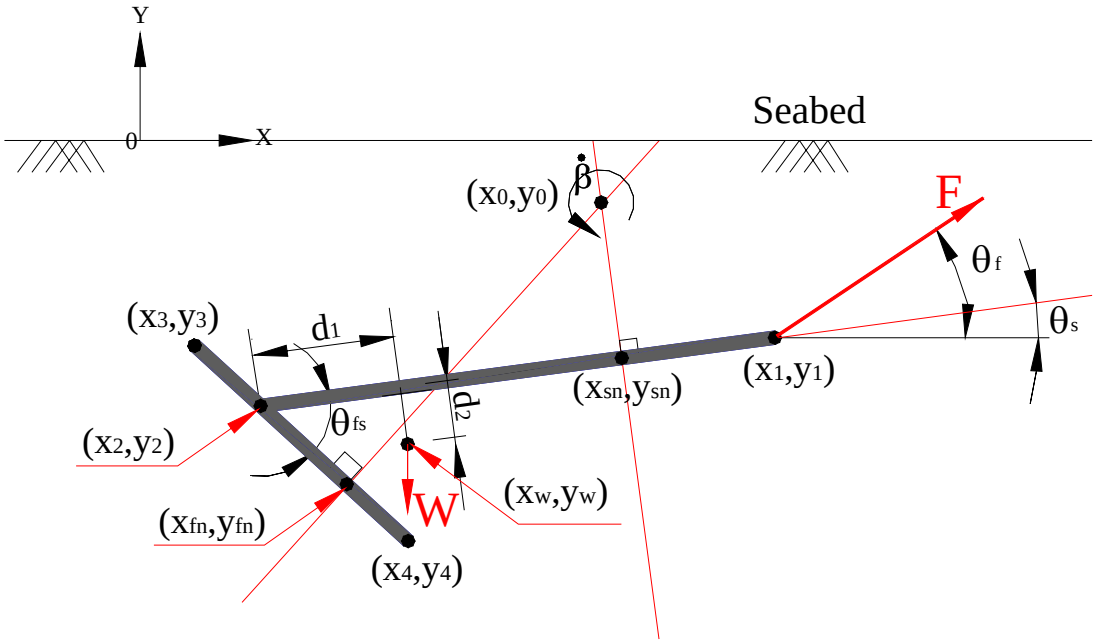

Fig. 5.1 Definition sketch for analysis of drag anchor

Definitions of the terms in Fig. 5.1 are as follows

F=anchor line force

W=anchor weight

$\dot{\beta}$ =virtual angular velocity of anchor

θ_{fs} =angle between shank and fluke

θ_f =angle between force line and seabed

θ_s =angle between shank and seabed

The coordinates of specific points in the Fig. 5.1 are

(x_0,y_0)=center of rotation

(x_1,y_1)=line attachment point (shackle point)

(x_2,y_2)=fluke-shank intersection point

(x_3,y_3)=head of fluke

(x_4,y_4)=tip of fluke

(x_w,y_w)=center of gravity of anchor

(x_{sn},y_{sn})=intersection point between shank and line normal to shank passing through (x_0,y_0)

(x_{fn},y_{fn})=intersection point between fluke and line normal to fluke passing through (x_0,y_0)

For convenience, coordinates on the fluke are sometimes described in terms of a *t-p* local coordinate system, with *t* and *p* corresponding to directions tangential and normal to the long axis of the fluke, respectively. For example, as Fig. 5.2 shows the local coordinated system for the fluke. A similar system is used for the shank.

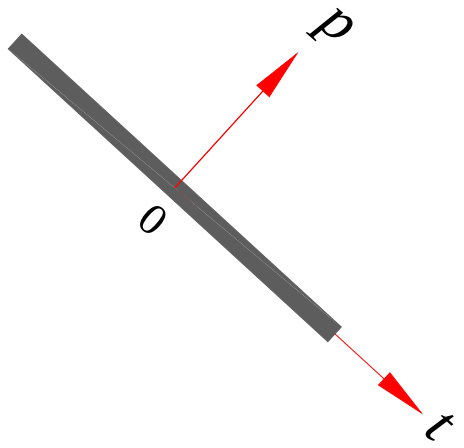

Fig. 5.2 Local coordinate for fluke

5.1 Kinematics of the drag anchor

As it can be seen Fig. 5.3, the kinematics of the fluke motions can conveniently be expressed in terms of a velocity parallel to the long axis of the fluke v_{tf} and an angular velocity about a center of rotation located on the long axis of the fluke (x_{fn},y_{fn}). A local coordinate system may thus be established, with the *p* and *t* coordinates corresponding to directions normal and tangential to the fluke, respectively. The special cases of pure translation in directions normal or parallel to the fluke are described by a center of rotation located an infinite distance from the fluke. A description of motions of the anchor shank is treated in a similar manner. In terms of global coordinates, the components of velocity tangential and normal to the long axis of the fluke and shank are given by Eqs. 5.1.

$$V_{tf} = \sqrt{(x_0 - x_{nf})^2 - (y_0 - y_{nf})^2}\,\dot{\beta} \tag{5.1a}$$

$$v_{pf} = \sqrt{(x_{nf} - x)^2 + (y_{nf} - y)^2}\,\dot{\beta} \tag{5.1b}$$

$$V_{ts} = \sqrt{(x_0 - x_{ns})^2 - (y_0 - y_{ns})^2}\,\dot{\beta} \tag{5.1c}$$

$$v_{ps} = \sqrt{(x_{ns} - x)^2 + (y_{ns} - y)^2}\,\dot{\beta} \tag{5.1d}$$

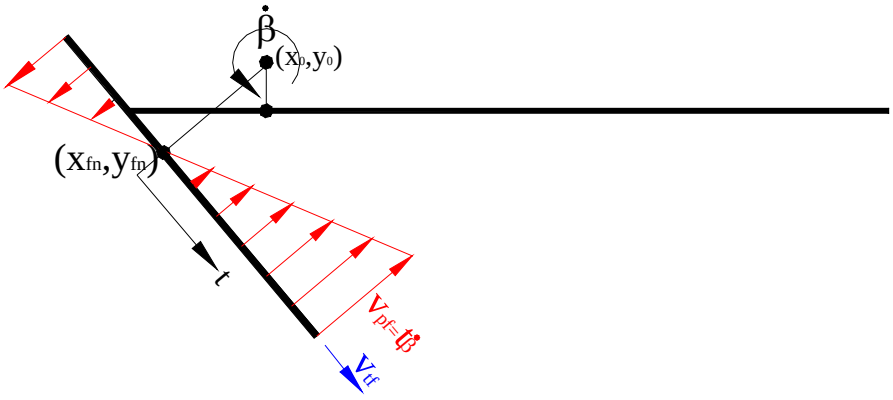

a. velocities of fluke

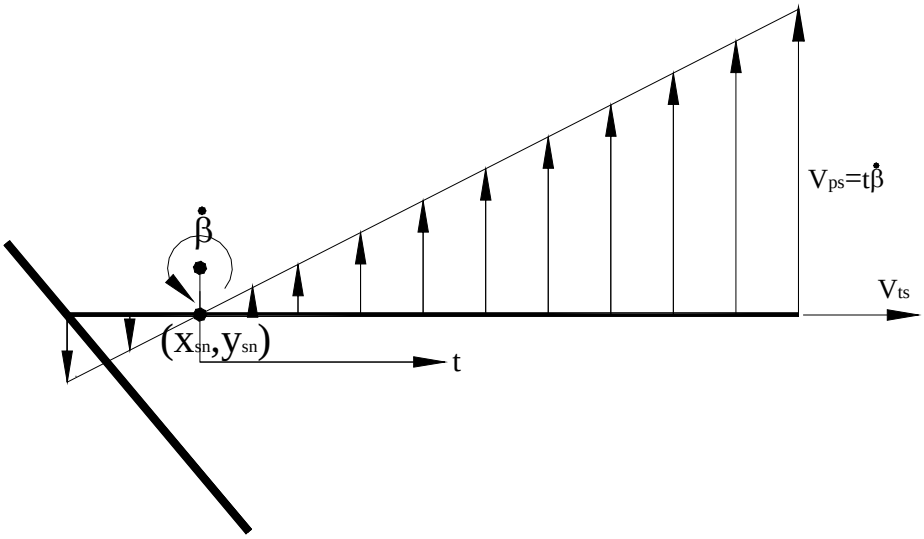

b. velocities of shank

Fig. 5.3 Velocities of drag anchor

5.2 Virtual energy dissipation on fluke and shank

5.2.1 Virtual energy dissipation due to tangential motion on fluke

The component of velocity parallel to the long axis of the fluke V_{tf} is constant for all points on the fluke. As shown by Eq. 5.1a, V_{tf} depends on the distance between point (x_{fn},y_{fn}) on the fluke and its center of rotation (x_0,y_0).

The energy dissipation rate at a point *(x, y)* along the fluke on a differential element is

$$d\dot{D}_{tf} = V_{tf} \times \alpha S_u(y) \times N_{tf} \times A_{tf}(s) \times ds \qquad (5.2)$$

where V_{tf} is velocity given by equation 5.1a

α = adhesion factor

$S_u(y)$ = undrained soil strength at a depth y

N_{tf} = tangential resistance factor of fluke (assumed to be one)

s = chord length

$A_{tf}(s)$ = the width of the fluke

$$ds = \sqrt{dx^2 + dy^2} = dx\sqrt{1+\left(\frac{dy}{dx}\right)^2} = dx\sqrt{1+m^2} \qquad (5.3)$$

where $m = \frac{dy}{dx}$

Thus we get the differential dissipation rate per increment of horizontal distance dx.

$$d\dot{D}_{tf} = V_{tf} \times \alpha S_u(y) \times N_{tf} \times A_{tf}(s) \times \sqrt{1+m^2}\,dx \qquad (5.4)$$

The adhesion factor, α is often taken as the reciprocal of soil sensitivity, $\alpha \approx 1/s_t$. The tangential components of resistance are assumed to be unaffected by the conditions of anchor rotation.

5.2.2 Virtual energy dissipation due to normal motion on fluke

As can bee seen in Fig. 5.3a, the normal velocity V_{pf} varies linearly along the fluke. It is determined by the product of the rotation rate times the distance between normal intersection point (x_{fn},y_{fn}) and the point (x,y) on fluke.

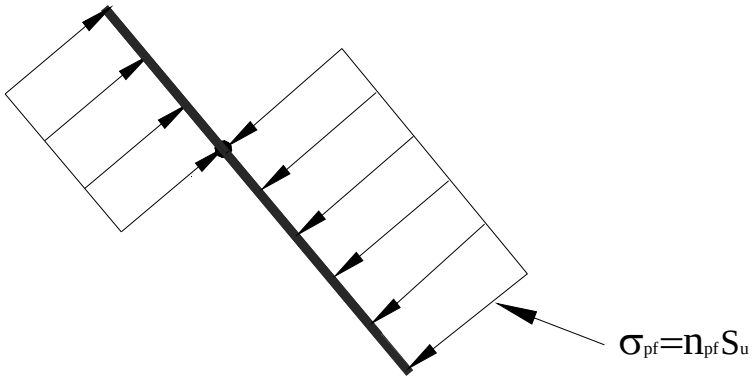

Fig. 5.4 Normal resistance on fluke

As it can be seen in Fig. 5.4, it is assumed that the resistance opposing the normal velocity is uniform along the fluke such that the differential dissipation rate is

$$d\dot{D}_{pf} = V_{pf} \times S_u(y) \times n_{pf} \times A_{pf}(s) \times \sqrt{1+m^2}\,dx \qquad (5.5)$$

where V_{pf} is defined by equation 5.1b

n_{pf} = bearing resistance factor of fluke (will be discussed in Chapter VI)

A_{pf} = bearing area of fluke and the other parameters are as defined in Eq. 5.2

5.2.3 Virtual energy dissipation on ends of fluke

If the fluke has a significant thickness then the dissipation due tip resistance should be considered. Fig. 5.5 shows schematic of tip resistance of the fluke.

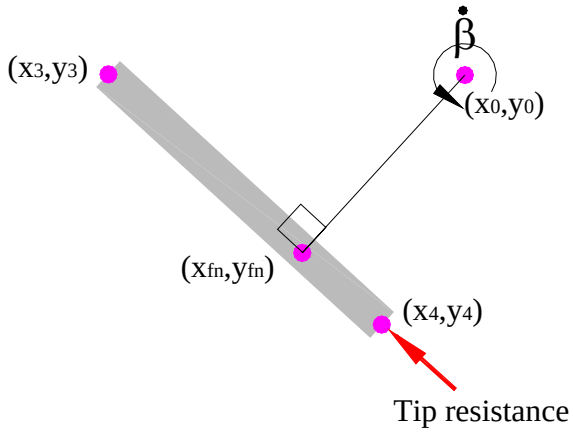

Fig. 5.5 End resistance on tip of the fluke

The dissipation rate at the end of the fluke can be expressed as follow:

$$\dot{D}_{ef} = V_{ef} \times N_{ef} \times S_u(y_4) \times A_{ef} \qquad (5.6)$$

where $V_{ef} = V_{tf}$ (parallel velocity of fluke)

N_{ef} = resistance factor, assumed to be approximately 12

$S_u(y_4)$ = undrained soil strength at depth y_4 (tip of fluke)

A_{ef} = area of tip of fluke

5.2.4 Virtual energy dissipation due to tangential motion on shank

The component of velocity parallel to the long axis of the shank V_{ts} is constant for all points on the shank as shown in Fig. 5.3b. The parallel velocity of the shank V_{ts} depends on the distance between point (x_{sn},y_{sn}) on the shank and its center of rotation (x_0,y_0). Therefore, the energy dissipation rate at a point (x, y) along the fluke on a differential element is

$$d\dot{D}_{ts} = V_{ts} \times \alpha S_u(y) \times N_{ts} \times A_{ts}(s) \times ds \qquad (5.7)$$

where V_{ts} is velocity given by Eq. 5.1c

α = adhesion factor

$S_u(y)$ = undrained soil strength at a depth y

N_{ts} = tangential resistance factor of shank (assumed to be one)

s = chord length

$A_{ts}(s)$ = side resistance area of shank along a chord

$$ds = \sqrt{dx^2 + dy^2} = dx\sqrt{1+\left(\frac{dy}{dx}\right)^2} = dx\sqrt{1+m^2} \qquad (5.8)$$

where $m = \dfrac{dy}{dx}$

Thus we get the differential dissipation rate per increment of horizontal distance dx

$$d\dot{D}_{ts} = V_{ts} \times \alpha S_u(y) \times N_{ts} \times A_{ts}(s) \times \sqrt{1+m^2}\,dx \qquad (5.9)$$

The adhesion factor, α is often taken as the reciprocal of soil sensitivity, $\alpha \approx 1/s_t$. The tangential components of resistance are assumed to be unaffected by the conditions of anchor rotation.

5.2.5 Virtual energy dissipation due to normal motion on shank

As can bee seen in Fig. 5.3, the normal velocity varies linearly along the shank. It is determined by the product of the rotation rate times the distance between normal intersection point (x_{sn} ,y_{sn}) and the point (x,y) on shank. Fig. 5.6 shows the assumed resistance on shank.

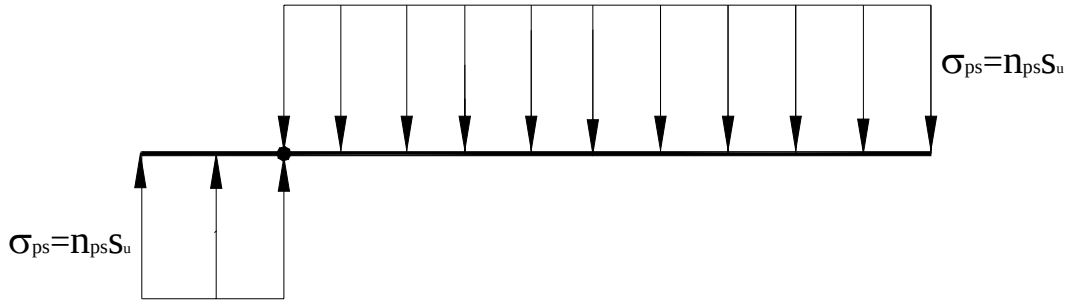

Fig. 5.6 Normal resistance on shank

It is assumed that the resistance opposing the normal velocity is uniform along the fluke such that the differential dissipation rate is

$$d\dot{D}_{ps} = V_{ps} \times S_u(y) \times n_{ps} \times A_{ps}(s) \times \sqrt{1+m^2}\,dx \qquad (5.10)$$

where V_{ps} is defined by Eq. 5.1d

n_{ps} = bearing resistance factor of shank

A_{ps} = bearing area of shank and the other parameters are as defined in Eq. 5.2

5.2.6 Integration for total rate of energy dissipation

Eqs. 5.4 and 5.5 provide expressions for the rate of virtual energy dissipation per unit horizontal length of fluke associated with the tangential and normal components of velocity, respectively. Eqs. 5.9 and 5.10 provide expressions for shank. Total virtual energy dissipation rates must be computed by integrating the energy dissipation rates all over the anchor. Eq. 5.11 shows total energy dissipation rates.

$$\dot{D}_T = \dot{D}_{tf} + \dot{D}_{pf} + \dot{D}_{ef} + \dot{D}_{ts} + \dot{D}_{ps} \tag{5.11}$$

where $\dot{D}_{tf}$ = Virtual energy dissipation due to tangential motion on fluke

$\dot{D}_{pf}$ = Virtual energy dissipation due to normal motion on fluke

$\dot{D}_{ef}$ = Virtual energy dissipation on ends of fluke

$\dot{D}_{ts}$ = Virtual energy dissipation due to tangential motion on shank

$\dot{D}_{ps}$ = Virtual energy dissipation due to normal motion on shank

The algorithm developed in this research performs the integration using a numerical integration method, especially Simpson's rule. To achieve adequate numerical accuracy, the fluke and shank are sub-divided into 20 horizontal length increments.

5.2.7 External work

A. The weight of drag anchor

The center of gravity of the anchor is located by the coordinates x_w and y_w as shown in Fig. 5.7 and given by Eqs. 5.12.

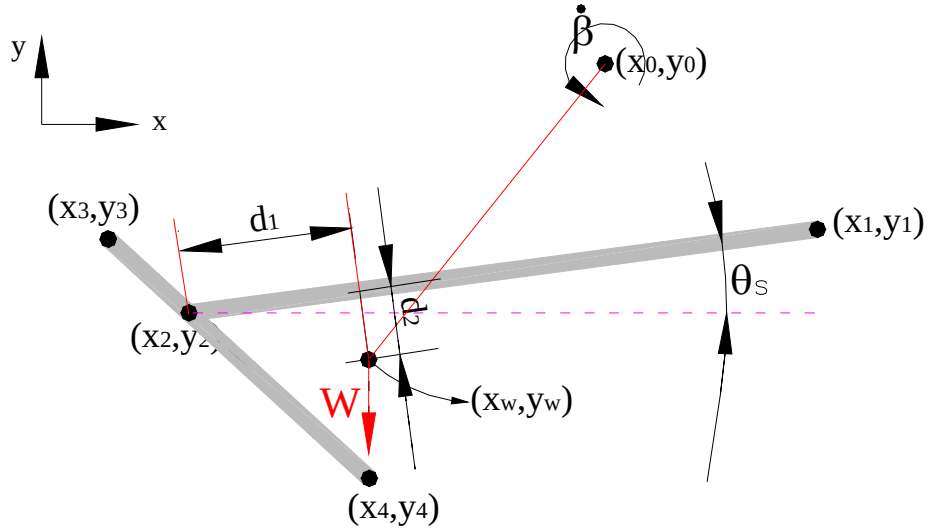

Fig. 5.7 Weight of drag anchor

$$x_w = x_2 + d_1 \cos\theta_s + d_2 \sin\theta_s \tag{5.12a}$$

$$y_w = y_2 + d_1 \sin\theta_s - d_2 \cos\theta_s \tag{5.12b}$$

The weight of the anchor acts in direction of gravity, giving the external virtual work performed by the anchor weight as:

$$\dot{w}_w = W \times (x_0 - x_w)\dot{\beta} \tag{5.13}$$

B. Resultant force, F

The anchor line force, F, is the principal unknown. The relevant geometry is shown in Fig. 5.8.

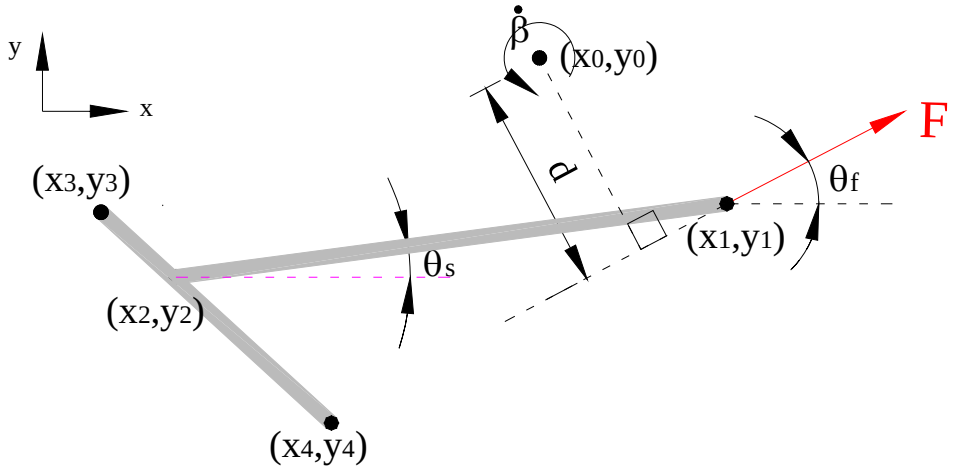

Fig. 5.8 Resultant force F

From Fig. 5.8, the equation of the line of action of the anchor line force *F* is:

$$y = \tan\theta_f (x - x_1) + y_1 \tag{5.14a}$$

or alternatively:

$$\tan\theta_f \cdot x - y + y_1 - \tan\theta_f \cdot x_1 = 0 \tag{5.14b}$$

The distance between center of rotation (x_0, y_0) and line of action of the force, *d*, is

$$d = \frac{\tan\theta_f \cdot x_0 - 1 \cdot y_0 + y_1 - \tan\theta_f}{\sqrt{\tan^2\theta_f + (-1)^2}} \tag{5.15}$$

The virtual velocity of the anchor line load is

$$v = abs\left(\frac{\tan\theta_f \cdot x_0 - 1\cdot y_0 + y_1 - \tan\theta_f}{\sqrt{\tan^2\theta_f + (-1)^2}}\right)\dot{\beta} \tag{5.16}$$

and the external work rate is then

$$\dot{w}_F = F \times abs\left(\frac{\tan\theta_f \cdot x_0 - 1\cdot y_0 + y_1 - \tan\theta_f}{\sqrt{\tan^2\theta_f + (-1)^2}}\right)\dot{\beta} \tag{5.17}$$

Total external work rate done is in the mechanism is then

$$\begin{aligned}\dot{w}_t &= \dot{w}_w + \dot{w}_F \\ &= W \times (x_0 - x_w)\dot{\beta} + F \times abs\left(\frac{\tan\theta_f \cdot x_0 - 1\cdot y_0 + y_1 - \tan\theta_f}{\sqrt{\tan^2\theta_f + (-1)^2}}\right)\dot{\beta}\end{aligned} \tag{5.18}$$

The total internal energy dissipation is then set equal to the external work rate giving

$$\dot{D}_T = W \times (x_0 - x_w)\dot{\beta} + F \times abs\left(\frac{\tan\theta_f \cdot x_0 - 1\cdot y_0 + y_1 - \tan\theta_f}{\sqrt{\tan^2\theta_f + (-1)^2}}\right)\dot{\beta} \tag{5.19}$$

The upper bound estimate of the resultant force F can then be calculated as

$$F = \frac{\dot{D}_T - W \times (x_0 - x_w)\dot{\beta}}{abs\left(\frac{\tan\theta_f \cdot x_0 - 1\cdot y_0 + y_1 - \tan\theta_f}{\sqrt{\tan^2\theta_f + (-1)^2}}\right)\dot{\beta}} \tag{5.20}$$

5.3 Optimization of resultant force *F*

An upper bound estimate of the resultant force *F* is calculated using Eq. 5.20. If the angle of force is fixed in this equation then the center of rotation is the only variable. Therefore, it is necessary to minimize *F* with respect to coordinates (x_0, y_0) in Eq. 5.20 to get the best solution. A contour plot of resultant forces at each center of rotation can be drawn to graphically find the optimum center of rotation corresponding to a minimum *F*. This process is similar to finding the best estimate of the safety factor in slope stability analysis. To understand procedure of computing a minimum resultant force, an example problem is shown in Fig. 5.9. Table 5.1 indicates the relevant geometric parameters for the example anchor. In this example, the anchor fluke is considered to be rectangular with 3m width.

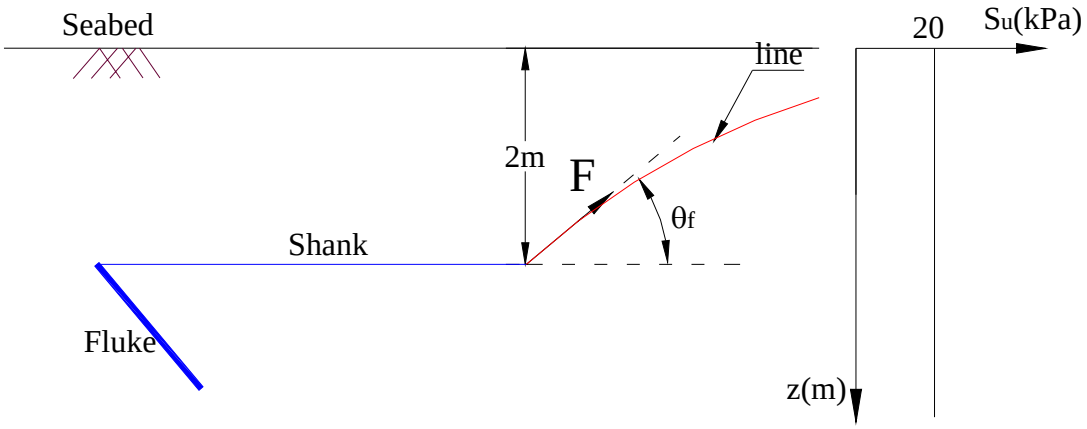

Fig. 5.9 Anchor initial position and soil strength condition
for optimization of resultant force, F

Table 5.1 Geometry of drag anchor used example study

Embedded Anchor Initial Position	
Anchor Line Attachment Point	x_1=0, y_1=-2m
Fluke-shank intersection point	X_2=-4, y_2=-2m
Anchor properties	
Fluke length, m	1.5
Fluke-shank angle, degrees	50
Fluke bearing area per unit length, m^2/m	3
Fluke shear area per unit length, m^2/m	6
Plate type of shank	
Shank bearing area per unit length, m^2/m	0.2
Shank shear area per unit length, m^2/m	0.4
Bridle type of shank	
Shank bearing area per unit length, m^2/m	0
Shank shear area per unit length, m^2/m	0

This example considers cases in which the anchor line angle is fixed at 5^o and 10^o, respectively. The resultant force can be calculated at a grid of trial centers of rotation. Associating the calculated force with its trial center of rotation, we can draw contour lines as shown in Fig. 5.10 and Fig. 5.11.

As it can be seen in Figures 5.10, in the case of a 5^o force angle, the center of rotation occurs at infinite distance from the anchor. On the other hand, as shown in Fig.

5.11, in case of 10^{o} force angle, center of rotation occurs near the anchor. Its optimum center of rotation is located at (*-0.4, 0.6*) as indicated in Fig. 5.11.

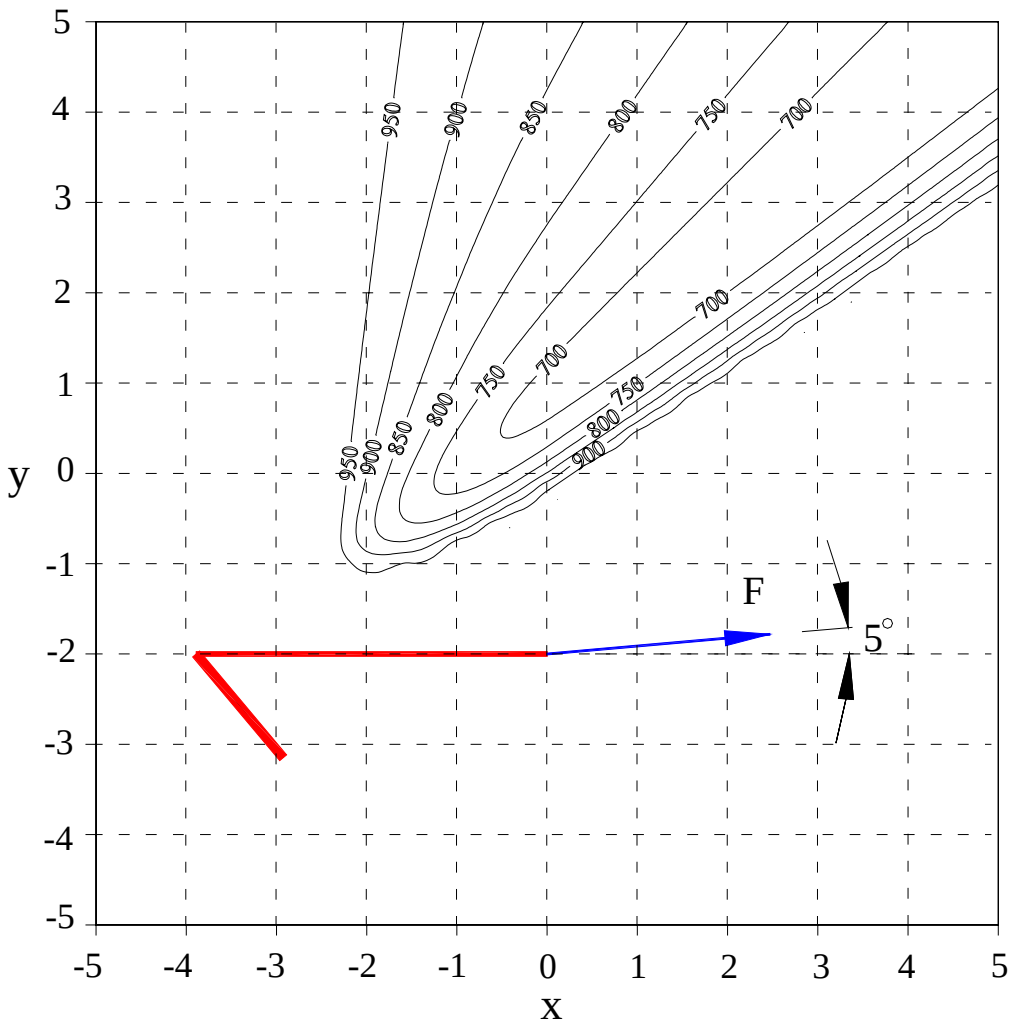

Fig. 5.10 contour of resultant force (beam shank, $\theta_f = 5^{o}$)

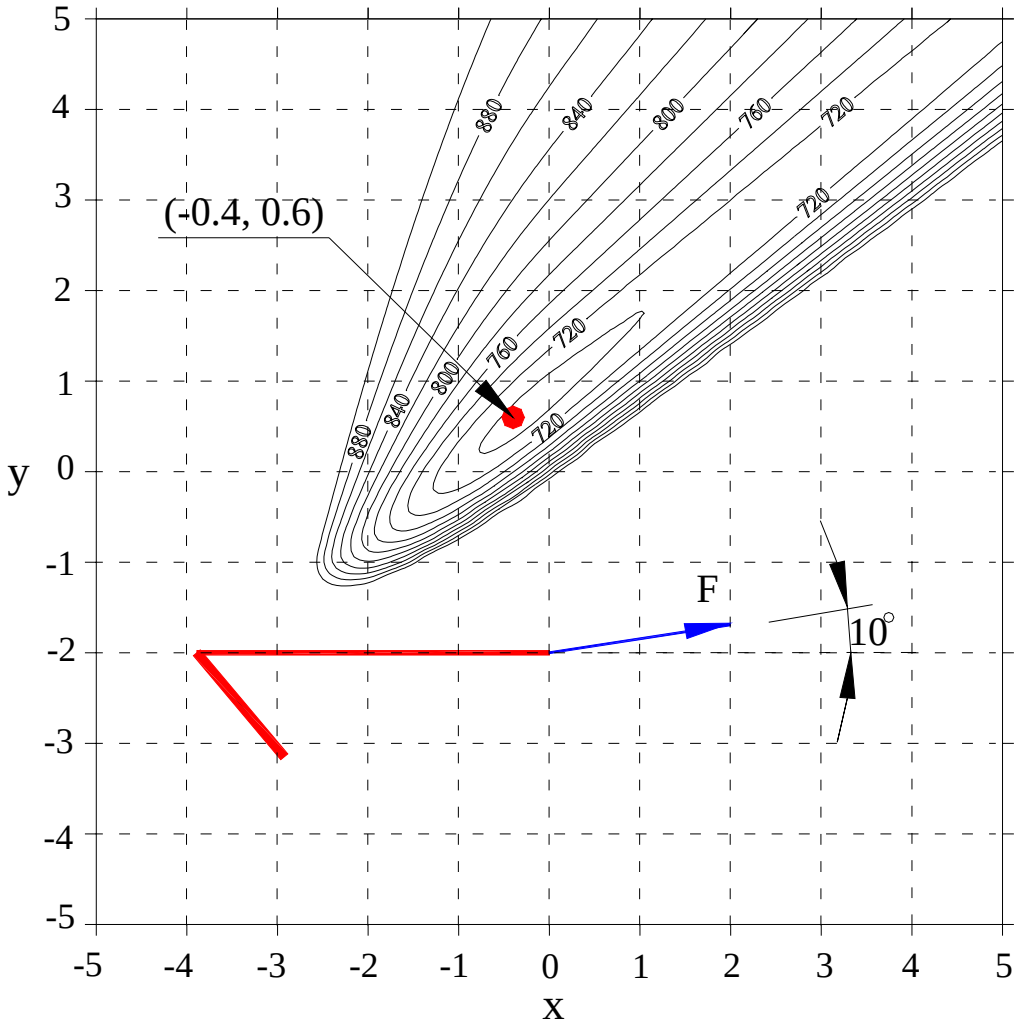

Fig. 5.11 Contour of resultant force (plate shank, θ_f =10^o)

5.4 Characteristic curve

In this study, two types of shank are considered as a rigid beam type and a bridle type as shown in Figure 1.5. As previously mentioned the beam type shank is resisted by soil forces normal to and parallel to its surface. The soil forces in the bridle case are neglected for its small resistance. For example, the Stevpris and the Bruce MK5 have beam type shanks, while the Stevmanta of Vryhof is a bridle type. If anchor is embedded at a given depth then the optimum resultant force F must be calculated for a range of force angles. In this study, the locus of points relating anchor line force angle θ_f to resultant force F will be referred to as the characteristic curve. As an example, consider the anchor embedded as shown in Fig. 5.9, with the anchor geometry and undrained soil strength as described in Table 5.1.

Table 5.2 and Fig. 5.12 show the results of the analysis and optimization procedure presented in Section 5.1 to 5.3 for a range of anchor line force angle θ_f. Also shown is the anchor line tension T computed for Eq. 2.10. Fig. 5.13 shows traces of the optimum centers of rotation corresponding to each force angle. Table 5.3 and Fig. 5.14 show similar calculations for the case of an anchor having a bridle shank. Fig. 5.15 shows traces of the optimum centers of rotation corresponding to each force angle for bridle shank.

The highlighted row in Tables 5.2 and 5.3 show the break point which anchor collapse. As it can be seen in Fig. 5.12 and 5.14, intersection point is defined as a point which anchor resultant force curve and anchor line curve intersect each other. This

intersection point defines the unique solution for anchor resultant force (magnitude and direction) for a given anchor depth and orientation.

As shown in Fig. 5.12 and Fig. 5.14, the characteristic curves with the two types of shank are considerably different. In the case of a beam shank, the resultant force *F* steeply increases with anchor line angle until 9^o. The characteristic curve then abruptly breaks, follows a plateau between 9^o and 15^o, and then decreases. For the bridle shank, the curve peaks at 20^o and the resultant force drops off immediately. For both the beam and bridle shank cases, the anchor tends to translate in a direction parallel to the fluke up until θ_f reaches the break point, at which point the anchor tends to rotate. This is further illustrated in Fig. 5.13 showing the location of the center of rotation as a function of force angle for the beam shank. In the case of a bridle shank as shown in Fig. 5.15, the center of rotation abruptly jumps from infinity to a point on the fluke as soon as the force angle θ_f reaches the break point value, in this case $(\theta_f)_{break} = 20^o$.

The behavior of an anchor with a beam shank therefore differs from that of one with a bridle shank in several important respects. The characteristics curve of a beam shank anchor exhibits a flat plateau when the break point is reached, in contrast to the sharp peak of the bridle anchor characteristic curve, also significantly differs from that of the beam shank anchor, in the case of this example, 20^o versus 9^o. Finally, the bridle anchor follows two modes. At angles below the break point the anchor trends to translate, while at angles above the break point it rotates about a point located on the fluke. In contrast, for a beam shank anchor the optimum center of rotation gradually migrates towards the fluke as the force angle θ_f is increased beyond the break point.

Using this curve in combination with the anchor line resistance curve we can project the anchor performance. The anchor line load equation was discussed in Section 2.2 in detail. For a given depth of attachment we can construct a curve of anchor line load as line inclination (corresponding to the force on the shank) as shown in Fig. 5.12 and 5.13. Applying these curves to predicting anchor performance is discussed in the following section.

Table 5.2 Characteristics at initial condition (beam shank)

Force angle	Optimum coordinates of center of rotation		Minimum resultant force	Line load
(degree)	x_0	y_0	F (kN)	T (kN)
5	1.00E+08	83909963	632.946	4727.241
6	1.00E+08	83909963	649.227	3282.806
7	1.00E+08	83909963	666.575	2411.858
8	1.00E+08	83909963	685.091	1846.579
9	0	0.872	691.368	1459.025
10	-0.074	0.811	693.32	1181.81
11	-0.389	0.546	693.37	976.703
12	-0.391	0.545	693.97	820.702
13	-0.778	0.22	693.75	699.296

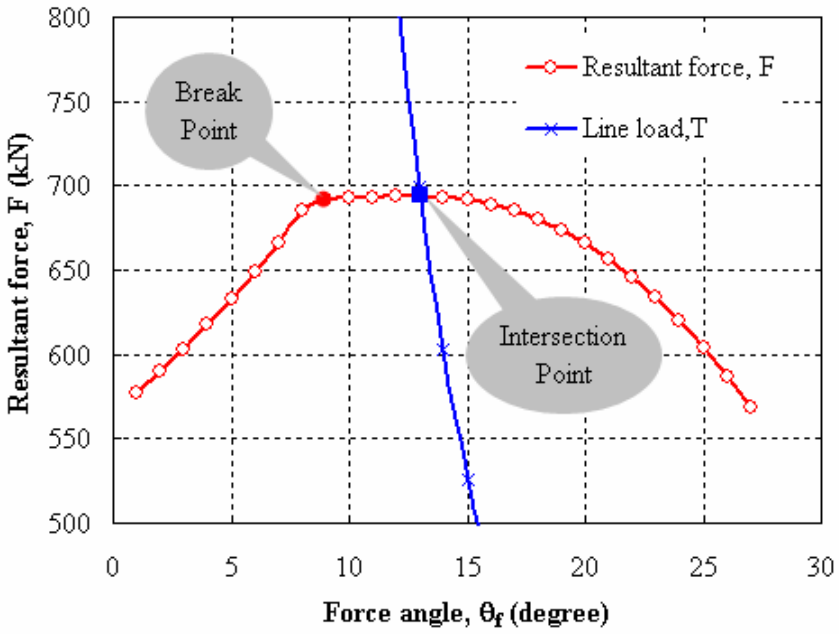

Fig. 5.12 Characteristic curve at initial condition (beam shank)

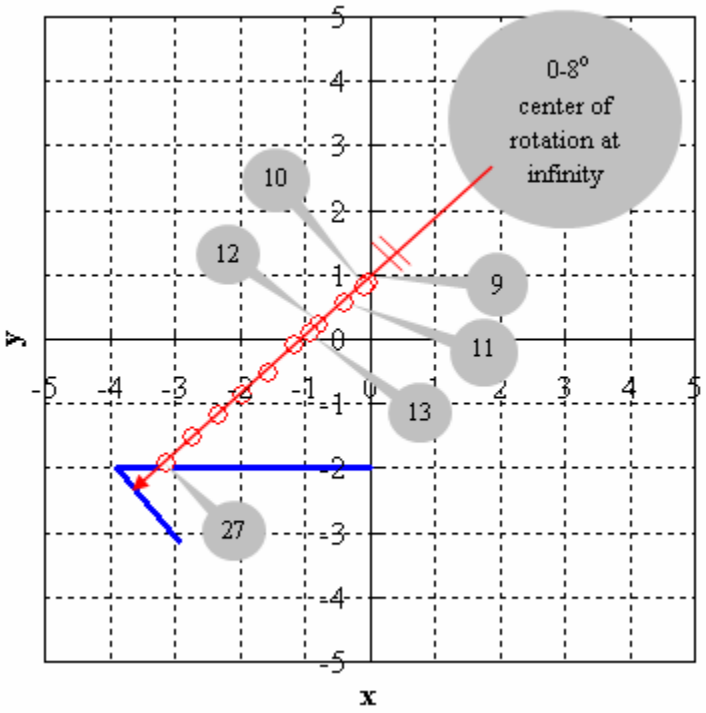

Fig. 5.13 Trace of optimum center of rotation (beam shank)

Table 5.3 Characteristics at initial condition (bridle shank)

Force angle	Optimum coordinates of center of rotation		Minimum resultant force	Line load
(degree)	x_0	y_0	F (kN)	T (kN)
17	1.00E+08	83909963	460.675	408.931
18	1.00E+08	83909963	480.504	364.756
19	1.00E+08	83909963	502.277	327.371
20	-3.627	-2.313	516.829	295.453
21	-3.601	-2.345	485.046	267.984
22	-3.602	-2.344	456.493	244.176
23	-3.601	-2.345	431.165	223.405

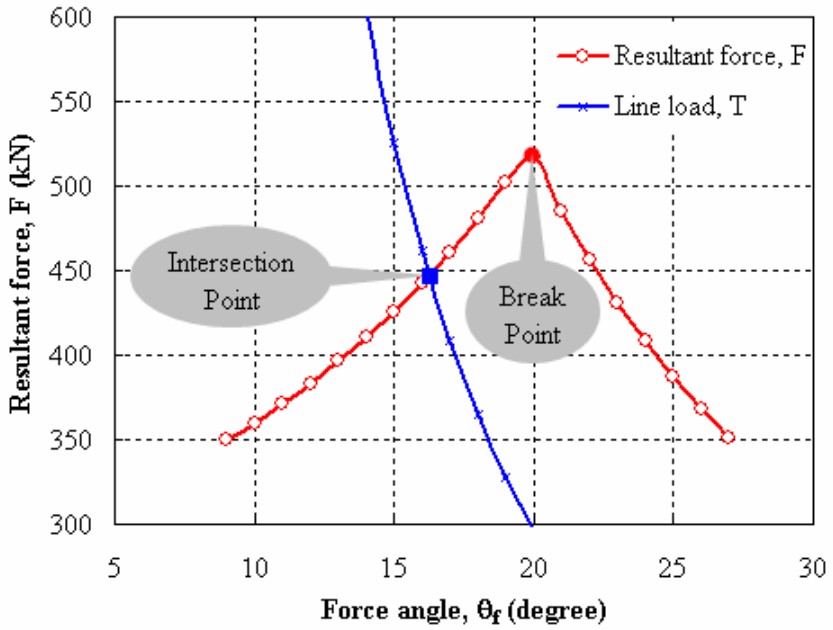

Fig. 5.14 Characteristic curve (bridle shank)

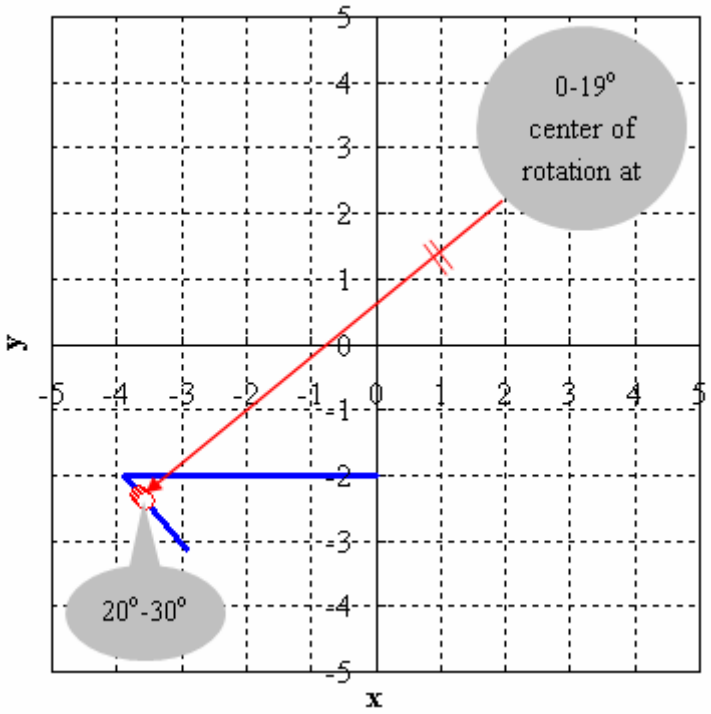

Fig. 5.15 Trace of center of rotation (bridle shank)

5.5 Prediction of anchor trajectory

Based on the approach described in the preceding sections for computing the anchor line force for a given anchor depth and orientation trajectory in the following steps:

1. The characteristic curve for the anchor, $F\text{-}\theta_f$ is developed using the UBM program for a specific anchor position and orientation.
2. The characteristic curve for the anchor line, $T\text{-}\theta_f$ is developed using the anchor line solution (Eq. 2.10). Typical curves are shown in Fig. 5.16.

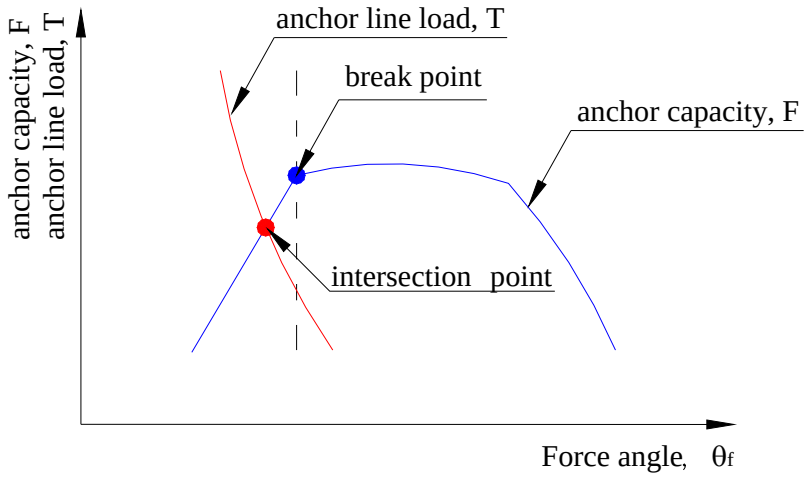

Fig. 5.16 Characteristic curves (beam shank)

3. When the intersection point is left of the break point, the anchor is advanced parallel to the fluke some incremental depth, for example $\Delta z = 1m$. When the intersection point is right side of the break point the anchor is rotated about its optimal center of rotation some incremental angle, for example $\Delta\theta_s = 1^\circ$. The depth and angle increments (Δz and $\Delta\theta_s$) can be adjusted to control numerical accuracy.

4. Step 1, 2 and 3 are repeated until the fluke is parallel to the seabed.

Fig. 5.17 shows the procedure of the UBM for drag anchor as a flow chart.

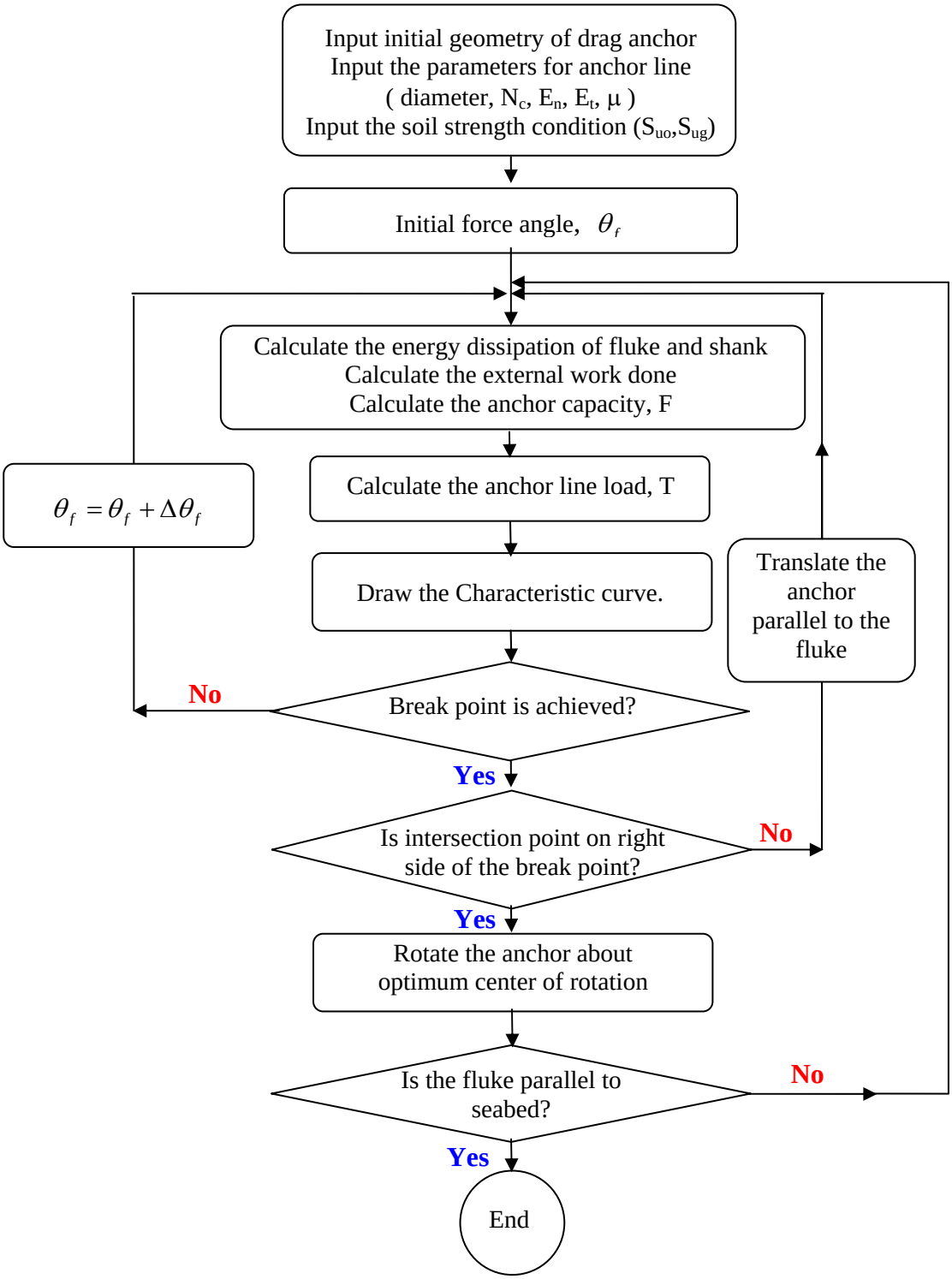

Fig. 5.17 Flow chart for UBM

5.6 Example simulation of UBM

An anchor is embedded as shown in Fig. 5.18. The shank is parallel to the seabed and the anchor line is attached to the shackle at depth of 1m. The anchor geometry is the same as in Table 5.1 for the beam shank. Undrained soil strength increases linearly with depth as shown in Fig. 5.18.

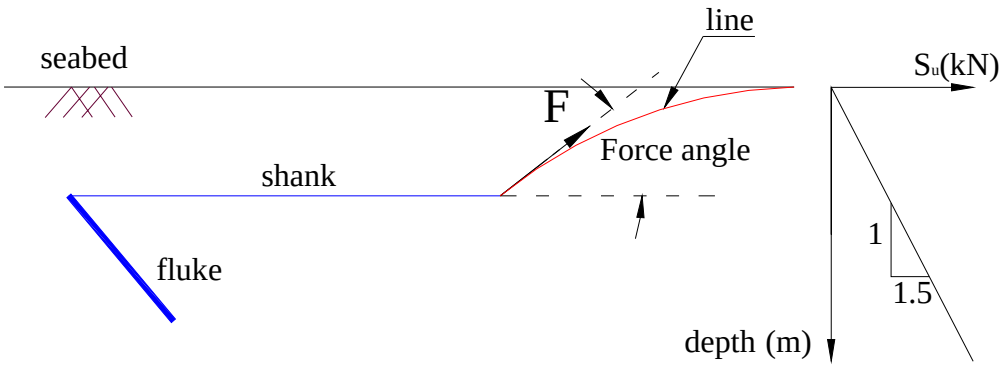

Fig. 5.18 Initial position of drag anchor

The characteristic curve for this initial position is shown in Fig. 5.19. As indicated the break point occurs at a force angle of 14^{o}.

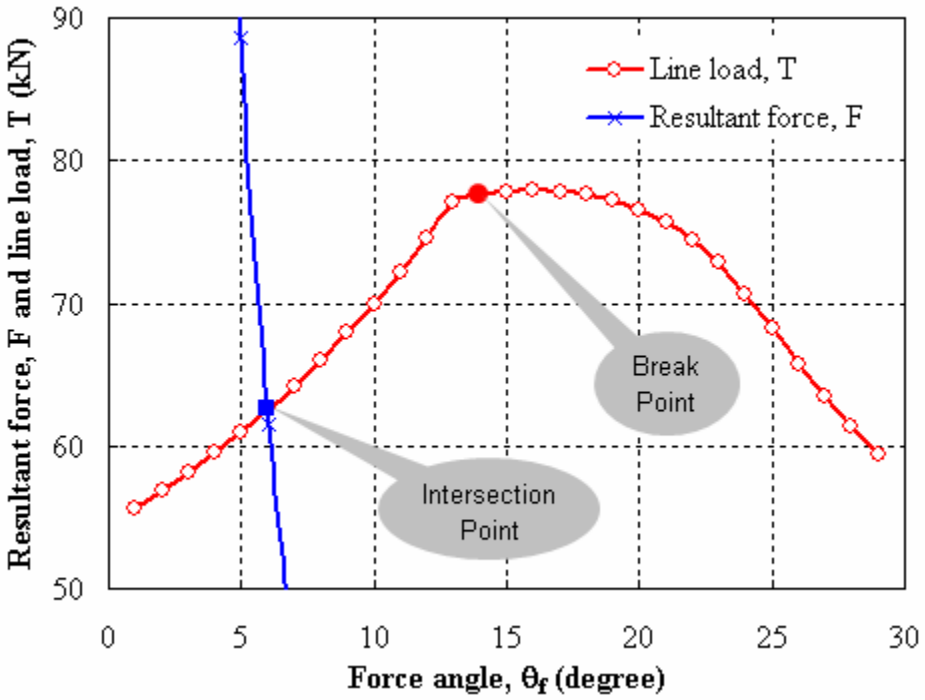

Fig. 5.19 Characteristic curve at initial condition

Table 5.4 shows the characteristic values of drag anchor at a given depth z=1m with shank angle of zero degree. Fig. 5.20 shows that the critical center of rotation (x_0,y_0) for the mechanism occurs at a large distance from the anchor until the force angle reaches 14^o. The center of rotation jumps abruptly to near the anchor when the force angle approaches 14^o. At this force angle the mechanism involves rotation of the anchor.

Initially, the anchor characteristic curve (F-θ_f) and the anchor line load curve (T-θ_f) intersect left side of break point. In this case, the anchor collapse mechanism is translation parallel to the fluke as indicated by the center of rotation being essentially infinitely far away from the anchor.

Table 5.4 Trace of center of rotation, resultant force and line load (z=1m)

Force angle (degree)	Optimum coordinates of center of rotation		Minimum resultant force	Line load
	x_0	y_0	F (kN)	T (kN)
11	1.00E+08	83909964	72.161	18.313
12	1.00E+08	83909964	74.519	15.388
13	1.00E+08	83909964	77.06	13.112
14	0	1.775	77.667	11.306
15	-0.389	1.448	77.825	9.848
16	-0.763	1.037	77.959	8.656
17	-0.78	1.022	77.852	7.667

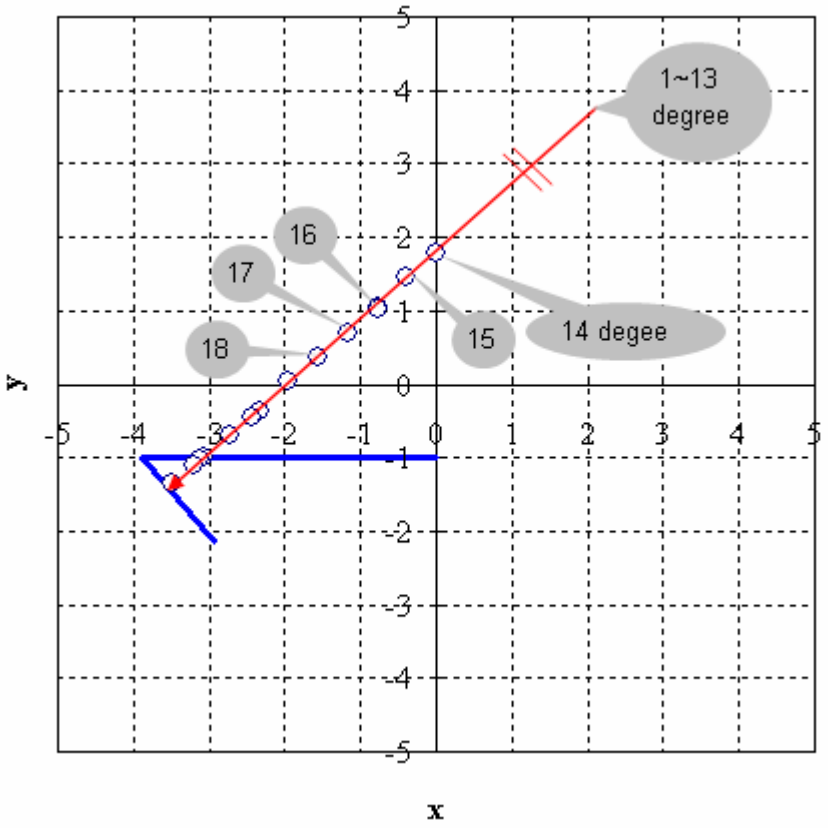

Fig. 5.20 Trace of center of rotation at initial condition (z=1m)

- Step 1

From this initial condition, the drag anchor is translated parallel to the fluke a small vertical increment with the force angle assumed constant. For example, if depth Δz =2m is used, then the anchor is moved to a new location as shown in Fig. 5.21.

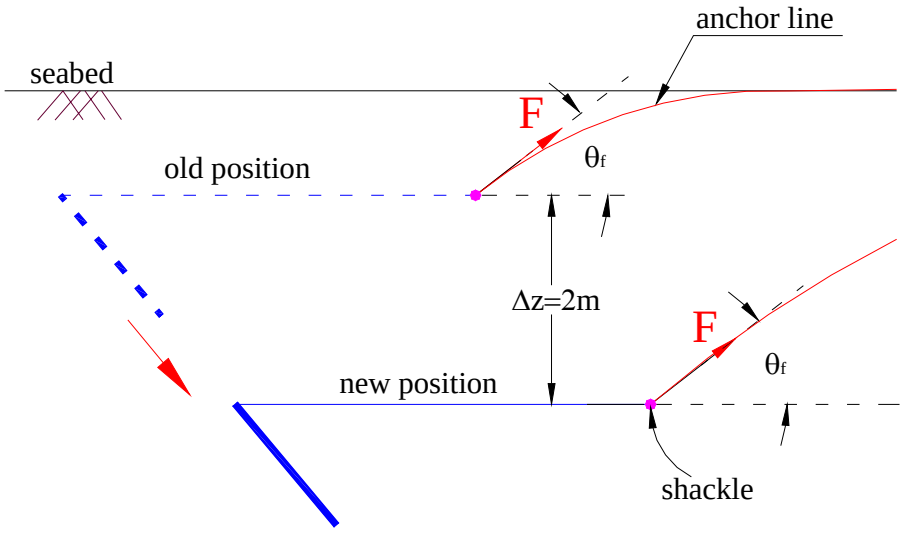

Fig. 5.21 Translation of drag anchor (z=3m)

Table 5.5 shows the characteristic values of drag anchor at a given depth z=3m with shank angle of zero degree. A new characteristic curve is developed at the new position as shown in Fig. 5.22. Fig. 5.23 shows traces of the optimum centers of rotation with varying force angle. Using the new curve, a decision is made whether to translate or to rotate the anchor. The intersection point where the anchor line load intersects the characteristic curve is still left side of the break point. Hence the anchor is translated to the next location with Δz =2m. The new position is shown in Fig. 5.24 and the line attachment point (x_1,y_1) is depth of 5m.

Table 5.5 Trace of center of rotation, resultant force and line load (z=3m)

Force angle	Optimum coordinates of center of rotation		Minimum resultant force	Line load
(degree)	x_0	y_0	F (kN)	T (kN)
7	1.00E+08	83909962	164.22	407.001
8	1.00E+08	83909962	168.782	311.61
9	1.00E+08	83909962	173.659	246.21
10	1.00E+08	83909962	178.882	199.43
11	0	-0.22543	181.311	164.819
12	-0.389	-0.55184	181.792	138.493
13	-0.389	-0.55184	181.984	118.006
14	-0.392	-0.554	182.233	101.75
15	-0.778	-0.878	181.942	88.636

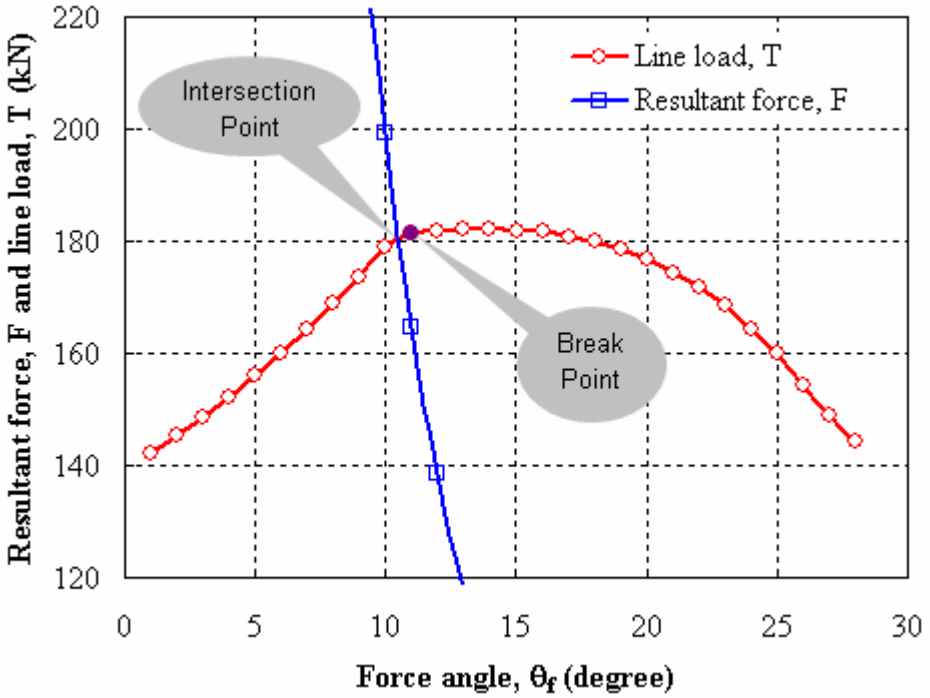

Fig. 5.22 Characteristic curve (z = 3m, $\theta_s = 0^\circ$)

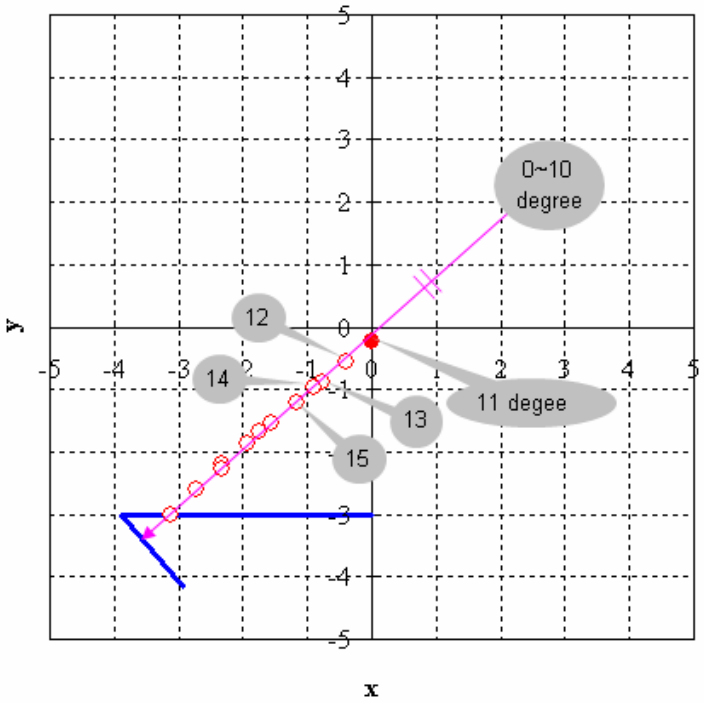

Fig. 5.23 Trace of center of rotation (z = 3m, $\theta_s = 0^\circ$)

- Step 2

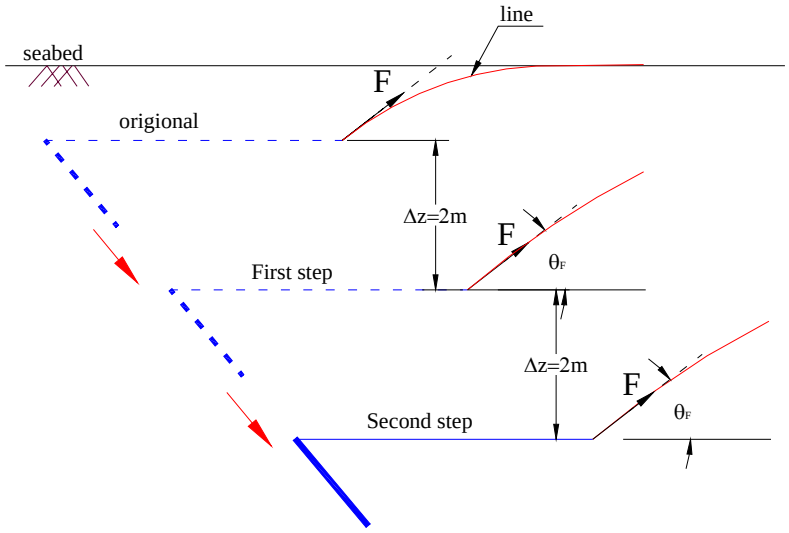

Fig. 5.24 Anchor position of second step (z=5m, $\theta_s = 0^\circ$)

Table 5.6 shows the characteristic values of drag anchor at a given depth z=5m with shank angle of zero degree. At this new position a new characteristic curve is determined again as shown in Fig. 5.25. The optimum centers of rotation are shown in Fig. 5.26 at new position. The previous procedure is repeated.

Table 5.6 Characteristic data (z=5m, $\theta_s = 0^\circ$)

Force angle	Optimum coordinates of center of rotation		Minimum resultant force	Line load
(degree)	x_0	y_0	F (kN)	T (kN)
8	1.00E+08	83909960	271.546	865.584
9	1.00E+08	83909960	279.392	683.918
10	0	-2.128	284.902	553.974
11	-0.34743	-2.419	285.831	457.829
12	-0.389	-2.549	286.077	384.704

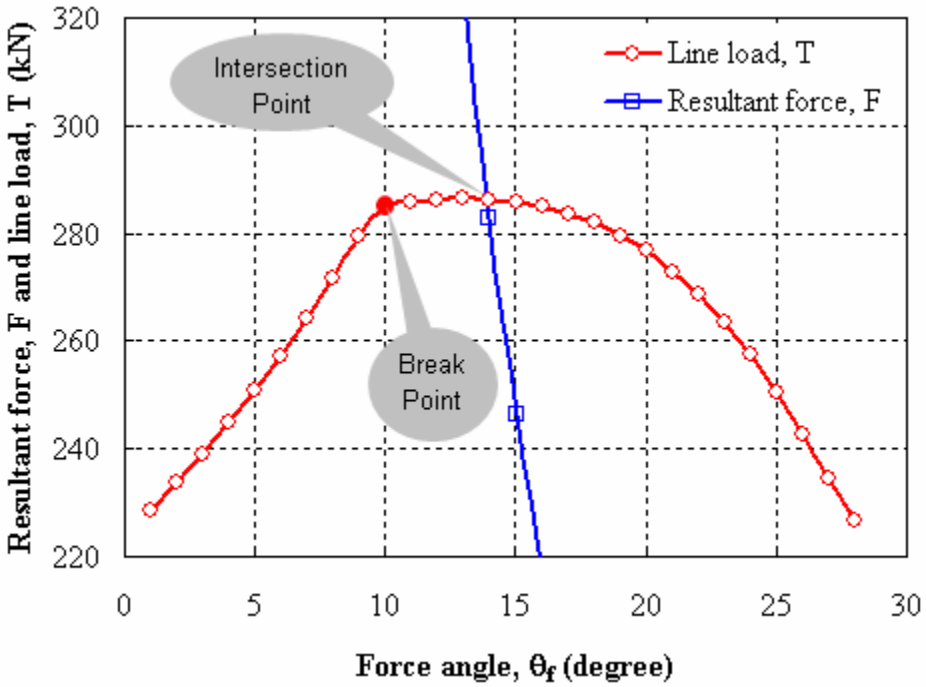

Fig. 5.25 Characteristic curve (z = 5m, $\theta_s = 0^\circ$)

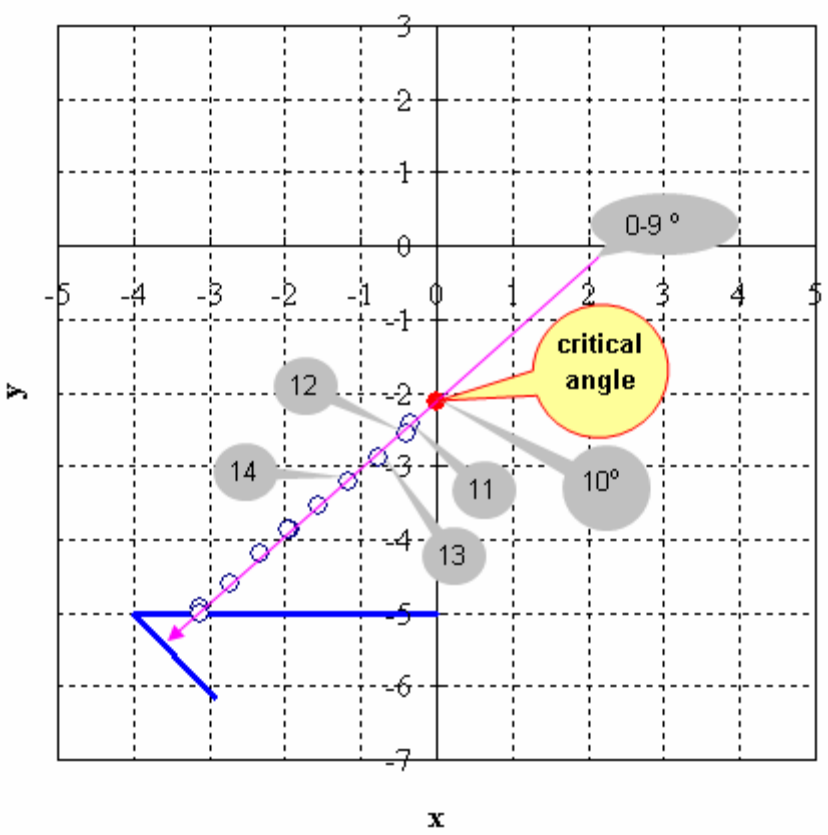

Fig. 5.26 Trace of center of rotation (z = 5m, $\theta_s = 0^\circ$)

In this case the intersection point is now on the right side of the break point. This collapse mechanism then involves a translation and rotation of the anchor, that is, the anchor is rotated about the critical center of rotation (x_0,y_0) as shown in Fig. 5.27. For examples, an increment angle $\Delta\theta = 2^\circ$ is used then the next anchor position is displayed with solid line in Fig. 5.27. The old anchor position is indicated by a dashed line in Fig. 5.27.

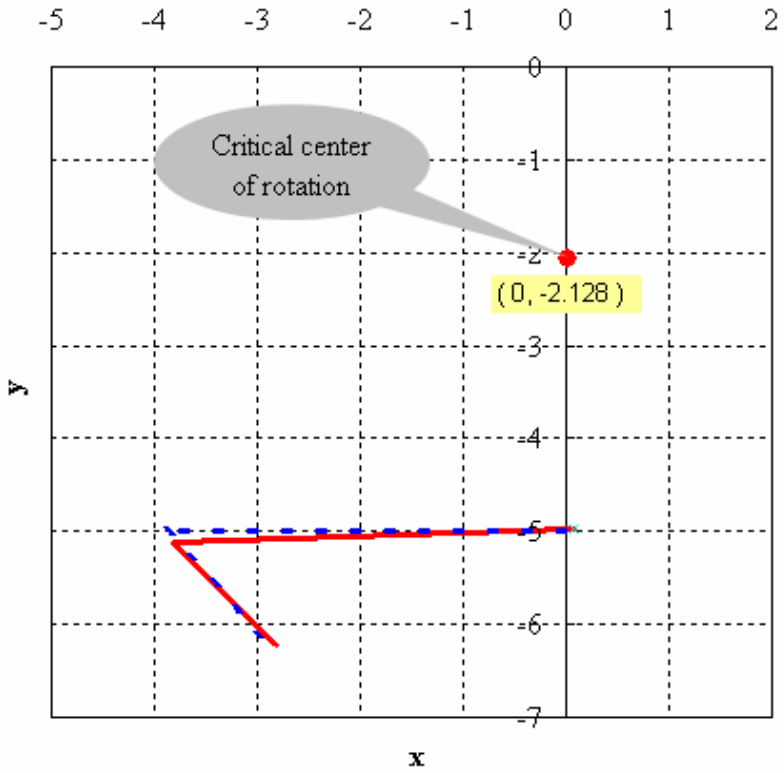

Fig. 5.27 Rotation of anchor (z = 4.972m, $\theta_s = 2^\circ$)

- Step 3

The characteristic curve is then recalculated at this new location as shown in Fig. 5.27 with 2^o of shank angle. The procedure is repeated. Note that because the anchor rotates this effectively displaces the characteristic curve to the left (i.e. the angle in the plot is the angle with the horizontal). The anchor next breaks when the force angle is 12^o and the intersection point is again right of the break point. The anchor is rotated again about the center of rotation (*0.016,-2.063*). A new characteristic value is calculated as indicated in Table 5.7 and it is shown in Fig. 5.28. And the optimum centers of rotation are shown in Fig. 5.29 at new position with varying force angles. This procedure is repeated until the fluke angle is parallel to the seabed.

Table 5.7 Characteristic data ($\theta_s = 4^\circ$)

Force angle	Optimum coordinates of center of rotation		Minimum resultant force	Line load
(degree)	x_0	y_0	F (kN)	T (kN)
9	1.00E+08	90040402	268.857	683.918
10	1.00E+08	90040402	276.325	553.974
11	1.00E+08	90040402	284.309	457.829
12	-0.10025	-2.12928	290.465	384.704
13	-0.26638	-2.27886	291.423	327.795
14	-0.478	-2.469	291.698	282.64
15	-0.474	-2.567	292.02	246.21

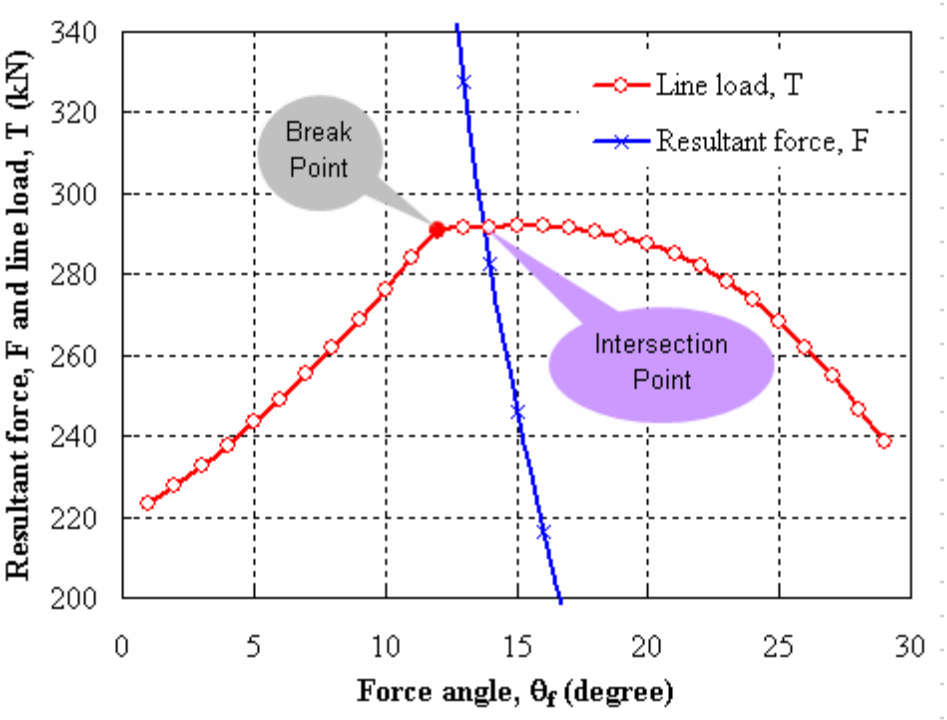

Fig. 5.28 Characteristic curve ($\theta_s = 4^\circ$)

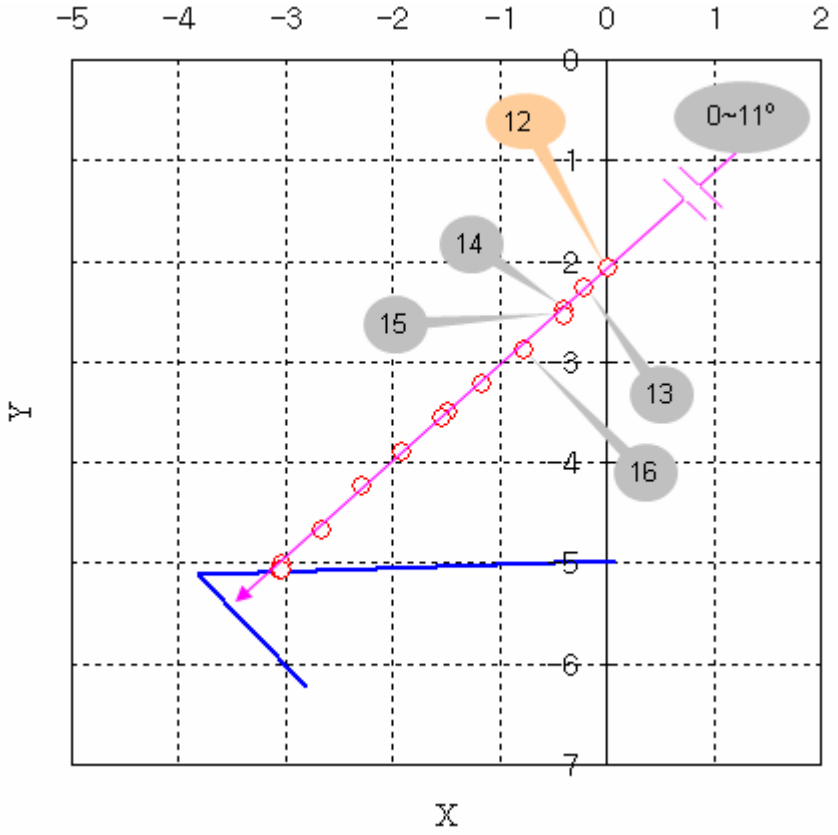

Fig. 5.29 Trace of center of rotation ($\theta_s = 4^\circ$)

- Trajectory curve

The drag anchor trajectory is hence determined by this procedure by repeating the steps resulting in a gradual penetration and rotation of the anchor. This procedure is repeated until the fluke angle is reached to zero, i.e., the fluke is parallel to seabed. Fig. 5.30 shows the trajectory of shackle of drag anchor and Fig. 5.31 shows the resultant forces at shackle for a given drag distance.

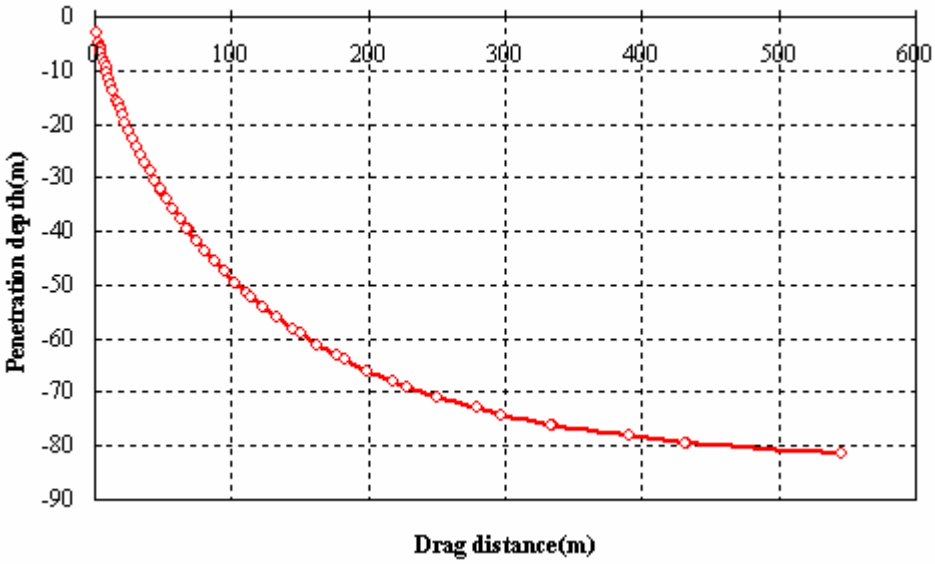

Fig. 5.30 Trajectory curve of model anchor

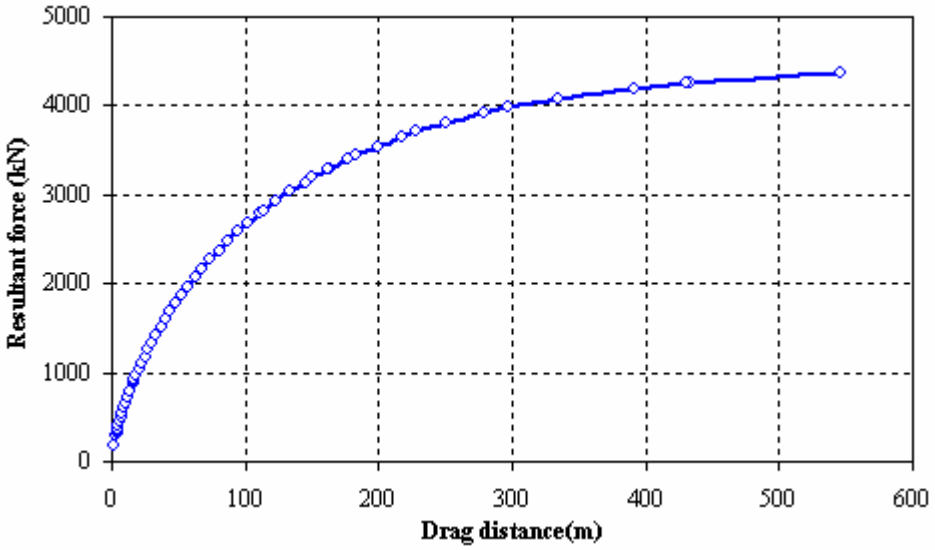

Fig. 5.31 Resultant force of model anchor

CHAPTER VI

BEARING FACTORS FOR UBM

6.1 Normal, tangential and rotational motion

The UBM analysis presented in the previous chapter was formulated in terms of bearing factors relating soil undrained shear strength, S_u, to unit resistances (force per unit area) normal and parallel to the surfaces of the fluke and shank. Specific definitions used in this dissertation are:

n_{pf} = bearing factor relating normal stress on fluke to S_u

n_{tf} = bearing factor relating shear stress on fluke to S_u

n_{ps} = bearing factor relating normal stress on shank to S_u

n_{ts} = bearing factor relating shear stress on shank to S_u

An alternative approach can be employed using “global” bearing factors relating total force to shear strength S_u

N_{pf} = bearing factor relating normal stress on fluke to S_u

N_{tf} = bearing factor relating tangential stress on fluke to S_u

N_{mf} = bearing factor relating moment stress on fluke to S_u

N_{ps} = bearing factor relating normal stress on shank to S_u

N_{ts} = bearing factor relating tangential stress on shank to s_u

Local bearing factors can be related to global factors as will be discussed subsequently.

Two issues arise in connection to bearing factors:

1. What are appropriate bearing factors for conditions of pure translation (normal or tangential) and rotation?
2. What are the interaction effects for combined motions?

The virtual motion of the anchor considered shown in Fig. 6.1. The anchor is assumed to rotate about a point (x_0,y_0) with virtual angular velocity, $\dot{\beta}$.

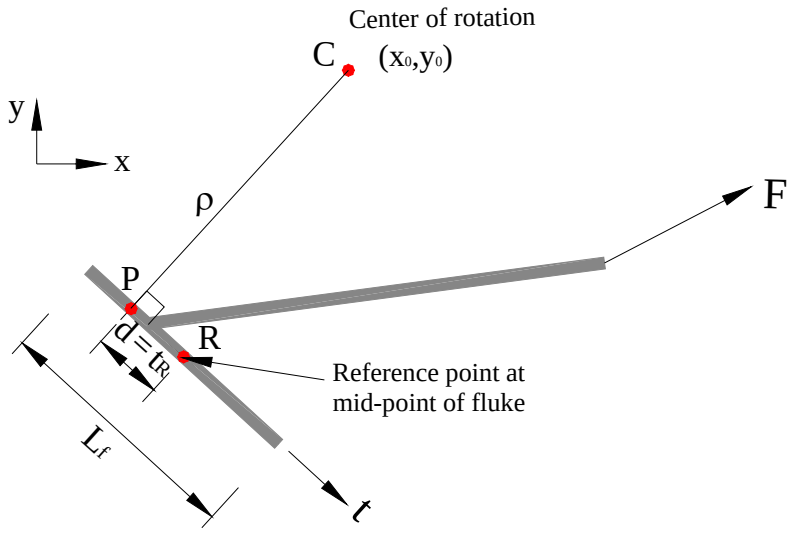

Fig. 6.1 Kinematics of anchor motion

Most of the papers related to drag anchors suggest that the fluke is the dominant influence on both installation and capacity and thus attraction is focused on fluke behavior. For dissipation calculations, the rotation of the fluke can be decomposed in three components of motion with respect to the reference point shown in Fig. 6.1: rotation about the reference point, translation parallel to the fluke, and translation normal to the fluke as shown in Fig. 6.2.

Three limiting cases of motion exist:

a. Pure rotation: If ρ =0 and t_R=0, a condition of pure rotation about the mid-point of the fluke exist.

b. Pure tangential translation: If $\frac{\rho}{L_f}$ and $\frac{\rho}{t_R}$ are sufficiently large, a condition of pure translation in a direction parallel to the fluke is approached.

c. If $\frac{t_R}{L_f}$ and $\frac{t_R}{\rho}$ are sufficiently large, a condition of pure translation normal to the fluke is approached. This condition can occur when P is located a large distance off of the fluke and the distance t_R because large.

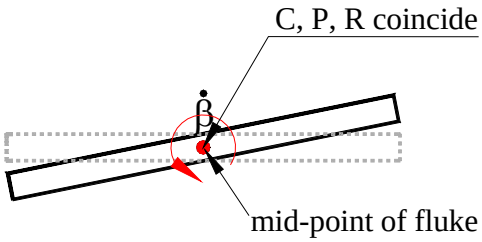

a. Rotation

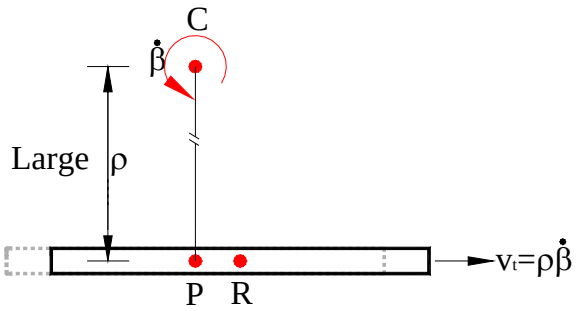

b. Movement parallel to the fluke

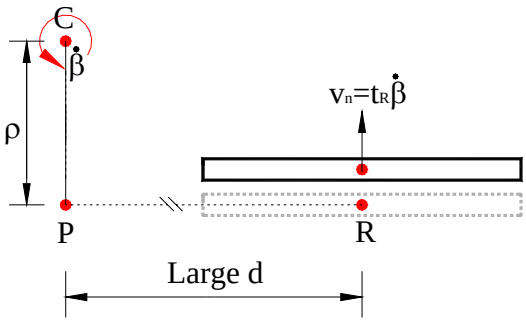

c. Movement normal to the fluke

Fig. 6.2 Three components of fluke rigid body motion

6.2 Bearing factors for pure translation and rotation.

A first step in characterizing soil resistance to fluke penetration involves determining the bearing factors for conditions of pure rotation, pure tangential translation, and pure normal translation. This section develops these bearing factors. Section 6.2.3 will develop interaction functions for general conditions of combined motions.

6.2.1 Pure rotation

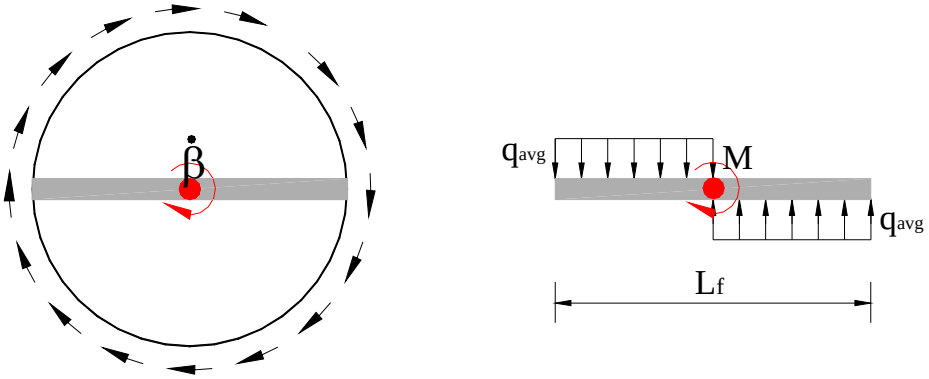

a. Upper bound mechanism b. Assumed average resistance

Fig. 6.3 Upper bound analysis for pure rotation

Fig. 6.3 shows a plane strain mechanism for the failure undergoing pure rotation

From Fig. 6.3a

$$M\dot{\beta} = \pi L_f \cdot \frac{L_f}{2}\dot{\beta} \cdot S_u \qquad (6.1a)$$

$$M = \frac{\pi {L_f}^2 S_u}{2} \qquad (6.1b)$$

From Fig. 6.3b

$$M = q_{avg} \frac{L_f}{2} \cdot \frac{L_f}{4} \cdot 2 = \frac{q_{avg} {L_f}^2}{4} \tag{6.2}$$

The normal stresses resisting the motion are assumed to be uniform along the fluke surface as shown in Fig. 6.3.

From Eq. 6.1b and Eq. 6.2 we can have q_{avg}

$$\frac{{L_f}^2}{4} q_{avg} = \frac{\pi {L_f}^2 S_u}{2} \tag{6.3}$$

or

$$q_{avg} = 2\pi S_u = 6.28 S_u \tag{6.4}$$

Thus, the moment bearing resistance factor for conditions of pure rotation, N_{mf}, can be taken as approximately equal to 6.

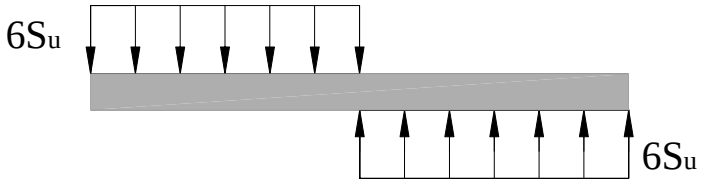

Fig. 6.4 Resistant distribution on fluke for pure rotation

6.2.2 Pure translation normal to fluke

O'Neill et al. (2003) suggested failure mechanism of plate as shown in Fig. 6.5. We can apply this failure mechanism in case that center of rotation is at infinite distance from the edge of fluke.

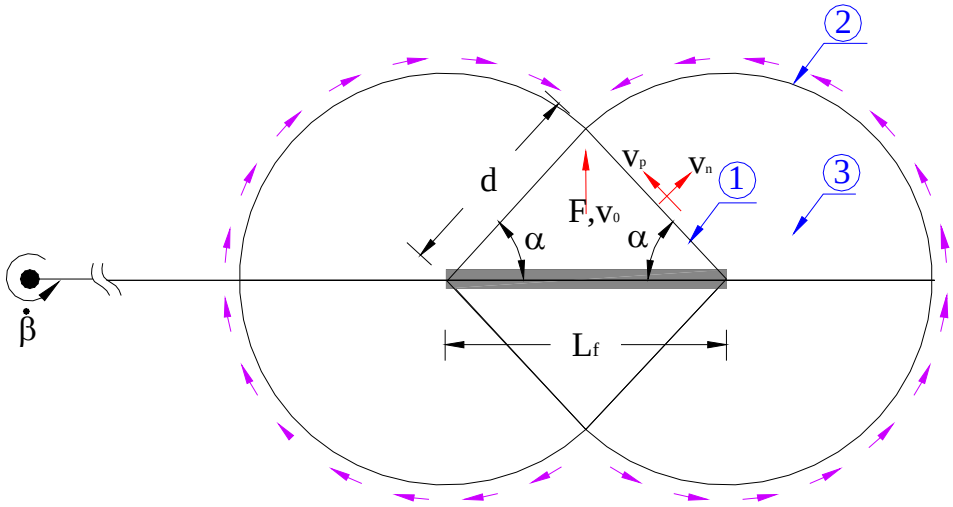

Fig. 6.5 Upper bound analysis (center of rotation is at an infinite from fluke) (O'Neill et al. 2003)

As it is shown in Fig. 6.5, calculation dissipation can be use by symmetry. And the thickness of plate is ignored in this study.

$$d = \frac{L_f / 2}{\cos\alpha}, \quad v_p = v_0 \sin\alpha, \quad v_n = v_0 \cos\alpha \tag{6.5}$$

Slip on interface at ①

$$\dot{D}_1 = v_0 \sin\alpha \frac{L_f / 2}{\cos\alpha} s_u = \frac{s_u L_f v_o \tan\alpha}{2} \tag{6.6}$$

Slip on interface at ②

$$\dot{D}_2 = \frac{L_f/2}{\cos\alpha}(\pi-\alpha)v_0 \cos\alpha \; s_u = \frac{L_f s_u(\pi-\alpha)v_0}{2} \tag{6.7}$$

Dissipation at ③

$$\gamma_{\max} = \frac{v_n}{r} = \frac{v_0\cos\alpha}{r}$$

$$\begin{aligned}\dot{D}_3 &= \int_0^{\frac{L_f/2}{\cos\alpha}} \int_\alpha^\pi \frac{s_u v_0 \cos\alpha}{r}\, r\,d\theta\,dr \\ &= s_u v_0 \cos\alpha(\pi-\alpha)\frac{L_f/2}{\cos\alpha} = \frac{L_f s_u(\pi-\alpha)v_0}{2}\end{aligned} \tag{6.8}$$

Summarizing

$$\frac{1}{4}F v_0 = \dot{D}_1 + \dot{D}_2 + \dot{D}_3$$

$$\frac{1}{4}F v_0 = L_f S_u v_o\left(\frac{\tan\alpha}{2} + \pi - \alpha\right)$$

$$\frac{F}{L_f s_u} = 4\left(\pi - \alpha + \frac{\tan\alpha}{2}\right) \tag{6.9}$$

when $\alpha = 45^\circ$ then $\frac{F}{L_f s_u} = 11.42$ which is minimum.

As discussed in Section 6.1, a condition of pure translation normal to the fluke approaches when the ratio d/L_f becomes sufficiently large. The question then arises as to how large d/L_f must be for this limiting condition to be approached. The case shown in Fig. 6.6, where the center of rotation is at the end of the fluke ($t_R=L_f/2$) can provide some insight into this issue.

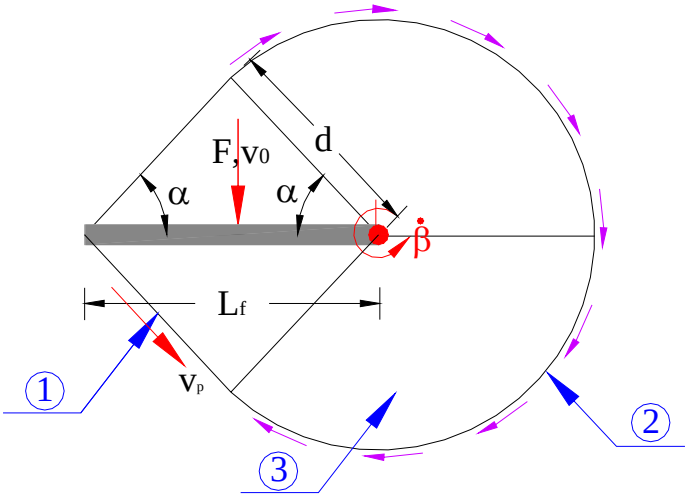

Fig. 6.6 Upper bound analysis (center of rotation is at end of the fluke)

The following paragraphs present an upper bound analysis of the case shown in Fig. 6.6. The thickness of plate is ignored in this study.

$$d = \frac{L_f / 2}{\cos\alpha}, \quad V_p = \frac{v_0}{\sin\alpha} \tag{6.10}$$

Slip on interface at ①

$$\dot{D}_1 = \frac{L_f / 2}{\cos\alpha} \frac{v_0}{\sin\alpha} s_u = \frac{L_f S_u v_o}{\sin 2\alpha} \tag{6.11}$$

Slip on interface at ②

$$\dot{D}_2 = \frac{L_f / 2}{\cos\alpha} (\pi - \alpha) \frac{v_0}{\sin\alpha} s_u = \frac{L_f S_u v_o (\pi - \alpha)}{\sin 2\alpha} \tag{6.12}$$

Dissipation at ③

$$\gamma_{\max} = \frac{v_p}{r} = \frac{v_0}{r \sin\alpha}$$

$$\dot{D}_3 = \int_0^{\frac{L_f/2}{\cos\alpha}} \int_\alpha^\pi \frac{s_u v_0}{r \sin\alpha}\, r d\theta dr = \frac{L_f s_u v_0 (\pi - \alpha)}{\sin 2\alpha} \tag{6.13}$$

Summarizing

$$\frac{1}{2} F v_0 = \dot{D}_1 + \dot{D}_2 + \dot{D}_3$$

$$\frac{1}{2} F v_0 = \frac{L_f v_0 s_u}{\sin 2\alpha} \{1 + 2(\pi - \alpha)\}$$

$$\frac{F}{L_f s_u} = \frac{2\{1 + 2(\pi - \alpha)\}}{\sin 2\alpha} \tag{6.14}$$

when $\alpha = 50.12^\circ$ then $\frac{F}{L_f s_u} = 11.25$ which is minimum.

Recall that the bearing factor for pure translation ($t_R = \infty$) was n_{pf} =11.42, when the center of rotation is shifted to the end of the fluke ($t_R = L_f / 2$), the bearing factor declined a relatively small amount to n_{pf} = 11.25. Therefore, for practical purposes any motions in which as a condition of $d \geq L_f / 2$ can be considered pure translation normal to the fluke when selecting the bearing factor n_{pf}.

6.3 Interaction effects

Section 6.2 discusses bearing resistance factors for conditions of pure rotation and translation. This section presents proposed interaction functions for general combined motions.

6.3.1 Interactions between tangential and other motions

In this study, no interaction effects are assumed between tangential and other components of resistance. Specifically, the resistance factor for translation parallel to the long axis of the fluke in n_{ps}=1.0 for all conditions of motion (all d and ρ in Fig. 6.1). Similarly, the bearing factor for translation normal to the fluke (n_{pf}) is unaffected by tangential motions; i.e., independent of ρ in Fig. 6.1.

6.3.2 Interactions between normal translation and rotation

According to the results of upper bound analysis in previous section, the resistance factor for the fluke is estimated to be 6.28 in case that the center of rotation is at the midpoint of fluke. On the other hand, in case that center of rotation is at the edge of fluke the resistance factor is estimated to be 11.25 and 11.42 when the center of rotation occurs far from the anchor. We estimated resistance factor at three points, i.e., midpoint of fluke, edge of fluke and infinite distance from fluke, respectively. From this study, we can assume that the resistance factor, n_{pf} , is constant as approximately 12 outside of the fluke.

Yet to be defined is how the resistance factor, n_{pf}, varies between 6 and 12 within the fluke. The approached followed herein is to consider some simple variations of n_{pf} with t_R and assess their implications with regard to global fluke bearing factors, N_{pf} and N_{mf}. For example, as shown in Fig. 6.7, n_{pf} functions can be assumed to be linear.

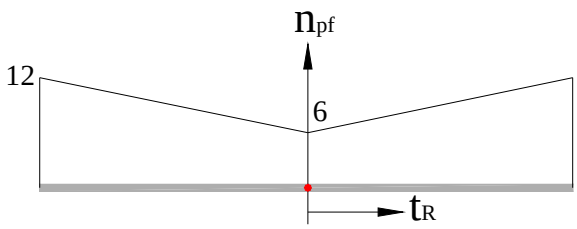

Fig. 6.7 Assumed variation of n_{pf} with t_R

The net forces V, H and M act on the reference point as shown in Fig. 6.8.

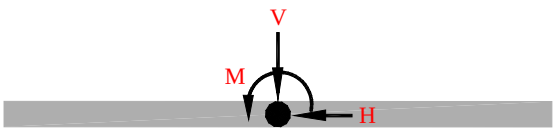

Fig. 6.8 Interaction forces acted on midpoint of fluke

For the purposes here the horizontal resistance is assumed to be uncoupled from the moment and normal load. First consider the linear case. If fluke is a rectangular plate and the undrained soil strength is homogenous, then the failure mechanism of the fluke is shown in Fig. 6.9.

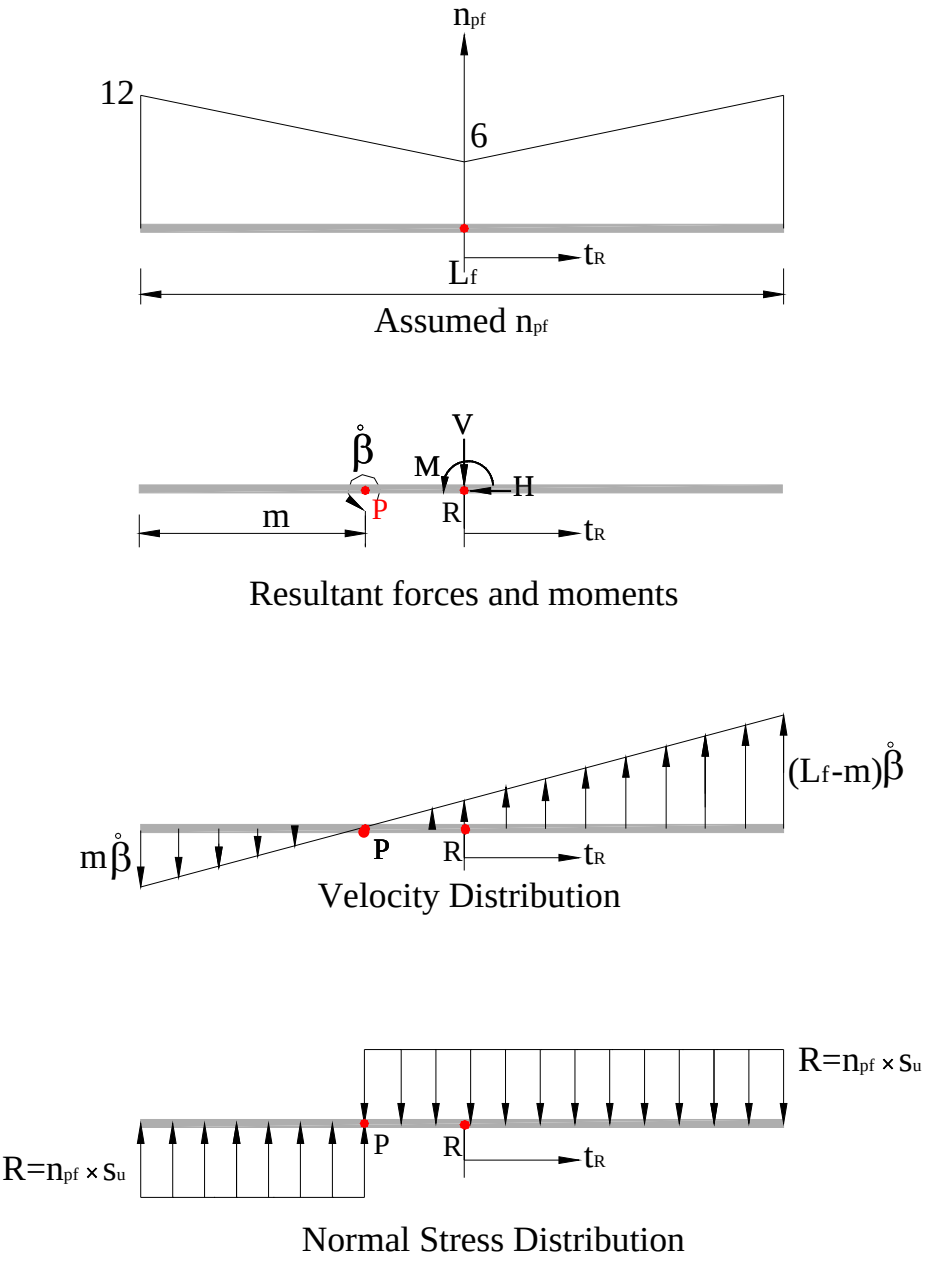

Fig. 6.9 Upper bound mechanism of fluke for linear n_{pf}

Bearing factor n_{pf} varies linearly with distance from center of rotation from 6 at midpoint of fluke to 12 at edge of fluke. Thus, n_{pf} is calculated as Eq. 6.15.

$$n_{pf} = 6 + 6\left(\frac{t_R}{L_f/2}\right) = 6\left(1 + \frac{t_R}{L_f/2}\right) \tag{6.15}$$

Where, t_R is the distance from center of the fluke to the center of rotation.

The net vertical force, V, is then

$$V = 2t_R\, n_{pf}\, s_u = 12\, t_R\left(1 + \frac{t_R}{L_f/2}\right)s_u \tag{6.16}$$

and the moment, M, is

$$M = 2\left[\frac{L_f}{2} - t_R\right]\left[t_R + \frac{\frac{L_f}{2} - t_R}{2}\right] n_{pf}\, s_u \tag{6.17}$$

N_v and N_m are then normalized bearing factors.

$$N_{pf} = \frac{V}{S_u L_f} \tag{6.18a}$$

$$N_{mf} = \frac{4M}{S_u L_f^{\,2}} \tag{6.18b}$$

The interaction diagram showing the implied relationship between N_{pf} and N_{mf} is shown in Fig. 6.10.

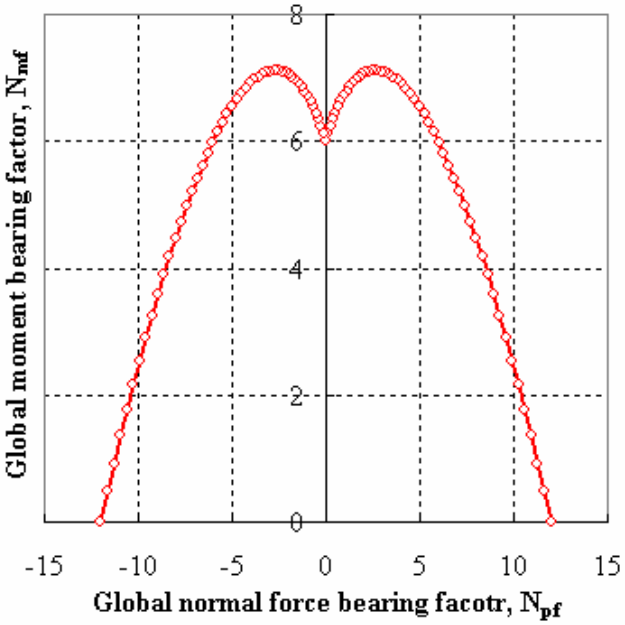

Fig. 6.10 Interaction diagram of N_{pf} and N_{mf} for linear n_{pf} function

Note that the shape of this curve follows directly from our assumptions regarding the normal stress distribution. It is significant that this interaction curve is not convex. Technically this violates the requirement for plastic yield conditions and hence the assumed linear n_{pf} function is not considered as appropriate for this model. This leads us to investigate a different assumed shape as shown in Fig. 6.11.

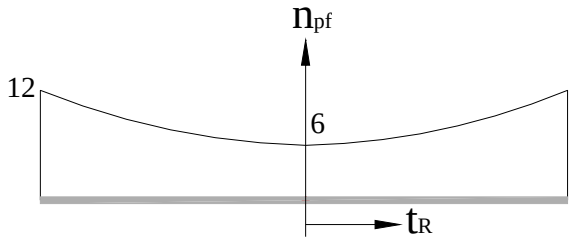

Fig. 6.11 n_{pf} function of quadratic type

This n_{pf} function is defined

$$n_{pf} = 6\left[1+\left(\frac{t_R}{L_f/2}\right)^2\right] \tag{6.19}$$

This leads to the following expressions for normal force and moment

$$V = 2\, t_R\, n_{pf}\, s_u = 2t_R \times 6\left[1+\left(\frac{t_R}{L_f/2}\right)^2\right]\times s_u \tag{6.20}$$

$$\begin{aligned} M &= 2\left[\frac{L_f}{2}-t_R\right]\left[t_R+\frac{\frac{L_f}{2}-t_R}{2}\right] n_{pf}\, s_u \\ &= 2\left[\frac{L_f}{2}-t_R\right]\left[t_R+\frac{\frac{L_f}{2}-t_R}{2}\right] 6\left\{1+\left(\frac{t_R}{L_f/2}\right)^2\right\} s_u \end{aligned} \tag{6.21}$$

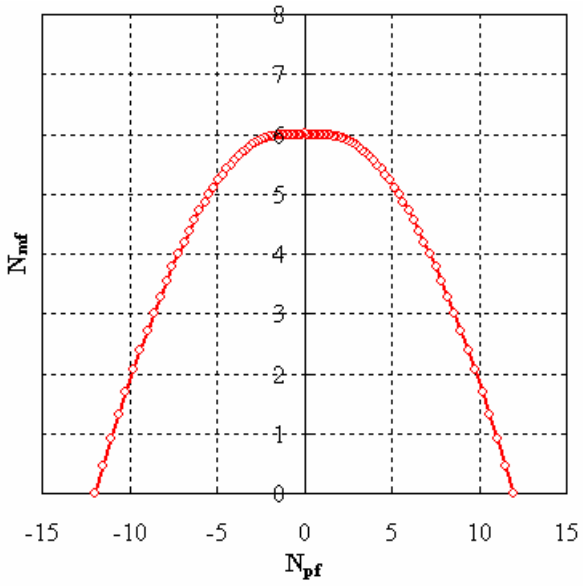

Fig. 6.12 Interaction diagram for quadratic type n_{pf} function

Fig. 6.12 shows the interaction diagram with quadric type n_{pf} function. This interaction curve is convex and in fact is in reasonable agreement with O'Neill et al.'s (2003) result derived independently. This N_{mf} -N_{pf} diagram is compared with that of O'Neill et al.'s in Fig. 6.13. For this reason, a quadratic n_{pf} function is considered a reasonable assumption. That is, the function is reasonably consistent with more rigorous methods but maintains the simplicity of closed form expression for the traction on the anchor components. This in turn allows us to calculate dissipation rates without complex operations.

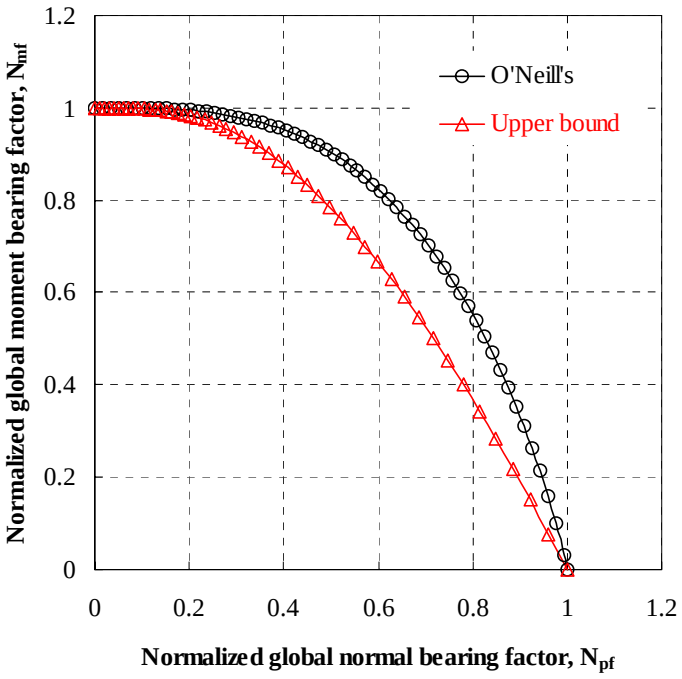

Fig. 6.13 Comparison the UBM and O'Neill et al's interaction curves

6.4 Reference point

The next step in this process is to extend these results to anchors with different shaped flukes. For this purposes we assume that the normal stresses are distributed in a similar way as for the plane strain approximation described above. To do this, we must define a reference point for any particular shape. For consistency of definition we take the reference point to be the center of rotation that results in the minimum energy dissipation rate. The net normal force, *V*, moment, *M* and tangential force, *H* are assumed to act at the reference point. In the upper bound method, the kinematics of the drag anchor involve rotation about an assumed point with virtual angular velocity, $\dot{\beta}$. Thus, the energy dissipation rate per unit area can be calculated directly as the local stress times the local respective velocity. In the case of a rectangular fluke in homogenous undrained soil, the energy dissipation has minimum value at the midpoint of the fluke. In the case of non-rectangular fluke or non-homogenous soil, the minimum energy dissipation point must be computed as discussed in detail below.

6.4.1 Rectangular fluke

As shown in Fig. 6.14, the fluke is a rectangular plate and the soil undrained strength is uniform with depth.

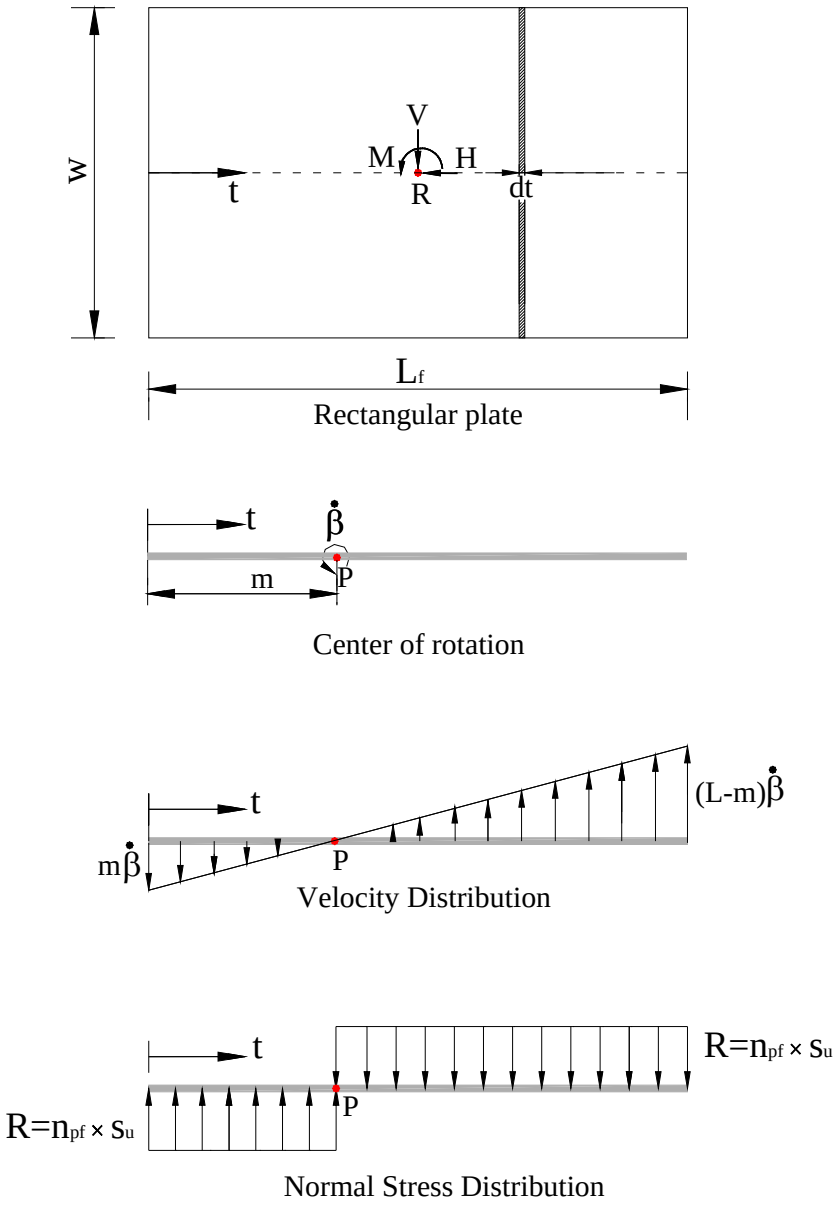

Fig. 6.14 Upper bound mechanism of fluke for rectangular fluke

where w = width of fluke

L_f = Length of fluke

m = center of rotation from 0

$A(t) = w\,dt$, Area of fluke at t

$n_{pf}(t_R)$ = constant decided by Eq. 6.19

$s_u(t)$ = constant, uniform soil strength

The rate of virtual energy dissipation, $\dot{D}$, is calculated by integrating the unit dissipation rates over the surface of the anchor

$$\dot{D} = \int_0^m n_{pf} s_u (m\dot{\beta} - t\dot{\beta}) w dt + \int_m^{L_f} n_{pf} s_u (-m\dot{\beta} + x\dot{\beta}) w dt$$

$$= w n_{pf}\, s_u\, \dot{\beta} \left(m^2 - mL_f + \frac{1}{2} L_f{}^2 \right) \qquad (6.22)$$

The minimum energy dissipation can be obtained by differentiating Eq. 6.22 with respect to m.

$$\frac{d\dot{D}}{dm} = 2m - L_f \qquad (6.23a)$$

$$\frac{d\dot{D}}{dm} = 0, \quad 2m - L_f = 0 \qquad (6.\ 23b)$$

$$m = \frac{L_f}{2} \qquad (6.23c)$$

Thus the minimum energy dissipation is generated when the reference point is at the midpoint of fluke.

6.4.2 Triangular fluke

As shown in Fig. 6.15, a triangular fluke is an example of a case where the reference point does not occur at the geometric center. The fluke is a triangular plate and the undrained soil strength is homogenous.

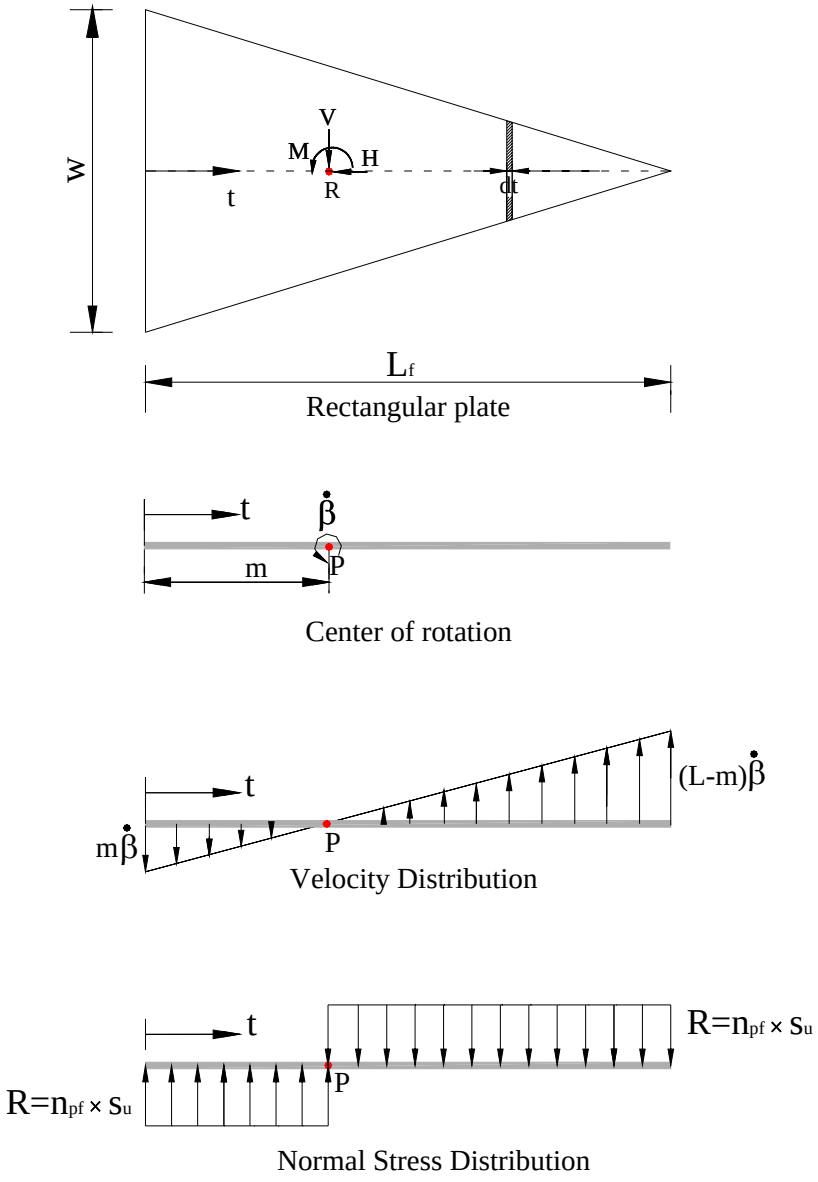

Fig. 6.15 Upper bound mechanism of fluke for triangular fluke

where w = width of fluke

L_f = Length of fluke

m = center of rotation from 0

$A(t) = \left(w - \frac{w}{L} t \right) dt$, differential area of fluke at t

$n_{pf}(t_R)$ = constant

$s_u(t)$ = constant

Total energy dissipation

$$D = \int_0^m n_{pf} s_u (m\dot{\beta} - t\dot{\beta})(w - \frac{w}{L_f} t) dt + \int_m^{L_f} n_{pf} s_u (-m\dot{\beta} + x\dot{\beta})(w - \frac{w}{L_f} t)\, dt \qquad (6.24a)$$

$$= w\, n_{pf} s_u\ \dot{\beta} \left\{ \int_0^m (m - t - \frac{m}{L_f} t + \frac{t^2}{L_f}) dt + \int_m^{L_f} (-m + t + \frac{m}{L_f} t - \frac{t^2}{L_f}) dt \right\} \qquad (6.24b)$$

$$= w\, n_{pf} s_u\ \dot{\beta} \left\{ m^2 - \frac{m^3}{3L_f} - \frac{mL_f}{2} + \frac{{L_f}^2}{6} \right\} \qquad (6.24c)$$

The center of rotation that gives the minimum energy dissipation can be obtained by differentiating Eq. 6.24 with respect to m.

$$\frac{d\dot{D}}{dm} = w n_{pf} s_u \dot{\beta} \left(2m - \frac{m^2}{L_f} - \frac{L_f}{2} \right) \qquad (6.25a)$$

$$\frac{d\dot{D}}{dm} = 0 \qquad (6.25b)$$

$$2m^2 - 4Lm + {L_f}^2 = 0$$

$$m = L_f \pm \frac{\sqrt{2}}{2} L_f \qquad (6.25c)$$

Thus $0<m<L_f$

$$m = (1 - \frac{\sqrt{2}}{2}) L_f \qquad (6.25d)$$

For example, for L_f=3, m is 0.8787 which is not the center of gravity of the fluke.

6.5 Interaction diagram for variable undrained soil strength profile

In marine soil, undrained soil strength is frequently normally consolidated clay with an undrained strength profile as shown in Fig. 6.16.

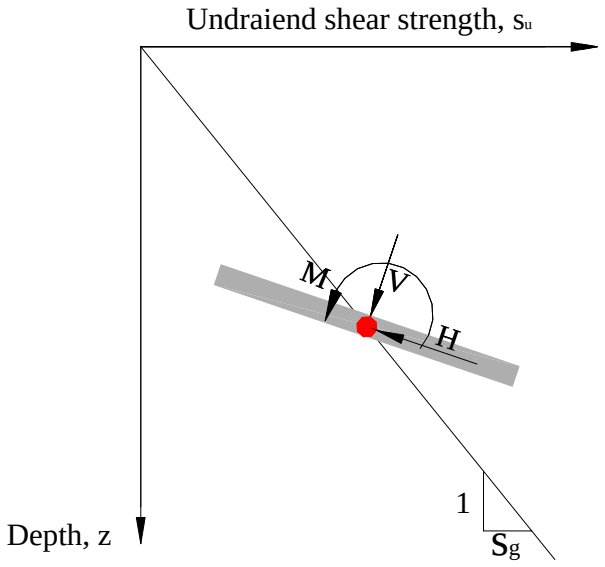

Fig. 6.16 Fluke embedded in variable undrained soil strength with depth

As shown in Fig. 6.16, soil strength on the fluke varies linearly with depth. Accordingly, soil resistance on the plate varies linearly as shown in Fig. 6.17. In this case, the reference point is not the midpoint even for a rectangular plate. If the midpoint of fluke is taken as the reference point, then the interaction diagram will not be convex. For this reason a better definition of the reference point is required. This will be discussed in detail in section 6.6.

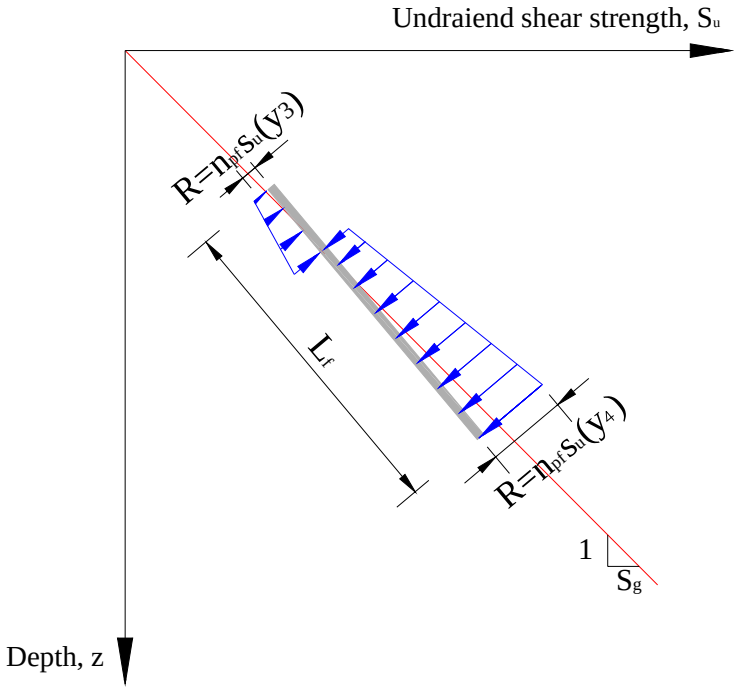

Fig. 6.17 Assumed resistance of fluke in linearly increasing soil strength with depth

As an example, a plate is embedded into a soil with strength gradient S_g, 1.0 kPa/m at 45 degree at a depth of 0 m as shown in Fig. 6.18. The length of plate is 1.5m and width is 3m. A quadratic n_{pf} function is considered. Soil resistance R can be considered as shown in Fig. 6.18. We can calculate the normal load V and moment M for

various centers of rotation using the center of gravity as a reference point. As shown in Fig. 6.19, when the center of gravity is used for reference point, the interaction diagram is not convex at head depth of 0m. However, in the case of head depth of 10m, interaction diagram has convex shape. According to these results, when undrained soil strength is varied with depth, interaction diagram is affected by location of the fluke. Thus we know that a reference point should be relocated to another point. A second choice is to locate the reference point locate at the plastic equilibrium point where the energy dissipation has minimum value. Fig. 6.20 shows the interaction diagram using the plastic equilibrium point a reference point. In this case the curve satisfies the convexity rule.

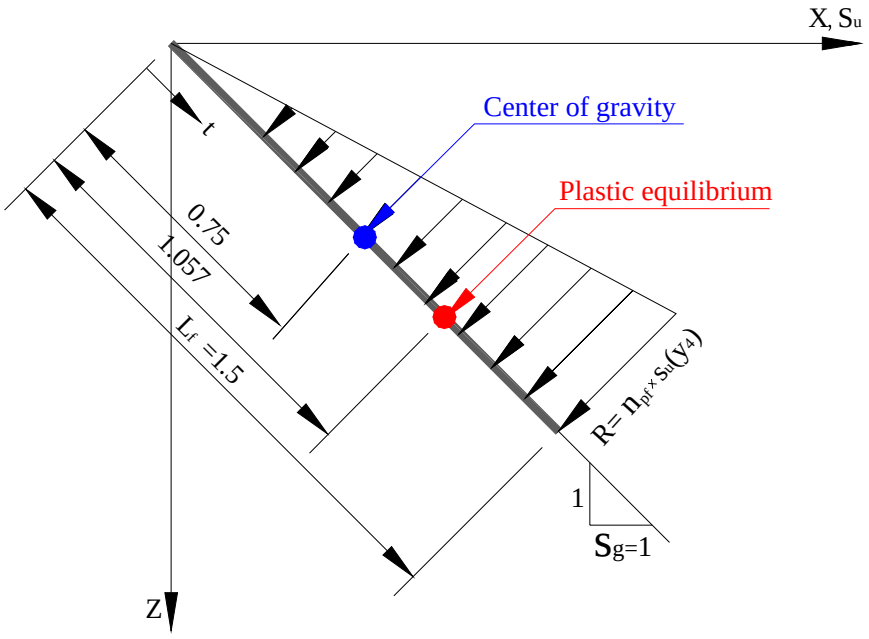

Fig. 6.18 Position of fluke and undrained soil strength condition (Head=0m)

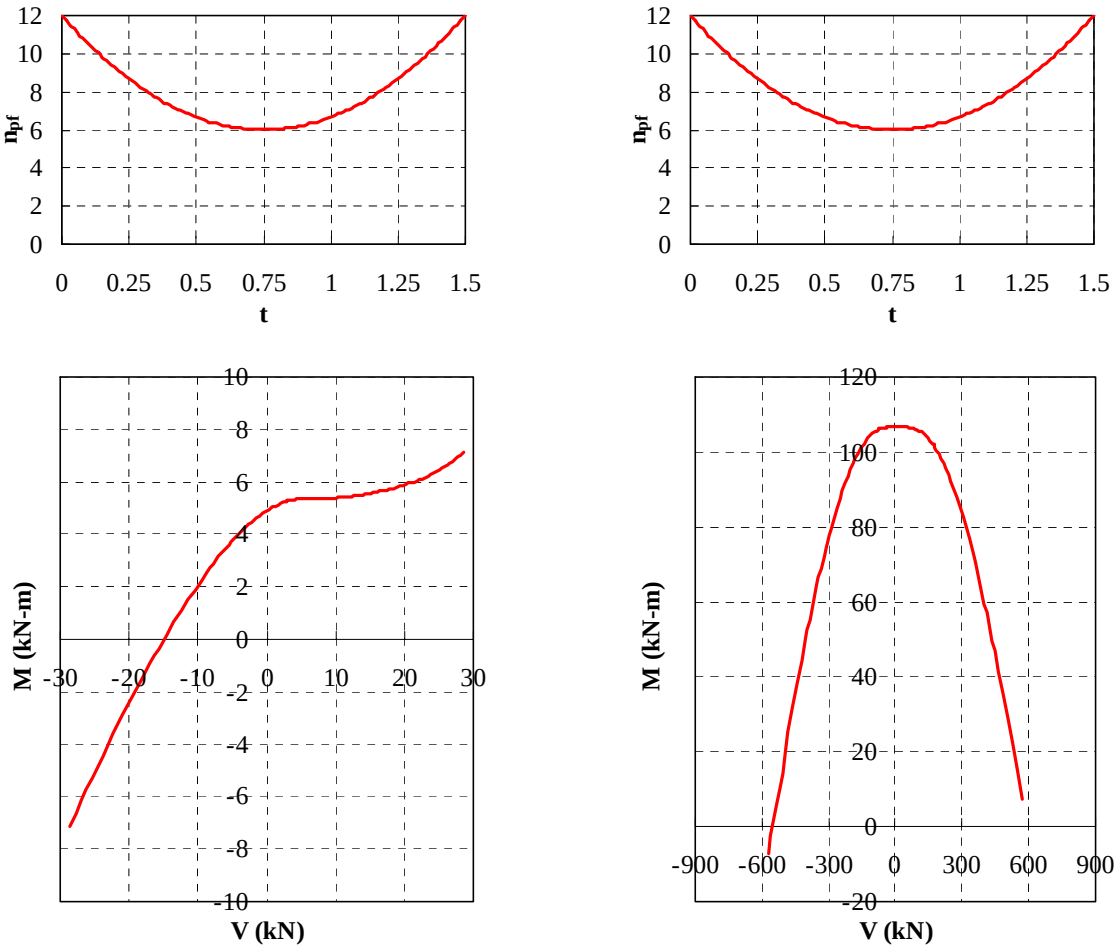

a. Head depth = 0m

b. Head depth = 10m

Fig. 6.19 Interaction diagram in the case of non-homogenous soil strength
(Reference point = Center of gravity of fluke)

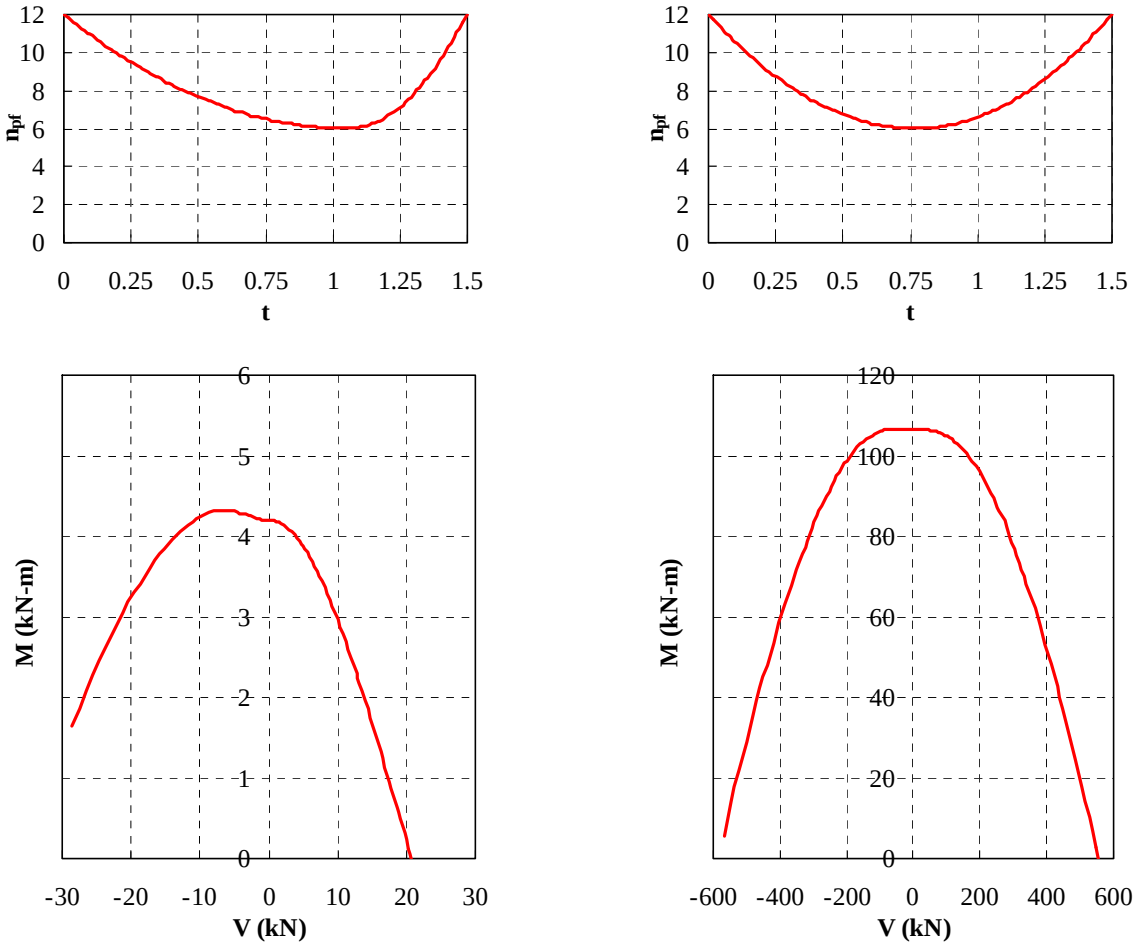

a. Head depth = 0m

b. Head depth = 10m

Fig. 6.20 Interaction diagram in the case of non-homogenous soil strength
(Reference point = Plastic equilibrium point)

6.6 Interaction diagram for general case

In a real drag anchor, the fluke is usually not a simple shape, it is a typically combination of several elements of different shapes. For example, Fig. 6.21 shows the fluke of the Stevpris anchor (Vryhfof 1999) comprised of composite plates with complex geometries.

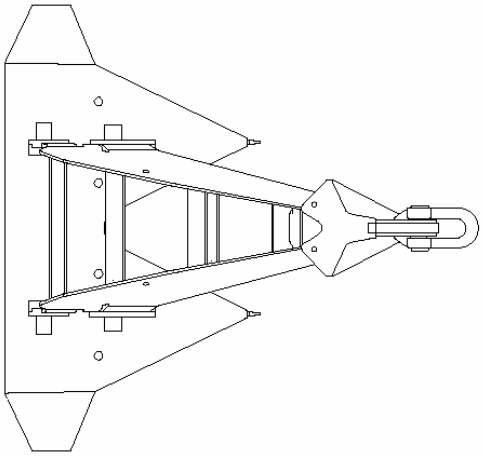

Fig. 6.21 Stevpris anchor (Vryhof 1999)

Also, undrained soil strength varies with depth in most marine soils. Thus, we must consider these factors in simulating drag anchor behavior. As discussed in Section 6.5, a reference point must be located corresponding to the center of rotation having minimum energy dissipation. As discussed in Section 6.4, the energy dissipations are expressed as Eq. 6.22 for rectangular fluke and Eq. 6.24c for triangular, respectively. Eq. 6.26 indicates energy dissipation of composite shapes of fluke. The rotation point that gives the minimum energy dissipation can be obtained by varying the location of the center of rotation, *m*, as indicated in Fig. 6.22.

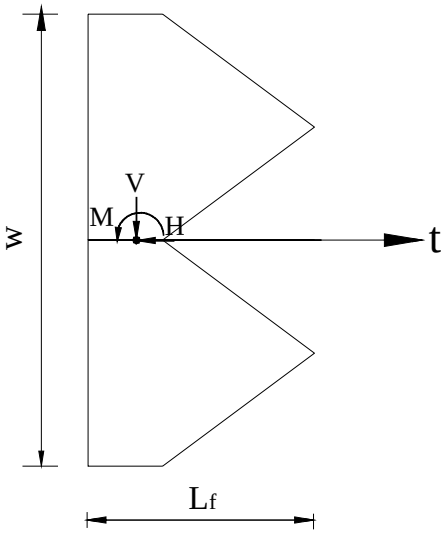

Fluke Geometry

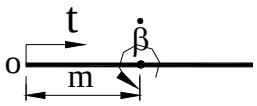

Center of Rotation

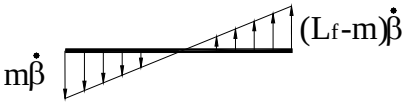

Velocity Distribution

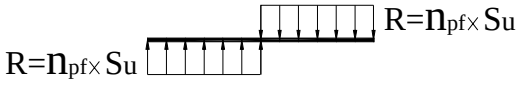

Stress Distribution

Fig. 6.22 Upper bound mechanism of actual fluke

The total energy dissipation is then

$$\dot{D} = \int_0^{L_f} n_{pf}\ s_u(y)\ v(t)\ 2A(t)\,dt \qquad (6.26)$$

where L_f = Length of fluke

$S_u(y)$ = Undrained soil strength

$v(t)$ = Virtual normal velocity at t

$A(t)$ = Area function of fluke at t

Area = $2A(t)dt$

In this equation, area function $A(t)$ is decided as shown in Fig. 6.23, i.e., it indicates half of the fluke width.

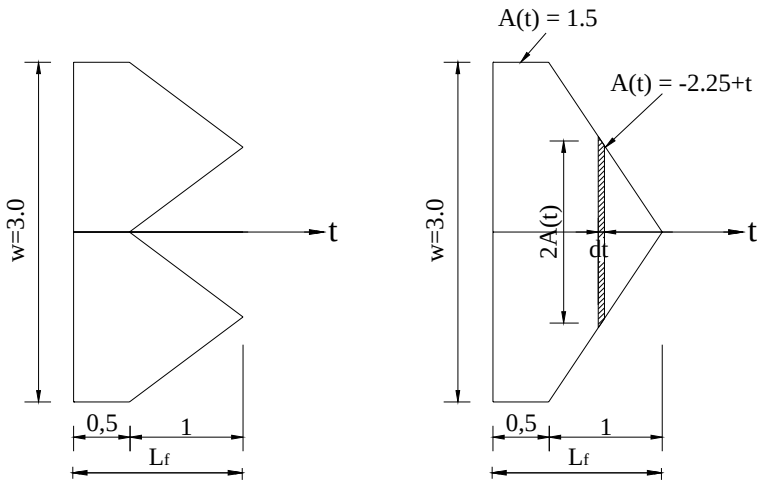

a. Origional fluke b. Modified fluke

Fig. 6.23 Area function for composite fluke

Total energy dissipation $\dot{D}$ can be calculated for each value of m using numerical integration. In calculating Eq. 6.26, the n_{pf} value is considered as a constant value. Once

the reference point is obtained, n_{pf} is taken as a function of t_R (distance between reference point and center of rotation) as described in Section 6.3.

6.7 Application of interaction diagram to upper bound model

It is known that the fluke characteristic play an important role in the behavior of a drag anchor. Thus, interaction effect between the soil and fluke should be considered in simulating drag anchor. The kinematics of the upper bound model involves a virtual rotation about a center of rotation. As has already been discussed, the resistance factor n_{pf} is varied from 6 at the reference point to 12 at edge of fluke in the case of a rectangular plate and homogenous soil conditions. Fig. 6.24 shows how to make an interaction diagram in case of a non-rectangular fluke.

Interaction diagrams can be drawn by the above procedure and this diagram can be checked to insure that the interaction diagram is convex. For cases where this is not the case another n_{pf} function can be tried. Alternatively a non-convex function can be used with this procedure but the solution should be classified as an estimate, not necessary an upper bound.

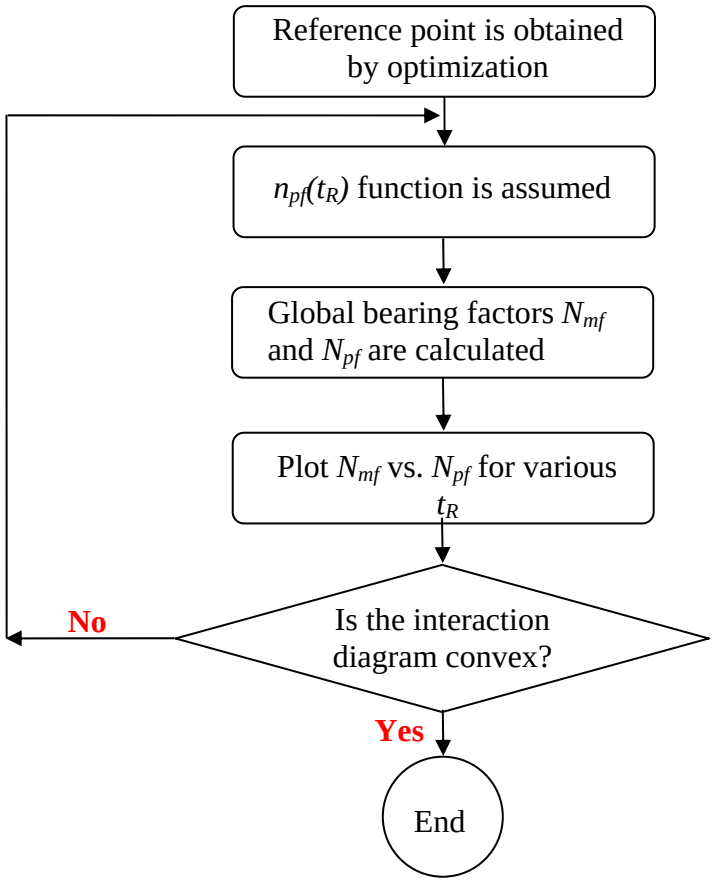

Fig. 6.24 Flow chart of making an interaction diagram for general case

6.8 Example study of composite fluke for interaction diagram

As an example of interaction diagram for general case, the composite section with combined with rectangular and triangular shape is suggested as shown in Fig. 6.25a. This section can be obtained by simplification of Stevpris anchor. As it can be seen in Fig. 6.25b, the undrained soil strength is linearly increased with depth.

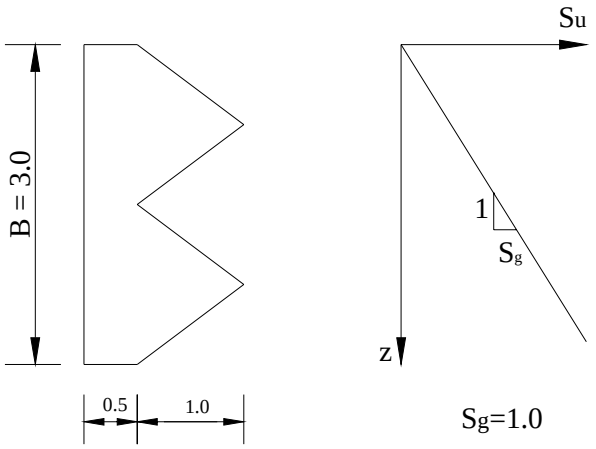

a. Fluke geometry b. Undrained soil strength

Fig. 6.25 Geometry of fluke and soil strength condition for composite fluke

Anchor is embedded as shown in Fig. 6.26, the fluke angle is 45 degree for given depth. We can decide the reference point which generates the minimum dissipation of energy. The resistance factor n_{pf} is assumed to be 6 when the center of rotation occurs at the reference point and 12 when the center of rotation occurs out of the fluke. However, we can not know how n_{pf} values vary within this composite fluke. Thus, n_{pf} function is assumed as quadratic curve for this composite fluke. Fig. 6.27 shows the n_{pf} function curve and interaction diagram for given depth.

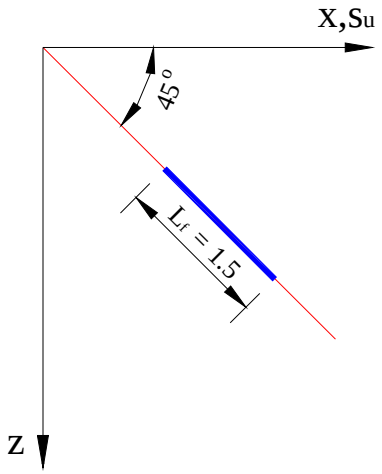

Fig. 6.26 Embedment of fluke for composite fluke

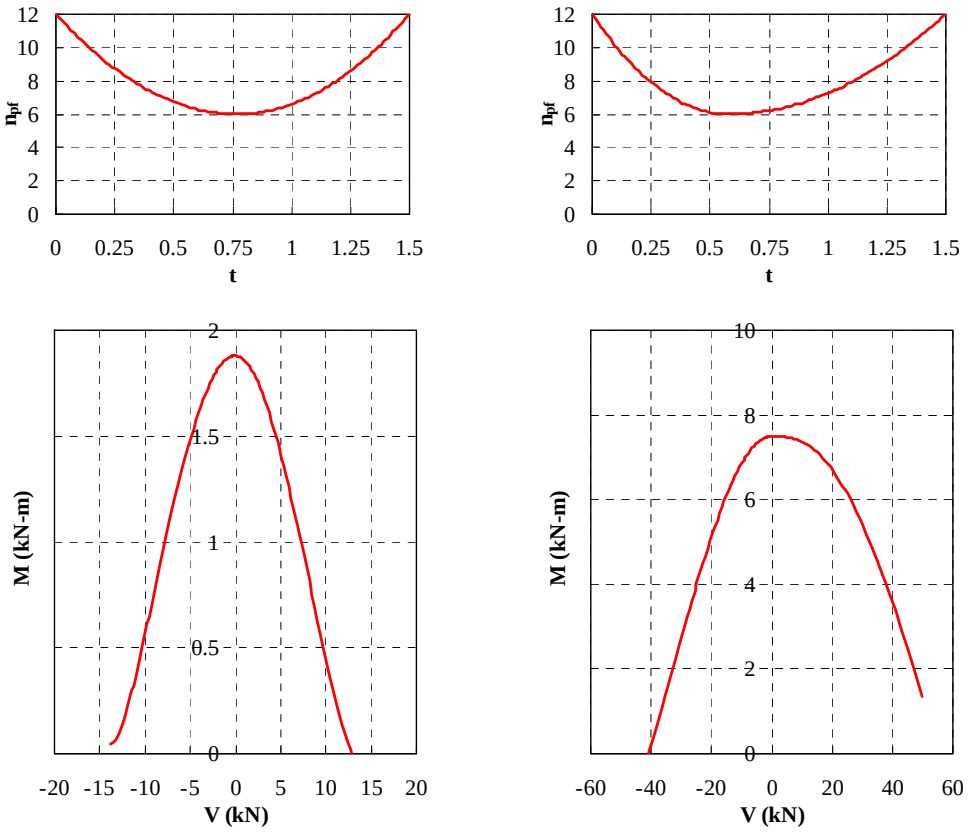

a. Head of fluke = 0m depth b. Head of fluke =1m depth

Fig. 6.27 Interaction diagram of composite fluke

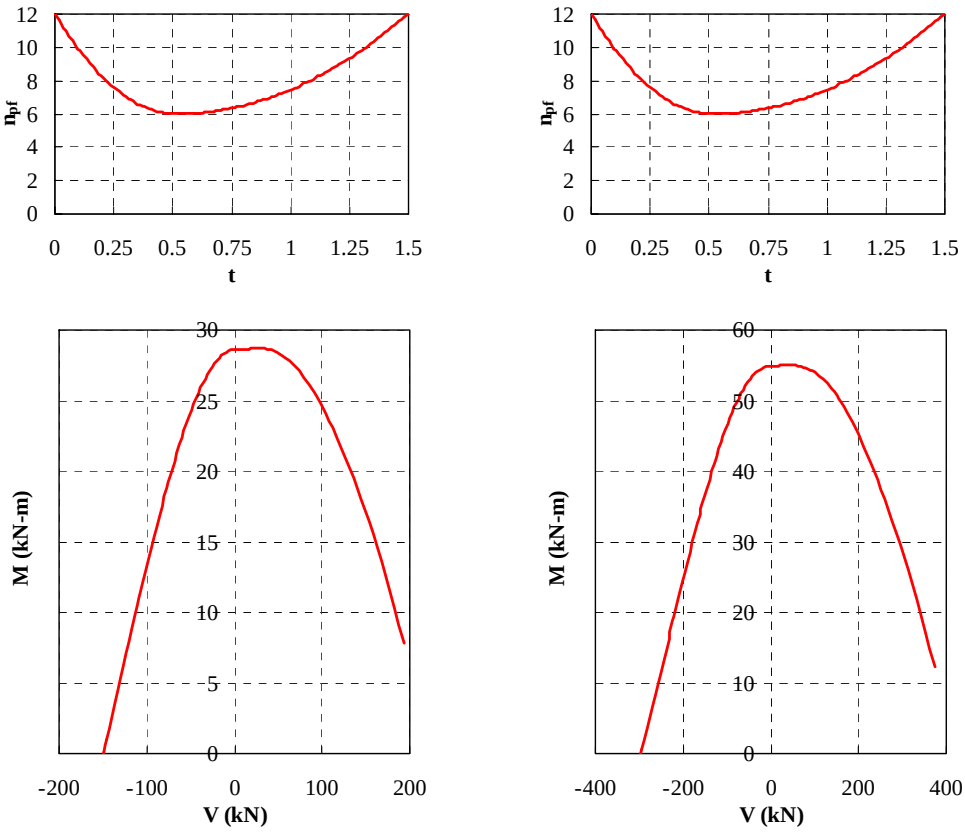

c. Head of fluke = 5m depth d. Head of fluke =10m depth

Fig. 6.27 Continued

CHAPTER VII

PARAMETER STUDIES

In this chapter on extensive parameter study is carried out varying the properties of the anchor, anchor line, and soil. The base case parameters are listed in Table 7.1 and initial condition of the anchor is shown in Fig. 7.1. The results achieved herein are determined by varying one parameter at a time.

Table 7.1 Geometry of drag anchor used parameter study

Embedded Anchor Position	
Anchor Line Attachment Point	x_1=0, y_1=-1m
Fluke-shank intersection point	X_2=-4, y_2=-1m
Fluke properties	
Fluke length, m	1.5
Fluke-shank angle, degrees	50
Fluke bearing area per unit length, m^2/m	3.0
Fluke shear area per unit length, m^2/m	6.0
Shank properties	
Shank bearing and shear area per unit length, m^2/m	0.0
Soil strength	
Uniform undrained soil strength, kPa	20.0

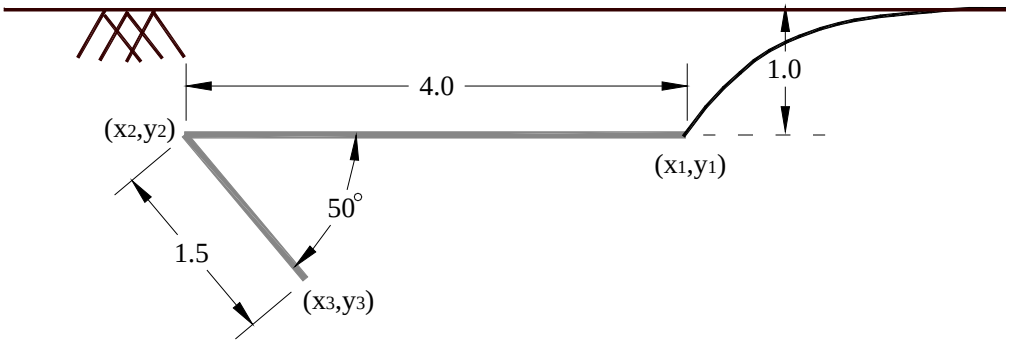

Fig. 7.1 Initial position of model anchor for parameter study (unit: m)

The concept of an anchor's characteristic curve is discussed in detail in Chapter V. The curve is a plot of the anchor capacity vs. the force angle for a given anchor position and orientation. Superposing the anchor line curve Eq. 2.10, we can determine the displacement pattern of the anchor. The characteristic curve is therefore a central concept in this approach to anchor analysis. Varying the fluke or shank parameters or soil profile varies the characteristic curve. Of course the anchor line curves will vary with soil strength or anchor line variations.

7.1 Fluke characteristics

The fluke is the most important element in determining the anchor behavior. First we will consider variations in the fluke shape while maintaining the area constant.

7.1.1 Effect of fluke moment of inertia

The anchor geometrics used in this study are following shown in Fig. 7.2. The fluke areas and centers of gravity are identical while the moments of inertia vary. As mentioned in Chapter V, flukes with the same area but different moment of inertia have

identical characteristic curves up to their respective break points. However, the location of the break point, and the shape of the curves to the right of the break point varies for different moment of inertia. The differences result from differences in the energy dissipation in the rotation mode. Dissipation in the translation mode parallel to the fluke plane is a function only of the fluke area. These differences can therefore be significant considerations in anchor design.

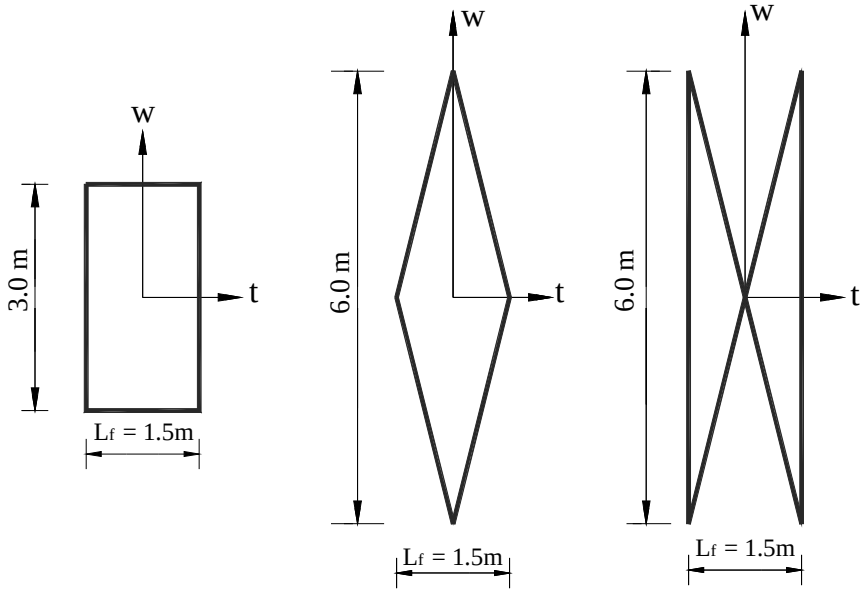

Fig. 7.2 Fluke geometry of drag anchor for effect of fluke moment of inertia

In the case of a rectangular fluke, dissipation normal to the fluke due to rotation is given by the following equation.

$$D_v = \int_{-L_f/2}^{L_f/2} t\dot{\beta} \times s_u(y) \times n_{pf} \times w(t)dt \qquad (7.1)$$

where $t\dot{\beta} = V_v$, velocity normal to the fluke

$S_u(y) =$ soil strength at depth, y

$n_{pf} =$ bearing capacity

$w(t) =$ width of the fluke as a function of location, x

For a homogenous soil strength profile, Eq.(7.1) gives

$$\dot{D}_v = 2\dot{\beta} s_u n_{pf} w \int_0^{L_f/2} t dt = \frac{1}{4}\dot{\beta} s_u n_{pf} w L_f^{\,2} \tag{7.2}$$

In the case of a diamond shaped fluke, the dissipation is

$$\begin{aligned}\dot{D}_v &= \int_{-L_f/2}^{L_f/2} t\dot{\beta} s_u(y) n_{pf} \left(-\frac{4w}{L_f}t + 2w\right) dt \\ &= 2\beta s_u n_{pf} \left[-\frac{4w}{L_f}\frac{t^3}{3} + wt^2 \right]_0^{\frac{L_f}{2}} \\ &= \frac{1}{6} s_u n_{pf} \dot{\beta} w L_f^{\,2}\end{aligned} \tag{7.3}$$

In the case of a butterfly fluke is

$$\begin{aligned}\dot{D}_v &= \int_{-L_f/2}^{L_f/2} t\dot{\beta} s_u n_{pf} \frac{4s}{L_f} t dt \\ &= 2\dot{\beta} s_u n_{pf} \frac{4w}{L_f}\left[\frac{1}{3}t^3\right]_0^{\frac{L_f}{2}} \\ &= \frac{1}{3} s_u n_{pf} \dot{\beta} w L_f^{\,2}\end{aligned} \tag{7.4}$$

Table 7.2 Summary of energy dissipation normal to the fluke

Type of fluke	Rectangular fluke	Diamond fluke	Butterfly fluke
Dissipation of normal to the fluke	$\frac{1}{4}s_u n_{pf}\dot{\beta}wL_f^{\ 2}$	$\frac{1}{6}s_u n_{pf}\dot{\beta}wL_f^{\ 2}$	$\frac{1}{3}s_u n_{pf}\dot{\beta}wL_f^{\ 2}$
Moment of inertia to the center of fluke	$\frac{1}{12}wL_f^{\ 3}$	$\frac{1}{24}wL_f^{\ 3}$	$\frac{1}{8}wL_f^{\ 3}$

According to Table 7.2, the order of energy dissipation is following:

Butterfly > Rectangular > Diamond

And it is consistent with a decreasing moment of inertia as shown in Table 7.2. Fig. 7.3 shows the relationship between dissipation of normal to the fluke and moment of inertia to the center of fluke. Form this curve we can see that dissipation of normal to the fluke and moment of inertia to the center of fluke have a linear relationship.

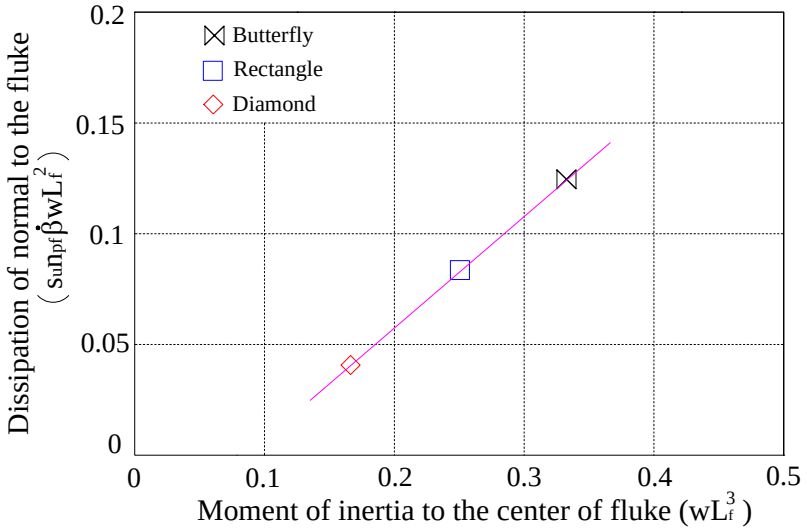

Fig. 7.3 Relationship between rates of energy dissipation vs. moment of inertia

A. Example case study

Table 7.3 through 7.5 shows the characteristic value of flukes used in this example study. The critical angles of rectangular, diamond and butterfly are 15.4^o, 13.7^o and 16.8^o, respectively. And resultant forces at break point of rectangular, diamond and butterfly are 431.6 kN, 403.3 kN and 455.8 kN, respectively.

The characteristic curves for the three shapes at an embedment depth of one meter are shown in Fig. 7.4 for the characteristics given in Table 7.1. The left sides of the curves prior to the break point are identical. However, the flukes with the smaller moments of inertia begin to reach the break point at which rotation begins to occur sooner than flukes with bigger moments of inertia.

Table 7.3 Characteristic of rectangular fluke at depth of 1m

Force angle (degree)	Center of rotation		Resultant force F (kN)	Line load T (kN)
	x_0	y_0		
15.2	100000000	83909964	429.131	255.759
15.3	100000000	83909964	430.759	252.426
15.4	-3.553	-1.402	431.654	249.159
15.5	-3.553	-1.402	426.924	245.954
15.6	-3.553	-1.402	422.288	242.811

Table 7.4 Characteristic of diamond fluke at depth of 1m

Force angle (degree)	Center of rotation		Resultant force F (kN)	Line load T (kN)
	x_0	y_0		
13.5	100000000	83909964	403.409	324.228
13.6	100000000	83909964	404.826	319.477
13.7	-3.542	-1.415	403.321	314.83
13.8	-3.539	-1.418	397.659	310.284
13.9	-3.534	-1.424	392.102	305.836

Table 7.5 Characteristic of butterfly fluke at depth of 1m

Force angle (degree)	Center of rotation		Resultant force F (kN)	Line load T (kN)
	x_0	y_0		
16.6	100000000	83909964	453.232	214.438
16.7	100000000	83909964	455.068	211.877
16.8	-3.602	-1.343	455.81	209.363
16.9	-3.602	-1.343	451.884	206.892
17	-3.601	-1.344	445.46	204.465

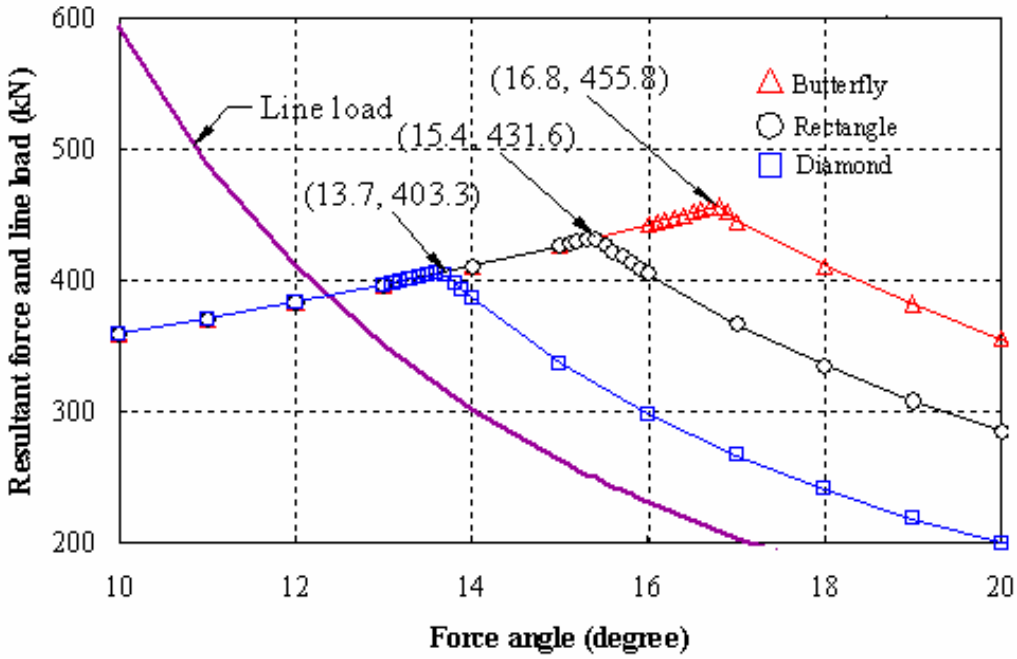

Fig. 7.4 Characteristic curves for different shapes of fluke at depth of 1m

As discussed in Chapter V, the optimum center of rotation (x_0,y_0) occurs at an infinite distance from the anchor while it is on the left side of the yield point. Therefore the preferred mechanism is translation parallel to the fluke and the dissipation normal to the fluke is essentially zero. On right side of the break point, the center of rotation occurs near the fluke. It indicates the anchor rotates about this point. In this case energy dissipation due to translation parallel to the fluke is typically much smaller than that due

to rotation. For uniform soil strength the characteristic curves are constant regardless of depth but the anchor line curves move to the right with depth. This is indicated in Fig. 7.5.

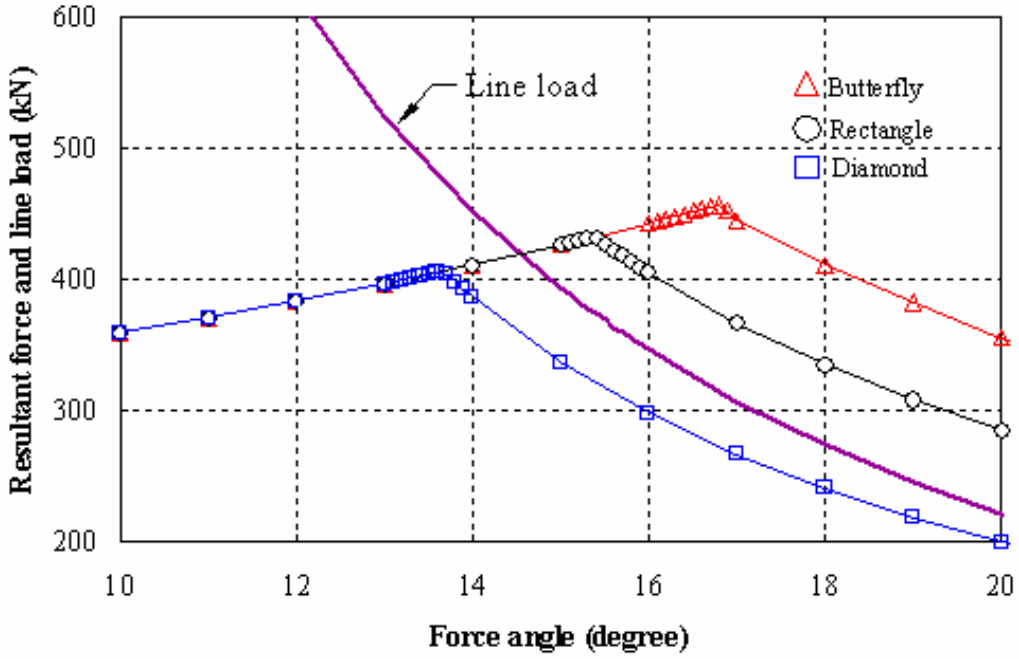

Fig. 7.5 Characteristic curves for different shapes of fluke at depth of 1.5m

In Fig. 7.5 the intersection of the characteristic curve and the anchor line curve for the diamond shaped fluke is to the right of the break point, indicating that the anchor will rotate. However, the rectangular and butterfly shaped flukes will translate parallel to the fluke since their intersection points are to the left of the break point. For the anchors penetrated to 2m depth the characteristic curve is shown in Fig. 7.6.

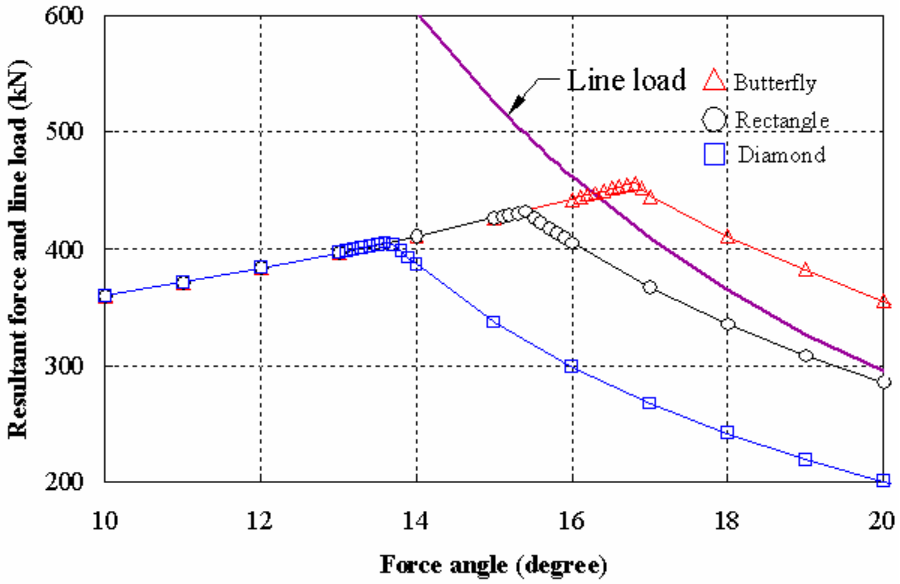

Fig. 7.6 Characteristic curves for different shape of flukes at depth of 2m

Here intersections of diamond and rectangle shaped fluke are on the right side of the break point indicating that these anchors will rotate at this depth. But butterfly anchor does not rotate at this depth.

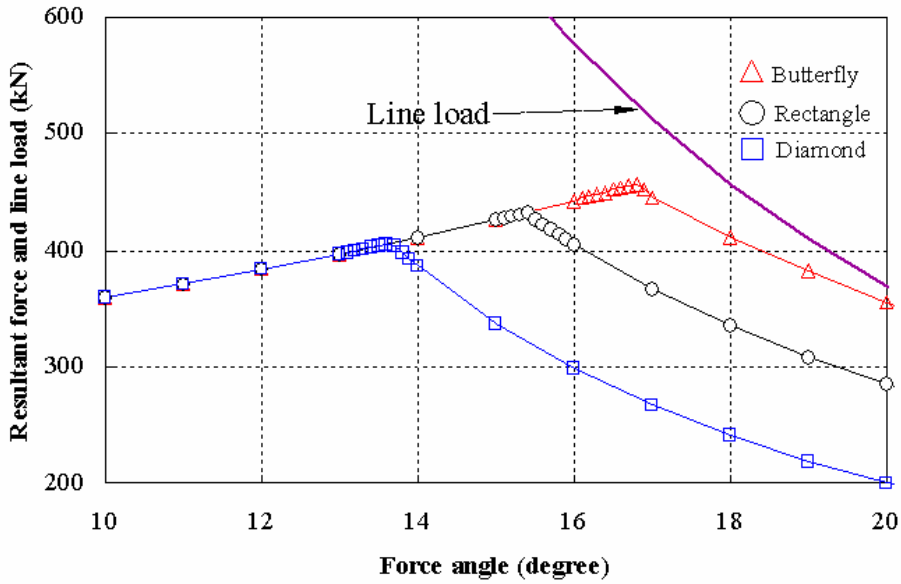

Fig. 7.7 Characteristic curves for different shapes of fluke at depth of 2.5m

Here intersections of all anchors are on the right side of the break point indicating that all anchors will rotate at this depth. As indicated in Fig. 7.4 through 7.7, the diamond shaped fluke rotates more quickly than the other anchors.

The trajectories of these anchors are plotted in Fig. 7.8. According to UBM model predictions, the depth of penetration decreases in the following order: butterfly fluke, rectangular and diamond. In other words, as the moment of inertia increases, the anchor penetrates deeper.

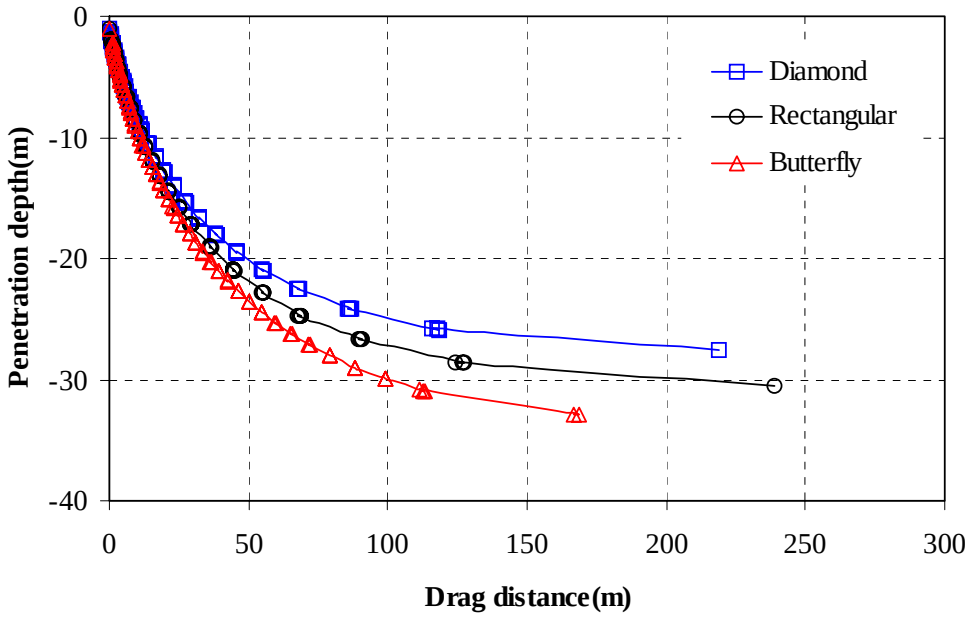

Fig. 7.8 Penetration depth vs. drag distance for different fluke moment of inertia

The capacities of drag anchors with drag distance are shown in Fig. 7.9. Note that the capacities are forces at the anchor line attachment point for uniform soil strength conditions. Thus they are relatively constant even though the anchor depth is increasing. The anchor capacity at the mudline would increase due to the increasing resistance on the anchor line with depth as shown in Fig. 7.10.

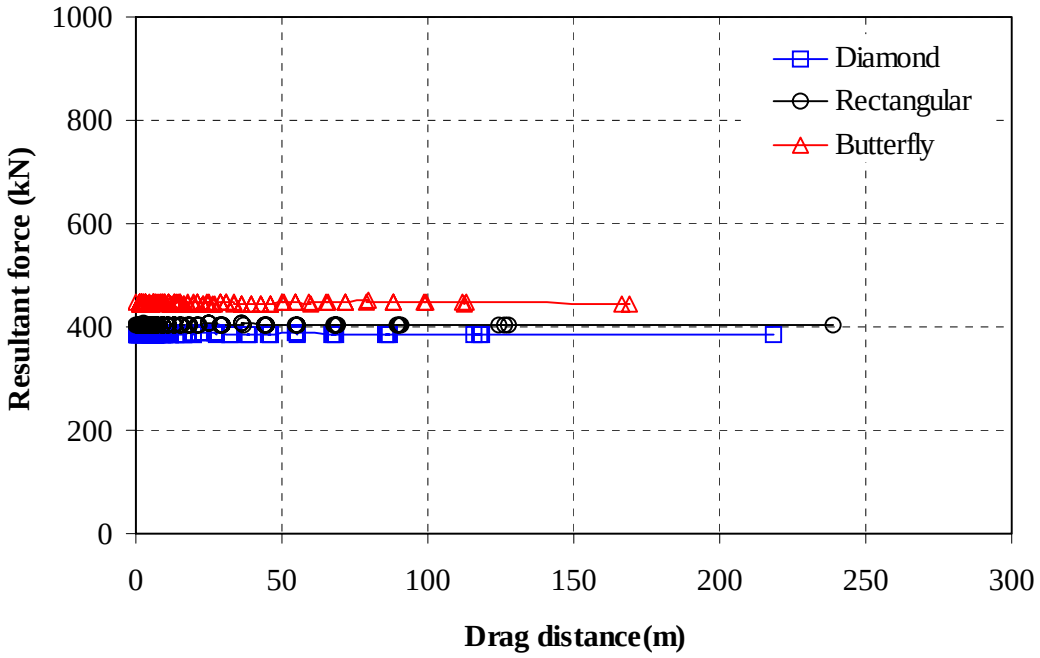

Fig. 7.9 Resultant force vs. drag distance for different fluke moment of inertia

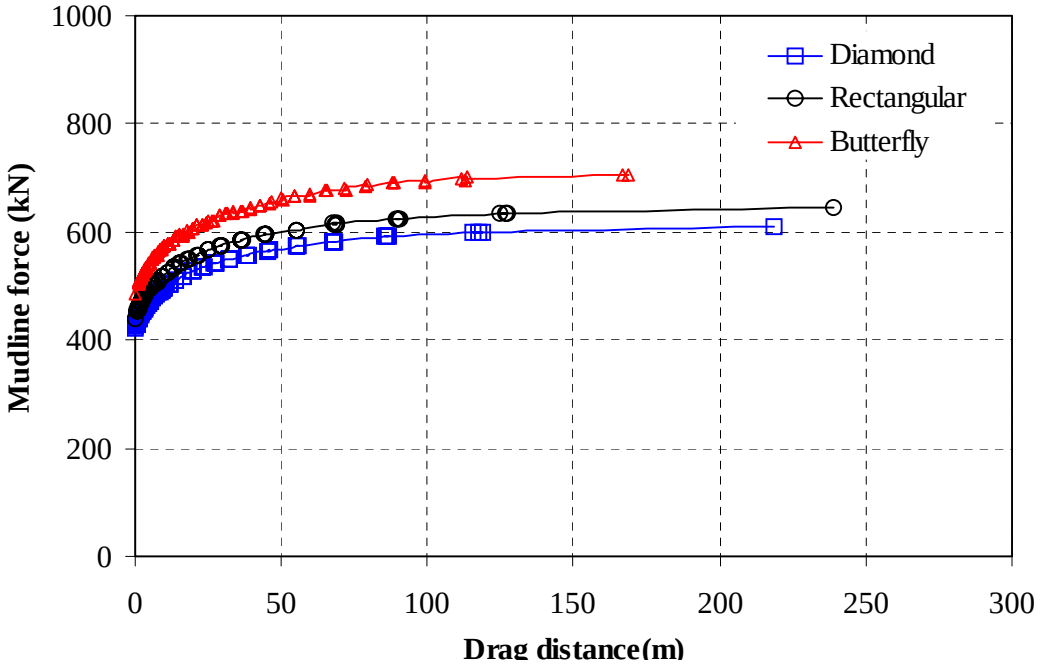

Fig. 7.10 Mudline force vs. drag distance for different fluke moment of inertia

7.1.2 Effect of fluke center of gravity

The anchor geometries considered here are shown in Fig. 7.11. Flukes have the same areas and basic rectangular shape but their aspect ratios vary.

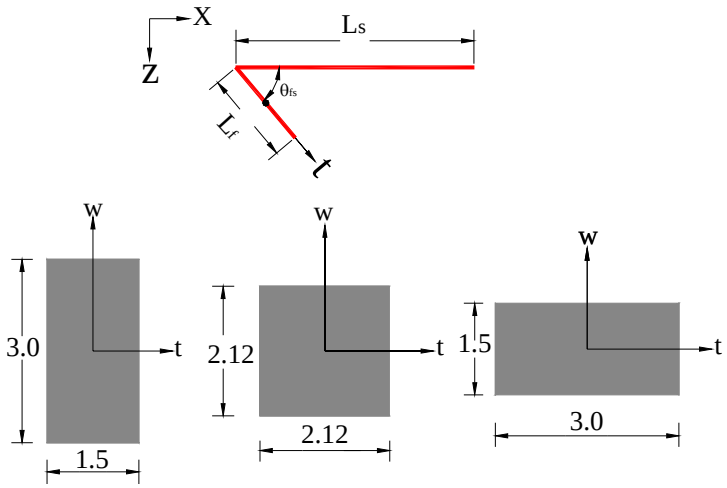

Fig. 7.11 Geometry of fluke for effect of center of gravity (unit=m)

Table 7.6 gives a comparison of energy dissipation rates due to normal velocities when the center of rotation is midpoint of fluke. And it indicates also moment of inertia to the center of fluke. A longer fluke has a larger moment of inertia and it is associated with a greater rate of energy dissipation.

Table 7.6 Dissipation rate and moment of inertia for effect of fluke center of gravity

Type of fluke	W x L (3 x 1.5)	W x L (2.12 x 2.12	W x L (1.5 x 3)
Dissipation normal to the fluke	$1.688\ s_u n_{pf} \dot{\beta}$	$2.382\ s_u n_{pf} \dot{\beta}$	$3.375\ s_u n_{pf} \dot{\beta}$
Moment of inertia to the center of fluke (m^4)	0.844	1.683	3.375

Fig. 7.12 shows the energy dissipation rate due to rotation of the fluke about its center of gravity versus moment of inertia about the fluke center of gravity. From this figure we can see that energy dissipation rate due to pure rotation of the fluke does not vary linearly with moment of inertia for rectangular flukes of different aspect ratios. This is in contrast to the results presented in Section 7.1.1.

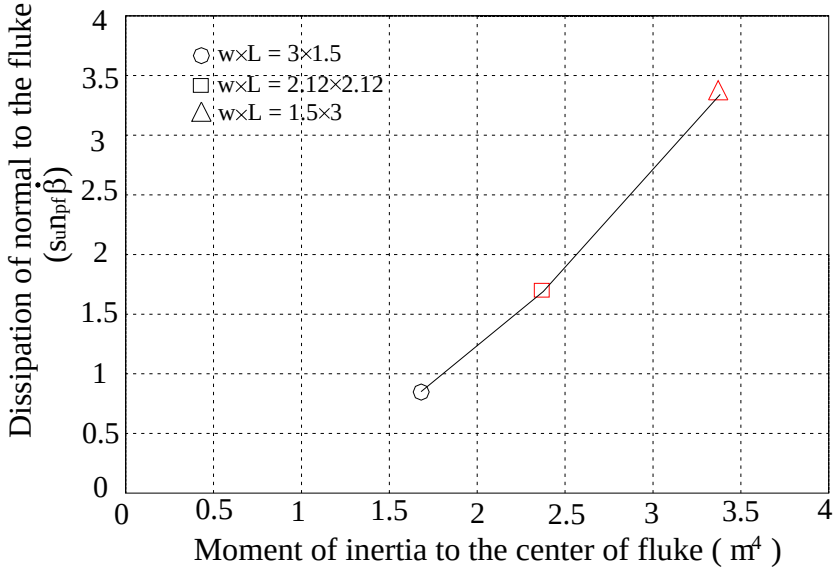

Fig. 7.12 Relationship between dissipation and moment of inertia for effect of fluke center of gravity

The characteristic curves of these flukes are shown in Fig. 7.13. As expected, the top most curve is for the longest fluke and the bottom most curve is for the shortest fluke.

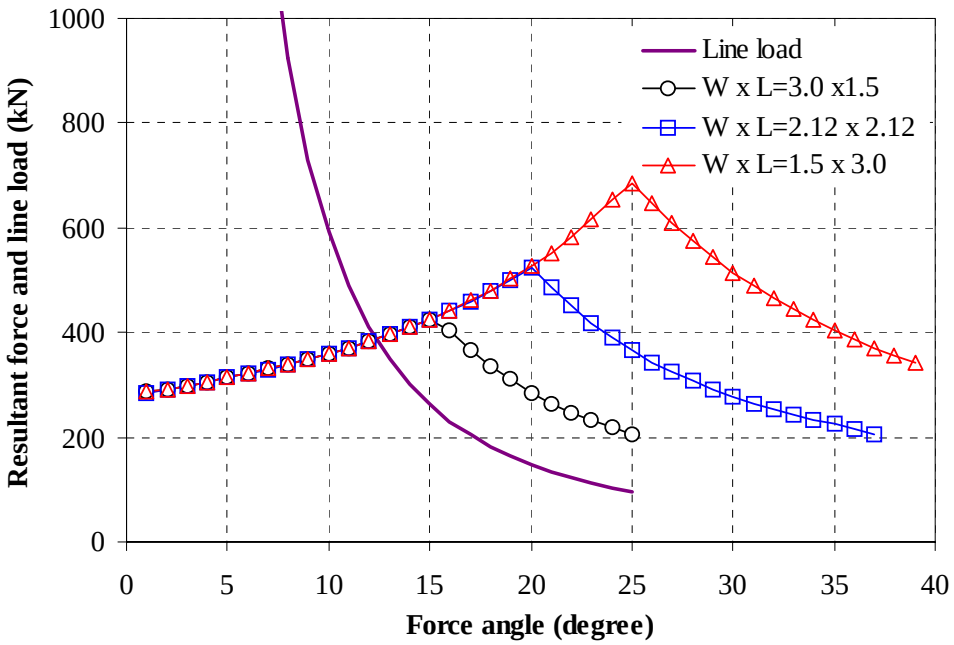

Fig. 7.13 Characteristic curve at depth of 1m (initial condition) for effect of fluke center of gravity

The penetration vs. drag distance curves are shown in Fig. 7.14. As you can see, the shortest fluke has the shallowest penetration depth. This can be explained by characteristic curve. During penetration, the shortest fluke rotates soonest. The resultant forces at the shackle curves are shown in Fig. 7.15. It indicates that the longest fluke has the largest resultant force at the shackle.

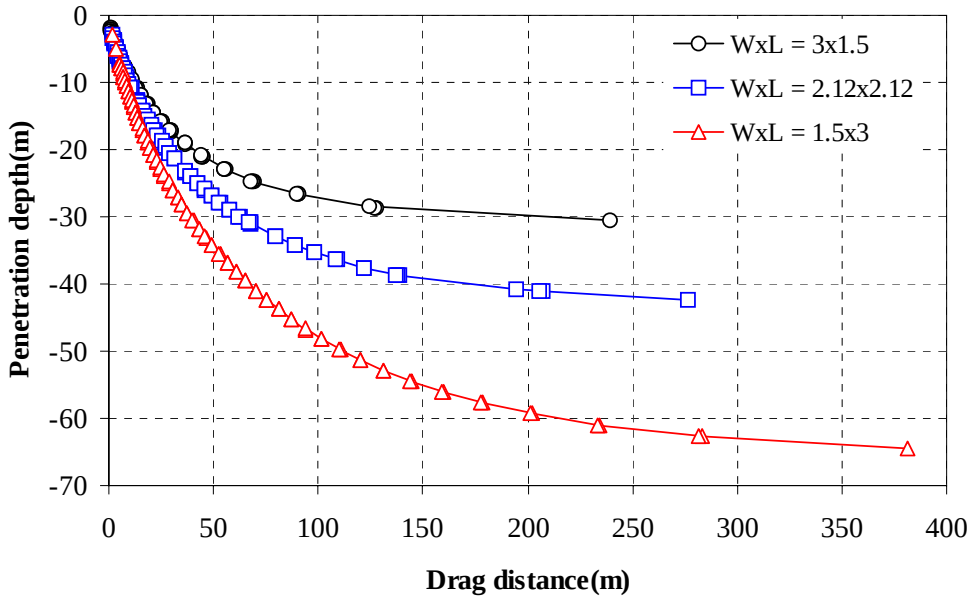

Fig. 7.14 Penetration depth vs. drag distance for effect of fluke center of gravity

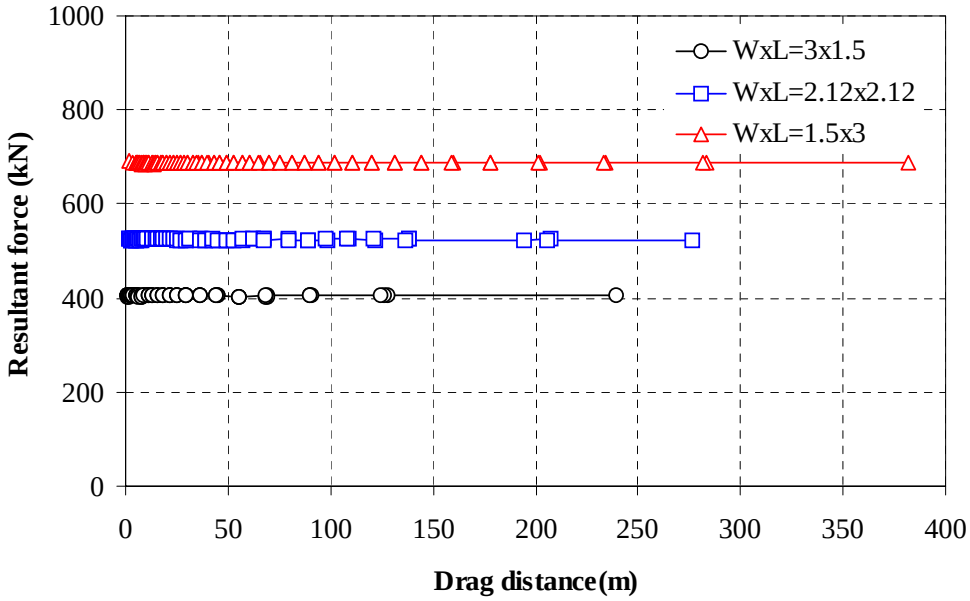

Fig. 7.15 Resultant force vs. drag distance for effect of fluke center of gravity

7.1.3 Fluke end bearing resistance

In this section we consider the effect of fluke end resistance by analyzing flukes varying plate thickness as shown in Fig. 7.16.

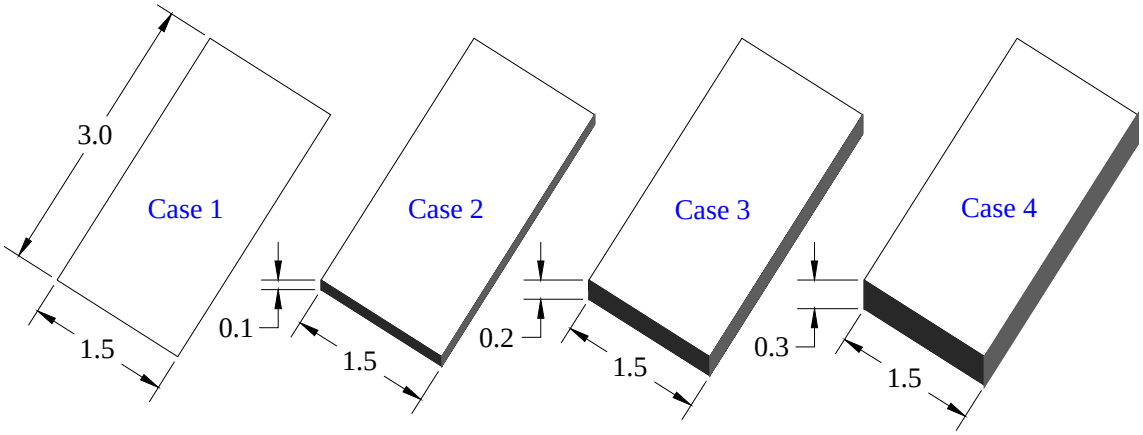

Fig. 7.16 Different depths of fluke for fluke end bearing resistance (unit: m)

The widths and length of all flukes are 3.0m and 1.5m, and their thicknesses are 0.0m, 0.1m, 0.2m and 0.3m, respectively. The ratios of L_f over D_f are correspond to 0, 1/15, 1/7 and 1/5, respectively. As discussed in Ch.5, the dissipation rate due to the resistance at the fluke tip is expressed as follows.

$$\dot{D}_{ef} = V_{ef} \times N_{ef} \times S_u(y_4) \times A_{ef} \qquad \text{(5.6 bis)}$$

where $V_{ef} = V_{tf}$ (parallel velocity of fluke)

N_{ef} = resistance factor, assumed to be approximately 12

$s_u(y_4)$ = undrained soil strength at depth y_4 (tip of fluke)

A_{ef} = area of tip of fluke

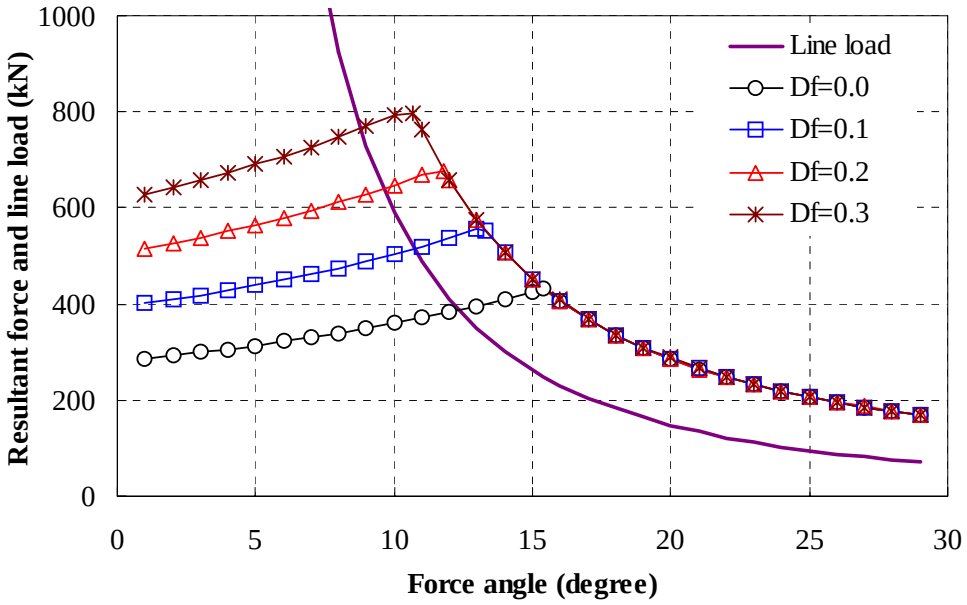

Fig. 7.17 Characteristic curves for different depths of fluke

The characteristic curves and the anchor line curves are shown in Fig. 7.17. As indicated the thicker flukes have the higher break points. As shown in Fig. 7.18 and Fig. 7.19, the penetration depth and anchor capacity increase with increasing thickness of the fluke.

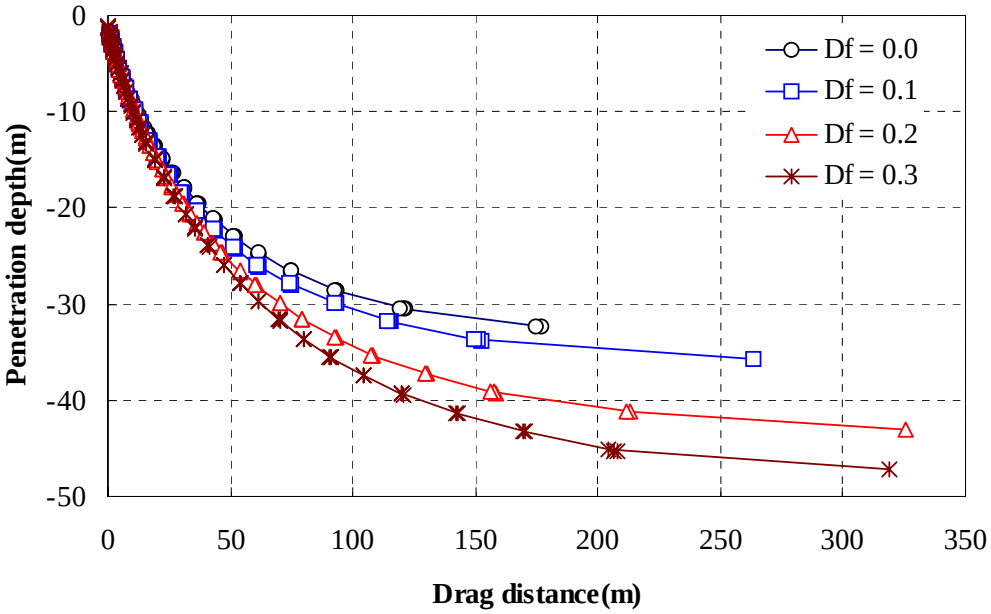

Fig. 7.18 Penetration depth vs. drag distance for different depths of fluke

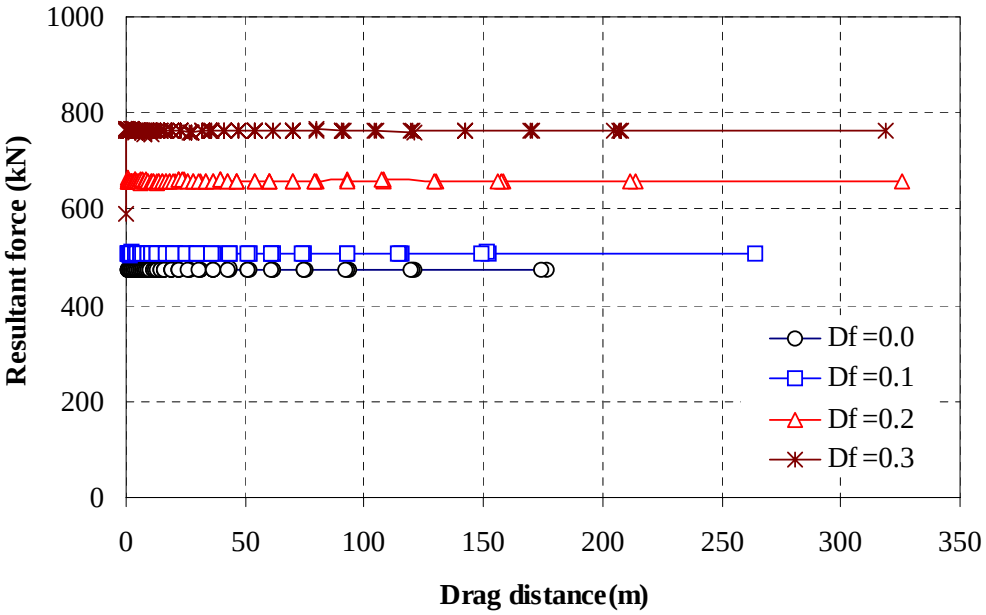

Fig. 7.19 Resultant force vs. drag distance for different depths of fluke

7.1.4 Soil sensitivity variation

As mentioned in Chapter II, the soil sensitivity affects the behavior of the anchor. For these purposes, it is assumed that only side shear resistance is influenced by soil weakening due to soil disturbance. It should be noted that the effect of soil sensitivity on the anchor line curve is not considered. Both consideration will be discussed in detail in Section 7.5.1. As shown in Fig. 7.20, the left sides of the curves for each sensitivity value are distinct while on the right side of the break point the curves merge together. Since right sides of yield point is governed by resistance of rotation. Thus, sensitivity does not influence the resultant force.

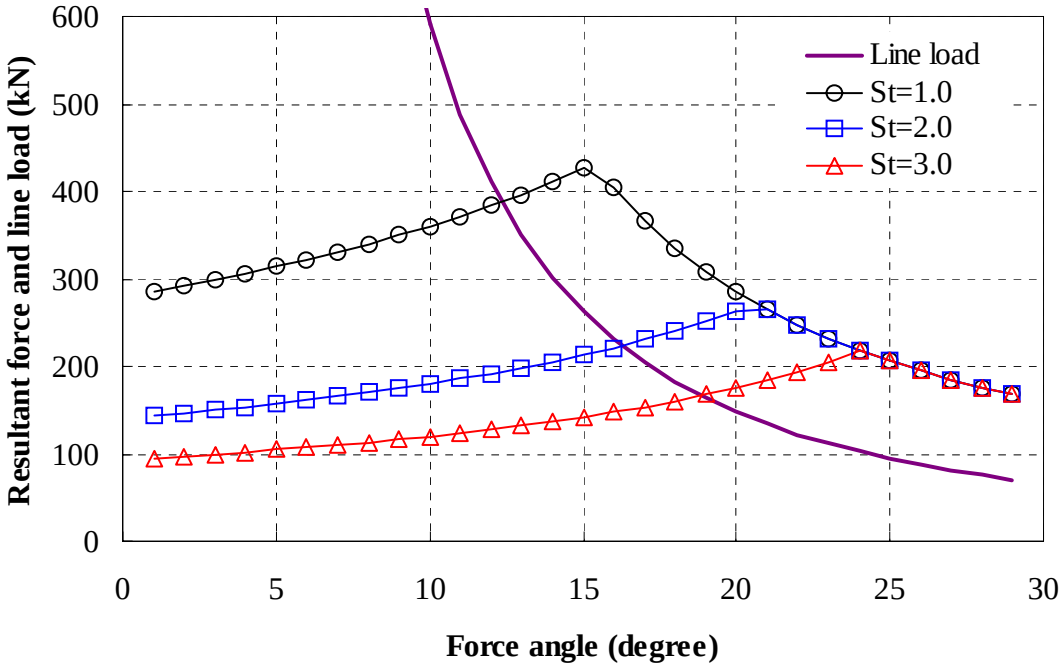

Fig. 7.20 Characteristic curves for different soil sensitivity

Fig. 7.21 shows the drag distance versus penetration depths computed to a drag distances at which the anchor no longer penetrates into the soil. These predictions

indicate that a higher sensitivity leads to a shallower penetration depth. However, an anchor seldom penetrates to its ultimate penetration depth in actual design and field condition. So we need to consider how the anchor behaves during the early stages of drag embedment, for example, ten fluke lengths of drag distance.

From Fig. 7.21, the penetration depth is almost same within this range. Thus we can conclude that effect of soil sensitivity is minor during the first ten fluke lengths of drag distance, which is generally of most interest in practical situations.

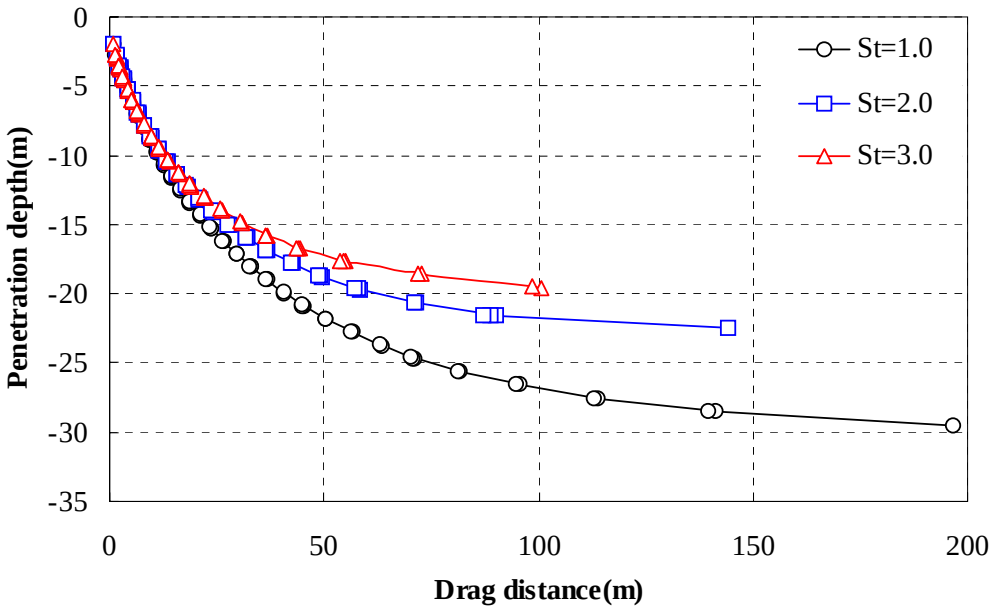

Fig. 7.21 Penetration depth vs. drag distance for different soil sensitivity

Fig. 7.22 shows the drag distance versus resultant force at anchor line attachment point. The resultant forces increases as the sensitivity decreases. Since the sensitivity effect reduces the side resistance of the fluke and shank as much as times of its reciprocal. According to this parameter study, we can conclude that sensitivity effect is not important factor to penetration depth, but it is very important to anchor capacity.

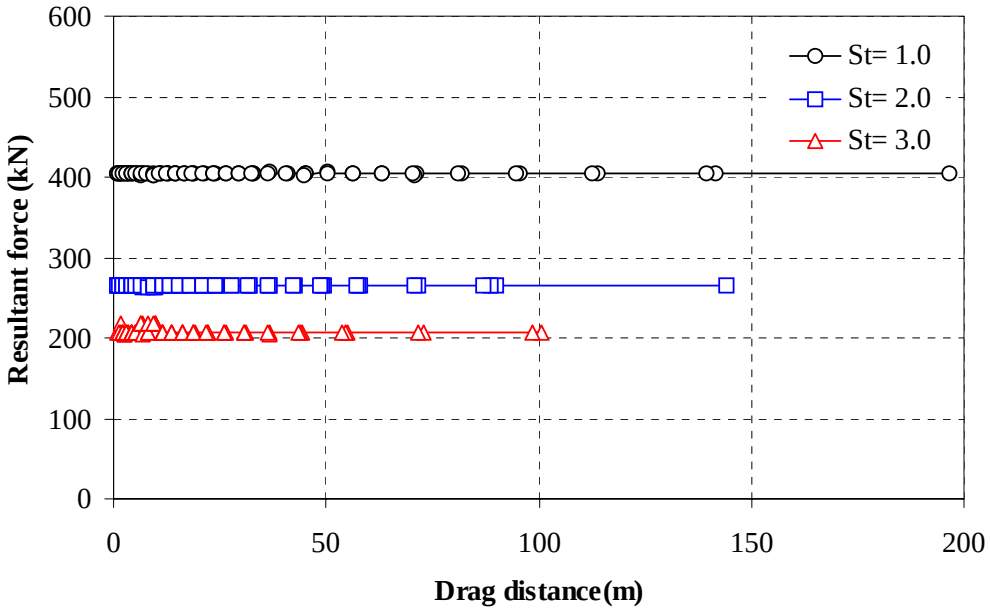

Fig. 7.22 Resultant force vs. drag distance for different soil sensitivity

7.1.5 Weight of the fluke

As shown in Fig. 3.1, 3.3 and 3.5, the fluke weight influence the anchor capacity. In general, there is a correlation between weight and area of the anchor. As an example, in case of chart for Bruce FFTS Mk 4 series, anchor capacities are plotted as a power law function of the anchor weight. However it should be noted that geometry of fluke is not varied in this study. The anchor geometry and undrained soil strength condition are basic condition given by Table 7.1. The weight of anchor studied here are 0kN, 15kN and 30kN, respectively. Fig. 7.23 shows the characteristic curve at 3m depth.

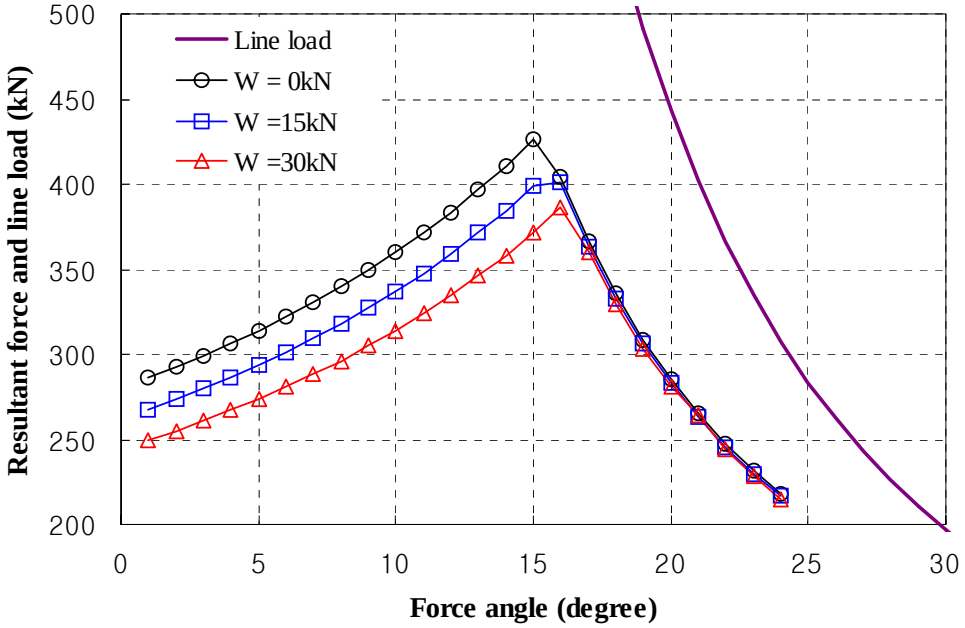

Fig. 7.23 Characteristic curve at depth of 3m for different weights of fluke

As it can be seen in Fig. 7.24 and 7.25, the weight of anchor does not play a key in anchor capacity and trajectory, except as it correlates to the size of anchor. Fig. 7.24 shows that identical anchor geometries with different anchor weight have almost identical trajectory curves. Further, Fig. 7.25 shows anchor weight to have small to no difference on anchor capacity.

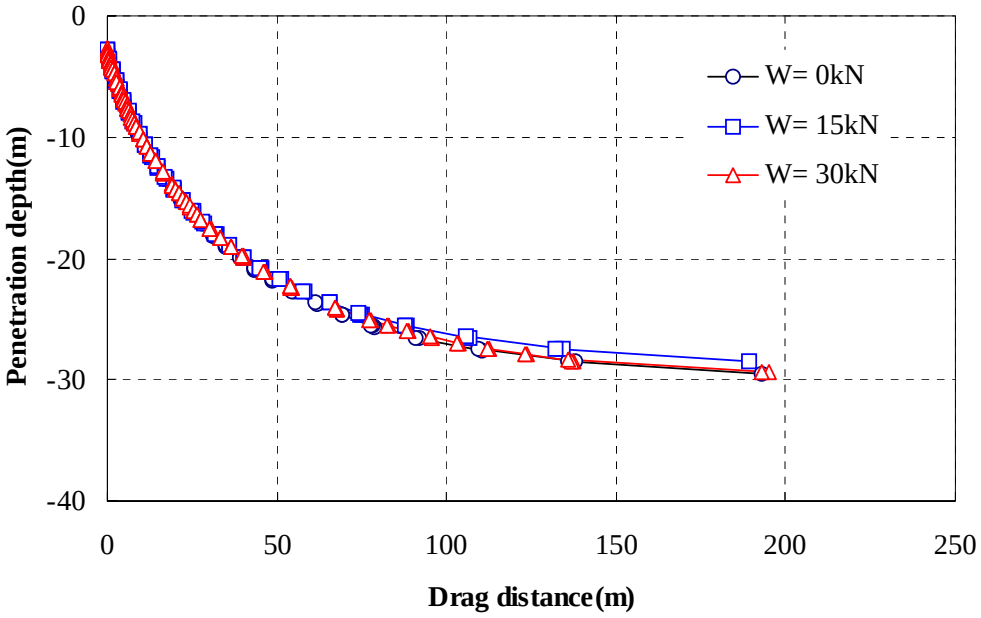

Fig. 7.24 Penetration depth vs. drag distance for different weights of fluke

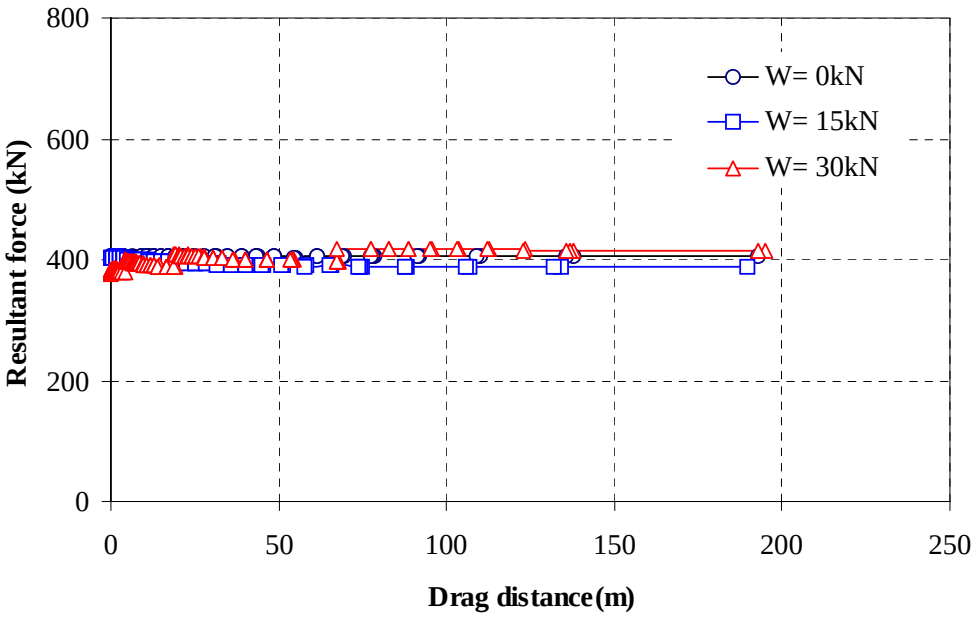

Fig. 7.25 Resultant force vs. drag distance for different weights of fluke

7.2 Shank geometry

In general, the shank geometry has less influences on anchor behavior than the characteristics of the fluke. Nonetheless, they can be significant. As indicated in Figure 1.4, modern high holding capacity anchors have twin shanks to reduce normal resistance; examples being the Vryhof Stevpris and Bruce FFTS Mk series. In cases of vertically loaded anchors with a bridle such as Vryhof Stevmanta, the shaft resistance can be negligible. The following sections consider the effects of shank shape, shank length, and the location of the fluke-shank attachment point.

7.2.1 Shape of cross section

In this section, the shape of cross section is studied. As shown in Fig. 7.26, all shanks have same area, but they have different section. In this study, the normal resistances of the shank are same in all cases because their thicknesses are identical.

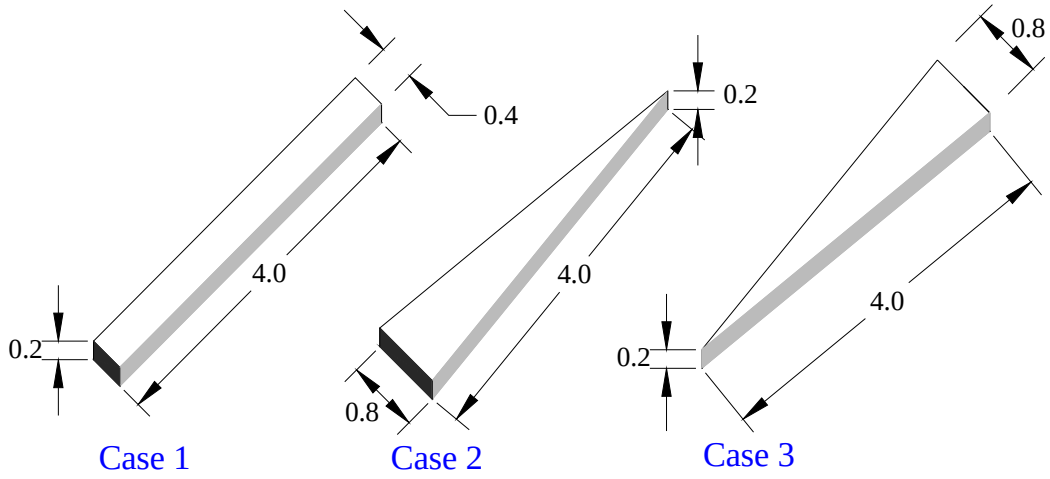

Fig. 7.26 Different shapes of shank

As shown in Fig. 7.27, the characteristic curves are exactly matched regardless of shape of shank. It indicates that different shape of shank does not influence the behavior of the anchor in uniform soil strength. Thus all of the anchors have the same depth of penetration and resultant force as shown in Fig. 7.28 and 7.29. This result of simulation can be applied when the real anchor is simulated. The shape of real anchor is very complicate but it can be simplified as rectangular if it has same area of original shank.

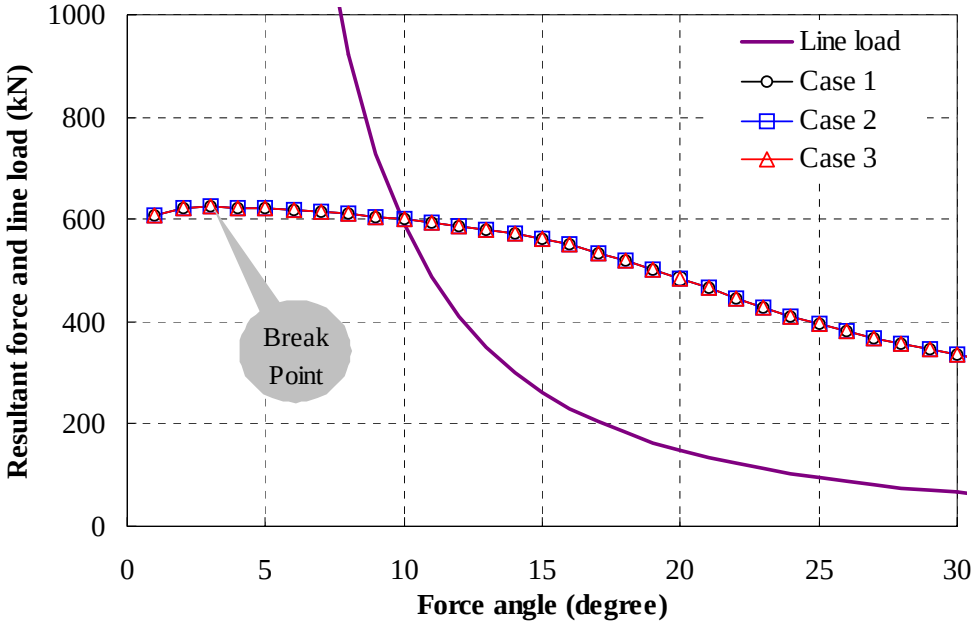

Fig. 7.27 Characteristic curves for different shapes of shank

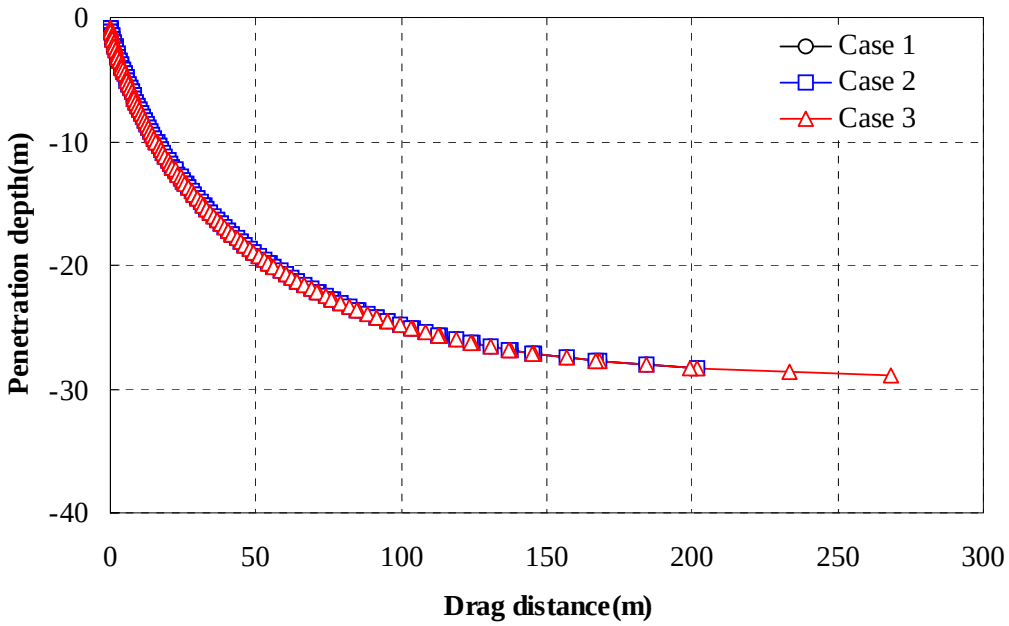

Fig. 7.28 Penetration depth vs. drag distance for different shapes of shank

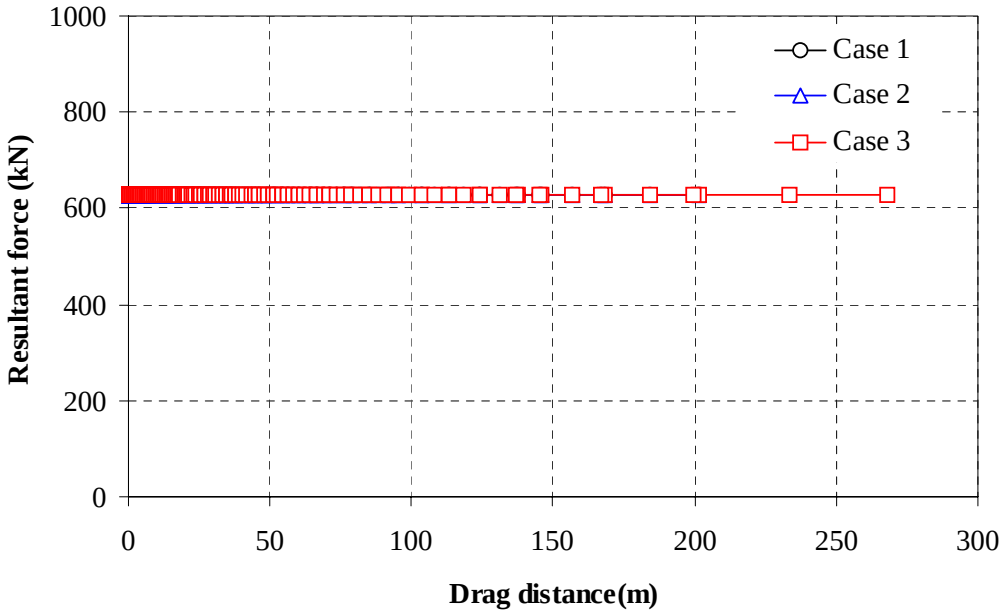

Fig. 7.29 Resultant force vs. drag distance for different shapes of shank

7.2.2 Length of shank

In this section the lengths of the shank are varied as shown in Fig. 7.30. As shown in Fig. 7.30, lengths of shank are 4m, 6m and 8m, respectively. Length of shank affects the point of application of the load. A longer shank will impose a larger moment on the fluke. It is therefore expected that the shorter shank will have the deeper penetration. Characteristic anchor curves for these three cases are shown in Fig. 7.31. The predicted trajectories shown in Fig. 7.32 clearly demonstrate that the shorter shank achieves greater penetration. Fig. 7.33 shows the resultant forces at anchor line attachment point versus drag distance. From these curves, it is evident that shortening the length of shank increases the resultant force.

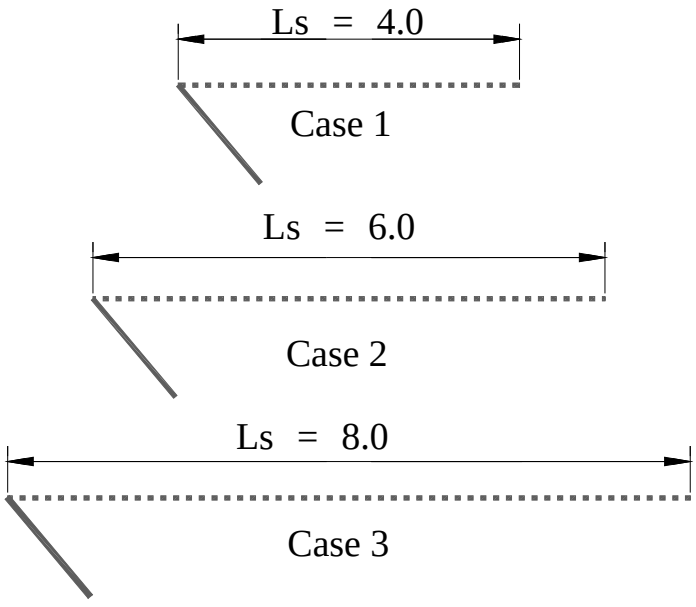

Fig. 7.30 Different lengths of shank

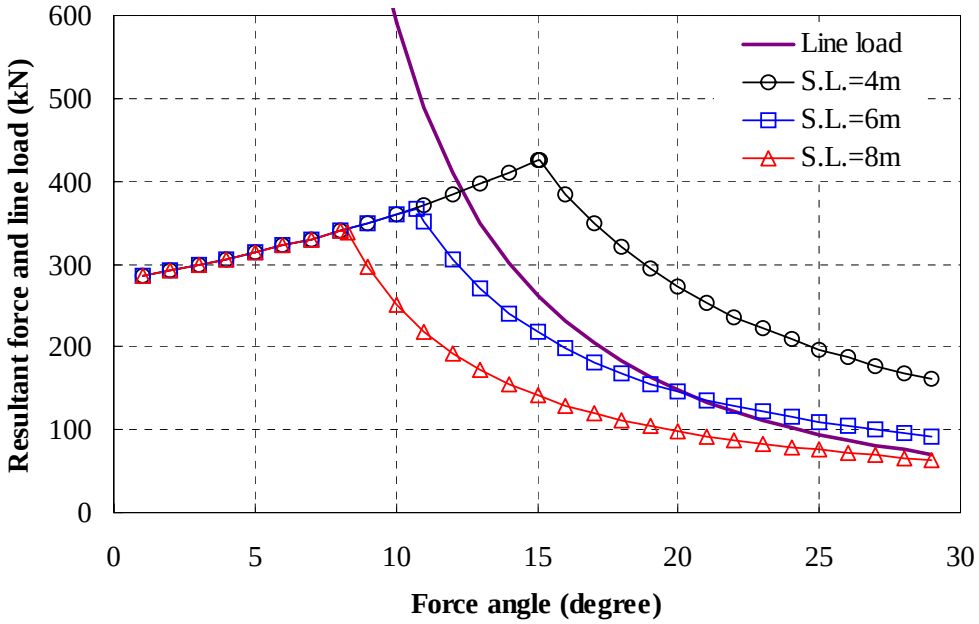

Fig. 7.31 Characteristic curves for different lengths of shank

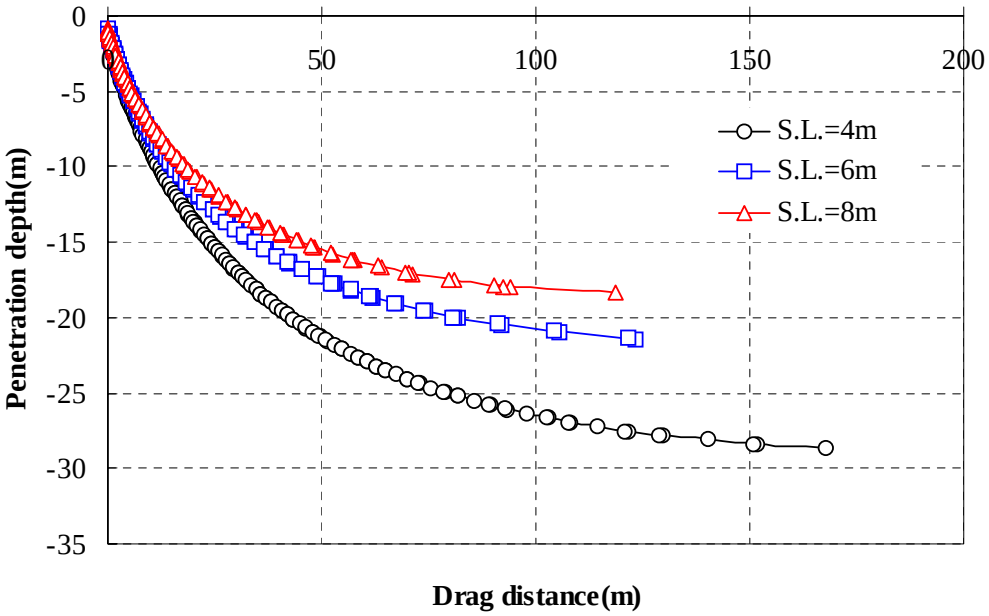

Fig. 7.32 Penetration depth vs. drag distance for different lengths of shank

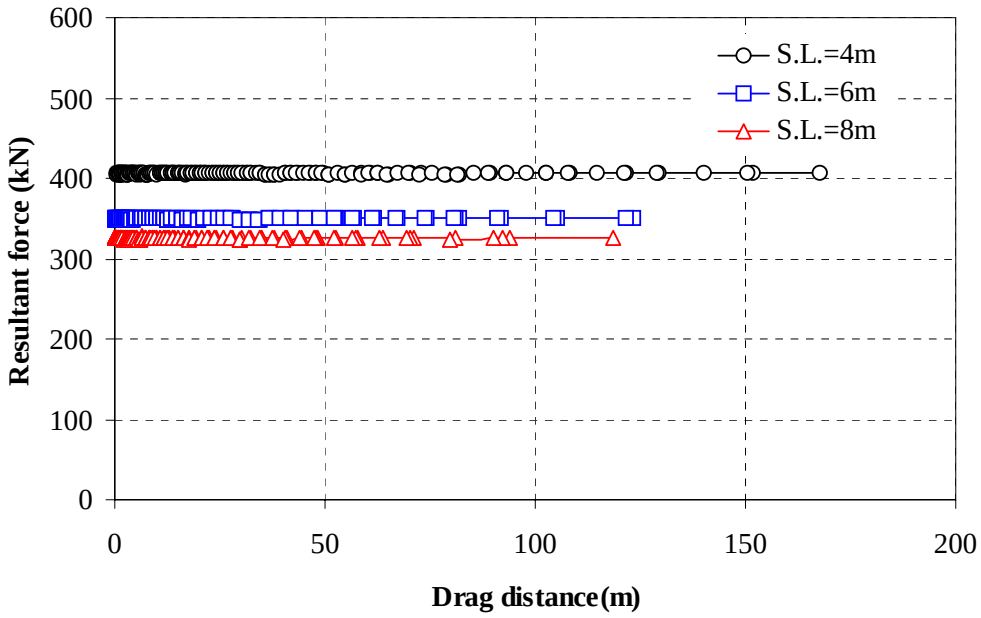

Fig. 7.33 Resultant force vs. drag distance for different lengths of shank

7.2.3 Location of fluke-shank attachment point

The fluke-shank attachment point influences the moment applied to the fluke which in turn affects the anchor performance. In this section, this effect is studied by varying the attached point location on the fluke. Fig. 7.34 shows the location of the attached point used study. The fluke-shank angle for all cases is 50 degree.

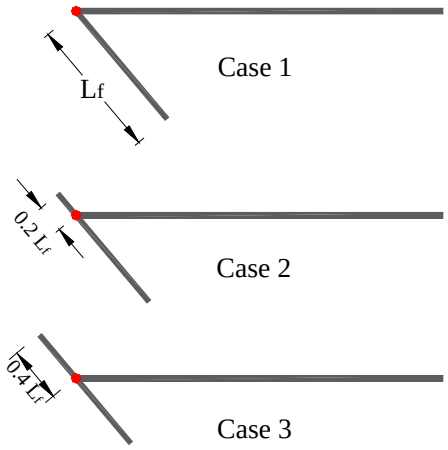

Fig. 7.34 Different fluke-shank attachments

Fig. 7.35 shows the characteristic anchor curve. These curves show that an attachment point closer to the center of fluke will cause the anchor to rotate more quickly. Accordingly, moving the fluke-shank attachment point away from center of the fluke will tend to increase the depth of anchor penetration.

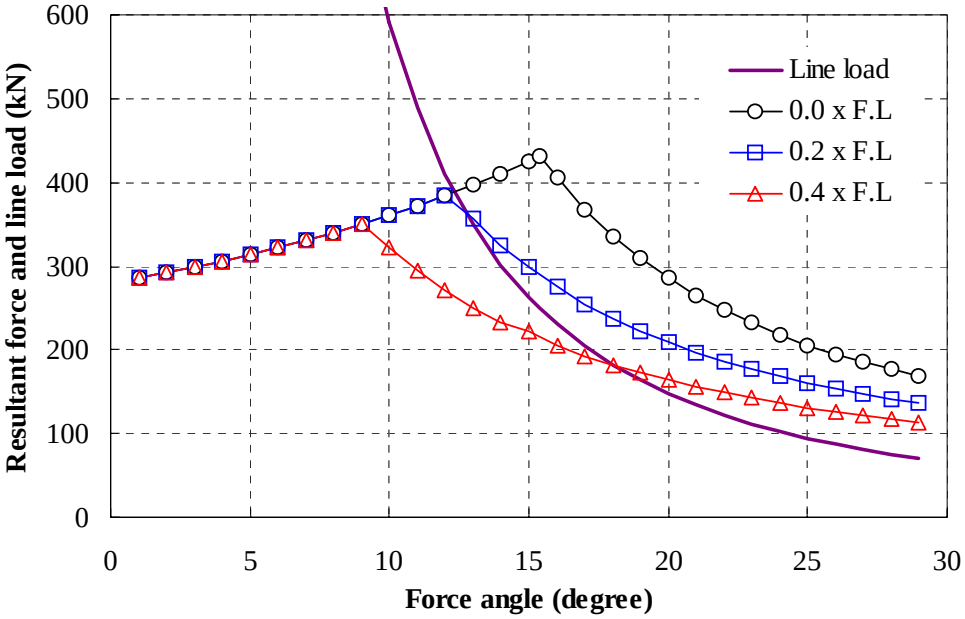

Fig. 7.35 Characteristic curve for different fluke-shank attachments

This effect is shown in Fig. 7.36, where moving the attachment point away from the center of fluke increases the predicted penetration depth. Fig. 7.37 shows the resultant forces at the anchor line attachment point. According to this figure, the resultant force is larger when the attached point is far from the center of fluke.

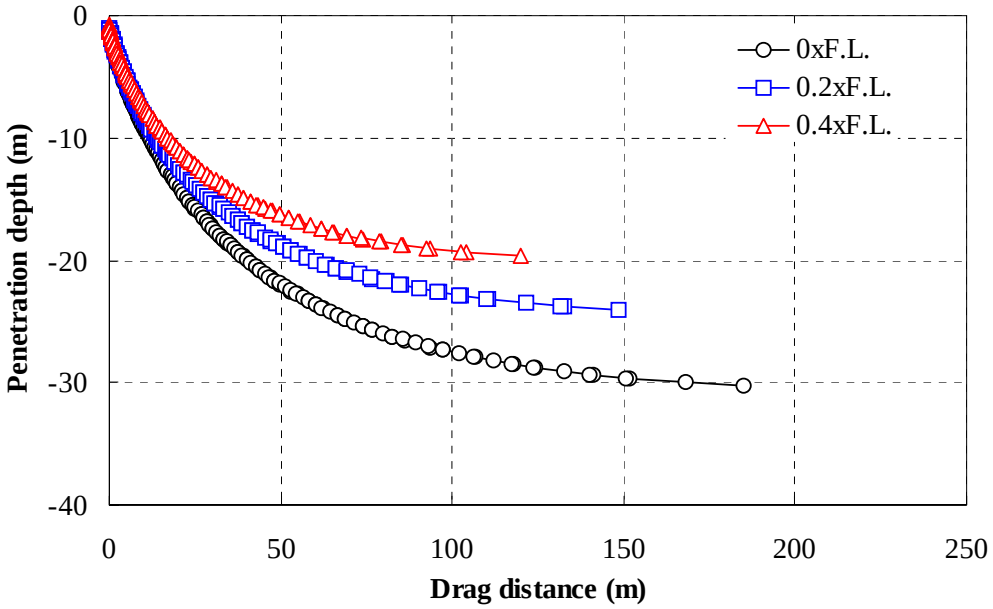

Fig. 7.36 Penetration depth vs. drag distance for different fluke-shank attachments

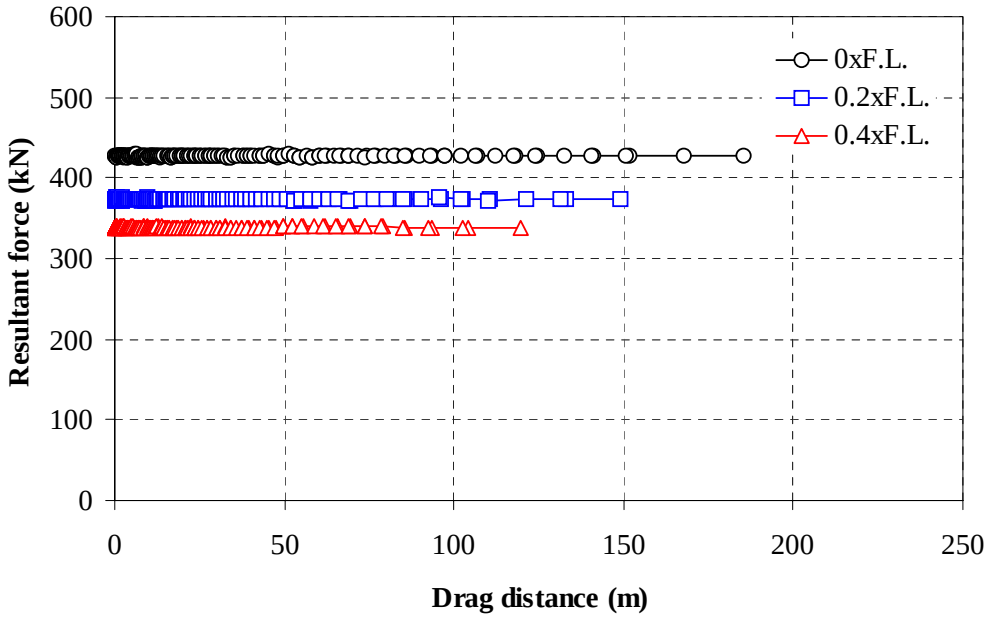

Fig. 7.37 Resultant force vs. drag distance for different fluke-shank attachments

7.3 Fluke-shank angle

It is well known that fluke-shank angle is a very important factor in the behavior of a drag anchor. Typical drag embedment anchors for use in soft clays have a 50 degree fluke-shank angle. In the case of hard clay and sand the fluke-shank angle is approximately 30 degrees. In this study, three types of fluke-shank angle are studied such as 30, 40 and 50 degree.

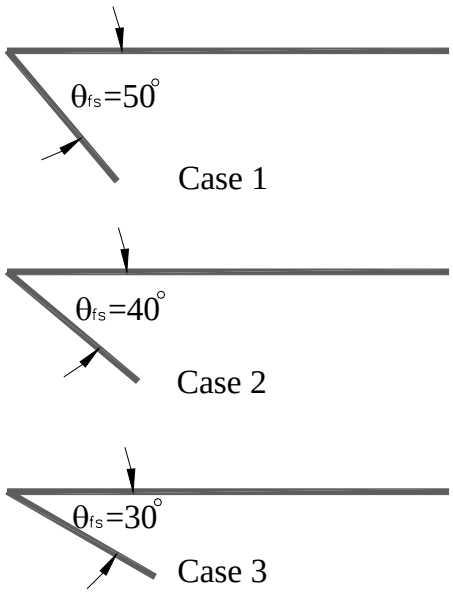

Fig. 7.38 Different fluke-shank angles

As shown in Fig. 7.39, the characteristic curves are somewhat different from previous examples. The curves for different fluke-shank angle do not coincide on the left side of break point, because the relationship between the force required to translate the anchor parallel to the fluke and the force angle vary. At low force angles the slope of curves are steeper for larger fluke-shank angles.

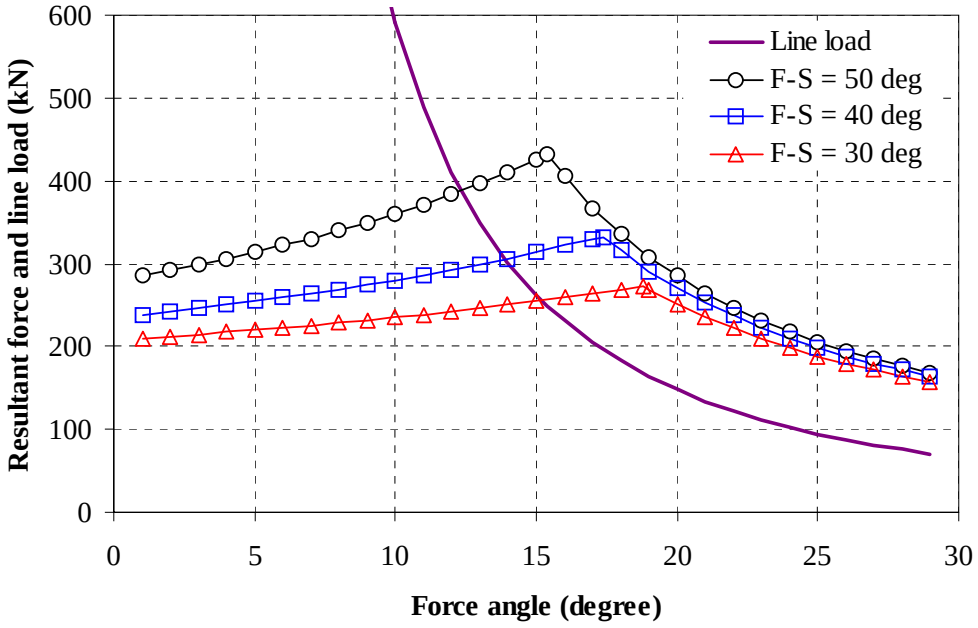

Fig. 7.39 Characteristic curves for different fluke-shank angles

The penetration depths are shown in Fig. 7.40. The larger the fluke-shank angle, the greater the penetration depth. It is evident that this is a very important parameter in anchor design. The Fig. 7.41 shows the resultant force at anchor line attached point. This figure indicates that the larger the fluke-shank angle, the greater the resultant force.

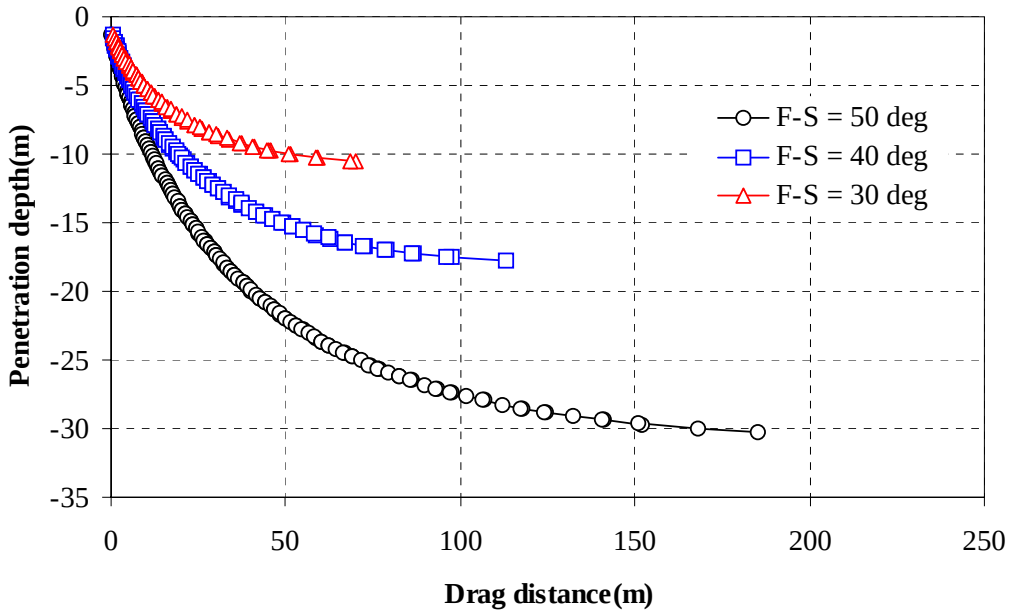

Fig. 7.40 Penetration depth vs. drag distance for different fluke-shank angles

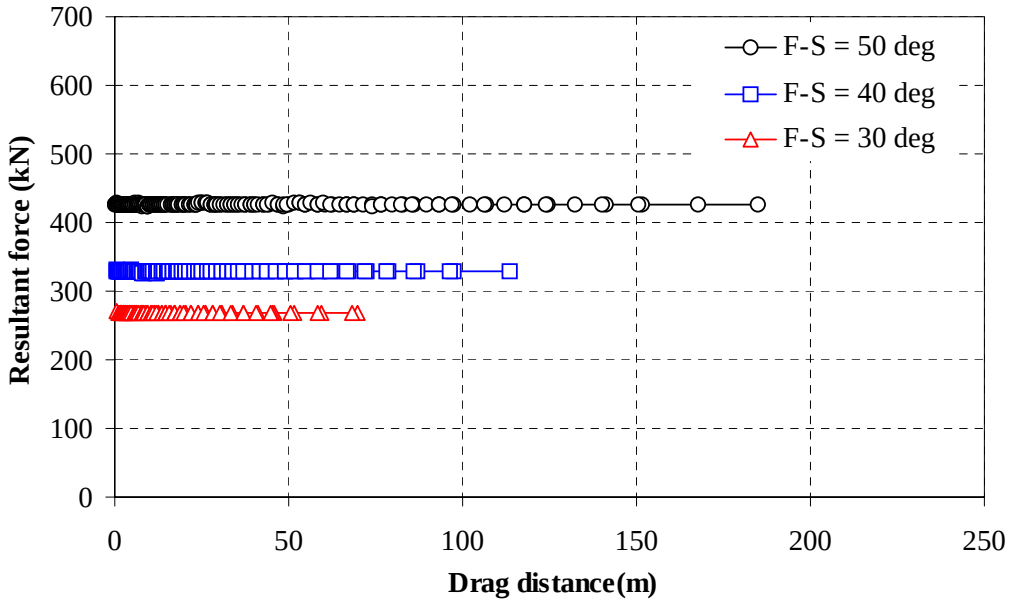

Fig. 7.41 Resultant force vs. drag distance for different fluke-shank angles

7.4 Line parameter

In Section 2.2 as shown in Eq. 2.9 and 2.10, the anchor line equation suggested by Neubecker and Randolph (1995) was discussed in detail. In this equation, the diameter of anchor line, the bearing capacity, N_c and the soil shear resistance are interrelated. Thus the relative effects of line diameter, N_c and soil sensitivity are studied here.

$$\overline{Q} = E_n d N_c \left[A + \frac{B(z_a + z)}{2} \right] \qquad (2.9bis)$$

$$\frac{T_a \theta_a^{\,2}}{2} = z_a \overline{Q} \qquad (2.10bis)$$

7.4.1 Line diameter

Fig. 7.42 shows the anchor line diameters studied here. The mid-size of anchor line diameter corresponds to the base case given Table 7.1. The small size is half of the mid-size and the large size is 50% larger than the mid size. The sizes of anchor line diameter studied here are 0.25m, 0.05m and 0.075m, respectively.

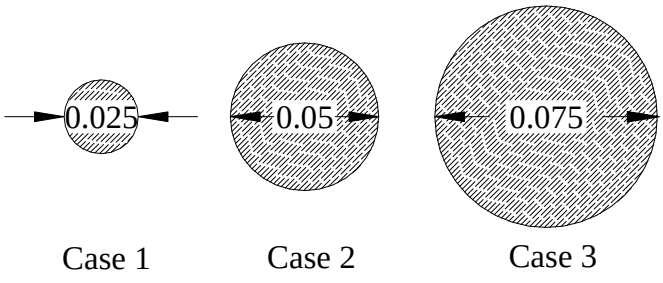

Fig. 7.42 Different anchor line diameters (unit: m)

The characteristic curves are shown in Fig. 7.43. The anchor line curves for varying diameters are superimposed on the base case characteristic curve. The analyses show that a thicker anchor line will interest the characteristic curve at a larger force angle. This implies that a thicker anchor line will cause the anchor to rotate earlier in the drag embedment process, resulting in a shallow penetration depth as shown in Fig. 7.44. Since the soil strength is uniform in this particular case, the resultant force at the anchor line attachment point is unaffected by anchor line thickness as shown in Fig. 7.45.

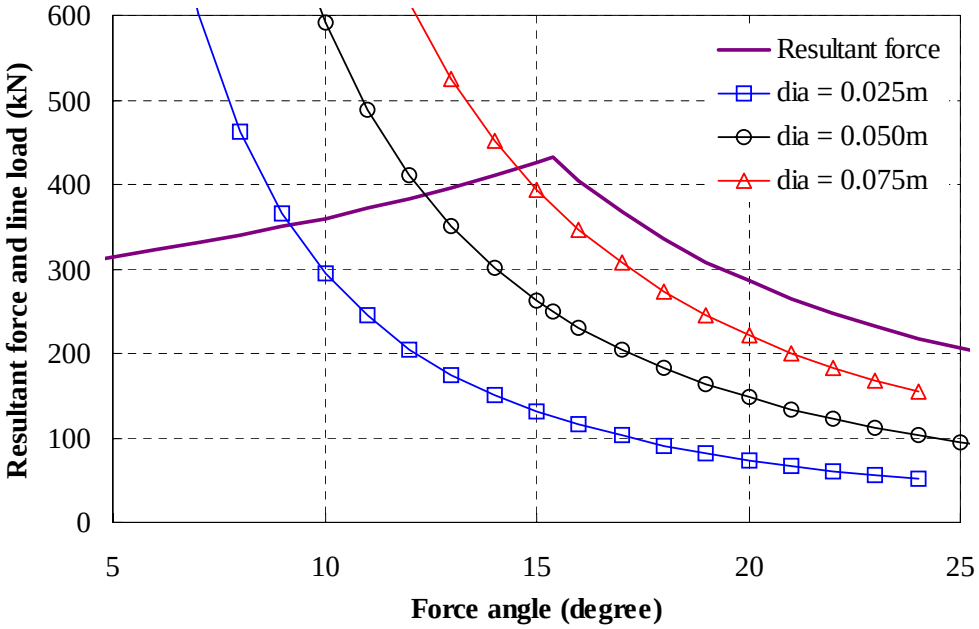

Fig. 7.43 Characteristic curve for different anchor line diameters

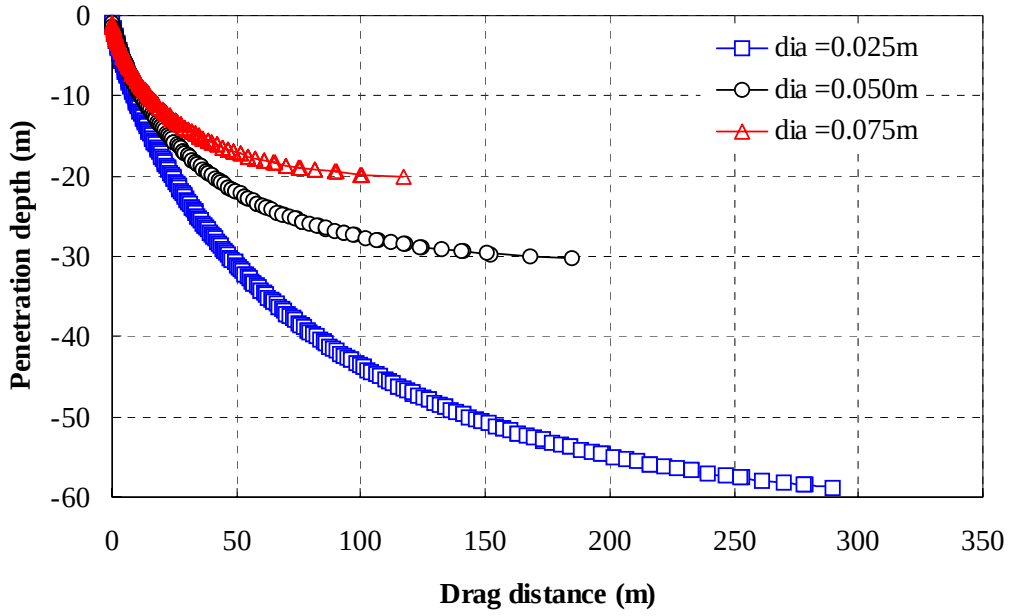

Fig. 7.44 Penetration depth vs. drag distance for different anchor line diameters

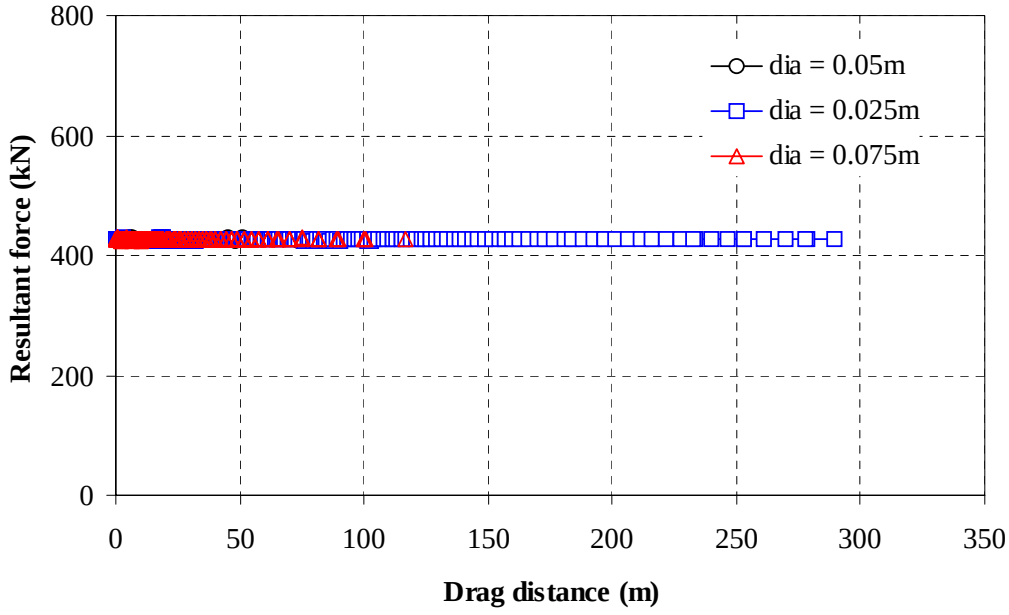

Fig. 7.45 Resultant force vs. drag distance for different anchor line diameters

Fig. 7.46 shows the mudline forces for the base case anchor with varying anchor line diameters. This figure shows that a thicker diameter results in a slightly greater mudline force. Since the mudline force depends on the resultant force and anchor line angle.

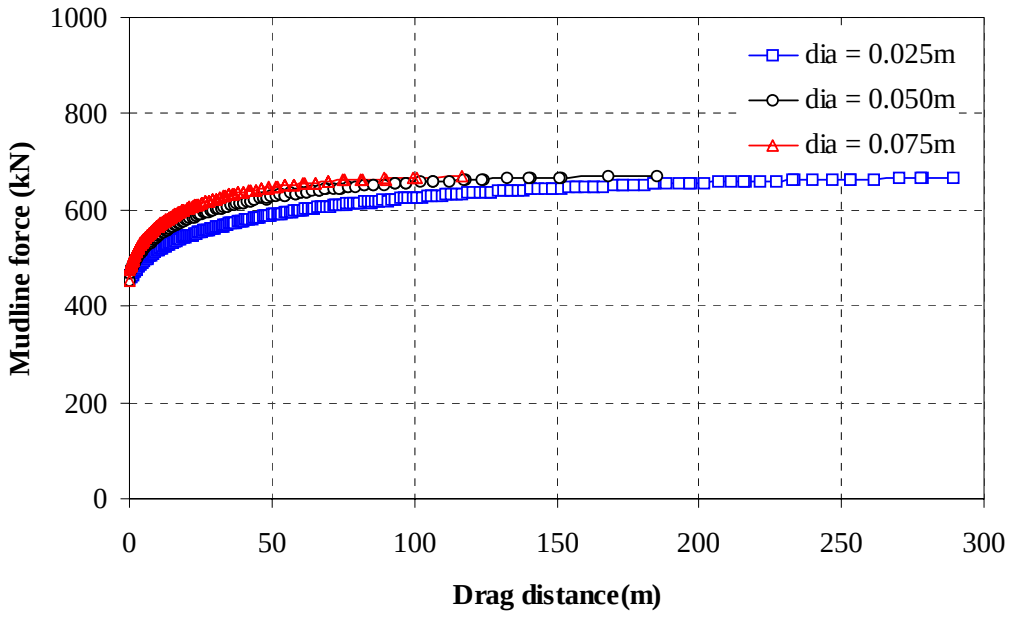

Fig. 7.46 Mudline force vs. drag distance for different anchor line diameters

7.4.2 Bearing resistance, N_c

As discussed in Chapter II there is not a clear consensus regarding the bearing capacity factor, N_c, to be used for the anchor line. Thus, it is useful to examine a range of values. The bearing pressure along the line is directly proportional to N_c, as indicated Equation 2.9.

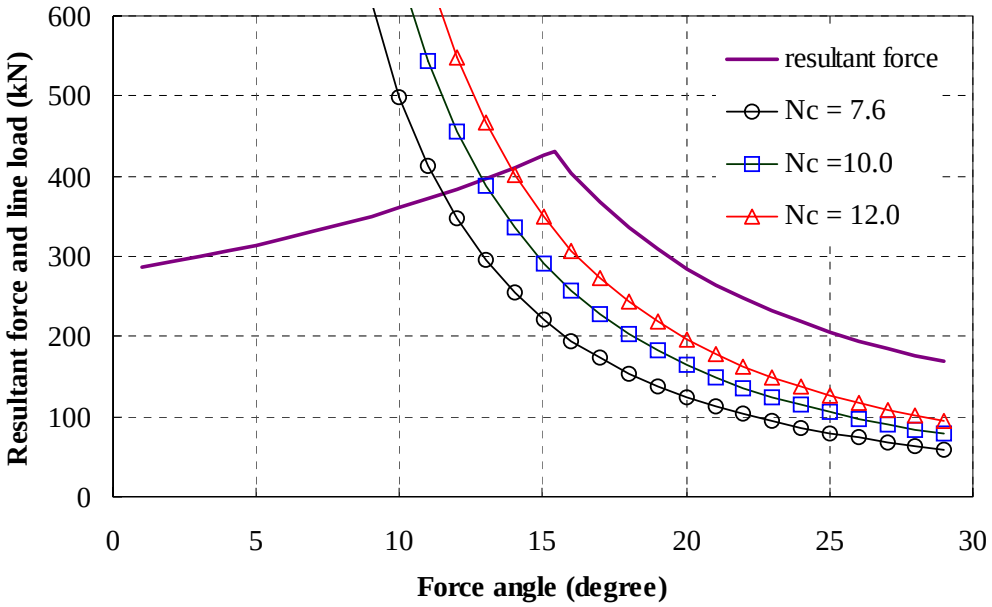

Fig. 7.47 Characteristic curves for different bearing resistances, N_c

As shown in Fig. 7.48, a larger N_c value leads to a penetration depth shallower. But, as previously discussed, for a uniform soil strength profile the resultant force is not affected by penetration depth, as shown in Fig. 7.49. Anchor line forces at the mudline are shown in Fig. 7.50. As far as anchor line tension at the mudline concerned, a larger N_c leads to a greater anchor line tension at the same drag distance.

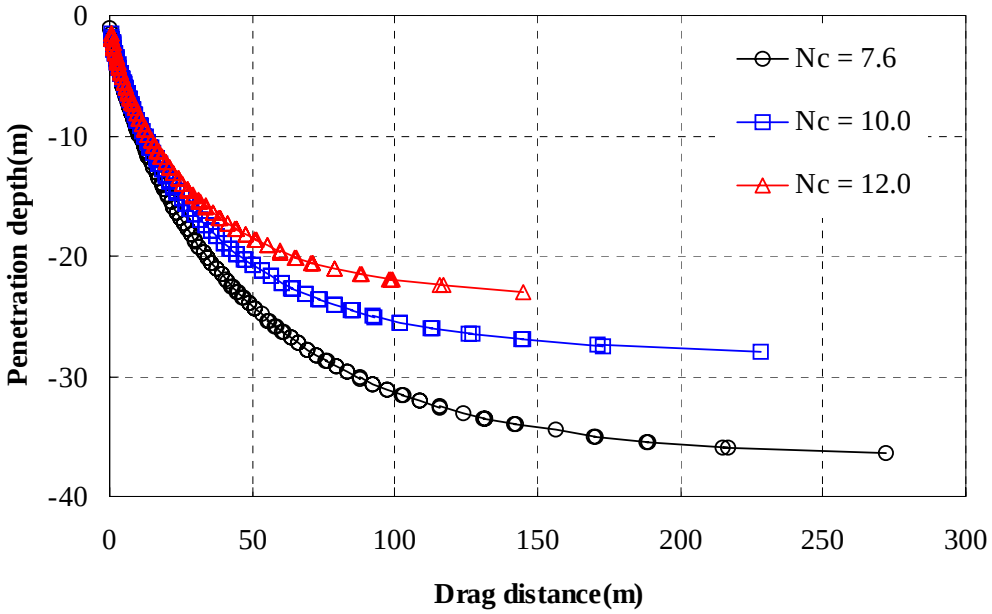

Fig. 7.48 Resultant force vs. drag distance for different bearing resistance, N_c

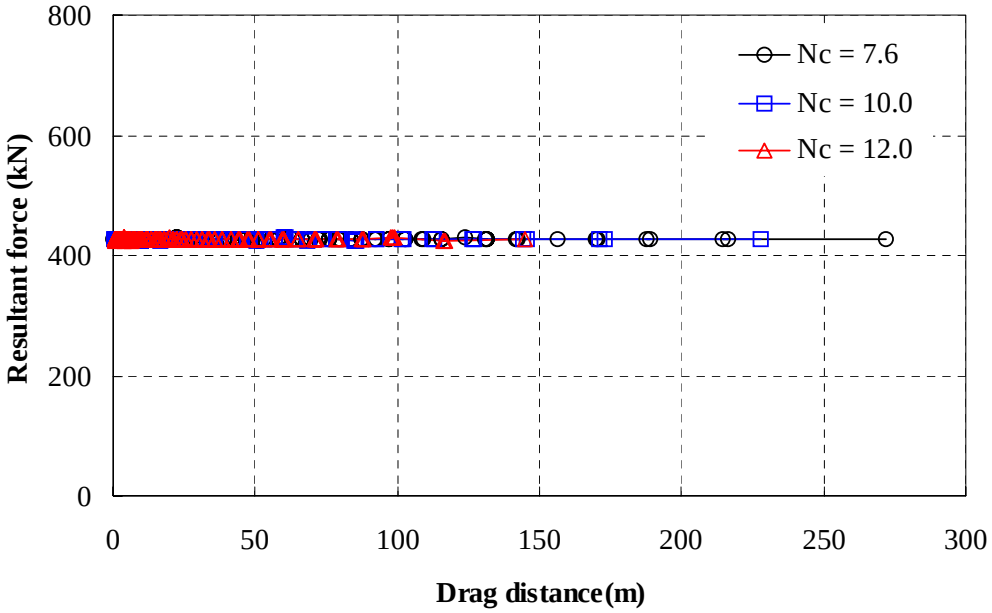

Fig. 7.49 Resultant force vs. drag distance for different bearing resistance, N_c

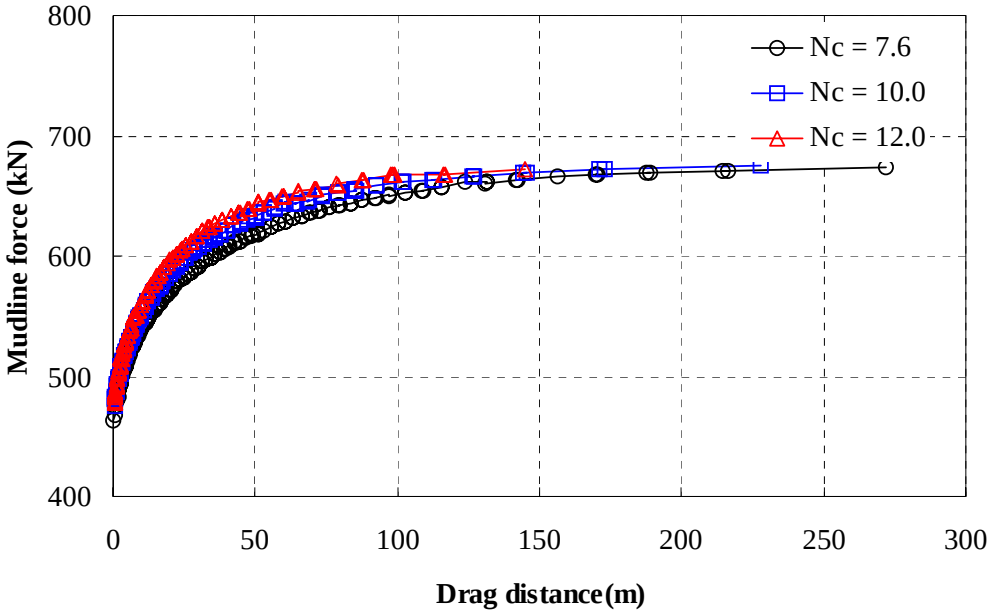

Fig. 7.50 Mudline force vs. drag distance for different bearing resistance, N_c

7.4.3 Sensitivity of soil

As discussed in Chapter II, the anchor line behavior is influenced by the soil adhesion factor. Typical α values are shown in Table 2.2. This study uses adhesion factors recommend by DVN EP-R302 (1999). The adhesion factor α can be usually estimated as $1/S_t$, where S_t is the sensitivity of the soil. Sensitivity is considered in estimating the shear resistance along the anchor line. Fig. 7.51 shows characteristic of anchor lines corresponding to each case. As shown in this figure, the lower sensitivity shifts the anchor line curve upwards.

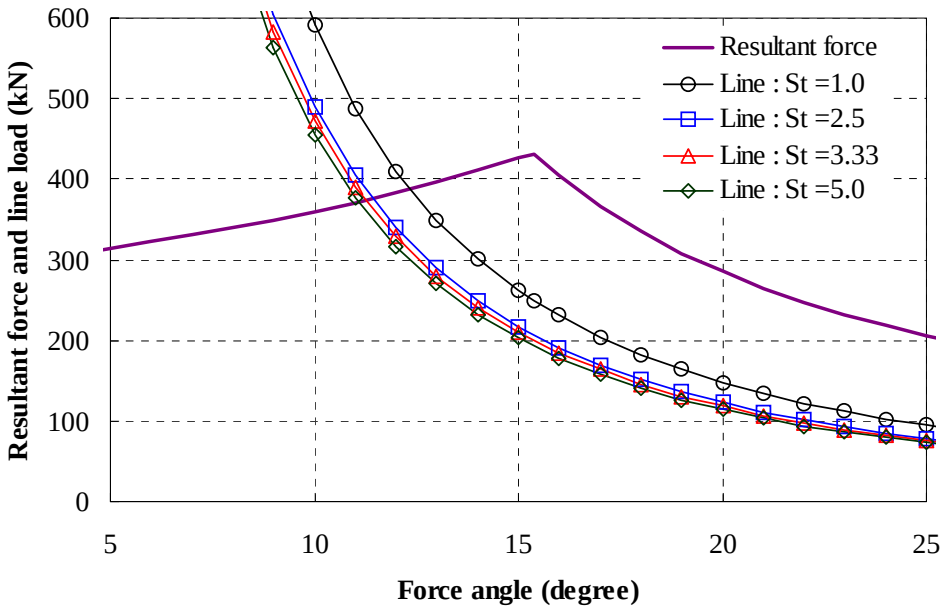

Fig. 7.51 Characteristic curves for different sensitivity

Fig. 7.52 shows penetration depth versus drag distance for different levels of S_t in the anchor line equation. As shown in Fig. 7.52, higher sensitivity leads to a greater penetration depth. Fig. 7.53 shows the resultant force versus drag distance. In the case of uniform soil strength the resultant force at the attachment point is constant. However, as shown in Fig. 7.54, the mudline load is larger in case of higher sensitivity due to deeper penetration.

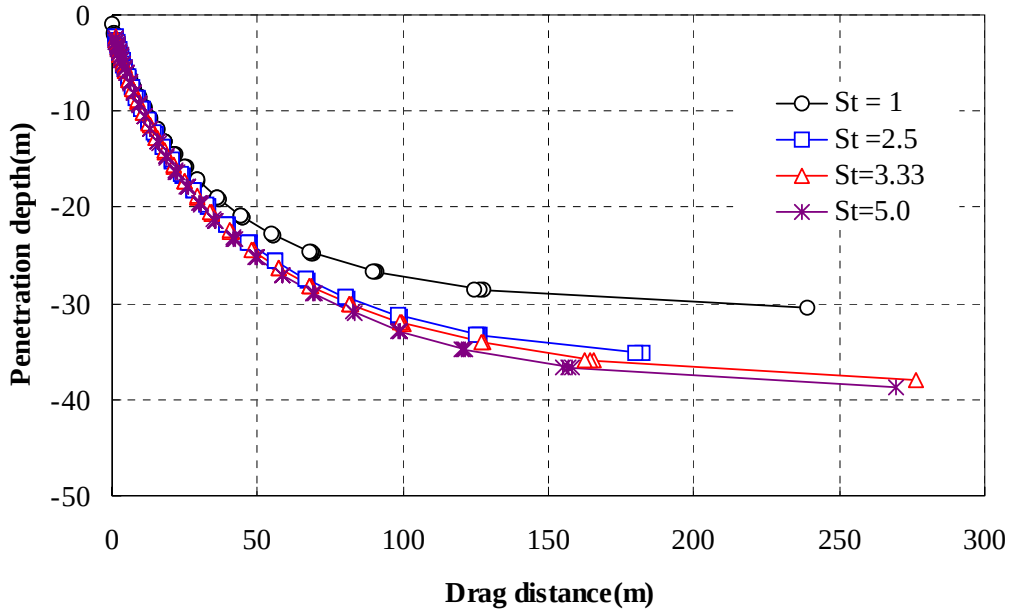

Fig. 7.52 Penetration depth vs. drag distance for different sensitivity

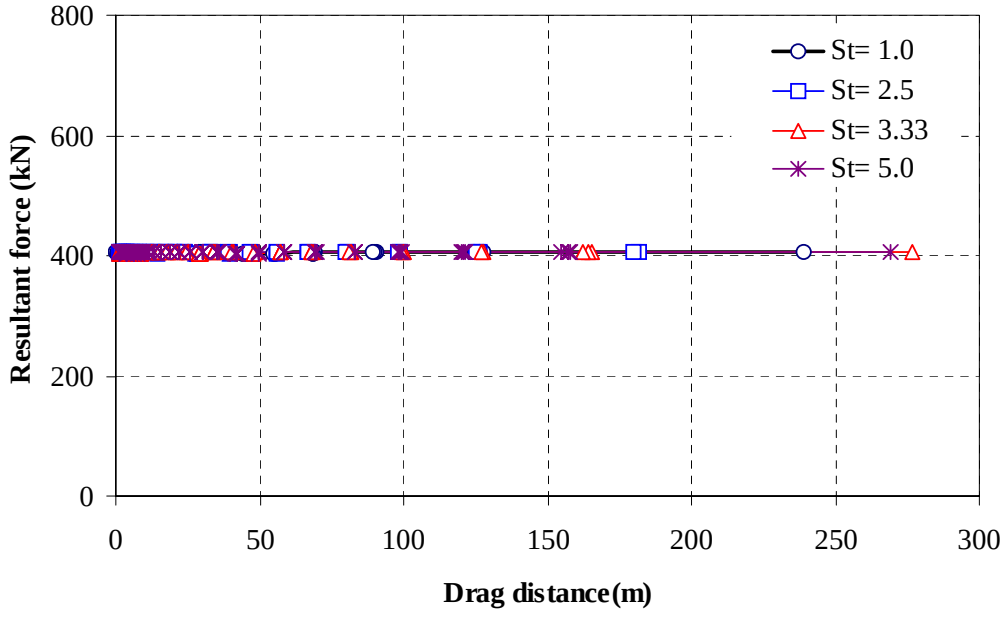

Fig. 7.53 Resultant force vs. drag distance for different sensitivity

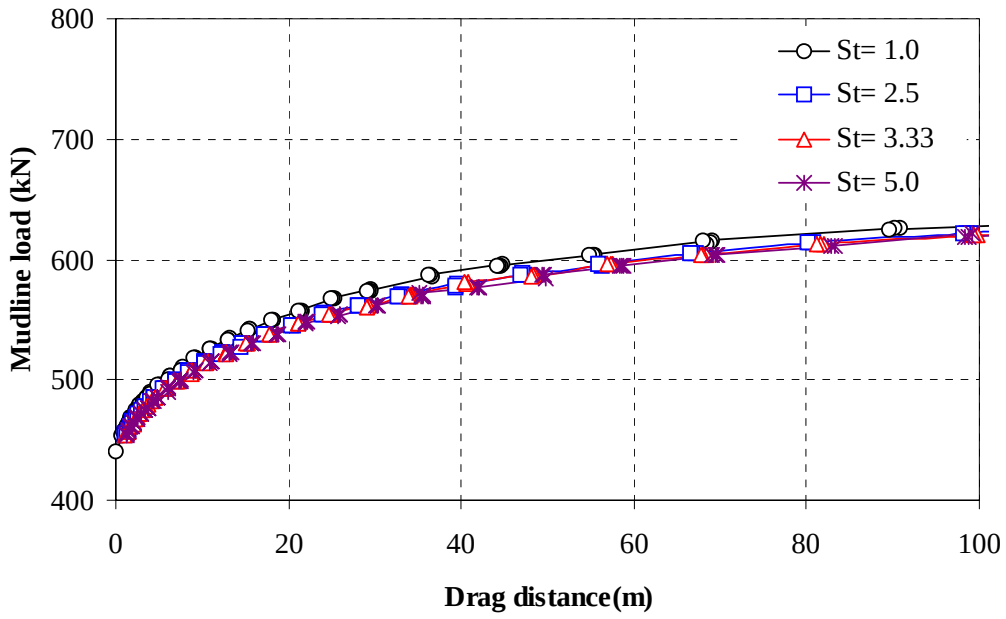

Fig. 7.54 Mudline load vs. drag distance for different sensitivity

7.5 Soil strength

In this section we will consider the effects of variations in soil strength parameters compared to the base case. In particular we will consider the effect of soil strength sensitivity, variations in uniform strength and variations in strength gradient.

7.5.1 Soil sensitivity for both anchor and anchor line

This section considers the effect of soil sensitivity on anchor performance. Remolding of the soil primarily affects the shear resistance along the surfaces of the shank and fluke. It is expected to have little effect on the stresses acting normal to these surfaces and, hence, is neglected in the latter case. Fig. 7.55 through 7.57 shows the effects of soil sensitivity on anchor performance for sensitivity of 1.0, 2.0 and 3.0. Fig.

7.55 shows the anchor characteristic curves and anchor line curves. The critical angles of sensitivity 1.0, 2.0 and 3.0 are 15.4^o, 21^o and 25^o, respectively. As shown in Fig. 7.56 the penetration depths decrease with increasing sensitivity. As shown in Fig. 7.57 the magnitudes of resultant forces are 431.6kN, 265kN and 205kN respectively. From this result we can see that resultant force is strongly influenced by sensitivity.

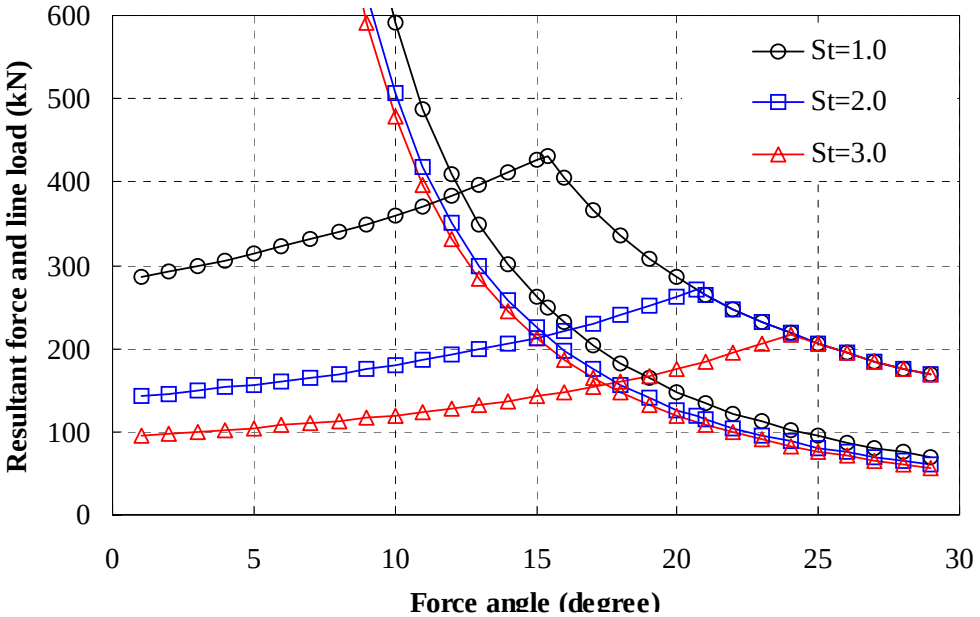

Fig. 7.55 Characteristic curves for different sensitivity on anchor and anchor line

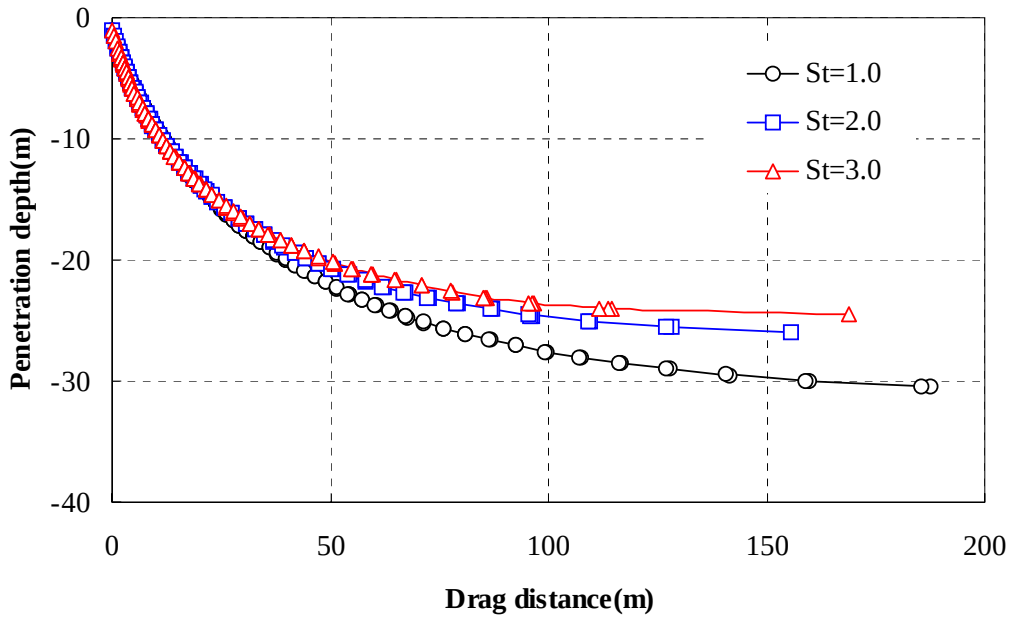

Fig. 7.56 Penetration depth vs. drag distance for different sensitivity on anchor and anchor line

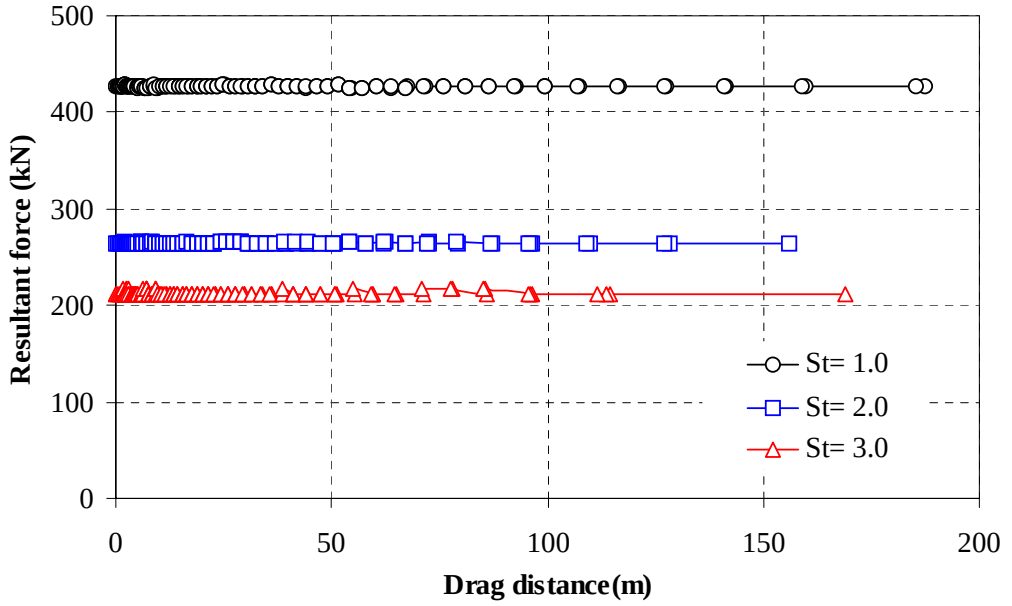

Fig. 7.57 Resultant force vs. drag distance for different sensitivity on anchor and anchor line

7.5.2 Magnitude of uniform soil strength

Here we consider the effect of varying for the case of uniform soil strength. The uniform soil strength profiles considered are in Fig. 7.58. The undrained soil strengths are 10kPa, 20kPa and 30kPa, respectively. All other conditions except soil strength are the same as the base case in this study.

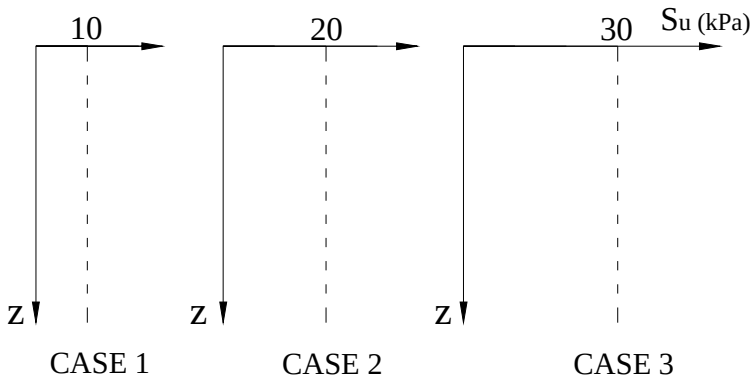

Fig. 7.58 Different magnitude of uniform soil strength

As shown in Fig. 7.59, intersection points between resultant force and line load curves occur at same force angle. The ordinates of the curves are linear functions of the soil strength hence normalizing the curves will result in single for both the anchor and anchor line functions.

Thus, characteristic curve breaks at the same force angle. This means that anchor rotates at the same force angle for given depth and orientation. For this reason anchors have same trajectory curves as shown in 7.60. But the resultant forces are different from each other at the line attachment point. As shown in Fig. 7.61, their

magnitudes are 202kN, 431.6kN and 607kN respectively and they have direct relationship with undrained soil strength.

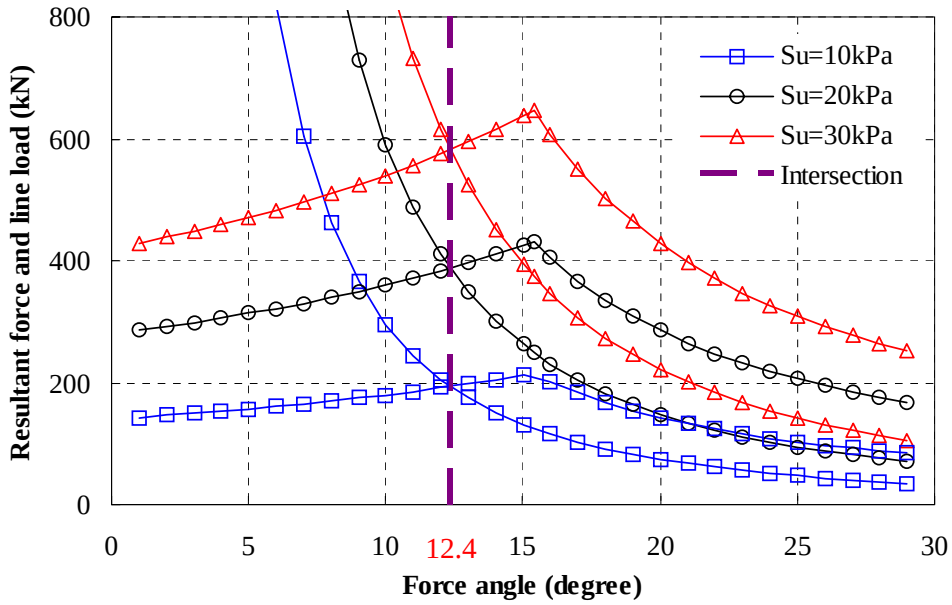

Fig. 7.59 Characteristic curves for different magnitude of uniform soil strength

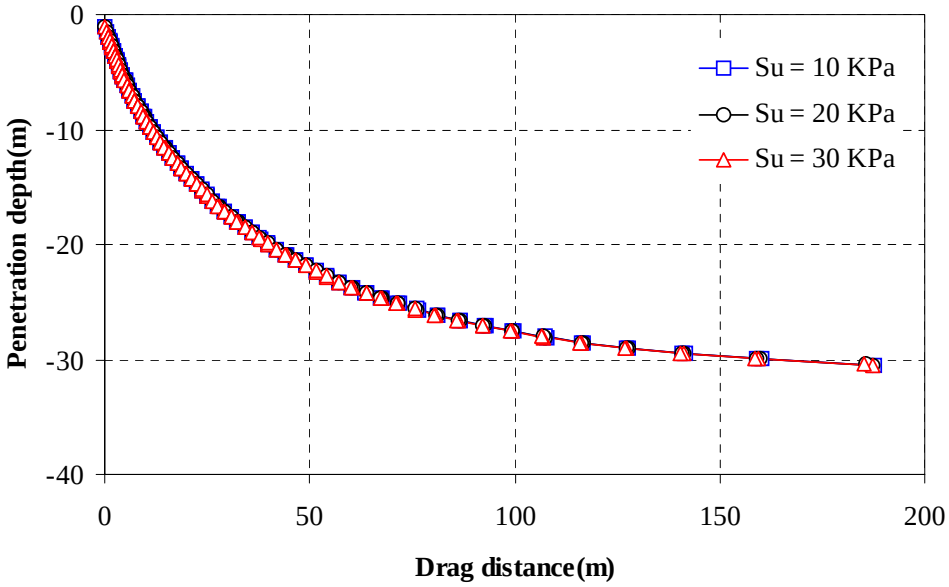

Fig. 7.60 Penetration depth vs. drag distance for different magnitude of uniform soil strength

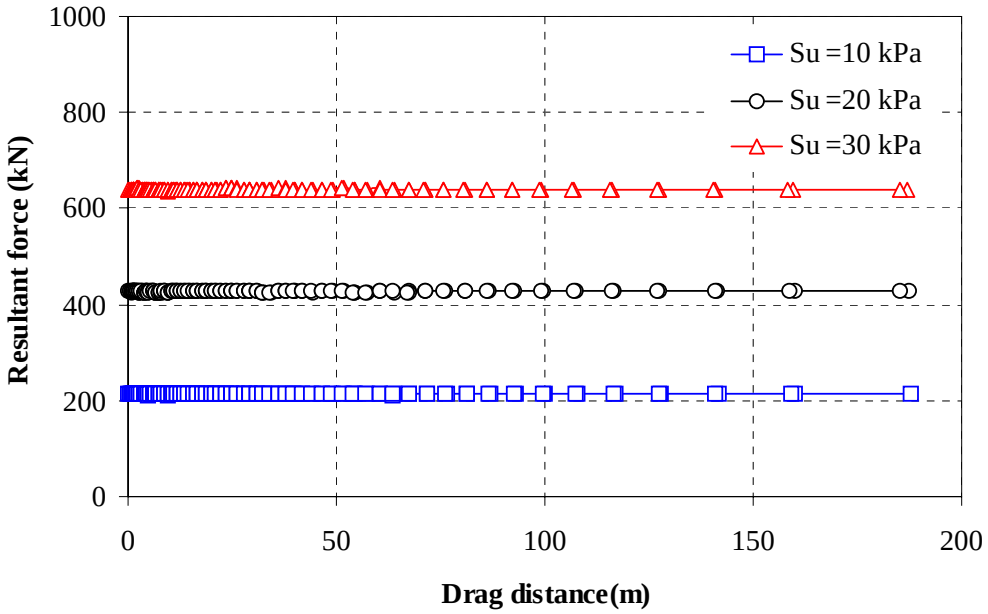

Fig. 7.61 Resultant force vs. drag distance for different magnitude of uniform soil strength

7.5.3 Effect of strength gradient

In this section we consider the effect of linearly increasing soil strength with depth. The strength gradients studied are 1.0kPa/m, 1.5kPa/m and 2.0kPa/m, respectively, as shown in Fig. 7.62.

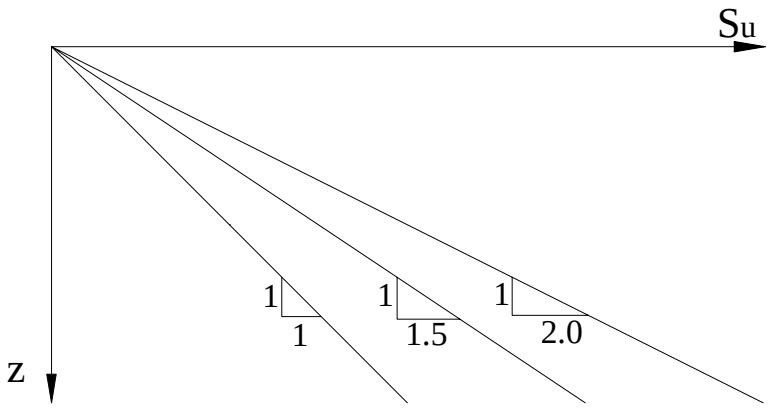

Fig. 7.62 Different strength gradients, Sg

As in the case for uniform soil strength, if the ordinates of the curves of the Fig. 7.63 are normalized by a characteristic strength then the characteristic curves collapse to a single curve, and the intersection points occur at the same force angle. Therefore anchor trajectory is independent of strength gradient as shown in Fig. 7.64. Fig. 7.65 shows drag distance versus resultant force at shackle. As expected, shackle force at any drag distance scales directly to strength gradient.

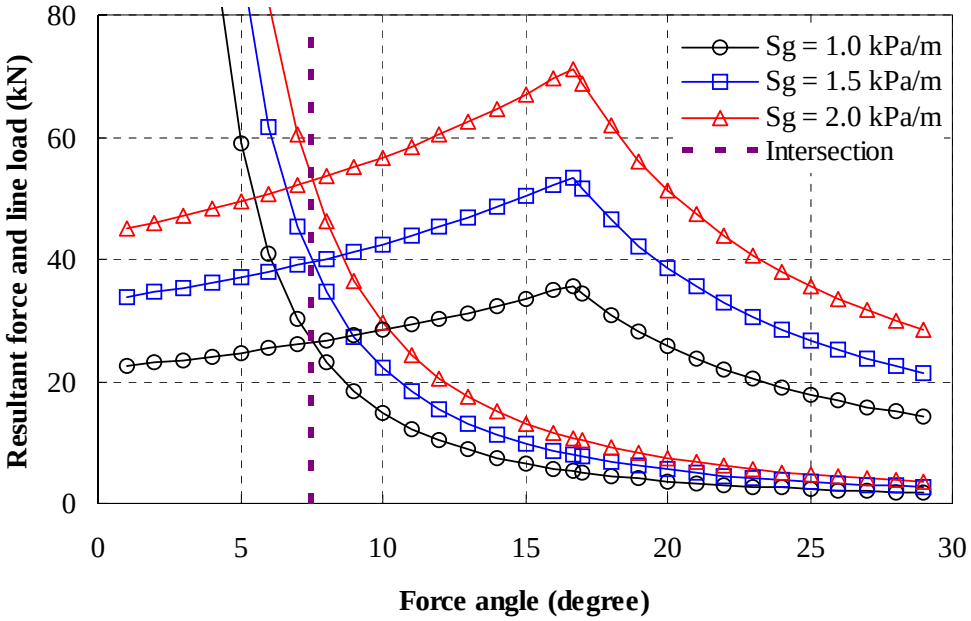

Fig. 7.63 Characteristic curves for different strength gradients

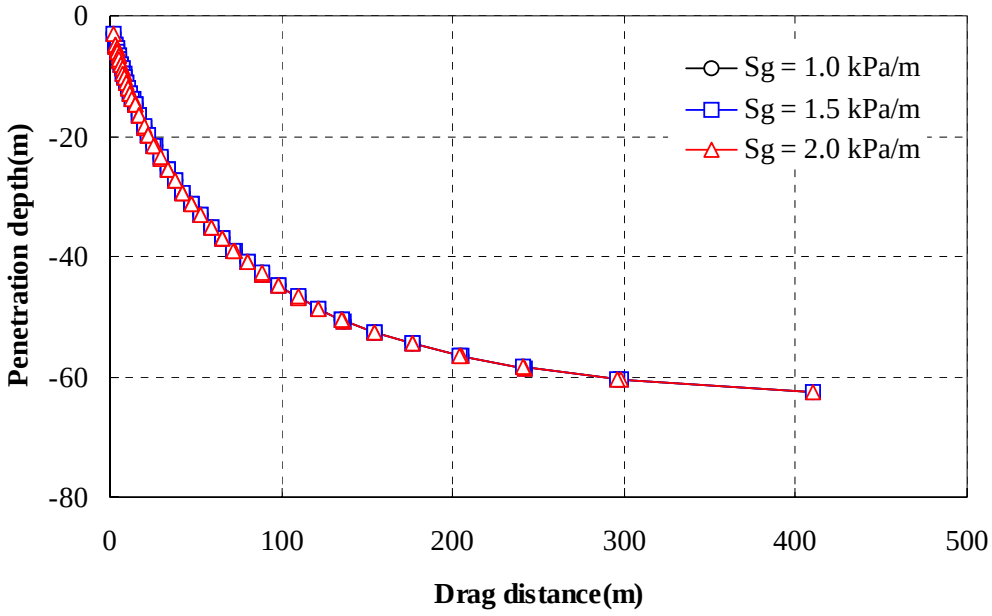

Fig. 7.64 Penetration depth vs. drag distance for different strength gradients

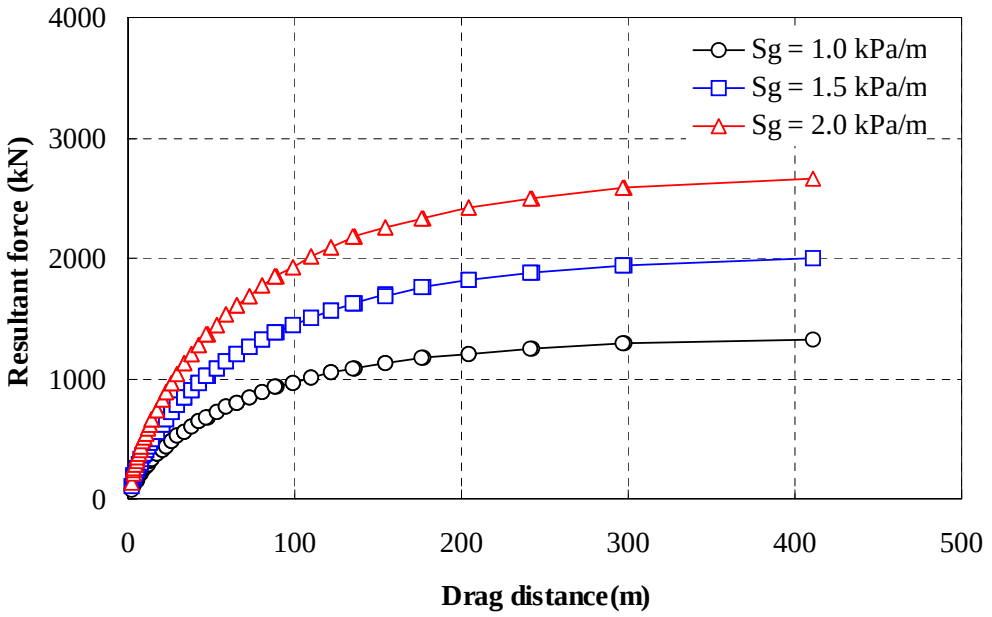

Fig. 7.65 Resultant force vs. drag distance for different strength gradients

CHAPTER VIII

VERIFICATION AND COMPARISON OF UBM

For the purpose of verification of the UBM, firstly comparisons with selected field tests and design charts have been conducted and are described in this chapter. Secondly, the UBM prediction is compared with centrifuge test results which were obtained by Randolph and his coworkers (2000). Finally, UBM compare with other methods for given same anchor, anchor line and soil properties.

8.1 Simulation of field tests

In this chapter, the UBM is used to simulate field tests where soils data and anchor performance were measured. The result of this simulation provides a means to test the UBM with real anchor performance.

8.1.1 Simplification of anchor geometry

As mentioned in Chapter VI, real anchors have very complex geometries. For example, Fig. 8.1 shows details of two anchors that are widely used offshore. As can be seen in this figure, the flukes and shanks are not simple rectangular or triangular plates. For modeling purposes, however, we need to simplify this complex shape. In simplifying the anchor geometries, results of parameter studies which were conducted in Chapter VII are helpful.

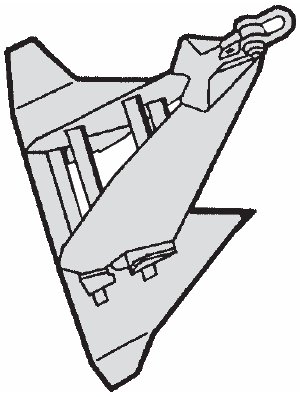

a. Vryhof Stevpris

b.BRUCE FFTS MK 4 ANCHOR

Fig. 8.1 Examples of real anchor

A. Fluke

The fluke plays a central role in the behavior of an anchor. The resistance of the soil varies with the area of the fluke. Thus, one rule adopted for simulation is to set the model area equal to the area of the real anchor. Since a numerical method is used for calculation in the UBM simulation the anchor component such as the fluke or shank is divided into small elements as shown in Fig. 8.2. All real flukes are symmetric about their centerline thus this property is exploited for numerical calculation. For each sub element of the anchor component, the internal energy dissipation is calculated for the assumed displacement increment. Subsequently, the total energy dissipation is obtained by summing these contributions. As mentioned in Chapter VI, the n_{pf} function is taken to be the quadratic type with value of 6 at the reference point of minimum energy dissipation and 12 at the edge of the fluke as shown in Fig. 8.3.

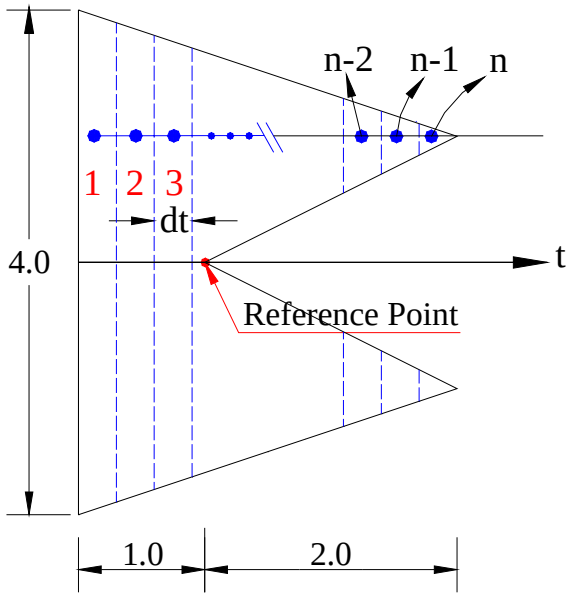

Fig. 8.2 Example simulation of real fluke

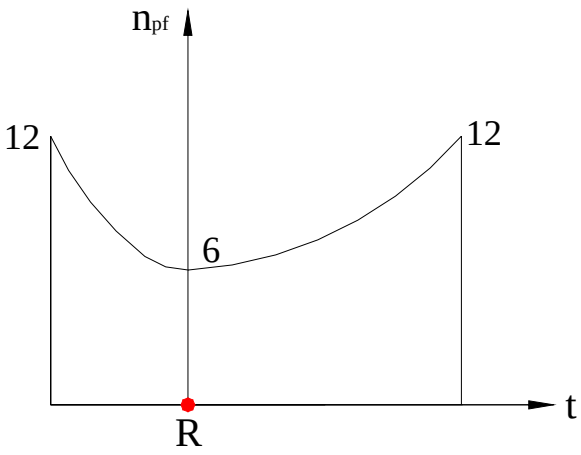

Fig. 8.3 n_{pf} function of real fluke

B. Shank

As was indicated in the parameter studies presented in Chapter VII, the shape of the shank is a minor factor in the behavior of the drag anchor. However, its size and length are very important. For simplification purposes in simulation the shank is considered to have a rectangular shape with its actual length. As shown in Fig. 8.1, the modern drag anchor has a shank composed of twin parallel plates to reduce the normal resistance of the soil. To simulate a twin shank, the bearing of the soil plug between the plates is not considered, i.e., the only side resistance of the shank plates is included in the model. Fig. 8.4 shows the procedure for simplification of the shank. In this figure, (a) shows the original shape of the shank, (b) shows an intermediate step and (c) shows the final simplification of the shank.

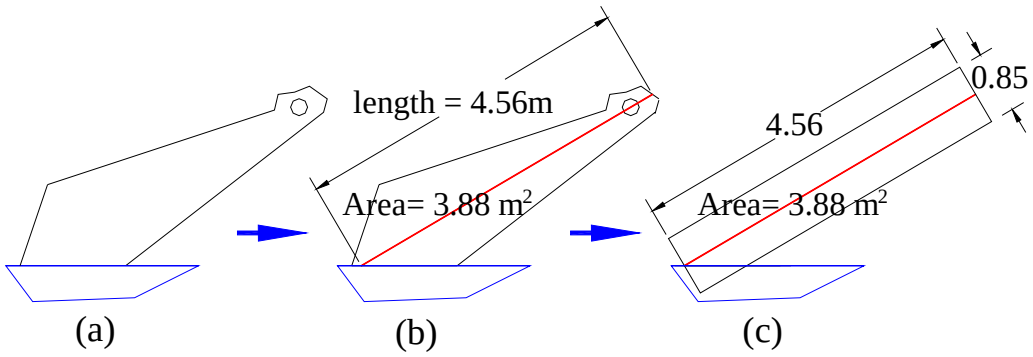

Fig. 8.4 Example simplification of shank

C. Fluke-shank attachment point

The fluke-shank attachment point is also a very important factor in the behavior of drag anchor. Usually the fluke has symmetry about its axis in two directions but the shank only has symmetry about one plane. Referring to Fig. 8.5, the *x*-*y* plane is a plane of symmetry but the *x*-*z* plane (*z* normal to the paper) is not. For this reason, we need to establish a rule to decide the axis of the shank. Based on the studies discussed in Chapter VI the axis of the shank is determined as shown in Fig. 8.5. The axis of the shank (*x* axis) is determined when the first moment of the shank about the *x* axis is zero as shown in Fig. 8.5.

$$I_x = \int y\, dA = 0 \tag{8.1}$$

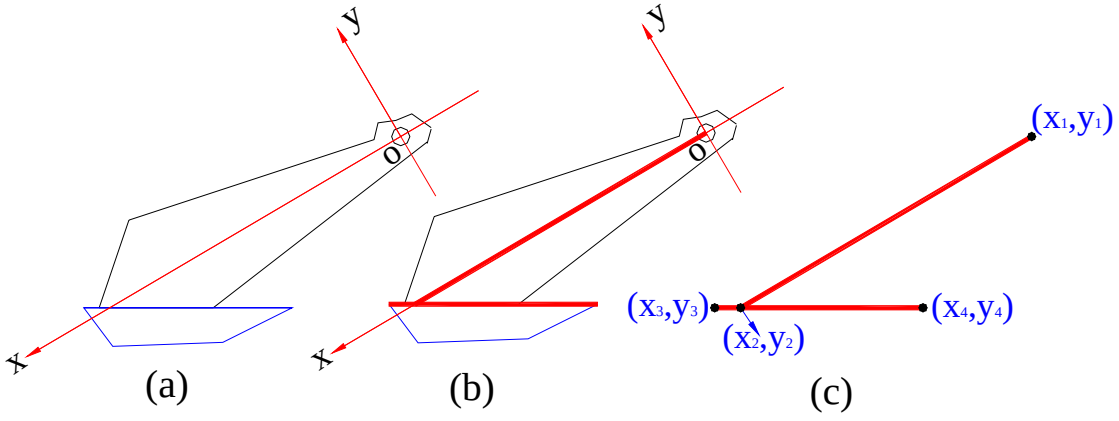

Fig. 8.5 Procedure of making a decision of fluke-shank attachment

8.1.2 Undrained soil strength condition

Undrained strength of normally consolidated marine clays typically increases linearly with depth. This is discussed in detail in Chapter I. The undrained soil strength is determined by in-situ tests such as the cone penetration test, vane shear test etc. as well as various laboratory tests. However, most of the in-situ tests available with the anchor field data do not give sensitivity values which are very important for simulating the side resistance of the anchor. For this reason, the sensitivity values are considered parametrically i.e., as two, three, etc., in the UBM simulation.

8.1.3 Bearing capacity factor, N_c

The global bearing capacity factor, N_c, was discussed in Chapter II in detail. In the UBM simulation, N_c is taken as a function of depth as shown in Fig. 8.6 to account for the effects of soil surface proximity.

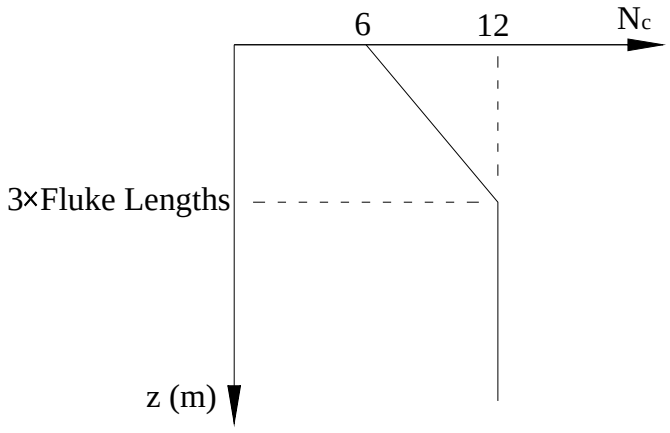

Fig. 8.6 Global bearing capacity factor, N_c

8.2. Comparison of anchor predictions as measured results

There have been a number of field tests of drag embedment anchors. Table 8.1 shows a selected list of field tests which are used here for comparison with UBM predictions. These data provide some indication of the robustness.

Table 8.1 Field tests of drag embedment anchors

No.	Project Name	Project Area	Year	Type of anchor
1	Joint Industry Project	Gulf of Mexico	1990	Vryhof Stevpris 68.6 kN
2	Liuhia 11-1 field	South China Sea	1996	Bruce FFTS MK4 392 kN
3	P-13 Site	Offshore Brazil	1997	Bruce Denla MK3 63.7 kN
4	South Timbalier Block 295	Gulf of Mexico	1996	Bruce Denla Mk2 12.74 kN
5	South Timbalier Block 295	Gulf of Mexico	1996	Vryhof Stevmanta 32 kN
6	Voador (P-27), Campos basin	Offshore Brazil	1998	Vryhof Stevmanta 102 kN

8.2.1 Joint Industry Project, Gulf of Mexico, 1990 – Stevpris 68.6 kN

These tests were conducted in the Gulf of Mexico by Omega Marine in 1990 as part of a Joint Industry Project. Three Stevpris anchors were tested in soft clay using a catenary mooring system. One of the tests was selected for simulation. The anchor geometry and soil conditions are indicated in Table 8.2. It should be noted that anchor geometry are simplified according to the procedure described previously. Fig. 8.7 and Table 8.2 show the geometry of the original Stevpris 68.6 kN.

Table 8.2 Anchor geometry and soil condition for Stevpris 68.6 kN

Property	Value
Anchor weight, W_a(kN)	68.6
Shank length, L_s(m)	4.485
Shank width, W_s(m)	3.93
Fluke length, L_f(m)	3.04
Fluke width, W_b(m)	Varied
Fluke depth, D_f(m)	0.2
Fluke-shank angle, (degree)	50
Anchor line diameter, b(m)	0.89
Surface undrained shear strength, S_{uo} (kPa)	0
Undrained shear strength gradient, S_{ug} (kPa/m)	1.57

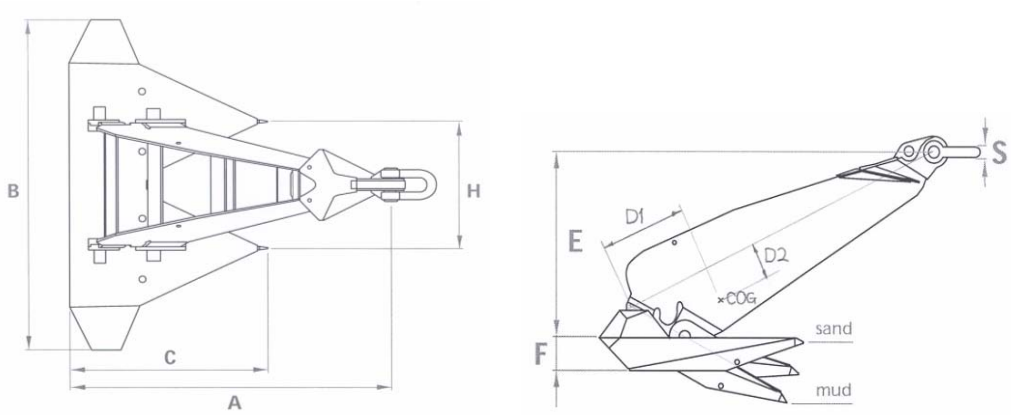

(a) Plane (b) Side

Fig. 8.7 Geometry of Vryhof Stevpris (68.6kN)

Table 8.3 Dimension of Vryhof Stevpris (68.6kN)

Weight (kN)	68.6
A (mm)	4936.
B (mm)	5320.
C (mm)	3028.
E (mm)	2514.
F (mm)	453.7
H (mm)	2055.
T (mm)	825.2
S (mm)	131.8
D_1 (mm)	2704.
D_2 (mm)	554.5
Area (m^2)	9.246

Four tests were conducted on the Stevpris 68.6kN and are shown in Fig. 8.8 and 8.9. These results provide the anchor penetration and mudline load versus horizontal drag distance. Fig. 8.8 shows the trajectory of anchors. We can see from this figure that in some cases the anchor had to be dragged several meters before it set i.e., began to dive. Fig. 8.9 shows relationship of the mudline load versus drag distance for the same set of tests. Test 7-4 was selected for simulation since this data shows the most consistent behavior. It is assumed that anchor is embedded at a point when the anchor is diving at the initial starting point with a 50 degree fluke angles as shown in Fig. 8.10. The sensitivity value for this simulation is assumed to be two. It is assumed that the anchor translates parallel to the bottom of the fluke.

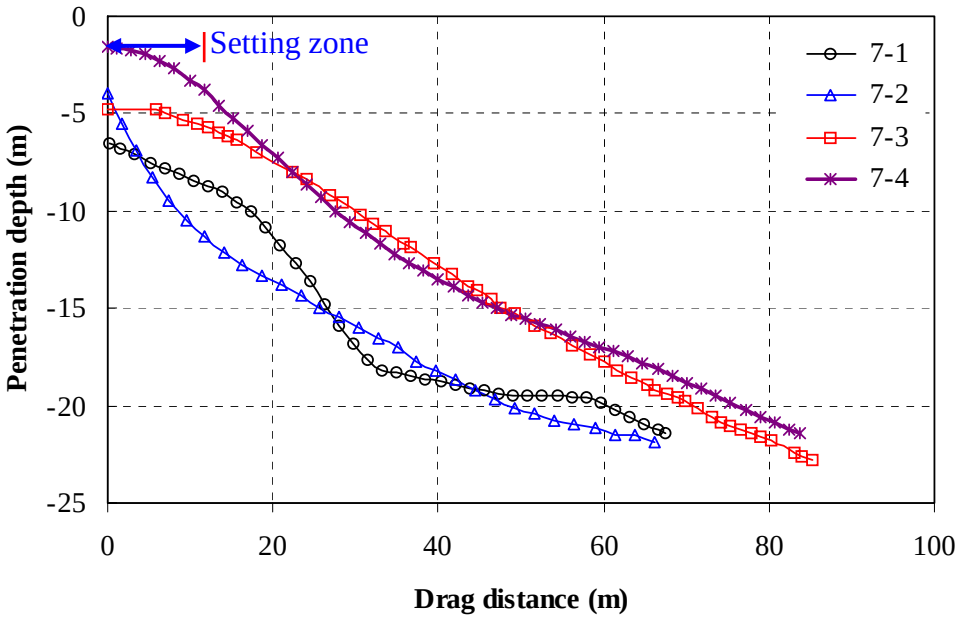

Fig. 8.8 Trajectory curves for Joint Industry Project: Gulf of Mexico 1990 (Vryhof Stevpris 68.6kN)

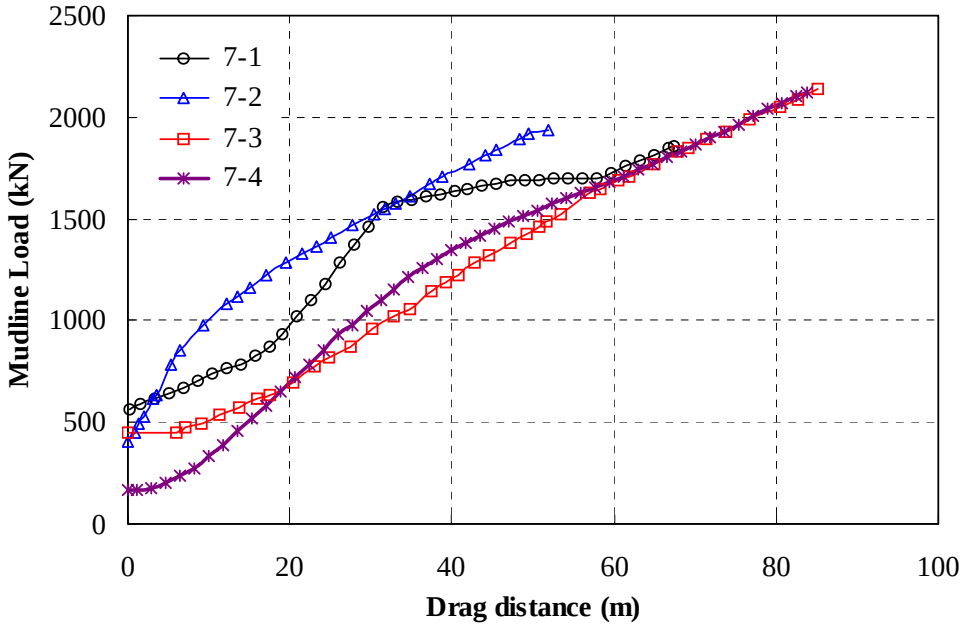

Fig. 8.9 Mudline load vs drag distance curves for Joint Industry Project: Gulf of Mexico 1990 (Vryhof Stevpris 68.6kN)

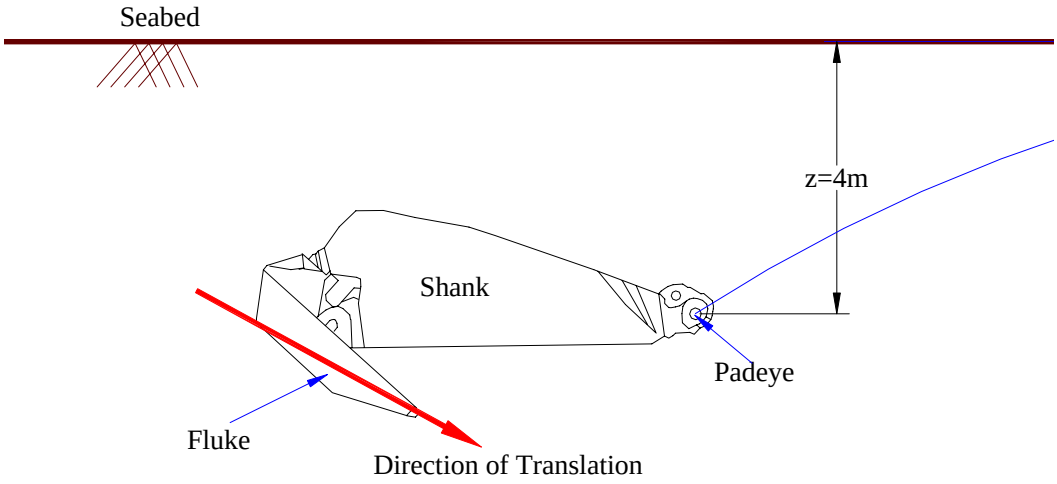

Fig. 8.10 Initial anchor position and direction of the translation

The results of the simulation are shown in Fig. 8.11 and 8.12 with measured data from the field test. As mentioned the measured data is shifted leftward to account for the fact that some drag was needed before the anchor set. Fig. 8.11 suggests that the

actual drag anchor did not penetrate to the ultimate penetration depth possible where the bottom of fluke angle is zero. Mudline load versus drag distance is shown in Fig. 8.12. From this comparison, we can see that the UBM simulation matches the field test data very well.

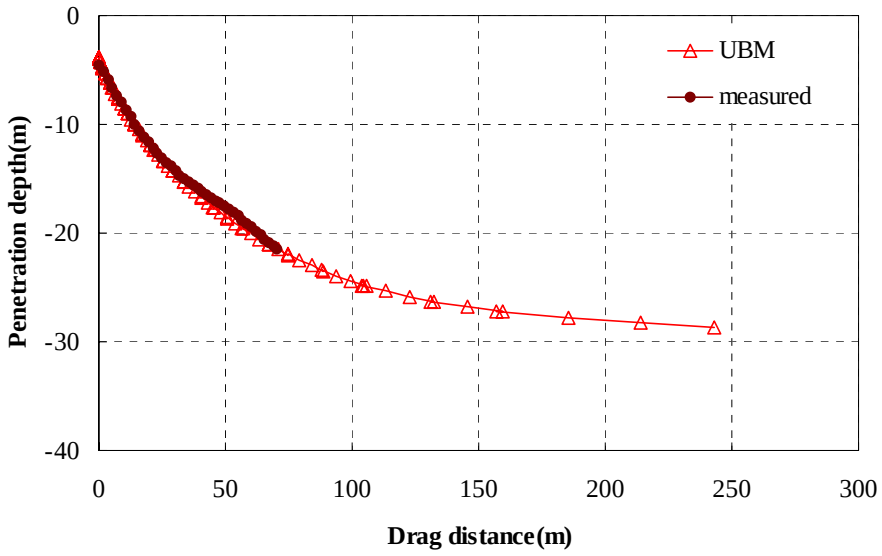

Fig. 8.11 Penetration depth vs. drag distance of Joint Industry Project

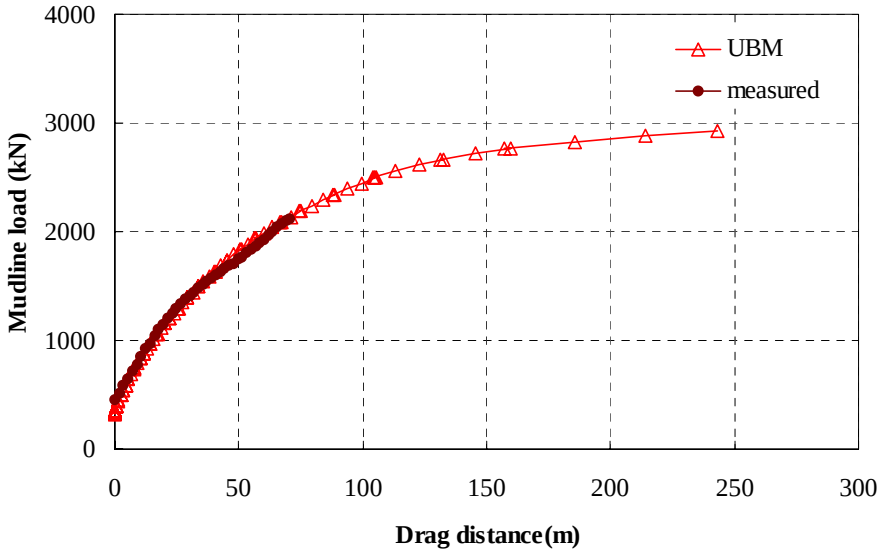

Fig. 8.12 Mudline load vs. drag distance of Joint Industry Project

8.2.2 Liuhua 11-1 field at South China Sea in 1996

The tests reported here were conducted in the Liuhua 11-1 field that is located 70km southeast of Hong Kong, in the South China Sea. These tests were carried out in 1996 by a contractor to Amoco. The Bruce FFTS MK4 anchors were tested in soft clay using a catenary mooring system. The anchor geometry and soil conditions are summarized in Table 8.4. It should be noted that these values are simplified for simulation.

Table 8.4 Anchor geometry and soil condition for Liuhua 11-1 field

Property	Value
Anchor weight, W_a(kN)	392
Shank length, L_s(m)	8.6
Shank width, W_s(m)	7.2
Shank depth, W_b(m)	0.2
Fluke length, L_f(m)	5.37
Fluke width, W_b(m)	varied
Fluke depth, D_f(m)	0.3
Fluke-shank angle, θ_{fs} (degree)	50
Anchor line diameter, b(m)	0.086
Surface undrained shear strength, S_{uo}(kPa)	0
Undrained shear strength gradient, S_{ug}(kPa/m)	1.6

Fig. 8.13 shows the anchor deployment for the floating production systems. The water depth is approximately 300m. Fig. 8.14 shows the dimension of the prototype anchor. Fig. 8.15 shows the penetration depths versus drag distance for the eleven anchors in the FPS system. Fig. 8.16 shows mudline load versus drag distance of Liuhua 11-1 field.

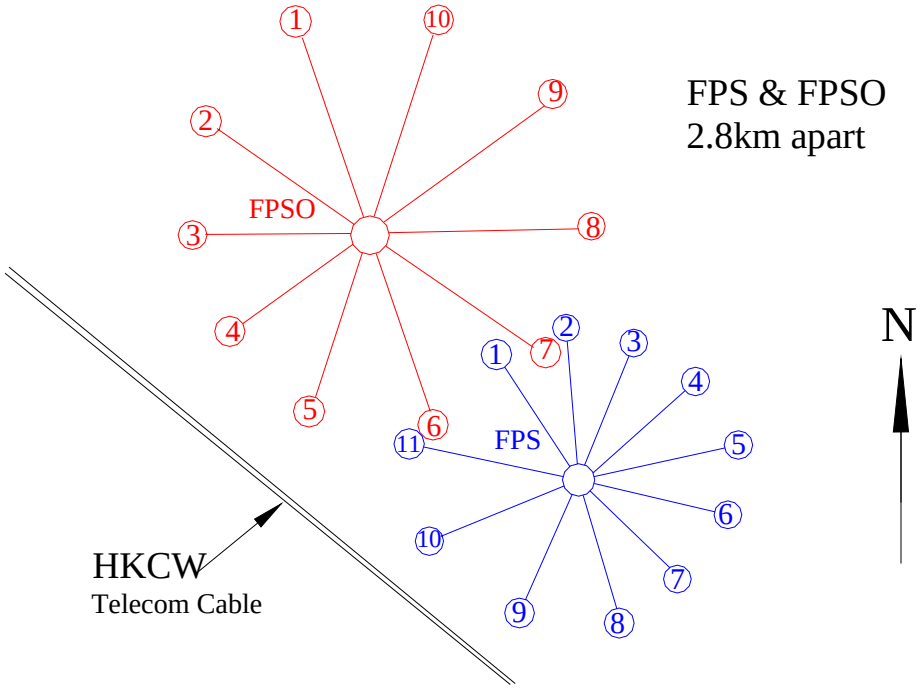

Fig. 8.13 Location and deployment of anchors for Liuhua 11-1 field

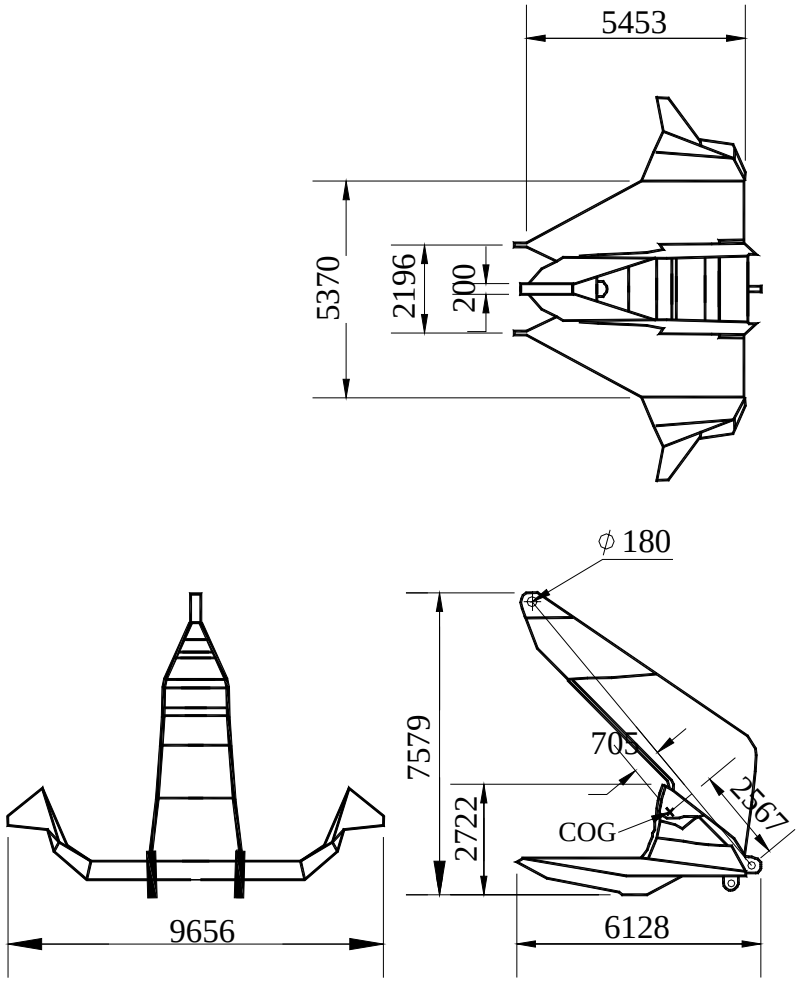

Fig. 8.14 Dimensions of Bruce FFTS MK4(unit: mm)

The penetration depth and drag distance values for the tests are summarized in Table 8.5. As indicated the range of penetration depths are from 9.8 to 14.3m and drag distance are from 19.8 to 30.5m.

Table 8.5 Results of test for Liuhua 11-1 field

Anchor line No.	FPS Mooring System Anchors		
	Line Load (kN)	Depth (m)	Drag distance(m)
1	5400	12.5	25.9
2	5449	12.5	25.9
3	5615	13.1	27.4
4	5811	13.7	29
5	5674	13.1	27.4
6	6037	14.3	30.5
7	4586	9.8	19.8
8	4567	9.8	19.8
9	5263	11.9	24.4
10	5527	12.8	27.4
11	4557	9.8	19.8

In the simulation, the initial fluke angle of the drag anchor is assumed to be 24 degrees by observation of measured data. Fig. 8.15 shows the penetration depth versus drag distance. The simulation indicates that the drag anchor penetrates at its initial orientation through the extent of the measured data as shown in Fig. 8.15. Fig. 8.16 shows the predicted mudline load versus drag distance. The measured data are located in closely below the curves with sensitivity of 1.0.

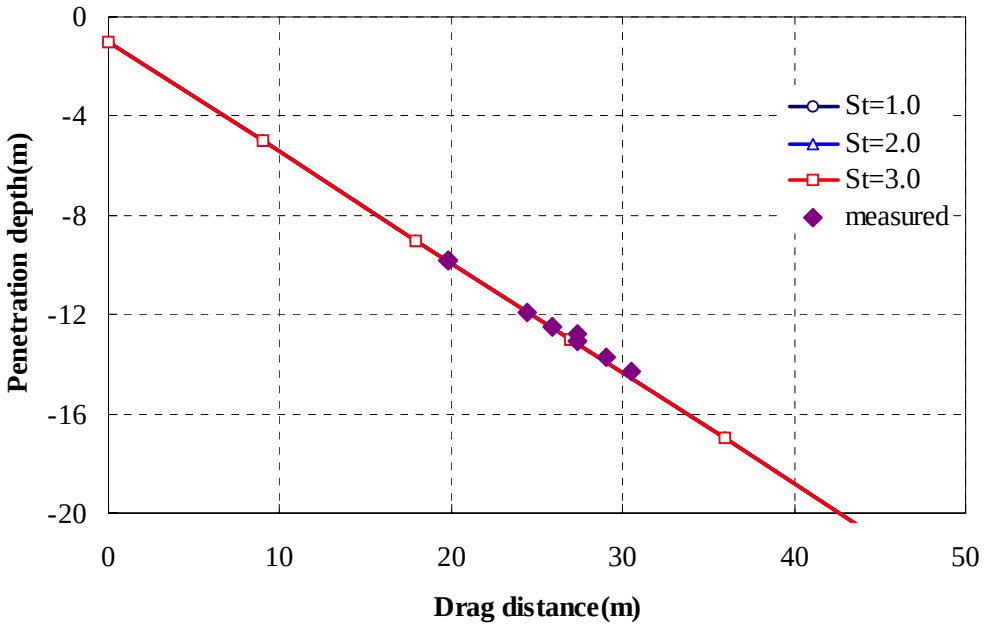

Fig. 8.15 Penetration depth vs. drag distance of Liuhua 11-1 field

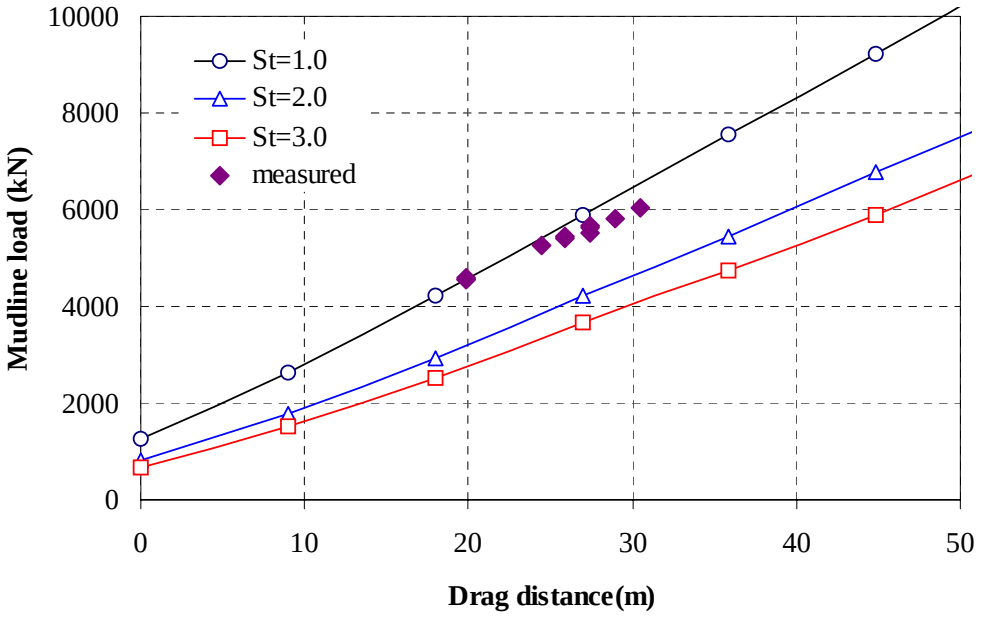

Fig. 8.16 Mudline load vs. drag distance of Liuhua 11-1 field

8.2.3 P-13 in offshore Brazil in 1997 - Denla MK3 (63.7 kN)

The tests reported here were conducted at the P-13 Site, Offshore Brazil (643m), in 1997 by a contractor to Petrobras. The Bruce Denla MK3 anchors were tested in soft clay using a taught leg mooring system. Initial starting point and anchor orientation are assumed as shown in Fig. 8.17. The details of the drag anchor, anchor line and undrained soil strength conditions are summarized in Table 8.6. The range of water depths at the site is from 588m to 643m. Fig. 8.18 shows the detailed dimensions of the Bruce Denla MK3 anchor. It should be noted that the reported anchor geometry has been simplified for simulation.

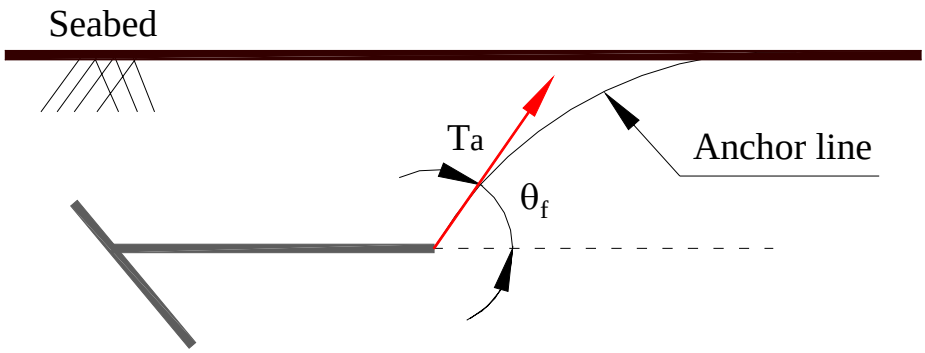

Fig. 8.17 Initial anchor position and orientation for P-13 tests

Table 8.6 Simplified anchor geometries and soil condition for P-13 tests

Property	Value
Anchor weight, W_a(kN)	63.7
Shank length, L_s(m)	4.75
Shank width, W_s(m)	0.1
Shank depth, D_s(m)	0.34
Fluke area (m^2)	10
Fluke length, L_f(m)	4
Fluke width, W_b(m)	Varied
Fluke depth, D_f(m)	0.4
Fluke-shank angle, θ_{fs} (degree)	50
Anchor line diameter, b(m)	0.086
Surface undrained shear strength, S_{uo}(kPa)	0
Undrained shear strength gradient, S_{ug} (kPa/m)	1.6

The example measured penetration data are shown in Fig. 8.19 along with the results of the simulation. From this figure we can see that the measured data are well matched by the simulation regardless of sensitivity value. The simulation shows that in the beginning of trajectory, the penetration versus drag distance curves virtually overlap each other. Since there is no measured data on anchor capacity in this test series we can not compare results of simulation with measured data for that aspect of behavior. The mudline load simulation results are shown in Fig. 8.20. As the sensitivity value increases, the mudline load decreases even though the depth is basically the same.

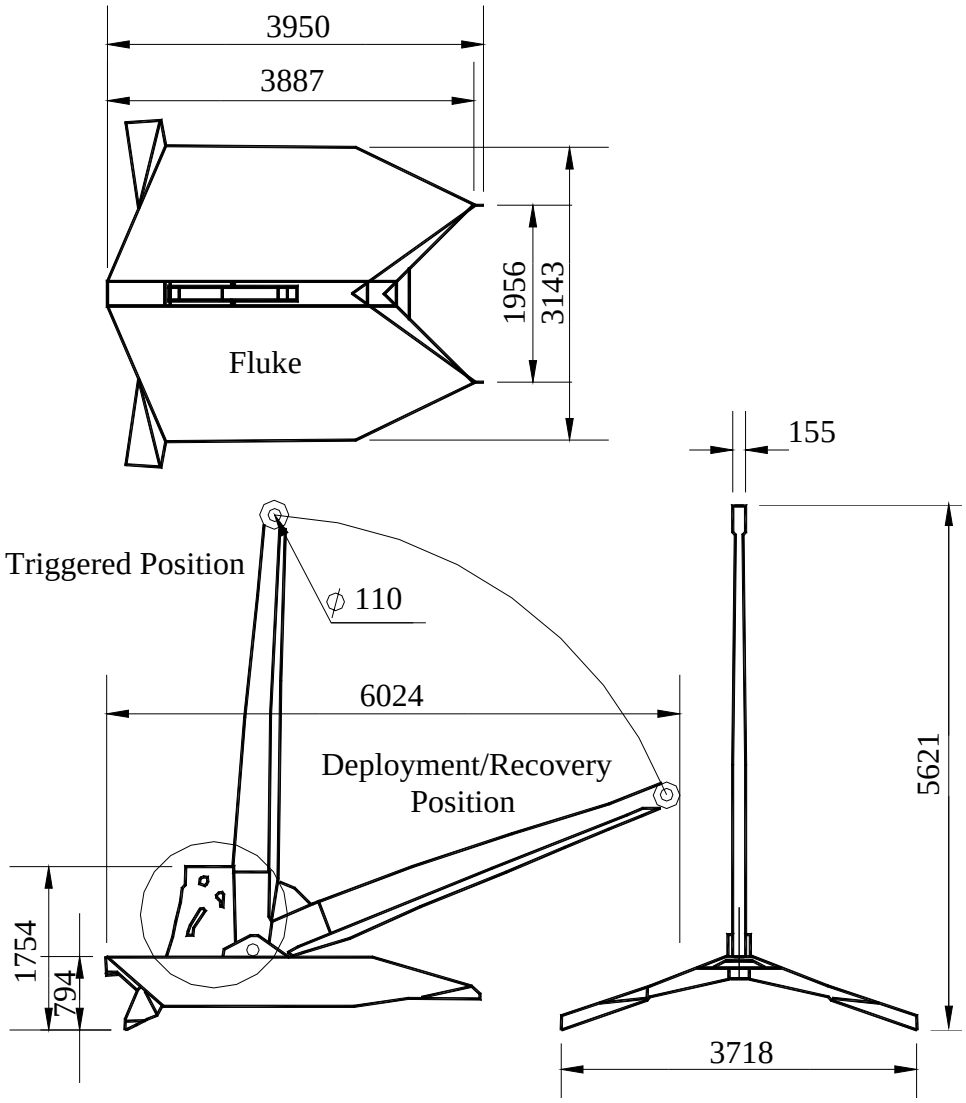

Fig. 8.18 Dimensions of Bruce Denla MK3 for P-13 Tests

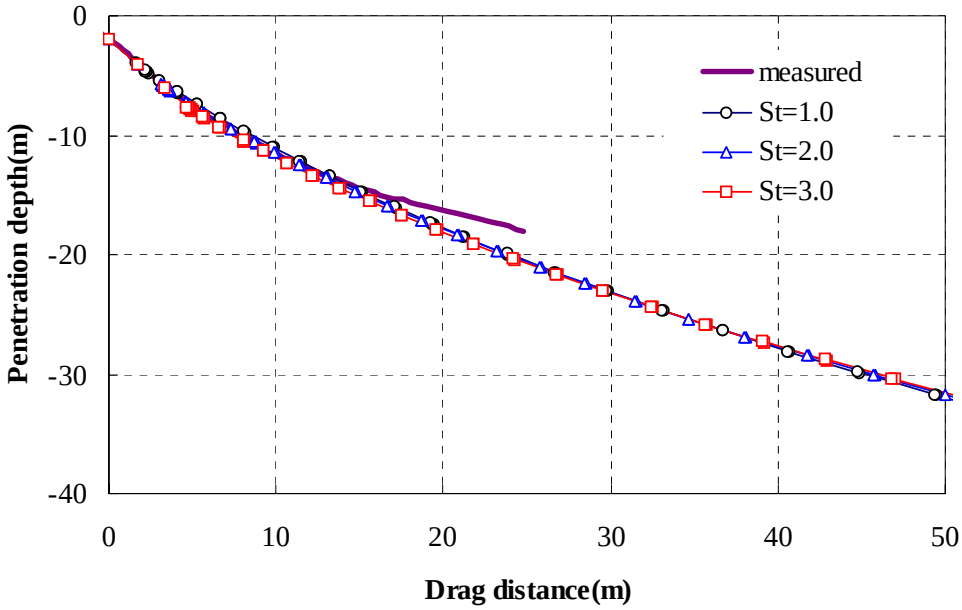

Fig. 8.19 Penetration depths vs. drag distance (Offshore Brazil "P-13" 1997)

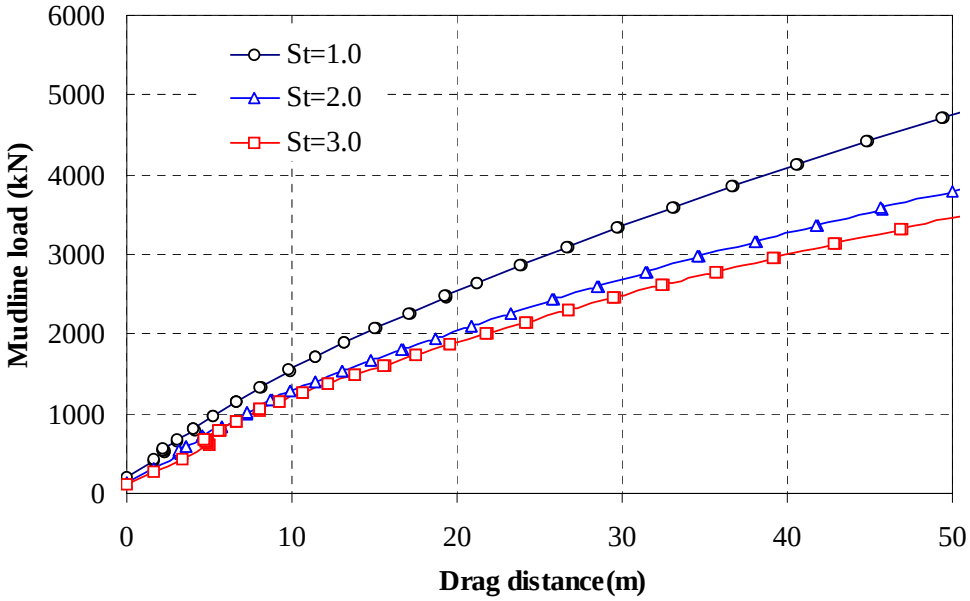

Fig. 8.20 Mudline load vs. drag distance (Offshore Brazil "P-13" 1997)

8.2.4 South Timbalier Block 295 in the Gulf of Mexico - Denla MK2

Large scale anchor tests were carried out in South Timbalier Block 295 in the Gulf of Mexico by Aker Maritime Contractors in 1996 as part of a Joint Industry Project. The water depth was measured 91m. A Bruce Denla MK2 anchor was tested in soft clay using a taut leg mooring system. The angle between the fluke and shank axes is estimated 65 degrees during installation. Test results provide the anchor penetration and deck tension load versus horizontal drag distance for the test. The anchor line forces at the seabed are estimated to be approximately 15kN less than deck loads.

Table 8.7 Simplified anchor geometry and soil condition for Timbalier Block 295

Property	Value
Anchor weight, W_a(kN)	12.74
Shank length, L_s(m)	3.0
Shank width, W_s(m)	0.24
Shank depth, D_s(m)	0.1
Fluke area (m^2)	4.58
Fluke length, L_f(m)	2.5
Fluke width, W_b(m)	varied
Anchor line diameter, b(m)	0.073
Surface undrained shear strength, S_{uo} (kPa)	0
Undrained shear strength gradient, S_{ug}(kPa/m)	1.6

Table 8.7 gives the simplified anchor geometry and undrained soil strength conditions used in the simulation. Fig. 8.21 shows the detailed dimensions of the Bruce Denla MK2 anchor.

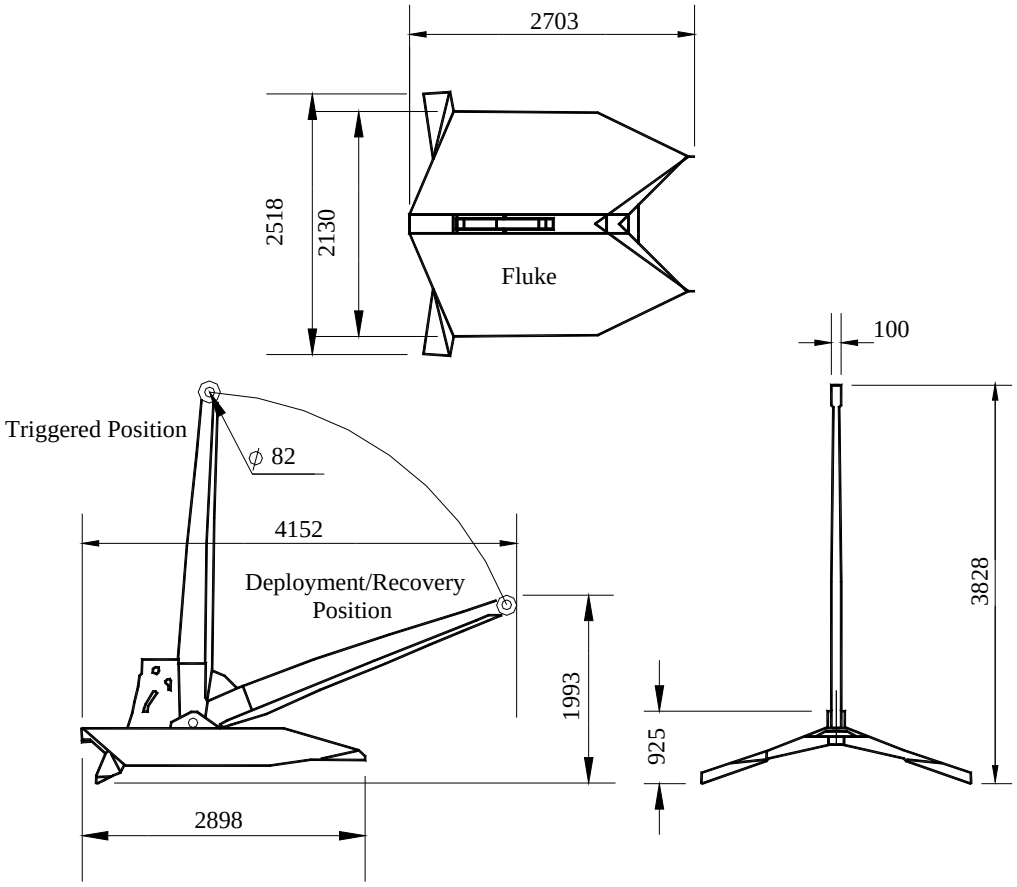

Fig. 8.21 Dimensions of Bruce Denla MK2 for Timbalier Block 295

Fig. 8.22 shows the example trajectory curve of test. As can be seen in this diagram the curve is not a typical anchor trajectory curve. At the beginning of the installation the anchor appears to be in a transition mode prior to setting for penetration. After 5m penetration anchor likely penetrates with its initial orientation. The initial fluke angle of the anchor is estimated to be approximately 25 degrees consistent with a trajectory along the fluke as shown in Fig. 8.22. The depth data after a drag distance of 60m does not seem to make sense and appears questionable. According to the Fig. 8.22, the initial anchor depth is taken as 5m and the initial fluke angle is taken 25 degree in the simulation. To compare the simulation with measured data, the measured data are shifted to leftward to fit an initial depth of 5m to compensate for the drag distance required to set the anchor. Results of the simulations are shown in Fig. 8.23 and 8.24 compared with measured data. Fig. 8.23 shows the line load at the seabed versus drag distance. As the anchor drag distance increases, the anchor line tension load at the mudline increases linearly as shown in this figure. As can be seen in Fig. 8.23, the results of simulation of the trajectory agree well with the measured data regardless of sensitivity value in 40m of drag distance. For the same reason the mudline load curves are shifted leftward to fit the initial depth of 5m. As can be seen in Fig. 8.24 the simulation matches the mudline load sensitivity value of 3.0, a reasonable value for typical GOM soft clays.

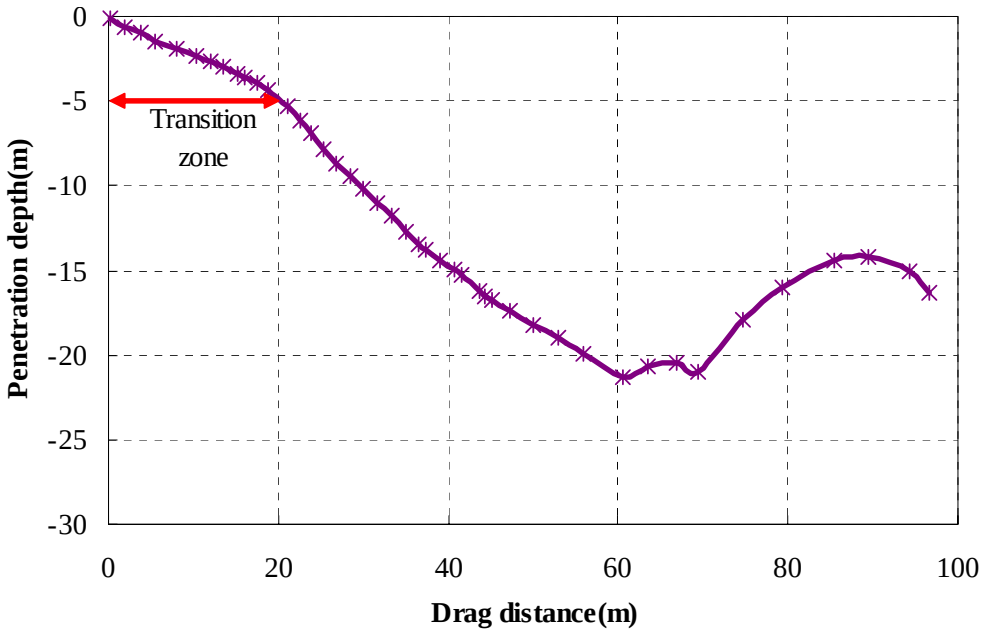

Fig. 8.22 Measured trajectory of Bruce Denla MK2 at South Timbalier Block 295

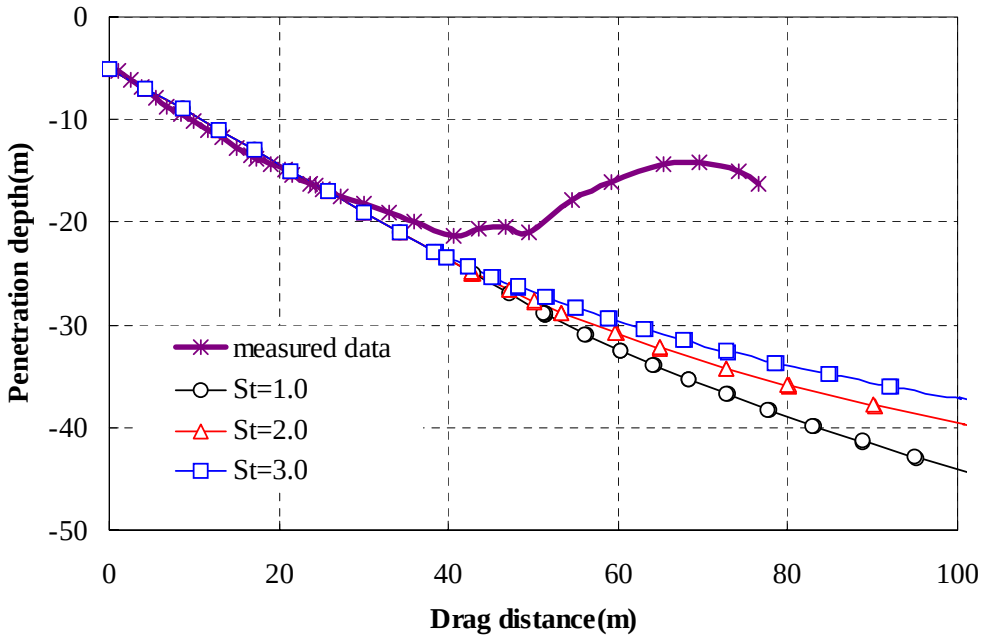

Fig. 8.23 Penetration depths vs. drag distance for South Timbalier Block 295

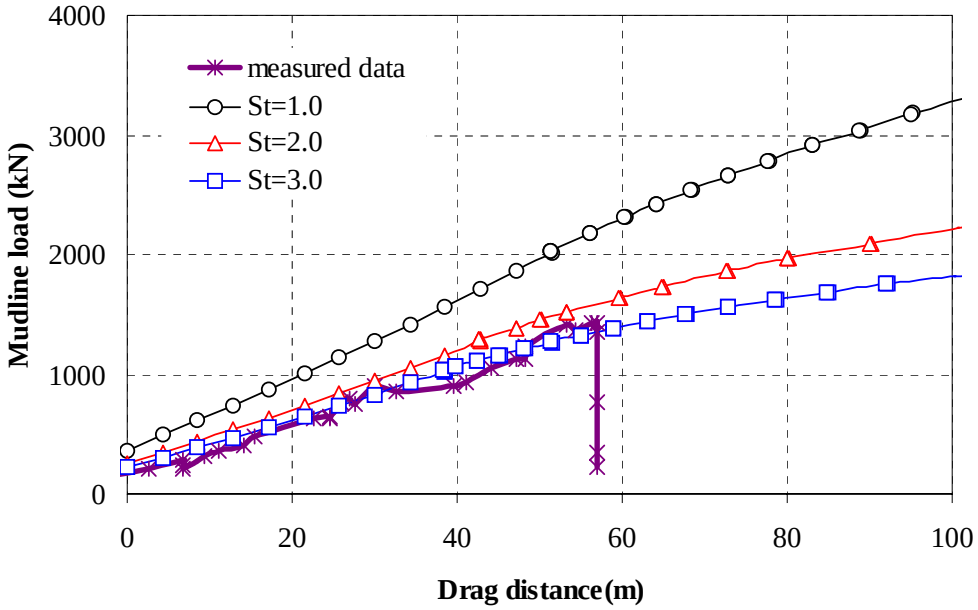

Fig. 8.24 Mudline laod vs. drag distance for South Timbalier Block 295

8.2.5 South Timbalier Block 295 in the Gulf of Mexico - Stevmanta 32kN

A large scale anchor test was conducted in the Gulf of Mexico at South Timbalier Block 295 by Aker Maritime Contractors in 1996 as part of a Joint Industry Project. The water depth at this site is 91m. A Vryhof Stevmanta anchor was tested in soft clay using a taut leg mooring system. The simplified anchor geometry details and soil conditions are given in Table 8.8. Fig. 8.25 shows the detailed dimensions of the prototype anchor.

Table 8.8 Anchor geometry and soil condition for South Timbalier Block 295

Property	Value
Anchor weight, W_a(kN)	31.16
Shank length, L_s(m)	3.98
Fluke length, L_f(m)	2.5
Fluke width, W_b(m)	Varied
Fluke depth, D_f(m)	0.1
Fluke-shank angle, θ_{fs} (degree)	45
Anchor line diameter, b(m)	0.073
Surface undrained shear strength, S_{uo}(kPa)	0
Undrained shear strength gradient, S_{ug}(kPa/m)	1.6

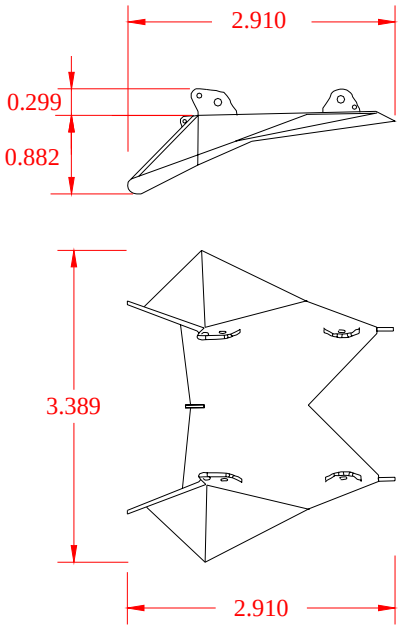

Fig. 8.25 Dimensions of Vryhof Stevmanta (32kN) for South Timbalier Block 295

Test results include the deck tension load versus horizontal drag distance. On average anchor line tension loads at seabed are estimated to be approximately 15kN less than deck loads. In this test continuous penetration data are not available for installation but a single point was measured giving the penetration depth 24m at a drag distance of 55m. To compare the measured data with results of the simulation, the measured data is shifted leftward 10m of drag distance to account for anchor settling. It should be noted that the amount of shifted drag distance is determined by trial and error. For the same reason the mudline load of measured data is shifted leftward.

Fig. 8.26 shows the penetration depth versus drag distance. As shown in this figure, the trajectory point of measured data is close to but slightly below the curve for sensitivity of 1.0. Fig. 8.27 shows the shifted mudline load versus the drag distance. The measured data is below the curve for sensitivity of three at the beginning of the penetration. However, during the penetration the measured curve approaches the curve with sensitivity of two.

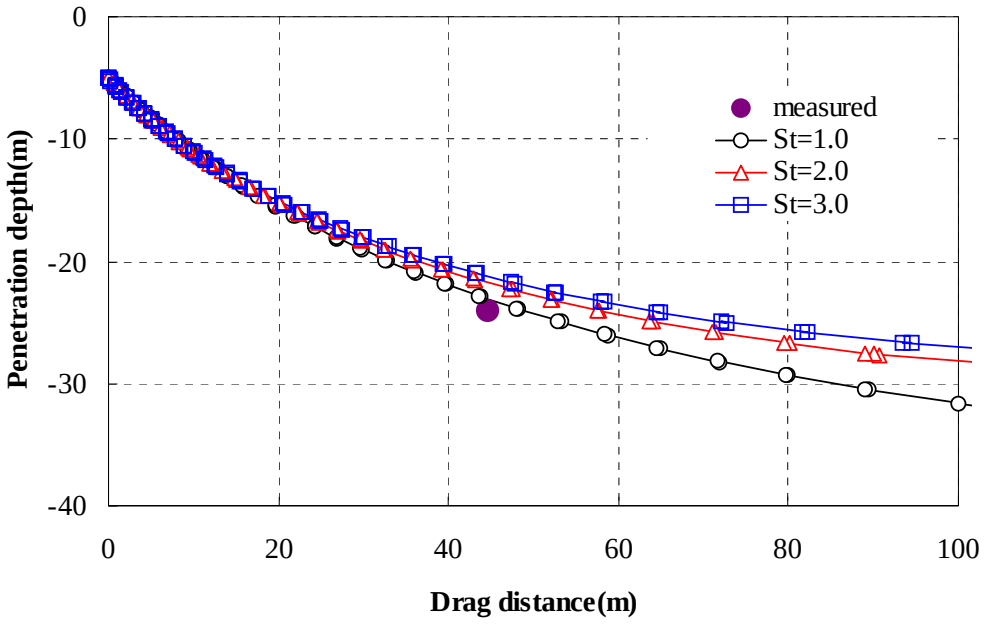

Fig. 8.26 Penetration depth vs. drag distance for South Timbalier Block 295

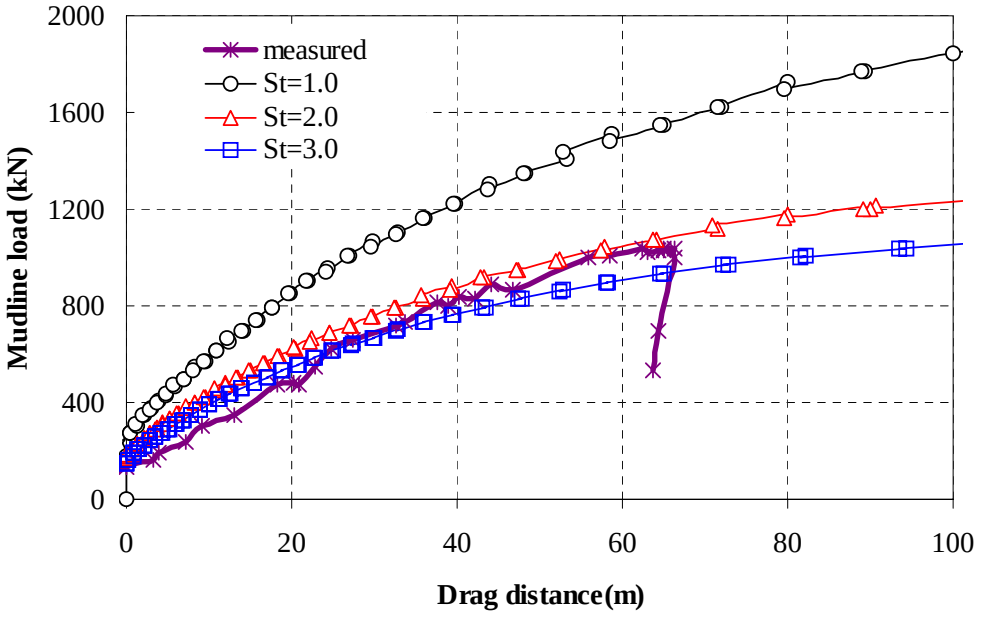

Fig. 8.27 Mudline load vs. drag distance for South Timbalier Block 295

8.2.6 Voador P-27, Campos basin offshore Brazil - Vryhof Stevmanta 102kN

A large scale anchor test was conducted at the Voador site, Campos basin P-27 by Petrobras in April 1998. The water depth at this site is from 510 to 570m. Vryhof Stevmanta anchors were tested in soft clay using a taut leg mooring system with 12 lines. Test results include the installation load and penetration depth at the special shackle versus horizontal drag distance. The special shackle is broken when the anchor line load reaches the expected load. Thus, anchor mode is converted from the translation mode to the vertical loading mode. In this test continuous measurements were not recorded but 12 data points of installation depth and installation load were measured for each mooring line. Fig. 8.28 shows the geometry of the Vryhof Stevmanta that used in these tests and Table 8.9 shows the dimensions of it. The anchor geometry and soil conditions for simulation are detailed in Table 8.10. Table 8.11 shows the data measured during installation. It should be noted that the anchor capacities shown in Table 8.11 were determined by the actual break load of the special shackle.

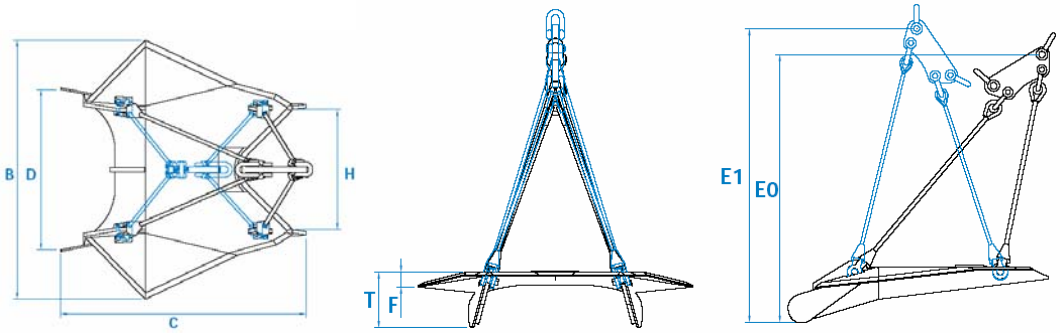

Fig. 8.28 Dimensions of Vryhof Stevmanta (102kN) for Campos basin P-27

Table 8.9 Dimension of Stevmanta (102 kN) for Campos basin P-27

Weight (kN)	102
B(mm)	4657
C (mm)	4410
D (mm)	2882
E_0 (mm)	4557
E_1 (mm)	4995
F (mm)	255
H (mm)	2162
T (mm)	948

Table 8.10 Anchor geometry and soil condition for Campos basin P-27

Property	Value
Anchor weight, W_a(kN)	102
Shank length, L_s(m)	5.0
Fluke area, m^2	11
Fluke length, L_f(m)	3.73
Fluke width, W_b(m)	varied
Fluke depth, D_f(m)	0.25
Fluke-shank angle, θ_{fs} (degree)	50
Anchor line diameter, b(m)	0.102
Surface undrained shear strength, S_{uo}(kPa)	5
Undrained shear strength gradient, S_{ug}(kPa/m)	2.0

Table 8.11 Installation of drag anchors

Mooring Line No.	Anchor capacity, F (kN)	Penetration Depth (m)	Drag Length (m)
1	3234	23.3	54.1
2	3097	26.1	52
3	2470	21.5	36.7
4	2470	22.9	37.2
5	2930	23.4	49.5
6	3156	24.9	49.2
7	2793	24.9	58.9
8	2724	21.5	35.4
9	2685	22.3	46.6
10	2822	25.1	39.3
11	2617	22.8	46.1
12	2646	23.2	37.6

Anchors are arranged as shown in Fig. 8.29. Fig. 8.30 shows a schematic of the mooring line system for P-27.

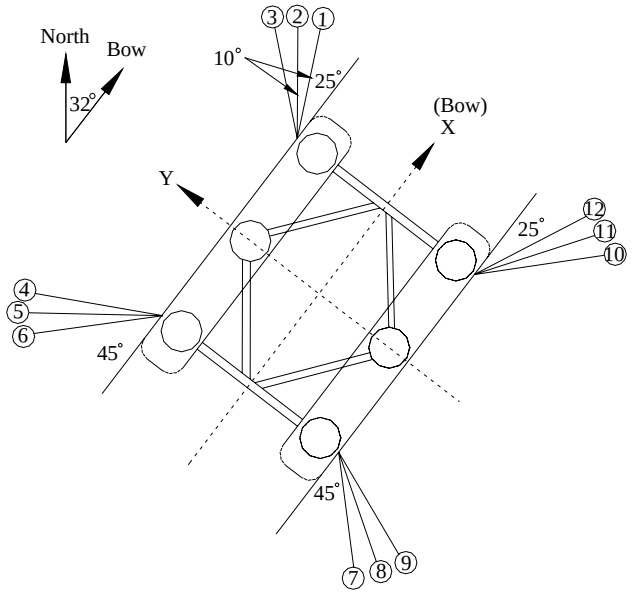

Fig. 8.29 Mooring arrangement for Campos basin P-27

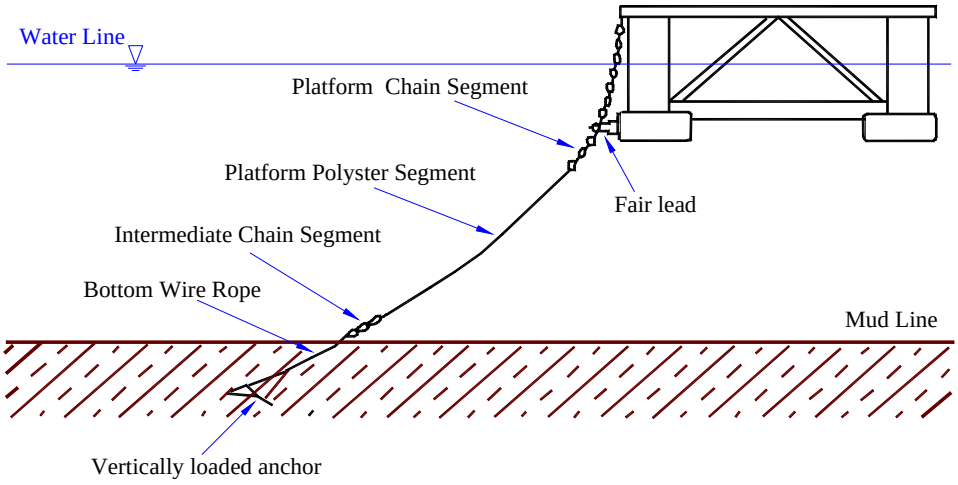

Fig. 8.30 Mooring line system for Campos basin P-27

To simulate this anchor, the initial fluke angles of the anchors were assumed to be 25 degrees with soil sensitivity values assumed to be between 2 and 4. Fig. 8.31 shows penetration depths versus drag distance for the simulation and the measured data. As shown in this figure the results of the simulation match field data very well. As in the previous study, soil sensitivity variation does not affect penetration depth in this range of penetration. The simulation shows that the anchor maintains its initial orientation within the range of the measured data. The initial fluke angles are varied from 20 degree to 30 degree in Fig. 8.31 showing the significant affect of the initial anchor orientation. Fig. 8.32 shows the anchor capacity at the shackle versus drag distance. According to this figure, the prediction assuming a sensitivity value of two is an upper bound of the measured data and the curve assuming a sensitivity value of four is the best prediction.

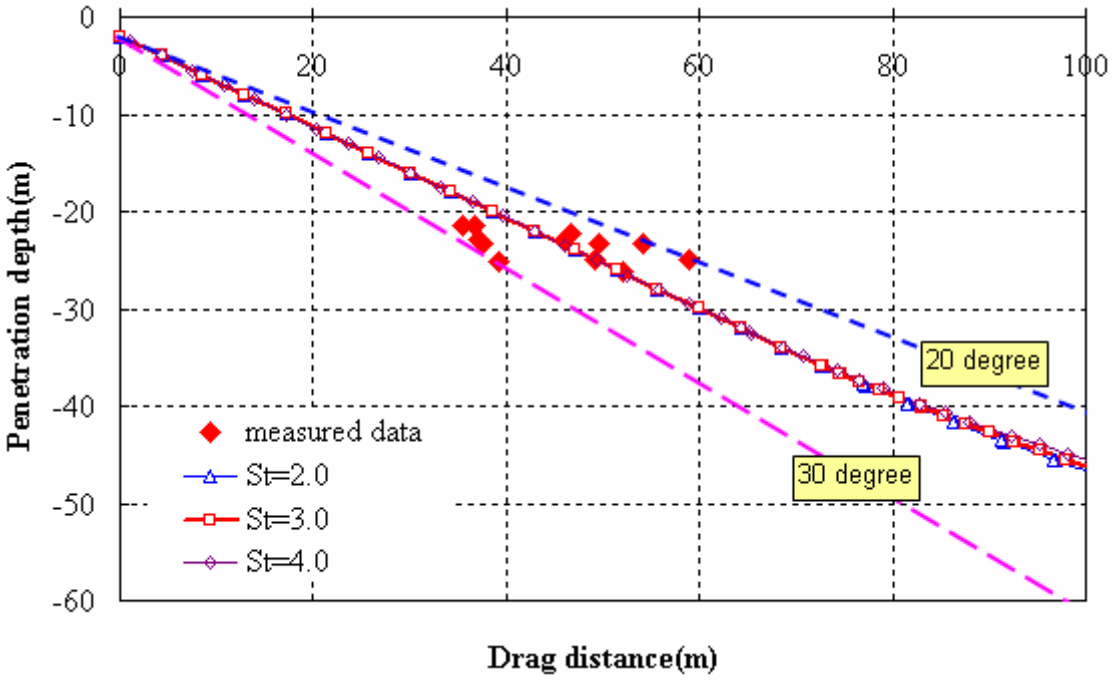

Fig. 8.31 Penetration vs. drag distance for Campos basin P-27

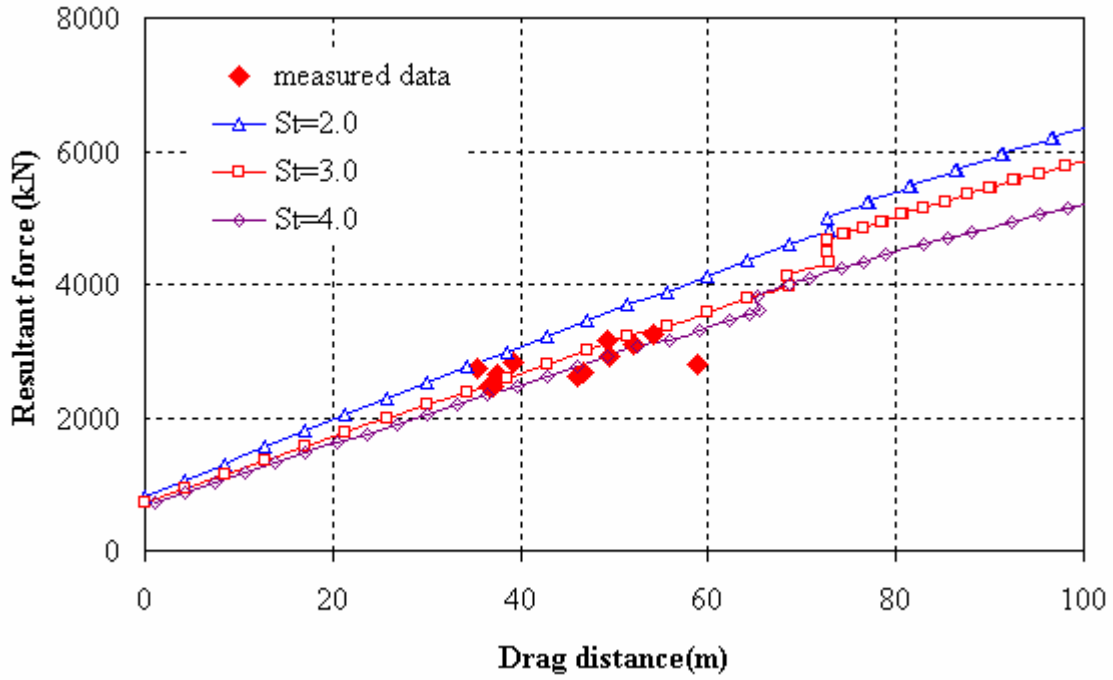

Fig. 8.32 Resultant force at shackle vs. drag distance for Campos basin P-27

8.3 Comparison of UBM simulation as design chart estimates

8.3.1 Stevpris of Vryhof

The design charts provided by Vryhof anchor as discussed in Chapter III are used for this comparison. For these purposes the Stevpris MK5 is selected for comparisons. Fig. 8.33 and Table 8.12 show a schematic and provide detailed dimensions of the Stevpris drag anchor, respectively. Again the anchor is simplified for simulation by procedure that is mentioned in Section 8.1.1.

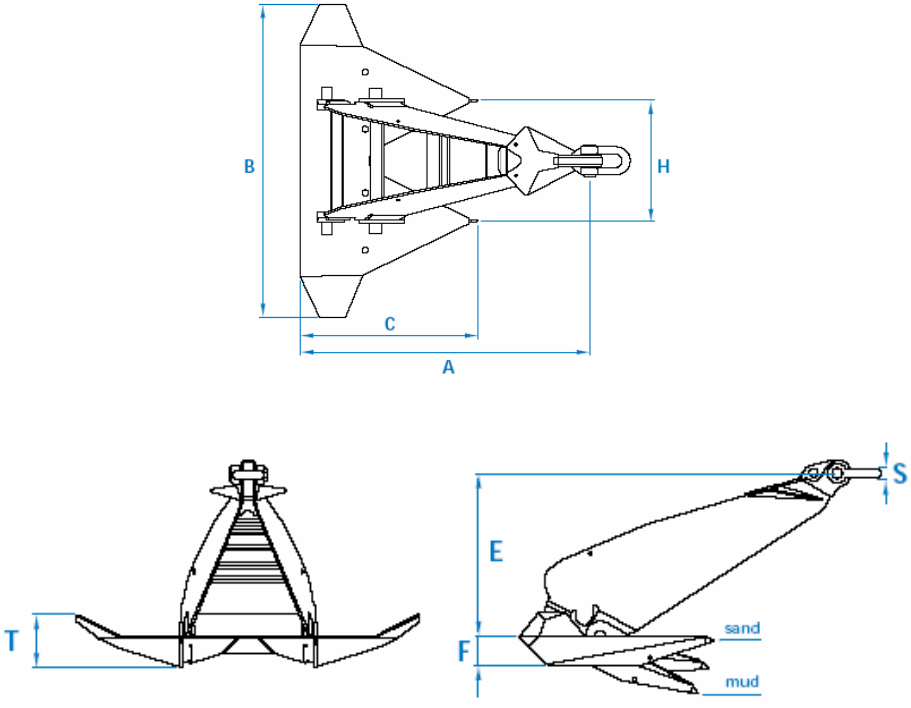

Fig. 8.33 Stevpris of Vrhyhof anchor

Table 8.12 Main dimensions Stevpris MK5 (unit: mm)

Weight	Nominal Dimensions (in mm)							
(kg)	A	B	C	E	F	H	T	S
5000	4412	4756	2707	2248	406	1837	738	110
10000	5559	5992	3410	2832	511	2315	929	140
15000	6364	6860	3904	3242	585	2650	1064	170
20000	7004	7550	4297	3569	644	2917	1171	190
30000	8018	8643	4919	4085	737	3339	1341	220
65000	10375	11184	6365	5286	954	4321	1736	300

According to Vryhof (1999), the Stevpris MK5 design curve shown in Fig. 8.34 represents anchor performance in very soft clays. Its design curve is based on the following nominal conditions. The undrained shear strength is 4kPa at the seabed with a strength gradient of 1.5kPa per meter depth. The relationship is described by the equation $s_u = 4 + 1.5 \times z$ with S_u in kPa and z the depth in meters below seabed. The sensitivity of the soil is taken as 2.0 since results of UBM and field test data are well matched in that case. The anchor lines are considered as wire and their diameter are 0.076m, 0.121m and 0.151m, respectively. The initial anchor position is at a depth of 2m and the shank is parallel to seabed. Fig. 8.34 shows simulation results for the three different anchor lines and the design curve indicated with dashed line by Vryhof anchor (1999).

According to the results of the simulation, as the diameter of the anchor line decreases, the ultimate resultant forces at the shackle increases. The reason for this is that for the small lines the anchor dives to a greater depth. The design chart is therefore more conservative as anchor line size decreases. There are a number of considerations in applying the design curves, for example, a small anchor penetrates to the ultimate penetration depth at a shorter drag distance than a larger anchor.

Fig. 8.35 shows the ultimate penetration depth versus size of the anchor on a log-log scale. As can be seen in this figure, the ultimate penetration depth has a linear relationship with anchor size on a log-log scale (power law relationship). We also see that the smaller diameter anchor line results in deeper penetration.

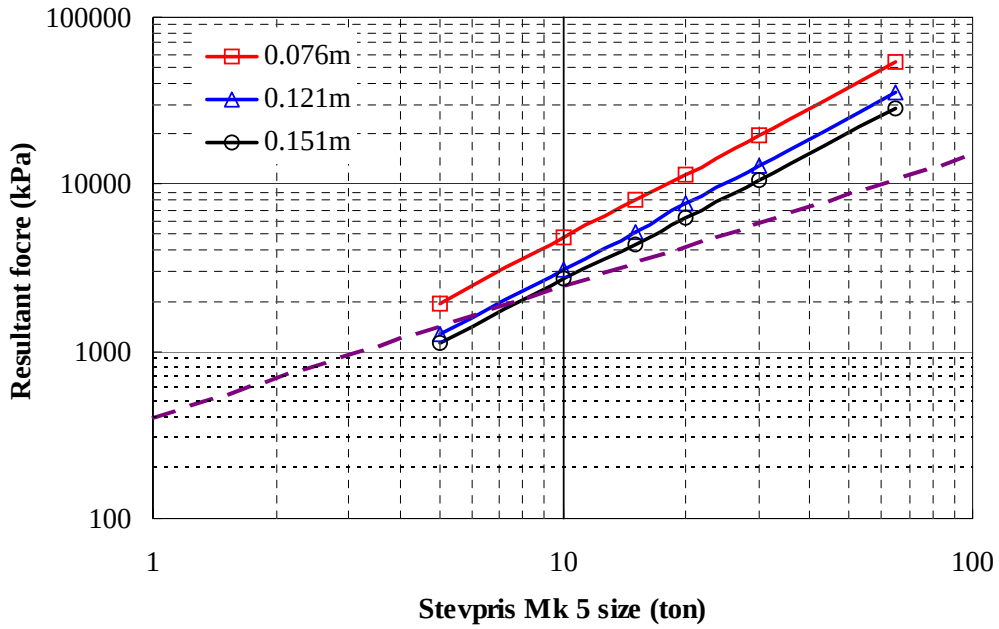

Fig. 8.34 UHC chart for Stevpris MK5

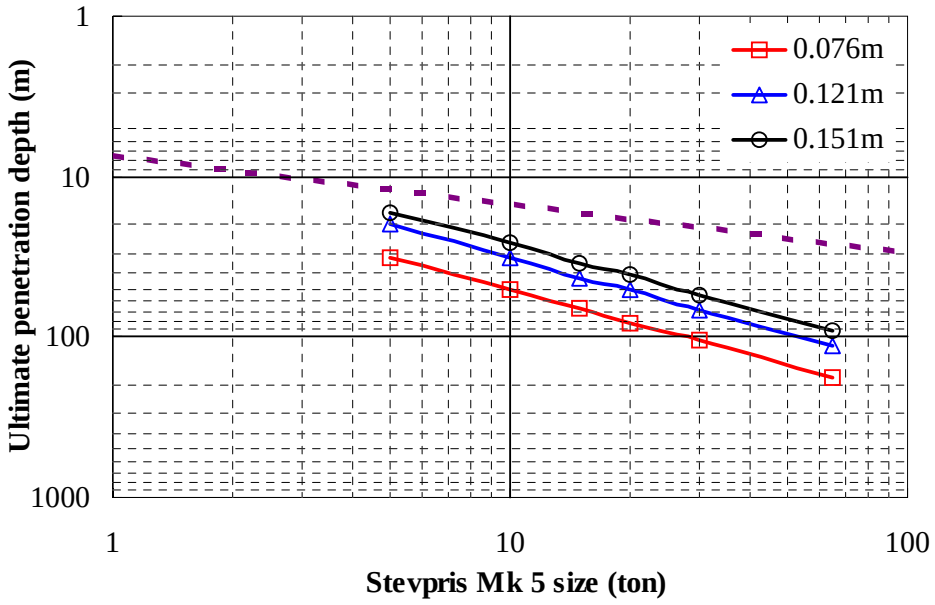

Fig. 8.35 Ultimate penetration depth vs. weight of Stevpris MK5

8.3.2 Bruce FFTS Mk 4 anchor

The design charts provided by Bruce anchor were discussed in Chapter III in detail. For this study the Bruce FFTS MK4 anchor is selected for comparison with simulation. Fig. 8.36 and Table 8.13 show the schematic and detailed dimensions of the Bruce FFTS MK4 drag anchor, respectively.

The Bruce FFTS MK4 design curves for very soft clay are shown in Fig. 8.37. The undrained soil strength is assumed to be zero at the seabed and it increases by 1.57kPa/m, i.e., it can be described by equation $S_u = 1.57 \times z$ with S_u in kPa and z being the depth in meters below seabed.

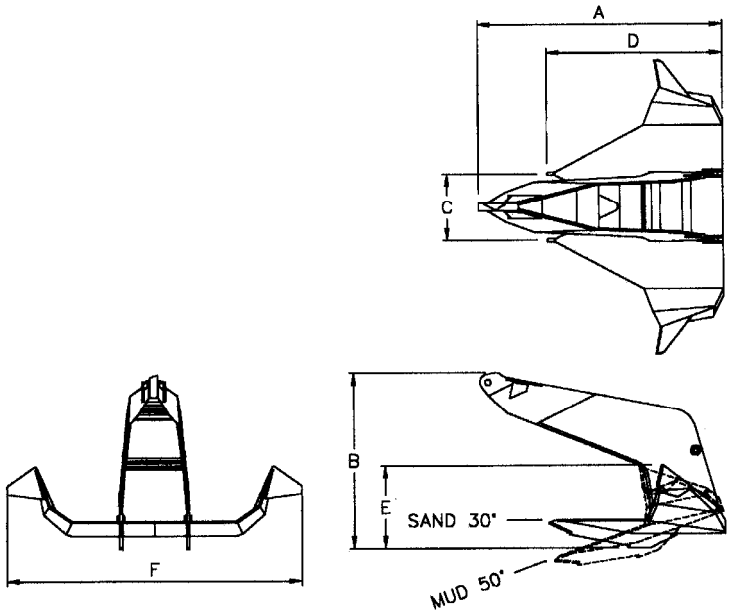

Fig. 8.36 Schematic of Bruce FFTS MK 4 anchor

Table 8.13 Dimension of Bruce FFTS MK4

Weight (kg)	Nominal Dimensions (in mm)				
	A	B	C	E	F
500	1827	1280	500	1303	606
1500	2648	1854	723	1888	878
3000	3409	2388	931	2431	1131
5000	4029	2822	1100	2873	1336
9000	4846	3394	1324	3456	1607
10000	5087	3563	1390	3628	1687
12000	5437	3808	1486	3878	1803
15000	5728	4012	1566	4085	1900
18000	6129	4292	1674	4371	2032
20000	6319	4426	1726	4507	2096
30000	7225	5060	1974	5153	2396
40000	8034	5627	2195	5730	2664

To simulate the Burce FFTS MK4 anchor, the anchor geometry is simplified and soil properties given by Bruce Anchor are used. In this simulation the sensitivity of soil is assumed to be 2.0. The anchor lines are assumed to be wire with varying diameters of 0.076m, 0.121m and 0.151m, respectively.

Fig. 8.37 shows the simulation results along with the design curve (dashed line) provided by Bruce Anchor. In the case of very soft clay and with wire anchor line, the design curve equation is HC=46.66($W^{0.92}$) which has power law relationship with anchor size. In this equation, HC means high holding capacity. The other three curves are based on UBM simulation. As the diameter of the anchor line increases, the ultimate resultant forces at the shackle decrease linearly on log-log scale. These results are qualitatively similar for the Stevpris anchor design curves. The design curves are conservative relative to all the simulations.

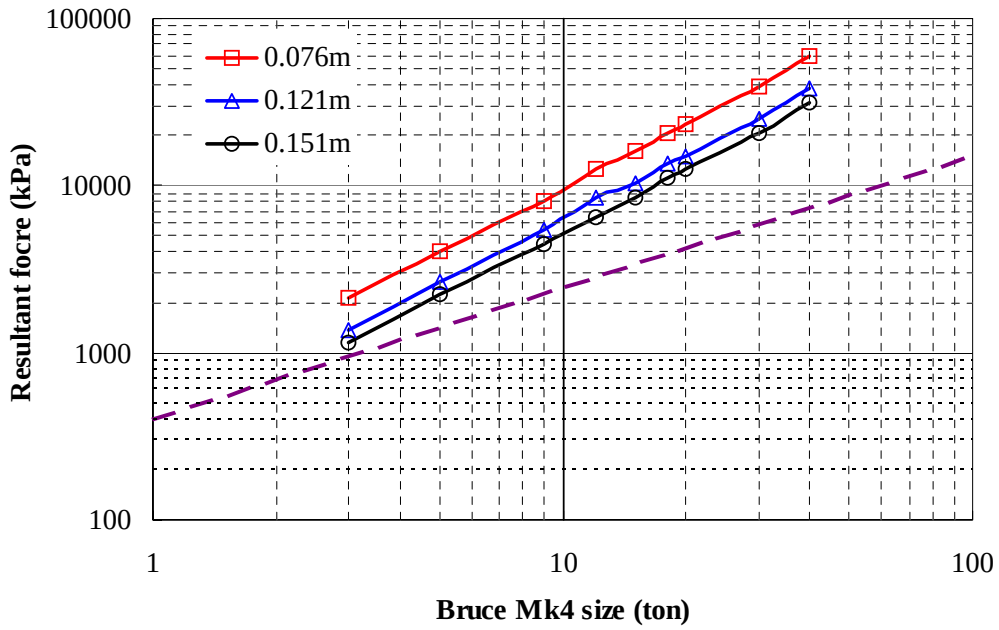

Fig. 8.37 UHC chart for Bruce FFTS MK4

Fig. 8.38 shows the ultimate penetration depth versus anchor size on a log-log scale. As can be seen in this figure, the ultimate penetration depth has power law relationship with anchor size. In addition the smaller diameter anchor line causes the deeper penetration and hence high capacity.

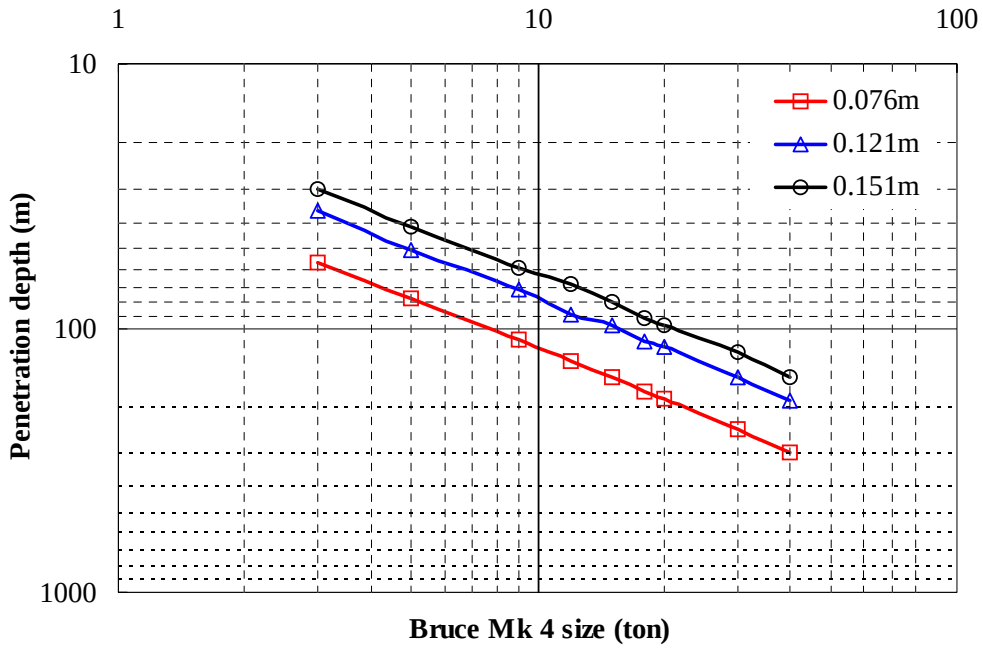

Fig. 8.38 Penetration depth vs. weight of Bruce FFTS MK4

8.4 Comparison of UBM simulation and centrifuge tests

In this section, centrifuge test results are compared with the UBM simulation. Randolph and his coworkers carried out these tests at the University of Western Australia. Fig. 8.39 shows a 1/160 model of a Vryhof Stevpris anchor tested in soft clay. Fig. 8.40 shows the dimensions of model anchor.

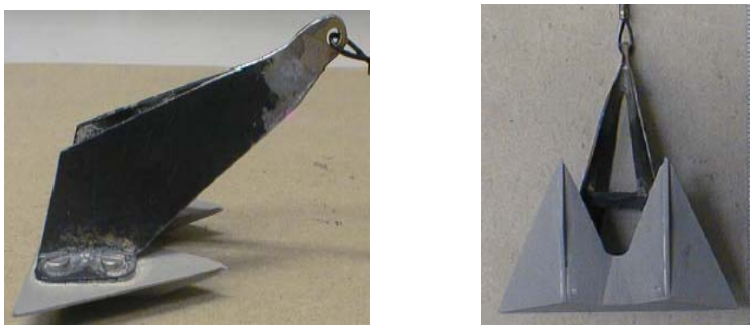

a. Side of model anchor b. Bottom of fluke

Fig. 8.39 Model anchor used centrifuge test (Phillips, R. 2001)

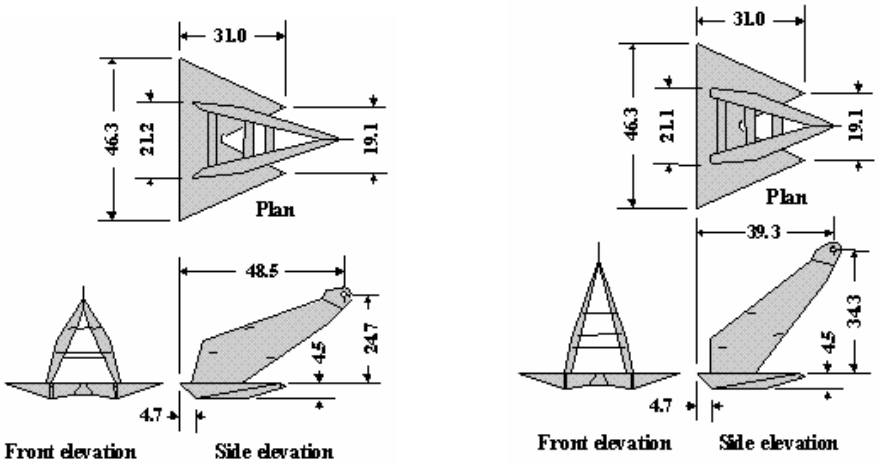

b. Fluke-shank angle -32^{o} b. Fluke-shank angle -50^{o}

Fig. 8.40 Dimension of model anchor (unit: mm)

8.4.1 Fluke-shank angle of 32 degree

Table 8.14 gives the details of the simplified anchor used in the simulation and the undrained soil strength for the test. Model anchor is simplified as shown in Fig. 8.41 for UBM simulation. The undrained strength is zero at seabed and the strength gradient S_g is 1.0 kPa/m. According to the in-flight vane tests, the average sensitivity is approximately 2.4 after 500 degrees of vane rotation. However the ratio for T-bar extraction resistance to insertion resistance is about 0.7, in other words a sensitivity of about 1.4. Fig. 8.42 shows a plot of anchor capacity versus drag distance at the attachment point, and Fig. 8.43 shows penetration depth versus drag distance.

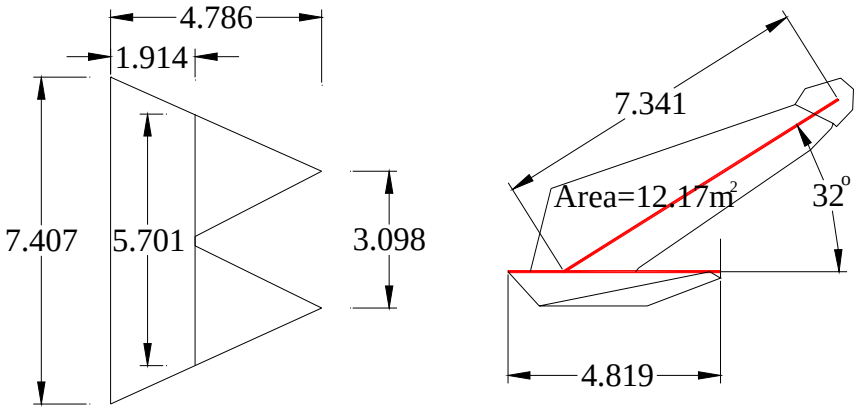

(a)Fluke (b) shank

Fig. 8.41 Geometries of simplified Stevpris anchor for fluke-shank angle of 32°

Table 8.14 Prototype anchor geometry and soil condition for F-S angle of 32 degree

Property	Value
Anchor weight, W_a(kN)	373.3 kN
Shank length, L_s(m)	7.341
Shank width, W_s(m)	1.658
Fluke length, L_f(m)	4.786
Fluke width, W_b(m)	Varied
Fluke depth, D_f(m)	0
Fluke-shank angle, θ_{fs} (degree)	32
Anchor line diameter, b(m)	0.24
Surface undrained shear strength, S_{uo} (kPa)	0
Undrained shear strength gradient, S_{ug}(kPa/m)	1

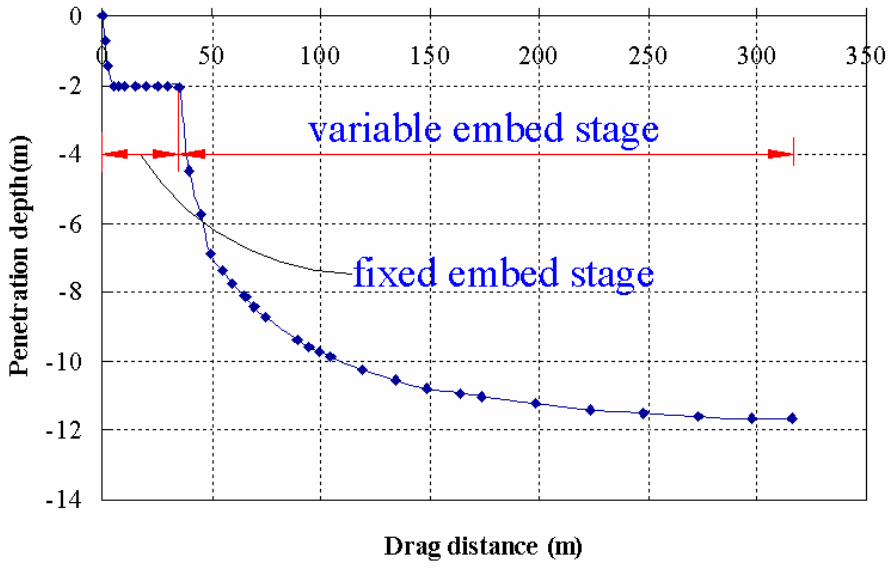

Fig. 8.42 Penetration depth vs. drag distance for fluke-shank angle of 32°

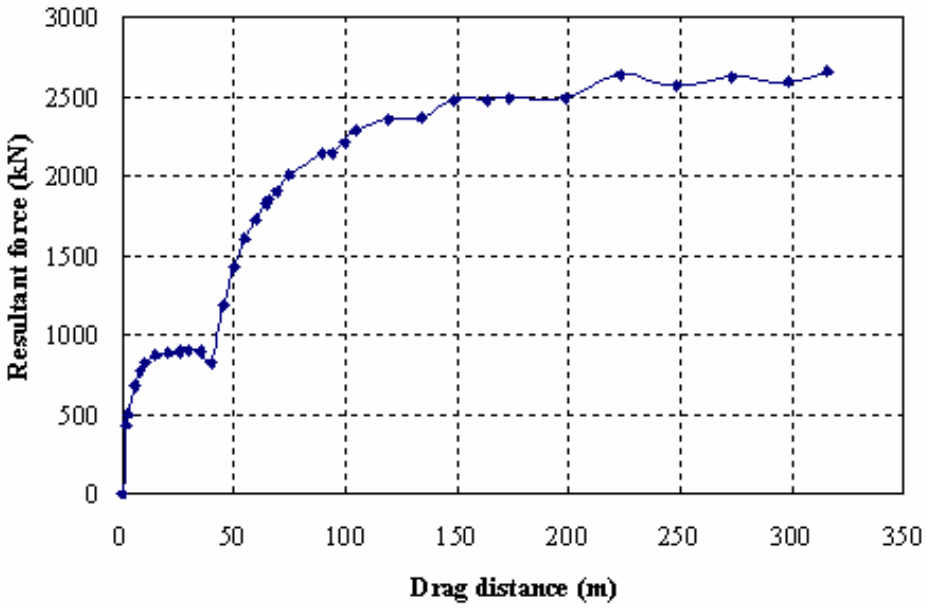

Fig. 8.43 Resultant forces vs. drag distance for Fluke-shank angle of 32°

Based on observations during the test, Randolph concluded that the anchor translated parallel to the bottom surface of fluke not the top surface as shown in Fig. 8.44. Thus, in this simulation using UBM, anchor translates with bottom of fluke.

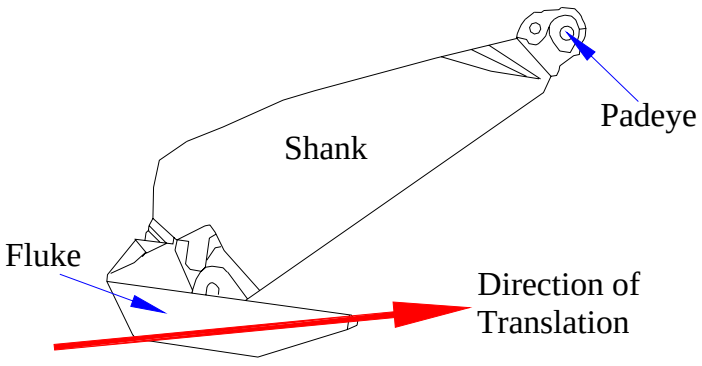

Fig. 8.44 Direction of travel of drag anchor (Phillips, R. 2001)

For the purpose of this study I removed the fixed embedment stage, and simply stated at the variable embedment stage. Fig. 8.45 and 8.46 show the comparisons of the test and the simulations for varying condition as shown in Table 8.14. According to the parameter study in Section 7.5.3, the trajectory curve does not depend on the magnitude of undrained strength gradient. In this comparison the trajectory curve matches the results of the centrifuge test. However, the resultant force at anchor line attachment point does not match the centrifuge test result. Thus, we postulate that the undrained strength may be stronger than suggested by the strength data. So I tried to simulate with several undrained strength gradient and sensitivity. As a result, as shown in Fig. 8.46, the simulation with undrained shear strength gradient of 1.5 and sensitivity of 1.0 was well matched with measured data.

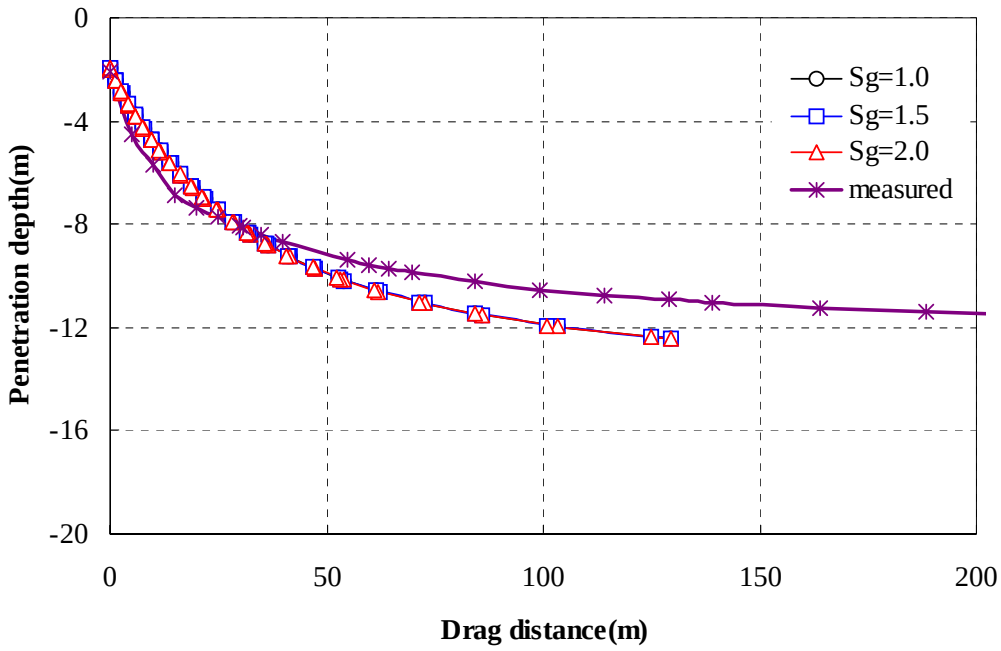

Fig. 8.45. Penetration depth vs. drag distance for F-S angle 32^{o} (S_t=1)

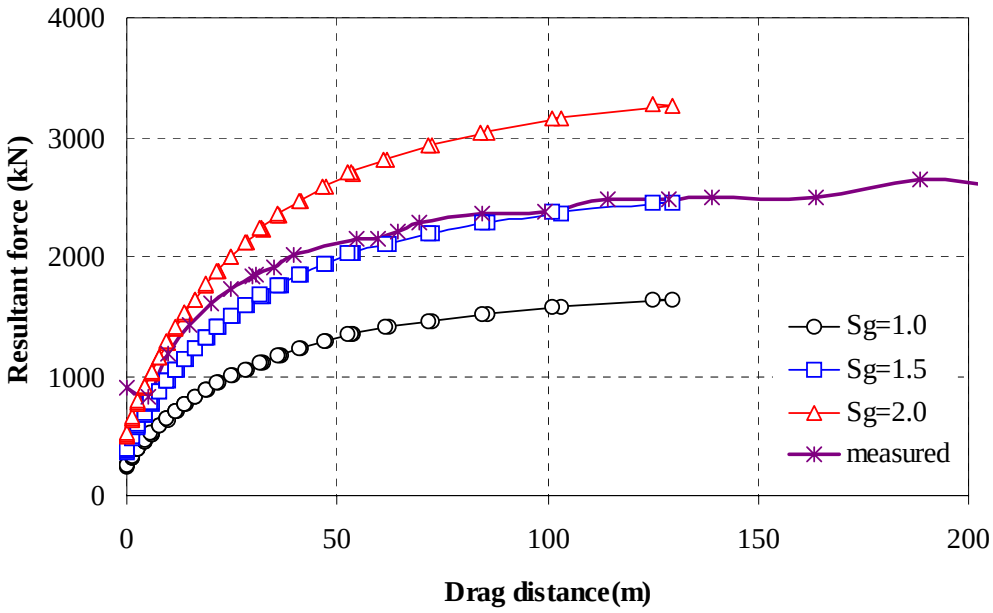

Fig. 8.46 Resultant force vs. drag distance for 32^{o} of F-S angle (S_t=1)

8.4.2 Fluke-shank angle of 50 degree

In this section, a Stevpris anchor with a 50 degree of fluke-shank angle is simulated and compared with test results of a centrifuge model anchor. Table 8.15 shows the geometry and soil conditions for the model anchor. The Stevpris anchor is simplified as shown in Fig. 8.47.

Table 8.15 Anchor geometry and soil condition for F-S angle of 50 degrees

Property	Value
Anchor weight, W_a(kN)	373.3
Shank length, L_s(m)	7.294
Shank width, W_s(m)	1.694
Fluke length, L_f(m)	4.786
Fluke width, W_b(m)	Varied
Fluke depth, D_f(m)	0
Fluke-shank angle, θ_{fs} (degree)	50
Anchor line diameter, b(m)	0.24
Surface undrained shear strength, S_{uo}(kPa)	0
Undrained shear strength gradient, S_{ug}(kPa/m)	1.0

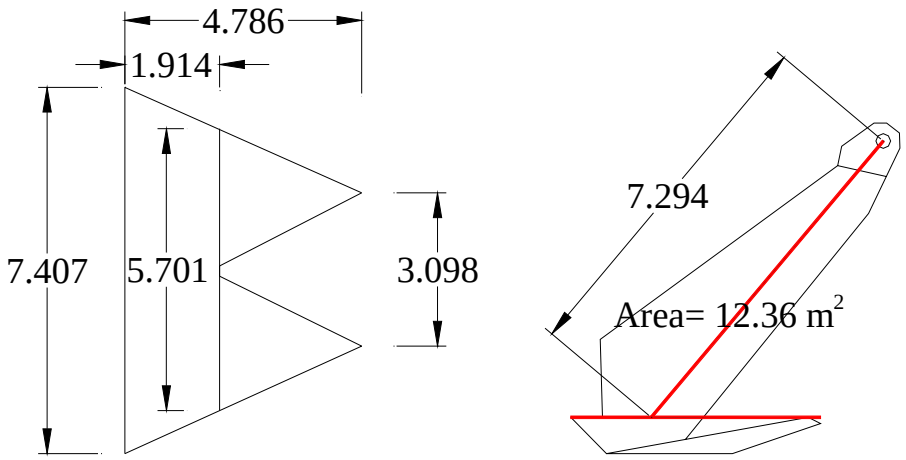

(a)Fluke (b) shank

Fig. 8.47 Geometries of simplified Stevpris anchor for F-S angle of 50°

Fig. 8.48 shows a plot of anchor capacity versus drag distance at the attachment point, and Fig. 8.49 shows penetration depth versus drag distance for fluke-shank angle of 50 degrees. A comparison between penetration depth versus drag distance for the model and simulation is shown in Fig. 8.50 and anchor capacity versus drag distance is shown in Fig. 8.51. Note that anchor installation stops at a certain depth due to a limitation in the depth of the centrifuge tester. The anchor needs some drag distance to set itself and this initial drag distance is removed. We have shown that the trajectory curve does not depend on strength gradient S_g in previous parameter studies. We have confirmed this behavior with the results shown in Fig. 8.50 where varying the strength gradient has virtually no effect on the penetration curves.

For the strength profile, $S_u = 1.0\,z$, the simulation curve matches measurement data well, but again the anchor capacity curve comparison does not match. To explore the possible reasons for this, the strength gradient is varied from 1.0kPa/m to 3.0kPa/m and it is found that anchor capacity versus drag distance curve is matches the case where the strength gradient is 1.5. It is concluded that the soil may be strength than the soil strength measurements suggest. For this case we assumed that the soil disturbance is not significant during anchor installation because the sensitivity is assumed to be one.

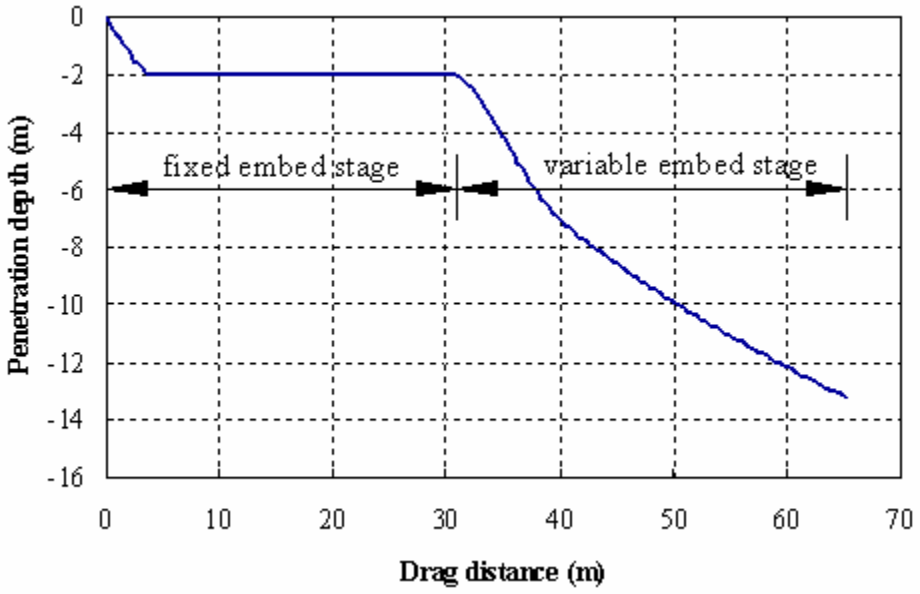

Fig. 8.48 Penetration depth vs. drag distance for F-S angle of 50°

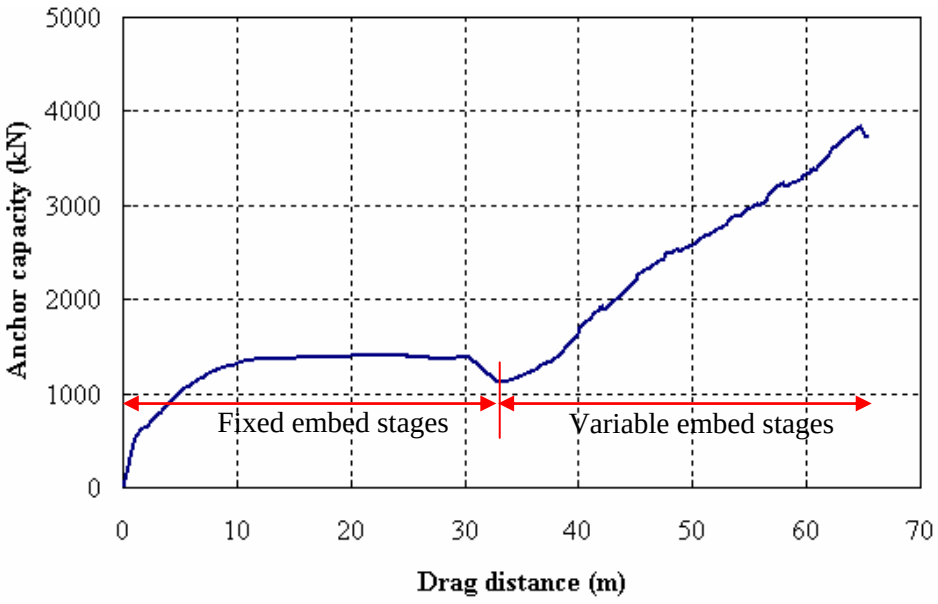

Fig. 8.49 Resultant forces vs. drag distance for F-S angle of 50°

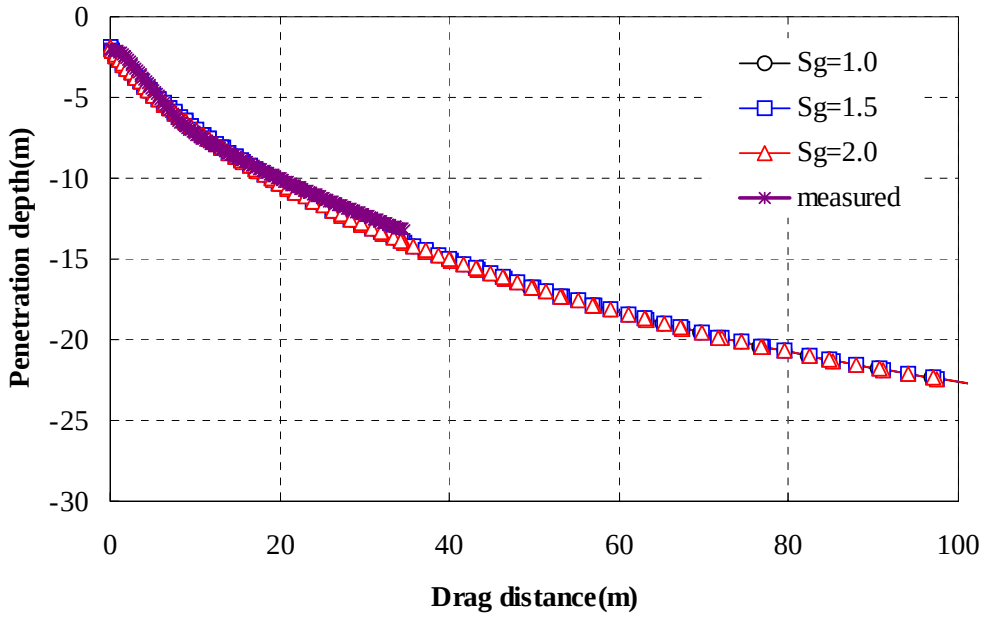

Fig. 8.50 Penetration depth vs. drag distance for 50° of F-S angle ($S_t = 1$)

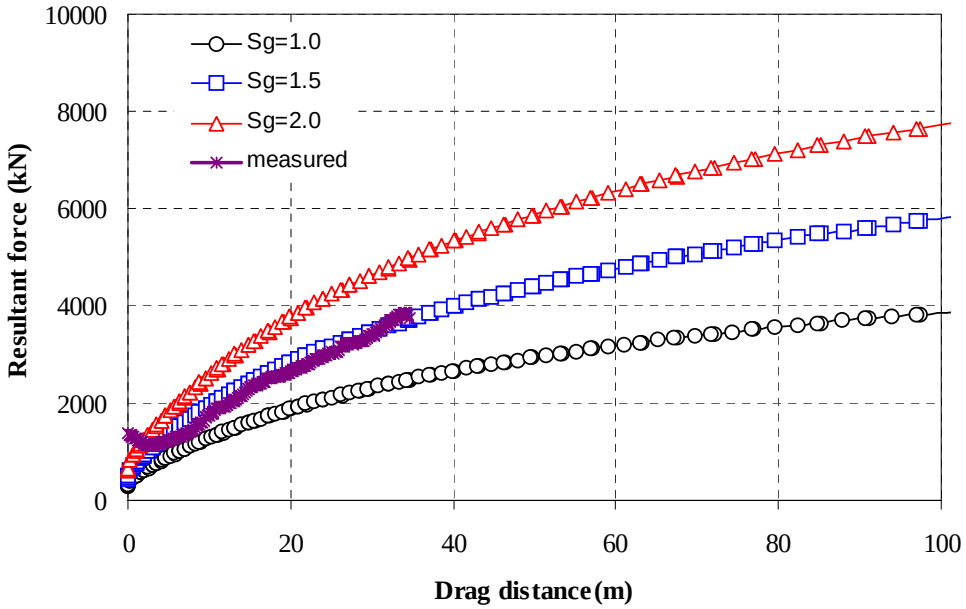

Fig. 8.51 Resultant forces vs. drag distance for 50° of F-S angle ($S_t = 1$)

8.5 Comparison with other methods

In this section, four different methods are compared with the UBM. These data are given by anchor installation analysis of deepwater anchor project in API (Murff 2001). The UBM simulation used same anchor and anchor line geometries and soil properties as shown in Fig. 8.52 and Table 8.16. At the initial position, an anchor is embedded at a depth of 1m and shank is placed parallel to the seabed. It is assumed that an anchor line is catenary so that it reaches horizontally at the mudline.

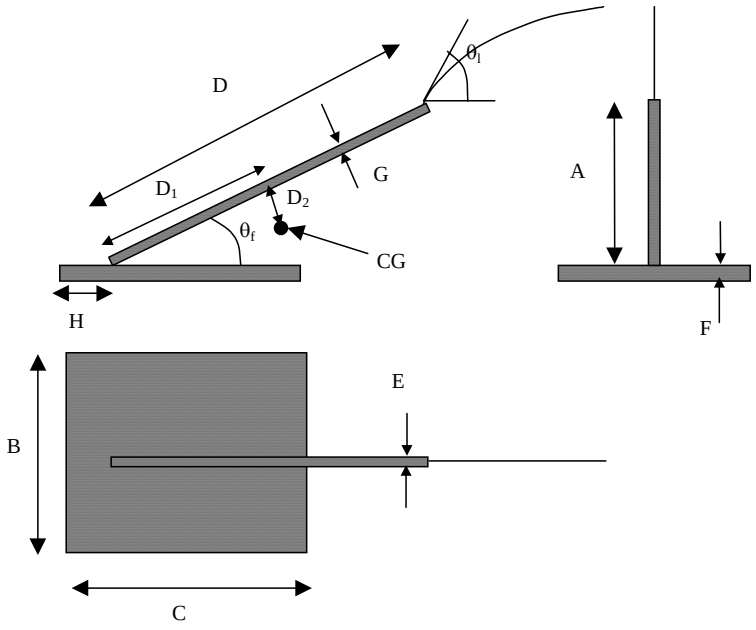

Fig. 8.52 Geometries model anchor for comparison of the UBM and other methods

Table 8.16 Anchor and anchor line dimensions and soil properties for comparison with other methods

Anchor	A	m	2.98
	B	m	3
	C	m	1.5
	D	m	3.89
	D_1	m	0.7
	D_2	m	0.49
	E	m	0.2
	F	m	0.2
	G	m	0.2
	H	m	0
	θ_f	[°]	50
	W_a	kN	15
Soil	S_{u0}	kPa	0
	S_g	kN/m	1.5
	γ	kN/m^3	18
	S_t	-	3.33
Anchor line	type	wire	
	Dia.	mm	50

Table 8.17 shows descriptions and developers of prediction methods used in this study.

Table 8.17 Summary of prediction methods (Murff et al. 2001)

Name	Description	Developer /Reference	Comments
NR, Syddig6	Advances and rotates anchor based on incremental limit equilibrium analysis w/ compatible anchor line calculations	Neubecker and Randolph (1995, 1996a), Thorne (1998)	Angle of resultant soil resistance assumed to be a function of the anchor geometry. Simplified closed form expression for simple cases.
DIGIN	Advances and rotates anchor based on incremental limit equilibrium analysis w/ compatible anchor line calculations	DNV (1998), Dahlberg (1998)	Assumes distribution of soil resistance forces on the anchor components

Fig. 8.53 shows the penetration depth versus the drag distance. The UBM curve is the shallowest of trajectory curves. Other three methods are overlapped until drag distance of 100m, after this point the curves are diverted. The curves of resultant forces at a shackle versus drag distance are nearly matched except the DNV method as shown in Fig. 8.54. The DNV predicts the lowest resultant force at a shackle.

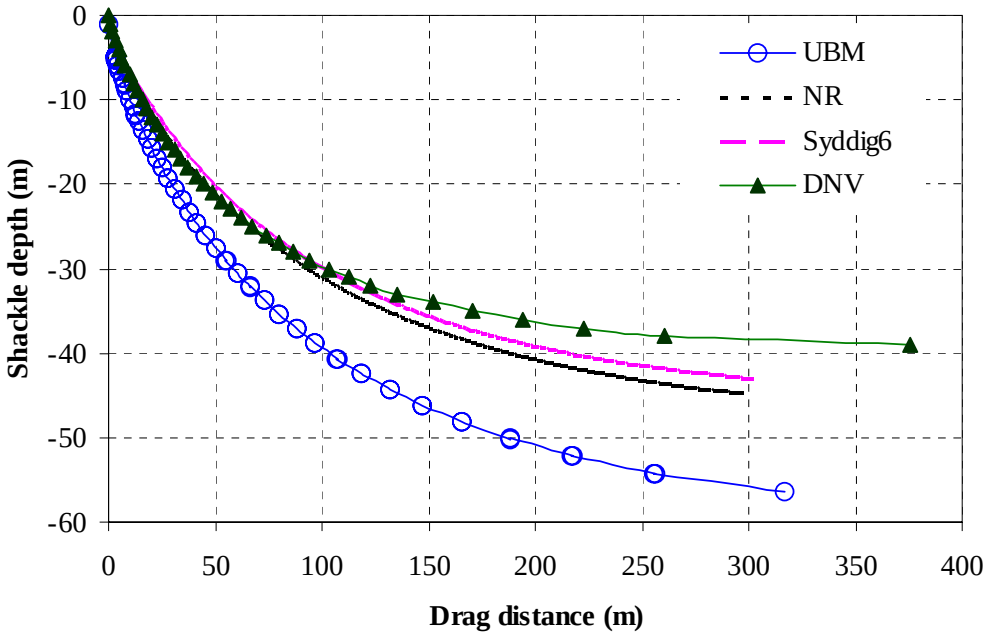

Fig. 8.53 Penetration depth vs. drag distance (S_t=3.3)

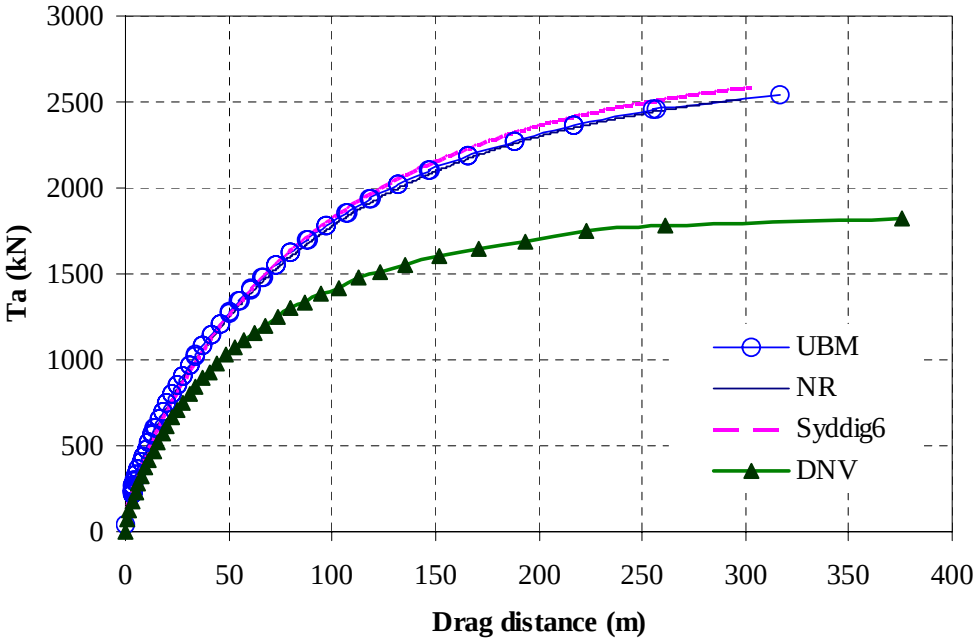

Fig. 8.54 Resultant force vs. drag distance (S_t=3.3)

CHAPTER IX

SUMMARY AND CONCLUSIONS

This study presents a upper bound plastic limit analysis to predict the trajectory of drag embedment anchors and estimate the anchor capacities. A virtual work analysis is formulated in terms of unit soil bearing resistance factors. For each increment of penetration analyzed in the drag embedment process, the coordinates of the center of rotation are optimized to determine the minimum collapse load corresponding to a given anchor orientation. Consideration of the anchor line configuration permits the determination of a unique anchor collapse load and orientation. An attractive aspect of the upper bound method is that the collapse mechanism is selected through an optimization procedure rather than relying on intuitive assumptions or empirical factors.

The unit bearing resistance factors presented in this dissertation were applied to general anchor geometries such as a composite fluke comprising rectangular and triangular plates. To do this, the study of interaction relationship was carried out in the case of a non-rectangular plate and normally consolidated clay. Thus, it is considered that the bearing resistance factor, n_{pf}, is six at the reference point and twelve at the edge of the fluke with quadric function.

To better understand the anchor behavior, extensive parameter studies were carried out varying the properties of the anchor, anchor line, and soil. Parametric studies using this model suggested the following:

1. In the case of uniform soil strength**,** energy dissipation rate varies linearly with moment of inertia.
2. Weight of the anchor is not an important factor in anchor behavior.
3. Increasing the length of the shank leads to a shallower penetration depth.
4. The shape of the shank does not strongly affect anchor behavior. Thus, it is reasonable to model it as a rectangular plate for the purposes of analysis.
5. Increasing the diameter of an anchor line leads to a shallower the penetration depth.
6. Penetration depth is not affected by either the magnitude of the undrained soil strength, S_u, or the soil strength gradient, S_g. This study considered only conditions of uniform strength, or linearly increasing strength with depth.

For the purpose of verification of the UBM, comparisons were made to selected field tests and design charts for Stevpris MK5 and Bruce FFTS MK4. The UBM predictions were also compared to centrifuge test results. These comparisons showed predicted anchor trajectories to be in good agreement with measured data. However, anchor capacities are affected by the parameters such as sensitivity and soil strength gradient. The comparisons between the UBM and the design charts for manufacturer's anchors show that design charts are more conservative than the UBM for larger anchor sizes.

REFERENCES

American Petroleum Institute (API) (1995). *Recommended practice for design and analysis of station keeping systems for floating structures*. American Petroleum Institute, API-RP-2SK., Washington, D.C..

Aubeny, C.P., Murff, J.D. and Roesset, J.M. (2001). "Geotechnical issues in deep and ultra deep waters." *International Journal of Geomechanics*, 13-25.

Bea, R. G., and Audibert, J. M. E. (1979). "Bearing capacity for foundations with cyclic loads.", *ASCE Journal of Geotechnical Engineering*, 114(5), 540-555.

Bruce Anchors (undated). *Brochure of Bruce FFTS MK 4*. Bruce Anchor Company, Douglas, England.

Chen, W.F. and Liu, X.L. (1990). *Limit analysis in soil mechanics*. Elsevier Publishing Co., Amsterdam, The Netherlands.

Dahlberg, R. (1998). "Design procedures for deepwater anchors in clay.", OTC 8837, *Proc. of the 30th Annual Offshore Technology Conf.*, Houston, Texas.

Dahlberg, R., and Strøm, P. (1999). "Unique onshore tests of deepwater drag-in plate anchors.", OTC 10989, *Proc. of the 31st Annual Offshore Technology Conf.*, Houston, Texas, 1-11.

Degenkamp, G., and Dutta, A. (1989). “Soil resistance to embedded anchor chains in soft clay.”, *ASCE Journal of the Geotechnical Engineering Division*, 115(10), 1420-1438.

DNV (1998). *Fluke anchors in clay – proposal for recommended practice No. 601*, Det Norske Veritas, Oslo, Norway.

DNV (1999a). *Design and installation of drag embedment anchors in clay, Recommended Practice RP-E301*, Det Norske Veritas, Hovik, Norway.

DNV (1999b). *Desgn and installation of drag-in plate anchors in clay, Recommended Practice RP-E302*, Det Norske Veritas, Hovik, Norway.

Dunnavant, T. W., and Kwan, C-T. T. (1993). “Centrifuge modeling and parametric analyses of drag anchor behavior.”, OTC 7202, *Proc. of the 25th Annual Offshore Technology Conf.*, Houston, Texas.

Foxton, P. (1997). “Latest development for vertically loaded anchors.”, *2nd Annual Conf. on Mooring & Anchoring*, Aberdeen, Scotland.

Gault, J. A. and Cox, W. R. (1974), “Method for predicting geometry and load distribution in an anchor chain from a single point mooring buoy to a buried anchorage.”, OTC 2062, *Proc. of the 6th Annual Offshore Technology Conf.*, Houston, Texas.

Graaf, I. F de, Verruijt, A., and Degenkamp, G. (1997). “The capacity of deep embedded anchors.”, *Proc. of the 8th International Conf. on Behaviour of Offshore Structures*, Delft, Netherlands, 125-131.

Merifield, R. S., Sloan, S. W. and Yu, H. S. (1999). *Stability of plate anchors in undrained clay, Research Report No. 174.02.1999*. Department of Civil, Surveying and Environmental Engineering, University of Newcastle, Australia

Merifield, R. S., Lyamin, A.V., Sloan, S. W., and Yu, H. S. (2003). "Three-dimensional lower bound solutions for stability of plate anchors in clay.", *Journal of Geotechnical Engineering Division*, ASCE, 129(3), 243-253.

Murff, J.D. (1999). "The mechanics of pile foundation collapse analysis, design, construction and testing of deep foundations." *Geotechnical Special Publication OTRC*, 88, 76-95.

Murff, J. D., and Anderson, H. (2001). *Deepwater anchor design practice-first year report to API.* Offshore Technology Research Center, Texas A&M University, College Station, Texas.

Murff, J.D. (2002). *Geo-mechanics class notes*. Texas A&M University, College Station, Texas.

NCEL (1987), *Drag embedment anchors for navy moorings*, Naval Civil Engineering Laboratory, Port Hueneme, California, Tech data Sheet 83-08R.

Neubecker, S. R., and Randolph, M. F. (1995). "Profile and frictional capacity of embedded anchor chain.", *Journal of Geotechnical Engineering Division*, ASCE, 121(11), 797-803.

Neubecker, S. R., and Randolph, M. F. (1996a). “The performance of drag anchor and chain systems in cohesive soil.”, *Marine Georesources and Geotechnology*, 14, 77-96.

Neubecker, S. R., and Randolph, M. F. (1996b). “Performance of embedded anchor chains and consequences for anchor design.”, OTC 7712, *Proc. of the 28th Annual Offshore Technology Conf.*, Houston, Texas, 1-10.

O’Neill, M.P., Bransby, M.F. and Randolph, M.F. (2003), "Drag anchor fluke–soil interaction in clays.", *Canadian Geotechnical Journal*, 40, 78-94.

Ruinen R. (2000). “The use of drag anchors and vertical loaded anchors (VLAS) for deep water moorings.” *Continuous Advances in Mooring and Anchoring*. Aberdeen, Scotland.

Ruinen R., and Degenkamp G. (1999). “Advances in the development and operational experience with Stevmanta VLAs in deep water environments.”, *4th IBC Conf. Mooring & Anchors*, Aberdeen, Scotland.

Phillips, R. (2001). *Advanced concept ARO 2001 centrifuge workshop.* US Army Engineering Research and Development Center, Vicksburg, Mississippi.

Stewart, W. P. (1992). “Drag embedment anchor performance prediction in soft soils.”, OTC 6970, *Proc. of the 24th Annual Offshore Technology Conf.*, Houston, Texas, 241-248.

Stewart Technology Associates (1995), *STA-Anchor user manual and technical documentation*, Stewart Technology Associates, Houston, Texas.

Thorne, C. P. (1998). “Penetration and load capacity of marine drag anchors in soft clay.”, *Journal of Geotechnical and Geoenvironmental Engineering*, ASCE, 124(10), 945-953.

Vivatrat, V., Valent, P. J., and Ponterio, A. A. (1982). “The influence of chain friction on anchor pile design.”, OTC 4178, *Proc. of the 14th annual Offshore Technology Conf.*, Houston, Texas, 153-156

Vryhof Anchors (1999). *Anchor manual 2000*. Krimpen ad Yssel, Netherlands.

VITA

Byoung Min Kim was born on June 27, 1968 in Jeonnam, Korea. He received his Bachelor of Applied Science degree in civil engineering from Korea University (Seoul, Korea) in February 1995, his Master of Science degree in civil engineering from Korea University (Seoul, Korea) in February 1997. For the next three years, he worked as a engineer in Daewoo Engineering and Construction Co. (Seoul, Korea), and he worked for several Consultant Engineering Company (Seoul, Korea). In September 2002, he started research towards this doctoral dissertation at the Texas A&M University, and received his Ph.D. degree from the Department of Civil Engineering in December 2005.

Address:

Byoung Min Kim

Jukong Apartment 305dong 104 ho

Gwangju city Gwangsan gu Woonnam dong

Republic of Korea, 506-764

Email Address:

kbm1004@hotmail.com